# Ultrafast electron emission and associated electron dynamics from low dimensional nanostructures

Ph.D. Thesis

*Author*:
**Madas Saibabu**

*Supervisor*:
**Mousumi Upadhyay Kahaly (Ph. D.)**
ELI-ALPS, ELI-HU Non-Profit Ltd., Wolfgang Sandner utca 3., Szeged, H-6728, Hungary

*Co-supervisor*:
**Subhendu Kahaly (Ph. D.)**
ELI-ALPS, ELI-HU Non-Profit Ltd., Wolfgang Sandner utca 3., Szeged, H-6728, Hungary


Doctoral School of Physics
Institute of Physics
University of Szeged
Faculty of Science and Informatics
2023
Szeged

*This thesis is dedicated to my parents, sister and my wife.*

# Contents

# List of Figures

# List of Tables

# Chapter 1

# Introduction

Materials manifest a diverse array of electronic phases, encompassing categories such as metals, semimetals, semiconductors, superconductors, and insulators [1–4]. Of particular intrigue is the observation that the physical attributes of these systems can be substantially modulated by external parameters. The investigation of a material's response within a laboratory environment, specifically its response to external perturbation such as temperature fluctuations, structural modification, chemical modification, interfacing with other material, external field, etc is of paramount significance in the comprehensive assessment of the material's stability, functionality, and its potential applications. Electrons, being light subatomic particles with a charge, respond rapidly to temperature variations. In materials, electronic motion represents an ultrafast phenomenon, occurring on timescales in the order of sub-femtoseconds to attoseconds ($10^{-15} - 10^{-18}$ seconds) [5], thanks to their low mass and high mobility. In contrast, ion motion is considerably slower, taking place on the timescale of picoseconds ($10^{-12}$ seconds) or longer due to their comparatively heavier mass, demonstrating a stark difference in temporal dynamics. Consequently, understanding and manipulation of ultrafast electronic processes in materials can greatly influence the materials response, like electron emission phenomena and external field-induced effects.

The ultrafast electron emission and electron dynamics depends on many factors, such as the nature of the material, i.e. the electronic structure, size, dimensionality, the type of external perturbation, among many others. Advances in electron emission materials and physics are driving a renaissance in science and technology, opening up new applications, such as energy conversion [6, 7] and ultrafast electronics [8], as well as improving traditional applications in electron imaging and high-energy science. These requirements have propelled the study of new materials and their emission mechanisms, often taking advantage of the unique electronic and thermal properties of low dimensional materials and nanoscale phenomena [8–10]. In contrast with their bulk counterparts, low dimensional structures may provide near-instantaneous electron emission [7, 11, 12]. They are fabricated from their bulk counterparts, resulting in spatial confinement [13] of the motion of electrons in a crystal in one, two or even all three directions. With adequate confinement, quantum mechanical effects lead to the discretization of the energy spectrum, i.e. the quantization of allowed energy levels and the momenta of electrons. Such quantization has profound effects on the ground state properties of these systems, as well as on the coupling between the electronic, nuclear and spin degrees of freedom [14], which consequently dictates the dynamic behavior too. The dimensionality of a material plays a crucial role in determining its electronic properties and ultrafast electron dynamics. Understanding and controlling these dynamics enable the design of novel materials and devices with enhanced functionalities for a wide range of technological applications.

Since the groundbreaking discovery of graphene in 2004 [15], the world of two-dimensional (2D) materials have been continuously expanding, comprising a vast range of condensed matter phases, such as metals [1], semiconductors [2, 16], insulators [17], semimetal [15], topological semimetal [3, 18], superconductor [19], Mott insulator [20], Bose-Einstein condensates [21]. 2D materials with atomic-thin thickness have gained immense popularity as a revolutionary material class that hold considerable potential in solid state technology. Recent advancements in fabrication techniques and

an enhanced understanding of the fundamental physical properties of 2D materials have paved the way for the successful integration of 2D materials based components across a broad range of device applications. These applications span a wide spectrum, encompassing fields such as optoelectronics [22], nanoelectronics [22], plasmonics [23], photodetection [24], nonlinear optics [25, 26], nanophotonics [27, 28], vacuum electronics [11], energy storage and conversion [29–31], and extending to emerging device paradigms like valleytronics [32], spintronics [33], twistronics [34], artificial neurons [35], and quantum emitters [36]. One of the significant features of 2D materials that are absent in their bulk counterparts is the possibility of mixing and matching 2D materials to obtain heterostructure with desirable properties.

One of the key factors which influences the ultrafast electron dynamics in materials is the external perturbation, as it introduces a powerful means to control and explore the behavior of electrons within materials [37]. External perturbations are of different kinds, including time-dependent laser fields (AC field), monochromatic field (DC field), temperature gradients, among many others. Ultrafast perturbations, such as femtosecond laser pulses (AC field), enable the investigation of ultrafast electron dynamics, offering insights into processes occurring on incredibly short timescales. This is pivotal for understanding energy relaxation and carrier dynamics in materials. Among several possible scenarios, the excited electrons can either escape in to the vacuum [38] or recombine with the parent ion, resulting in various ultrafast processes, such as high harmonic generation [39], etc. Furthermore, monochromatic pulses (DC field) play a crucial role in electron emission studies. A monochromatic pulse refers to electromagnetic radiation, often in the form of light, where all the photons have the same energy or frequency. The use of monochromatic pulses in electron emission studies provides a versatile and powerful tool to investigate electronic properties, excite specific states, and manipulate quantum behavior. Their precise energy control and selective excitation capabilities contribute to a deeper understanding of electron emission mechanisms and enable the exploration of material properties at the atomic and subatomic levels. To have an in-depth understanding on the behaviour of the materials under the influence of AC and DC fields, an integrated study is essential by considering suitable theoretical approaches and simulations, which is addressed in this study.

In my thesis, the primary aim is to understand the possible ways to tune and engineer the electron emission processes, by investigating diverse electron emission phenomena in relation to different materials and dimensionalities. As obvious, the electron emission process in a material is profoundly influenced by the internal electron dynamics within that material, such as energy distribution and thermalization of electrons, many-body effects that can alter the electronic band structure [6, 40] and affect the efficiency of electron emission mechanisms. Indeed many-body interactions, in particular exchange or correlation interactions between multiple electrons, play a significant role in the behavior of many atomic, molecular, and solid systems. The effects can manifest as large variations in binding energies, excitations, linear and nonlinear response and many other chemical/physical properties. Consequently, ultrafast electron dynamics within a material are affected.

Ultrafast electron dynamics captures the imprint of material's electronic and structural properties, providing valuable insights into how they respond to external stimuli and revealing the fundamental characteristics that define their behavior on extremely short timescales. This imprint encompasses information about energy transfer processes, carrier dynamics, and the interaction of electrons with the material's lattice structure, all of which are essential for understanding and manipulating the electronic properties of materials [7, 41]. Thus a combined understanding of electron emission and electron dynamics in materials have the power to influence not only the energy distribution but also the mechanisms governing electron ejection, leading to a spectrum of emission processes like photoemission, or thermionic emission. Thus, I also attempt to understand the ultrafast electron dynamics in atoms and low-dimensional solid materials, which is not only crucial for fundamental research but also has far-reaching implications in the development of advanced electron sources, photodetectors, and high-speed electronics, shaping the landscape of modern technology and scientific exploration.

It is important to note that conducting real-time experiments comes with inherent complexities, and access to large-scale experimental facilities which often are difficult to access. Through the utilization of numerical simulations and appropriate theoretical models, as attempted in my thesis, we can gain

a comprehensive understanding of intricate details and provide complementary knowledge, valuable support to experimental observations. This dissertation, driven by simulations, delves into the intricate realm of electron dynamics within atoms, metals, and two-dimensional nanostructures when subjected to external perturbations, including both DC and AC fields. It commences with a concise introduction, emphasizing the significance of ultrafast electron dynamics in materials, elucidating the factors that influence these dynamics, and delineating the characteristics of various electron emission processes. In the following Section 1.1, a brief introduction to the various kinds of emission processes and how they occur is explained.

## 1.1 Predominant electron emission processes

Electron emission can be categorized in to four types: (i) thermionic emission, (ii) photoelectric emission, (iii) secondary emission, and (iv) field emission. Except in field emission, electron emission occurs when the free electrons in the solid gain sufficient energy to overcome the potential barrier available at the surface of the solid. Whereas in *Field emission*, due to the intense external electric field, the surface potential barrier can be lowered, helping the electron to tunnel through the barrier and escape into the vacuum. The difference between the various forms of emission is the source of energy induced in to the solid. *Thermionic emission* occurs when heat is supplied to the solid. When the free electrons in solid gain energy from photons, *photoelectric emission* occurs. *Secondary emission* occurs when the energy required is gained from the kinetic energy of a bombarding particle. Sommerfeld's free-electron theory for metals, introduced in his 1928 work [42], has laid the foundation for numerous quantum mechanical theories concerning electron emission from metallic materials. Formulas derived from this theory are still in use to analyze relevant experimental data. For that reason, the free-electron theory is a good starting point for studying electron emission in solids, which is described in the following (1.1.1).

### 1.1.1 Electron emission from metals: The free-electron theory

The fundamental assumption in Sommerfeld's [42] free-electron theory for metals [43] is that the conduction band electrons in the metal are considered to be free, i.e. there is no interaction between the conduction band electrons and the nucleus. In this framework, one assumes that the free electronic states could be expressed as a plane wave $\psi_k$, which is given by

$$\psi_k(r) = \frac{1}{\sqrt{L^3}} \exp ikr \ , \tag{1.1}$$

where $L$ is the dimensionality of the metal, $L^3$ is assumed to be a very large volume of metal, $r$ is the position, and $k$ is the wave vector given by $k = \frac{2\pi}{L}(n_x, n_y, n_z)$, where $n_x, n_y,$ and $n_z$ are positive or negative integers. The energy of free electrons is given by $E = \hbar^2 k^2/2m$, where $m$ and $\hbar$ is the mass of the electron and the reduced Planck constant, respectively. To describe the valence electron states correctly, one should consider the spin orientation of the electron. For a given $k$, there are two electronic states (spin up and spin down). For a large $L$ (tending to $\infty$), the total number of electron states per unit volume with energies in the range $E$ and $E + dE$ is given by [44]

$$\rho(E)\ dE = \frac{2}{(2\pi)^3} \int\int\int_{E}^{E+dE} d^3k \ = \frac{1}{2\pi^2} \left(\frac{2m}{\hbar^2}\right)^{\frac{3}{2}} \sqrt{E}\ dE \ . \tag{1.2}$$

Within the framework of the Fermi-Dirac distribution, the probability of finding an electron in a particular state with energy $E$ is given by $f(E) = \frac{1}{1+\exp\left[(E-E_f)/k_B T\right]}$, where absolute temperature is denoted by $T$, and Boltzmann constant is represented by $k_B$. Under equilibrium conditions, the rate at which electrons, assuming that they move in direction parallel to $y$-$z$ plane from left to right, traverse a unit area, within a range of total energy from $E$ to $E + dE$ and normal energy, defined by $E_x = \hbar^2 k_x^2/2m$ between $E_x$ and $E_x + dE_x$ and denoted by $N(E, E_x)dE\ dE_x$, which is given by

$N(E, E_x)\ dE\ dE_x = \frac{2f(E)}{(2\pi)^3} \int\int\int_{(E,E_x)} \upsilon_x d^3k$, where $\upsilon_x \equiv \frac{1}{\hbar}\frac{\partial E_k}{\partial k_x} = \frac{\hbar k_x}{m}$ is the velocity of electrons moving in the normal direction (let it be $x$ direction) per unit area towards the metal's surface. $(E, E_x)$ denotes the states of electrons with a total energy ranging from $E$ to $E + dE$ and normal energy ranging from $E_x$ to $E_x + dE_x$ must encompass within the integration. With further simplification, one can show that $N(E, E_x)\ dE\ dE_x = \frac{m}{\hbar^3 2\pi^2} f(E) dE\ dE_x$. Hence, the total number of electrons whose normal energy is within the range of $E_x$ to $E_x + dE_x$ and impinge the barrier's surface from inside the metallic material is given as

$$\begin{aligned} N(E_x, T)\ dE_x &= \frac{m\ dE_x}{\hbar^3 2\pi^2} \int_{E_x}^{\infty} f(E)\ dE \\ &= \frac{m k_B T}{\hbar^3 2\pi^2} \ln\left[1 + \exp\left(-\frac{E_x - E_f}{k_B T}\right)\right] dE_x\ . \end{aligned} \tag{1.3}$$

Equation 1.3 is known as the supply function. In the following (1.1.2), using the free-electron theory discussed in this section, the mathematical framework to obtain electron emission from a metal surface is given.

### 1.1.2 Electron emission from a surface of a metallic material

Let's examine a semi-infinite metal extending from $x = -\infty$ to approximately $x = 0$. According to the free-electron theory of metals, the electron within the metal encounters a uniform potential. A specific amount of energy, equivalent to metal's work function ($\phi_B$), should be provided to the metal in order to emit an electron from the metal's surface. in classical electrostatics, the electron which is located at a certain distance from the ideal conductor's surface is drawn towards it, and this attraction is described by the well-established image potential, which is equal to $-e^2/16\pi\epsilon_0 x$. The negative sign indicates that the assumption here is that the $x$-axis extends outward from the metal's surface. Therefore, the potential experienced by the electron on the vacuum side of the metal-vacuum interface is described as follows

$$U(x) \approx E_f + \phi_B - \frac{e^2}{16\pi\epsilon_0 x}\ . \tag{1.4}$$

Many studies have confirmed that Equation 1.4 is valid for $x > 3$Å [45–49]. From the free-electron theory, it is assumed that Equation 1.4 remains applicable up to a crucial point $x_c$, where $U(x_c) = 0$. On the other hand, when the surface of the metal is subjected to an external electric field $F > 0$, an electrostatic component $-eFx$ is introduced to the right-hand side of the Equation 1.4, which can be expressed as

$$U(x) \approx E_f + \phi_B - \frac{e^2}{16\pi\epsilon_0 x} - eFx \qquad \text{for } x > x_c\ , \tag{1.5}$$

$$\approx 0 \qquad \text{for } x < x_c\ , \tag{1.6}$$

here $x_c$ is obtained from $U(x_c) = 0$. As the electric field's influence within the metal is considered insignificant, it is assumed that the total count of electrons with energy ranging from $E_x$ to $E_x + dE_x$ approaching the metal's surface barrier from within is same as its equilibrium value as defined in Equation 1.3. To pass through the surface potential barrier, each of these electrons have the probability $\mathcal{T}(E_x)$ which is determined by either Equation 1.4 or Equation 1.5. Miller and Good [50] derived an analytical expression for the transmission coefficient, which has gained popularity in the study of electron emission. Their approach applies to a slowly changing potential barrier, characterized by having precisely two classical turning points. In other words, when $E_x$ falls below the barrier, there are two real solutions to the equation $E_x - U(x) = 0$, denoted as $x_1$ and $x_2$, with $x_1$ being smaller than $x_2$. It is presumed that $E_x$ lies over the barrier, then these real solutions turn in to complex solutions. Assuming that all the criteria for their approach's suitability are met, the transmission coefficient is

given as

$$\mathcal{T}(E_x) = 1 + \exp\left[\Lambda(E_x)\right]^{-1} , \tag{1.7}$$

where $\Lambda(E_x) = -2i\int_{x_1}^{x_2}\Theta(x)dx$ and $\Theta(x) = \sqrt{\frac{2m}{\hbar^2}[E_x - U(x)]}$. The energy of the electrons in the normal direction, denoted as $E_x$, can be situated either beyond or under the surface potential barrier. When $E_x$ is significantly lower than the surface of the barrier, $\exp\left[\Lambda(E_x)\right] \gg 1$, and Equation 1.7 can be written as $\mathcal{T}(E_x) = \exp\left[-2\int_{x_1}^{x_2}|\Theta(x)|dx\right]$. Therefore, the emitted current density *J(F,T)* can be calculated by taking the product of the supply function $N(E_x, T)$, the total number of electrons emitted per unit area per unit time impinging the barrier from within the metal multiplied by the electronic charge '$e$'. The total current density can be written as [51]

$$J(F,T) = e\int_0^\infty N(E_x,T)\mathcal{T}(E_x)\ dE_x , \tag{1.8}$$

where $F$ and $T$ denote the applied electric field and temperature, respectively. According to the theory suggested by Murphy et al. [52], assuming the validity of the surface barrier defined in Equation 1.5 and utilizes Equation 1.7 to calculate $\mathcal{T}(E_x)$ for this barrier, starting from Equation 1.8, one obtains an expression for $J(F,T)$ that remains applicable for any value of $T$ and $F$. Their theory provides a systematic framework for deriving Fowler-Nordheim formula, which describes emission under intense external fields and low temperatures (Field emission), as well as the Richardson and Schottky formulas for thermionic emission, which applies to high temperatures with either weak or no applied field. As mentioned before, one of the ways to distinguish the emission processes is by how the electrons overcome the finite potential barrier. In the following sections, I will briefly introduce the different types of emission processes.

### 1.1.3 Thermionic emission

Thermionic emission occurs when the emitter's temperature is elevated, normally due to electric heating, and several conduction band electrons gain higher energy compared to other electrons and leak in to higher energy levels. These higher energy electrons may have sufficiently high velocities and a suitable direction that help them to overcome the surface potential energy barrier. At an elevated temperature and weak or zero applied electric field, the majority component of $J(F,T)$ (Equation 1.8) originates from a narrow energy range that is just above the surface potential barrier. For the electrons with energy $E_x \gg E_f$ that can escape, a theoretical analysis of Equation 1.3 results in a universal equation for the current density of electron emission as a function of work function $\phi_B$ and temperature ($T$), which is the standard Richardson-Laue-Dushman equation for thermionic emission [51, 53], and given as follows:

$$J_{RLD} = A_e T^2 \exp\Big[-\frac{\phi_B}{k_B T}\Big] , \tag{1.9}$$

where $J_{RLD}$ is the emitted current density (in the units of $A\ cm^{-1}$), $A_e$ is a constant ($120\ A\ cm^{-2}K^{-2}$), $\phi_B$ is the work function, Boltzmann's constant and temperature are denoted by $k_B$ and $T$, respectively. It is evident from Equation 1.9 that the emitted current density varies exponentially with respect to $\phi_B$ and $T$. In order to enhance the emission properties of the system much work has been devoted in finding materials with a low $\phi_B$ and a high melting temperature [54, 55].

### 1.1.4 Field emission

When an electric field is applied near emitter's surface, electron emission increases and results in a decreased work function $\phi_B$ or a rise in temperature as given in Equation 1.9. In addition, it is expected that when the electric field is high enough, electron emission may occur even at room temperature. This kind of emission is known as field emission. For the field emission to occur, the potential barrier height must be lowered to the level of the Fermi energy within the emitter, and the barrier's width

beyond this level must be narrow. Near ambient temperatures, electrons lack sufficient energy to surpass even a low potential energy barrier, so emission occurs as electrons tunnel through the barrier. When the temperature is very low, the supply function $N(E_x, T)$ (Equation 1.3) quickly decreases for $E_x > E_f$. On the other hand, for a given $F = 5\ Vnm^{-1}$, $\phi_B = 4.4\ eV$, $\mathcal{T}(E_x, F)$ rapidly decreases for $E_x < E_f$. Hence, the majority of the contribution to Equation 1.8 arises from the region near the Fermi energy level. Depending on this theory, similarly to the thermionic emission formula, Fowler and Nordheim [56] developed a theoretical formula as follows [51]

$$J_{FN} = A' F^2 \exp\left[ - B' \phi_B^{3/2} / F \right] , \tag{1.10}$$

where $A' \equiv e^3/[16\pi^2 \hbar \phi_B t^2(y)]$ and $B' \equiv \frac{4}{3e}\left(\frac{2m}{\hbar^2}\right)^{1/2} v(y)$, $t(y)$ and $v(y)$ with $y = \sqrt{e^3 F}/\phi_B$ are mentioned elsewhere [57]. The Fowler-Nordheim expression (Equation 1.10) is very important in the theory of electron emission and has found interesting applications [58].

The thermal-field (TF) emission occurs at moderate temperatures and under the influence of external electric fields that do not fall into either thermionic emission or field emission categories. An analytical expression for the TF emission was derived by Christov [59] with adequate accuracy for any given value of $F$ and $T$. In another work by Jensen et al. [60], an analytical TF emission equation is derived for which the FN and RLD equations are asymptotic limits. The correlation between the FN and RLD equations were unraveled by their theory, which also demonstrated a smooth transition from the regime where thermal effects prevail to the one where electric field effects predominate.

### 1.1.5 Photoelectric emission

Photoelectric emission is the process wherein electrons are emitted into the vacuum from the surfaces of the semiconductors or metals, caused by the absorption of electromagnetic radiation. For a long time, we have known two fundamental features of photoemission: (i) The maximum velocity of the emitted electrons does not depend on the intensity of the incident laser field, and (ii) As the frequency of the laser field is reduced, the velocity of the photoelectrons gradually decreases. When one plots the peak emission energy as a function of the driving laser field frequency, a linear relationship emerges. This represents that the peak emission energy is related to the frequency of the excitation by $\frac{1}{2} m \upsilon_m^2 = k_1 \omega - k_2$, where $m$ is the mass of electron, $\upsilon_m$ is the velocity of the maximum emission, $\omega$ is the frequency, $k_1$ and $k_2$ are constants given by the Einstein theory.

Some of the aspects of the photoelectric effect could be explained by the wave theory of light only with considerable difficulty. While it could account for the correlation between the photoelectric current and the intensity of electromagnetic radiation, it struggled to demonstrate why the emission velocity remained unaffected by changes in radiation intensity. Einstein employed quantum theory to provide an explanation for the photoelectric effect, for which he won the Noble Prize. He proposed that the energy from radiation was transmitted by photons, i.e. hypothetical particles that have an energy $h\omega$ and are localized in space, so that they can interact with an electron, transfer their entire energy, and disappear. From the transferred energy $h\omega$, a fraction of it, say $\phi_B$ (work function) will be utilized to surpass the surface potential energy barrier of the material. Hence, the maximum kinetic energy of the emitted electron, which is known as the Einstein photoelectric equation, and which can be used to determine the work function of materials experimentally, is given as [51]

$$\frac{1}{2} m \upsilon_m^2 = h\omega - \phi_B , \tag{1.11}$$

A comprehensive electron emission expression for field, thermal, and photoelectric emission was formulated by Jensen et al. [60]. Within this framework, the expressions RLD and FN are the limiting cases. It is explicitly designed to address the transitional regions where various emission processes can be compared. The ability to calculate these transitional regions is of considerable importance, particularly when evaluating their relative significance, such as in scenarios involving field-assisted photoelectric emission. The approach of calculating the total current density (in Section 1.1.2) and the

various emission processes discussed above are explained in detail in the reference [51].

So far, we have seen that the external energy input for the electron emission to occur is either by external electric heating (thermionic emission), or monochromatic electric field (field emission), or photon irradiation (photoelectric emission). However, in emission process, when the external energy source is an ultrashort femtosecond laser pulse, there exists an intricate interaction between electrons and lattice. In order to study the temporal evolution of lattice and electrons temperature and subsequent emission processes, a well known theoretical framework, i.e. two-temperature model is used in this work, which is briefly explained in the following section 1.2.1.

## 1.2 Laser-driven excitations; relevant models

### 1.2.1 Two temperature model (TTM)

When an ultrafast intense laser pulse (with a typical peak intensity exceeding $10^{19}$ $Wcm^{-2}$ and a central wavelength around 800 $nm$) interacts with a high-quality optical material surface, it rapidly ionizes the material, transforming it into a dense conducting plasma medium during its initial rise. Subsequently, as the femtosecond pulse reaches its peak intensity, it interacts with the dynamically evolving reflective plasma surface. The non-equilibrium energy transport associated with this interaction finds diverse applications in areas such as plasma optics [61], the generation of attosecond pulses [62], and the acceleration of charged particles [63], among many others. When the surface of a solid material is subjected to illumination of an ultrafast laser pulse with intensities ranging from $10^9$ to $10^{14}$ $Wcm^{-2}$, the resulting nature of the interaction depends on the specific properties of the material. In the case of a metal surface, it undergoes rapid thermal evolution, a fundamental phenomenon with broad implications in various domains, including but not confined to laser induced material damage, thermoreflectance, laser machining, ultrafast thermionic emission. Under the influence of a femtosecond laser, a metal exhibits intricate interactions between its electrons and lattice [64], which results in the temporal evolution of the electron and lattice sub-system's temperature [65–67], accompanied by fluctuations in carrier density, and subsequent equilibration dynamics. The processes, such as energy deposition, its redistribution and equilibration dynamics can be effectively captured by monitoring the thermal changes in these sub-systems, which are pivotal in various potential applications.

Numerous applications relevant to the advancement of next-generation electronics rely on the interfaces between metals and semiconductors. These applications are based upon ultrafast thermionic carrier injection, which occurs as electrons are rapidly transferred from the metal film to the semiconductor layer. This phenomenon takes place particularly when the electron temperatures within the metal are significantly higher than its lattice temperature [68, 69]. Furthermore, the concept of refrigeration based on thermionic emission has been theoretically proposed [70], which might have potential applications. Recent experiments on localized, transient thermal excitation of metals have revealed evidence of induced surface cooling resulting from subsequent emission [71, 72]. The energy relaxation of excited electrons in metals, the efficient emission of electrons and the overall impact of high-power laser irradiation on a solid surface are frequently described through the framework of the TTM, as proposed by Anisimov et al. [65]. Often, 1D [73–77] or 2D [78] TTM are used to explain the thermal changes caused by lasers in metals. However, these models fall short in fully describing the complete three-dimensional spatial variation of the laser-induced thermal effects in the metal films. They often do not consider the effects of laser polarization or the impact of varying angles of incidence. Therefore, a three-dimensional (3D) TTM provides a more realistic and appropriate description. It allows to capture the comprehensive 3D heat deposition by the laser source and accurately obtain the subsequent thermal evolution of the irradiated thin surface and the volume underneath. It is an extension of the 1D TTM, which is a widely used theoretical framework for describing ultrafast laser-matter interactions. The 1D TTM assumes that the laser energy is absorbed uniformly and instantaneously by the material, resulting in a rapid increase in electron temperature and a slower increase in lattice temperature. The 3D TTM expands upon this by accounting for the spatial dependence of temperature in all three dimensions. When a material is irradiated with an ultrashort laser

pulse, the excited electron reaches the continuum, resulting in an emission or it may also recombine with the ionic core and emit high energy photons, resulting in high harmonic generation, which is an unique tool to investigate the electronic structure and dynamics of material at the atomic level. This phenomenon varies in gases and solids, which are presented and explained in the following sections.

### 1.2.2 High harmonic generation (HHG)

HHG is a non-linear process that involves the interaction of the laser field with an atom, or a molecule, or a solid-state medium, which results in the emission of harmonics that are integer multiples of the frequency of the driving laser. HHG has emerged as a promising technique due to its ability to generate high-frequency light in the extreme ultraviolet (XUV) and soft X-ray regions of the electromagnetic spectrum. This region is difficult to access using conventional light sources, and therefore HHG provides a unique tool for exploring the structure and dynamics of matter at the atomic and molecular level. It has a wide range of applications, including XUV, soft X-ray generation, attosecond science [79], and laser-based atomic spectroscopy [80]. Furthermore, it has also shown potential for applications in spectroscopy [81], microscopy of matter [82], and modern photonics [83]. HHG is also capable of generating ultrashort light pulses with durations in the attosecond range, which is much shorter than the typical time scales for electronic and nuclear processes. This makes it possible to study ultrafast phenomena such as electronic dynamics with high temporal resolution.

In addition, HHG has the advantage of being a table-top technique that is relatively simple to implement compared to other sources of XUV and X-ray radiation, such as large-scale synchrotron light sources and free-electron lasers. Overall, the ability of HHG to generate high-frequency light in the XUV and soft X-ray regions of the electromagnetic spectrum, combined with its potential for applications in various fields, makes it a highly motivated and promising technique.

### 1.2.3 HHG in gases: a semi-classical description

The semi-classical description of HHG is a theoretical framework that explains the generation of high-frequency harmonics from an intense laser field in terms of the interaction of the laser field with the electrons of a gaseous medium. In this description, the motion of the electrons is treated classically, while the laser field is treated quantum mechanically. This model assumes that the laser field ionizes the medium and creates a population of free electrons, which are then driven by the laser field and can be accelerated back towards the medium, where they can recombine with the ionized cores and emit high-frequency light (see Figure 1.1(a)). Furthermore, this model describes the conditions necessary for HHG to occur, such as the intensity and frequency of the laser field, as well as the characteristics of the medium, such as its ionization potential and density.

The semi-classical description of HHG provides a qualitative understanding of the process and has been used to explain many of the experimental observations of HHG. However, it does not provide a complete description of the underlying physics and is limited in its ability to explain certain aspects of the process, such as the generation of attosecond pulses and the dependence of HHG on laser field polarization. In recent years, there have been efforts to develop more sophisticated models of HHG that incorporate quantum mechanical effects, such as the time-dependent Schrödinger equation, which provide more accurate and complete description of the process.

### 1.2.4 HHG in solids

Figure 1.1 illustrates the difference between the mechanism of HHG from atoms in gases and solids. In solids, there is a significant overlap between the electron wavefunctions of nearby lattice sites, which makes it suitable to describe the electron states in momentum-space using the Bloch theorem. A real-space representation of HHG in solids is shown in Figure 1.1(c), where an ionized electron from a lattice site can propagate over many lattice periods before recombining with any other lattice site. This process is coherent due to the lattice's periodicity. Unlike in gases, in solid-state HHG, an electron does not necessarily need to recombine with the parent lattice site, and therefore the ellipticity dependence

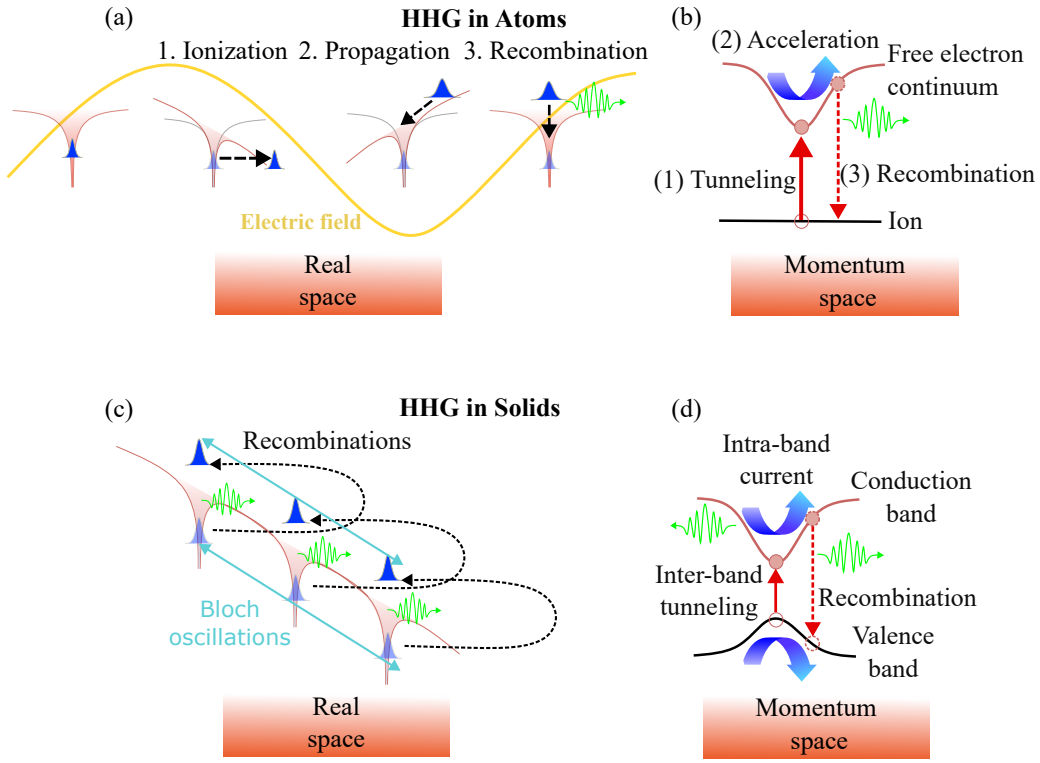


Figure 1.1: A schematic view of microscopic mechanisms for atomic and solid-state HHG. (a) Schematic of the three-step model in real-space for HHG in atoms comprising of tunnel ionization, propagation and recombination. (b) Momentum-space representation of (a), in which the electron tunnels in to the continuum state from the bound state, accelerates in the parabolic continuum band and then recombines with the parent ion emitting a higher frequency radiation. (c) Schematic representation of the HHG mechanism in solids in real-space with multiple possibilities. The excited electron can scatter from the periodic Coulomb potential, termed as Bloch oscillations, and recombine with the associated hole (ion), and recollide with the neighboring holes (ions) due to closely packed atoms. (d) The momentum-space representation of (c) by using two cosine bands with inter-band transitions between the valence and conduction band and intra-band Bloch oscillations in the conduction band, where high-frequency radiation is emitted in both the cases.

of HHG is entirely different. Circularly polarized harmonics can be generated in solids using a circularly polarized driving pulse, as demonstrated in the pioneering work by Ghimire et al. [84]. Additionally, in solid-state HHG, the energy cutoff is linearly dependent on the laser's electric field amplitude, whereas it was reported to be quadratic in HHG from gases. Therefore, a reciprocal-space explanation of the underlying mechanism is required.

Figure 1.1(d) presents a reciprocal-space illustration of solid HHG, where a two-band model is considered for a semiconductor having one valence and one conduction band. The HHG spectrum in solids has two main contributions. Firstly, the time-dependent interband polarization generates harmonics, where an intense laser field can excite an electron to the conduction band, creating a hole in the valence band. Secondly, the laser's electric field can accelerate the electrons and holes in their respective energy bands, resulting in an intraband current. In the strong-field regime, the interband and intraband contributions are interrelated, and their respective roles in different parts of the spectrum require further investigation. Notably, only the intraband current is expected to contribute to the spectrum's below-bandgap region. It is worth noting that unlike atomic HHG, which does not have an intraband current contribution, as the holes are localized within the atom [as shown in Figure 1.1(b)], when an electron moves adiabatically along a particular conduction band without scattering, it diffracts from the Brillouin-zone boundaries with a frequency of $\omega_B = e\mathcal{F}_0/\hbar a_0$, where $a_0$ is the lattice parameter. These diffractions give rise to dynamical Bloch oscillations, which lead to a linear

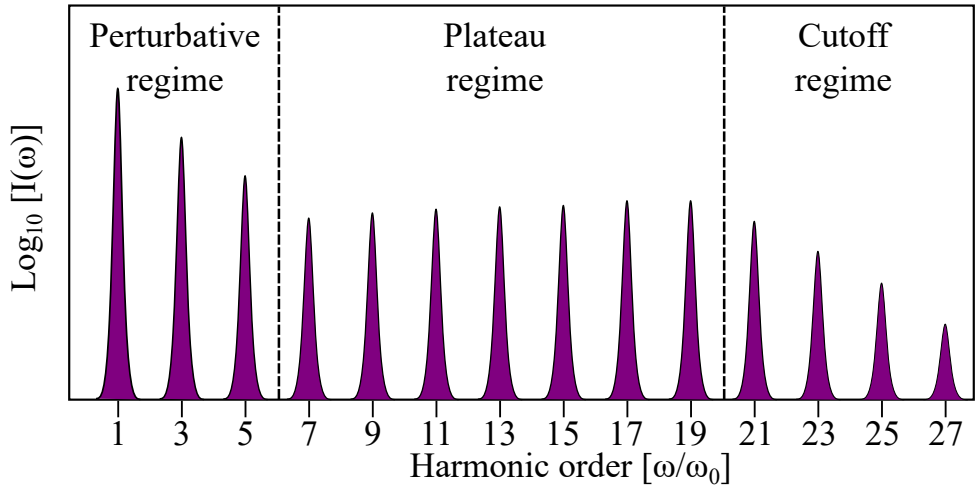


Figure 1.2: Schematic of a typical high harmonic spectrum of an atom under the influence of linearly polarized laser field.

dependence of the energy cutoff on the laser's electric-field amplitude in solid HHG [84].

One of the exciting aspects of solid HHG is that solids possess a high density of electrons and periodicity. In addition, high harmonics in solids are generated from lasers with intensities in the $TWcm^{-2}$ order, which is much lower compared to the intensity requirements of atomic HHG. Due to these exceptional properties, HHG from solids presents a compact and superior alternative as a source of coherent and bright attosecond pulses in the extreme ultraviolet and soft X-ray energy range [39]. In addition, solid-state HHG has the exciting capability of imprinting the anisotropic nature of the lattice onto the harmonic spectrum, which can contain rich information about multiple energy bands in actual materials [85]. Unlike the simplified two-band model in Figure 1.1(d), solid HHG arises from a large number of energy bands and can reveal interband coupling among different pairs of energy bands, resulting in multiple plateau structures in the HHG spectrum [86]. This makes solid-state HHG an ideal tool for studying both static and dynamic properties of the valence electrons in solids. In recent years, solid-state HHG has been used to explore exciting processes such as band structure tomography [87], quantum phase transitions [88], the realization of petahertz current in solids [89], and dynamical Bloch oscillations [90].

### 1.2.5 Features of the high harmonic spectrum

The spectra of high-order harmonics are often calculated with the Fourier transformation of the dipole moment $\boldsymbol{d}(t)$. Such spectra have several notable features as can be seen in Figure 1.2. In the spectra, the first regime is the perturbative regime which usually lasts up to the $3^{\text{rd}}$ to $5^{\text{th}}$ harmonics. The next is the plateau regime, where the generated high-order harmonics have similar intensities. The plateau is an indication of non-perturbative interaction among electrons and the external laser field. The next regime is the cutoff, beyond which the intensity of the generated harmonics reduces drastically. The energy at which the cutoff appears can be determined classically using the following expression: $E_{cutoff} = I_p + 3.17U_p$, where $I_p$ is the ionization potential of the target material and $U_p$ is the pondermotive energy of an electron interacting with the laser field, given as $U_p = E_0^2/4\omega^2$, where $E_0$ and $\omega$ are the amplitude and frequency of the laser field, respectively. Systems with inversion symmetry exhibit only odd harmonics in their spectrum, under the influence of a linearly polarized laser field. It is not necessary for the HHG spectra to have exact features as shown in the Figure 1.2. Different features of HHG are obtained when the laser field polarization is not linear, but rather circular.

## 1.3 Overview of the thesis

Following the detailed introduction of the thesis in this chapter, the theoretical approaches that are used in this dissertation are meticulously discussed in Chapter 2. The subsequent chapters contains the key findings derived from my investigation. In Chapter 3, I will present the analytical formalism to address the temperature dependent electron emission from a metallic target with thin coating, operating at a finite temperature. By considering a three-dimensional parabolic energy dispersion for the base material and an energy dispersion dependent on the thickness for the coating layer, along with the Fermi-Dirac statistics of electron energy distribution and Fowler's mechanism of electron emission, we examine how the emission flux is influenced by various physical properties including the Fermi level, work function, coating material thickness, and operating temperature. Our comprehensive analysis of the influence of coating thickness on the emission current reveals that thin coating layers exhibit superior emission characteristics at high temperatures (above 1000 $K$), whereas thicker coating layers are expected to yield better results in the low temperature regime. The predictions in this chapter are useful in designing new coated materials with appropriate thickness for applications in the field of thin film devices and field emitters.

In Chapter 4, I demonstrate the potential of monolayer phosphorene, a two-dimensional form of black phosphorus, as a highly efficient photo-thermionic emitter. To gain insights and understand its unique characteristics, we adopt a combined approach that integrates *ab-initio* quantum simulation tools with a semi-classical description of the emission process. Firstly, employing a density functional theory framework, we investigate the band structure of phosphorene. By analyzing the electronic band locations and band edges, we determine important parameters such as the Fermi level and work function. This enables us to establish a valid parameter space specific to the material and develop a formalism for estimating the thermionic electron emission current from phosphorene. Additionally, we illustrate how the emission current can be significantly enhanced through the influence of photon irradiation. Notably, we observe a substantial dominance of photoemission flux over thermionic emission flux, with the anisotropy of the phosphorene structure playing a crucial role in increasing the flux. To validate the approach over a broader range of parameters, we successfully compare our results with recently conducted experiments in a different context. These findings present a promising avenue for utilizing phosphorene-based thermionic and photo-thermionic energy converters.

In Chapter 5, I will present an effective numerical model that accurately describes the interaction between femtosecond laser pulses (duration $\geq 100\ fs$) and gold coated glass substrate film, specifically focusing on the resulting ultrafast thermionic emission. To capture the dynamics of temperature-dependent electrons and lattice temperature evolution, we employ a phenomenological TTM. The thermionic electronic emission features are described by a modified Richardson-Dushman equation. One of the key advancements of this study is the implementation of a 3D TTM that effectively accounts for time-dependent space-charge effects arising from the varying Coulomb interactions among the emitted electrons. Our investigation primarily focuses on the fluence regime that remains well below the damage threshold of gold. The obtained results offer valuable insights into the mechanism of ultrafast thermionic emission and suggest potential approaches to enhance emissions within the realm of ultrafast thermalized electron-phonon systems. The proposed 3D TTM not only provides comprehensive information about the three-dimensional thermal fields, surface temperature, and steady-state quantum effects occurring at the laser-metal interaction interface but also enables a better understanding of space-charge limited overall electron emission in complex high-temperature regimes under extreme excitation conditions.

Inclusion of multielectric effects in the study of HHG from atoms is very important as it enables to a more accurate understanding of the complicated process underlying HHG phenomenon. Hence, in Chapter 6, I will present state-of-the-art TDDFT simulations (which considers multielectron effects) that are used to thoroughly investigate the non-linear response of argon atom under the influence of a linear polarized laser field. Firstly, I will validate our numerical approach with the experimental findings by correctly reproducing the significant feature of HHG spectrum of argon, i.e. the Cooper minimum near 48 $eV$. Later, by a combination of TDDFT simulations, semi-classical analysis and

the state-of-the art experiments that were conducted by our collaborators, I showcase an efficient way to obtain and characterize highly elliptically polarized HHG from argon under the influence of a bi-chromatic counter rotating laser fields. Our analysis reveal that by appropriately tuning the central frequency of the second harmonic, the central frequency of the extreme ultraviolet (XUV) high harmonic radiation can be continuously tuned. Our simulation results supports the experimental findings, which reveal that the elliptical HHG radiation from argon can be tuned for an energy range of 150 $meV$.

In Chapter 7, I will investigate and present the effects of external strain on the electronic structure and consequent HHG, nonlinear response from 2D phosphorene under the influence of a linear polarized femtosecond laser pulse. Using the *ab initio* approach based on TDDFT, we reveal that the HHG process is responsive to the modulation of the band structures of monolayer phosphorene under biaxial tensile and compressive strains. This leads to a significant enhancement of harmonic yield. I show how by closing the band gap of phosphorene via compressive strain results in enhanced harmonic yield. The current study expands the research possibilities of phosphorene into a previously unexplored domain, indicating its potential for future utilization in extreme-ultraviolet and attosecond nanophotonics, and also providing opportunities to explore the ultrafast carrier dynamics and strong-field properties of this emerging material.

In a nut shell, the primary objective of this dissertation is to investigate and understand the external field driven ultrafast electron dynamics in different dimensional systems and to propose ways to enhance their electron emission properties. By suitable application of external stimuli, such as coatings, stress, photon irradiation, I examined how the electronic structure of the system can alter and subsequently yield enhanced emission properties.

# Chapter 2

# Methodology

The fundamental states of matter, i.e. solids, liquids, and gases consist of atoms, which are a collection of positively charged nuclei and negatively charged electrons interacting with each other. Repulsive forces exist between electrons ($e$-$e$) and between nuclei ($n$-$n$) and Coulomb forces exist between nuclei and electrons ($n$-$e$), which attract each other. The Hamiltonian of matter comprises all the mentioned interactions, along with two more terms, which are the kinetic energy of both nuclei and electrons, given as

$$\hat{H} = -\frac{\hbar^2}{2M_P}\sum_L \nabla_L^2 - \frac{\hbar^2}{2m_e}\sum_i \nabla_i^2 - \sum_{i,P}\frac{Z_P e^2}{|r_i - R_P|} + \frac{1}{2}\sum_{i\neq j}\frac{e^2}{|r_i - r_j|} + \frac{1}{2}\sum_{P\neq J}\frac{Z_P Z_J e^2}{|R_P - R_J|}\ , \tag{2.1}$$

where $\hbar$ is the reduced Planck constant, the electrons and nuclei are represented with lowercase and uppercase letters, respectively. $Z_P$ and $M_P$ denotes the charge and mass of nucleus, respectively, $m_e$ refers to electron mass, $r_i$ and $R_P$ are the position of electron and nucleus, respectively. This Hamiltonian is an integral part of the Schrödinger equation, given as,

$$\hat{H}\Psi = E\Psi\ , \tag{2.2}$$

where $\hat{H}$ is the Hamiltonian operator, $\Psi$ is the wave function $\Psi(r_1, r_2, ..., r_N)$, $r_i$ represents the position and spin of the $i^{th}$ electron and $E$ is the energy of the solid. The basic requirement in calculating the electronic structure of a system of $N$ non-relativistic particles is to find the solution of the static Schrödinger equation, which reveals many interesting physical properties of the system. Equation 2.1 can be represented as, $\hat{H} = \hat{T}_n + \hat{T}_e + \hat{V}_{ext} + \hat{V}_{int} + \hat{V}_{n-n}$, where $T_n, T_e$ are the kinetic energy of ions and electrons, respectively. In solids, nuclei are located at different positions in space and they produce a Coulomb potential, within which, electrons adapt and try to accommodate themselves. This given potential is "external" to electrons, hence, the name external potential '$\hat{V}_{ext}$'. The potential generated by the electrons is viewed as internal potential '$\hat{V}_{int}$'. The term '$\hat{V}_{n-n}$' refers to the Coulomb interactions between nuclei.

Until today, solving Equation 2.2 analytically and numerically has been impossible due to the presence of a very large number of electrons and nuclei, except for special cases, such as two-electron systems. To solve this problem, one has to use reasonable approximations. Over the years, much work has been dedicated to finding reasonable approximations to turn this fully interacting many-body Schrödinger equation to a tractable problem.

## 2.1 Born-Oppenheimer approximation

To solve the wave function for a single ethanol ($C_2H_6O$) molecule, one needs to solve the time-independent Schrödinger equation in spatial coordinates of the electrons and nuclei. In total, ethanol

contains 26 electrons and 9 nuclei, which makes the partial differential equation a function of 105 variables (3 spatial degrees of freedom for each electron and ion, neglecting the spin). In the Born-Oppenheimer (B-O) approximation [91], it is assumed that the mass of an ion is much larger than that of an electron ($M_I \gg M_e$), due to which there exists asymmetry in the kinetic energy of the electrons and ions given in Equation 2.1. As a result, the nuclear motion is much slower than that of the electron motion. This enables the B-O approximation to break the complex wave function into two separate wave functions (electronic and nuclear wave functions), given by $\Psi_{tot} = \Psi_{electron} \times \Psi_{ion}$. By assuming that the mass of the nuclei is much larger than the mass of the electron, one neglects the kinetic energy term of the nuclei. As a result, electronic part of the wave function is solved by freezing the nuclear positions $R$. This results in an electronic Schrödinger equation given by $\hat{H}_e(r,R)\Psi_{electron}(r,R) = E_e(R)\Psi_{electron}(r,R)$, where $r$ is the coordinate of electrons and $R$ is the fixed nuclei coordinate. Due to this simplification, the number of terms in $\hat{H}$ in Equation 2.1 decreases to:

$$\hat{H}_e = -\frac{\hbar^2}{2m_e}\sum_i \nabla_i^2 - \sum_{i,P}\frac{Z_P e^2}{|r_i - R_P|} + \frac{1}{2}\sum_{i\neq j}\frac{e^2}{|r_i - r_j|} \ . \tag{2.3}$$

It is important to note that electrons still interact with the nuclei with their respective potential. Hence, the kinetic and interaction potential of the nuclei $\hat{V}_{n-n}$ is most often calculated classically and added to the solution of the electronic Hamiltonian.

One of the drawbacks of the B-O approximation is that it cannot be applied for calculating properties where the nuclei motion is important. Although the B-O approximation is a major simplification in terms of computational speedup, the resulting equation is still difficult to solve. As a result, additional reasonable approximations are necessary to solve the many-body Schrödinger equation.

## 2.2 Modeling of materials using the Density Functional Theory

By using the B-O approximation and pseudopotentials (explained in later sections), the many-body Schrödinger equation (Equation 2.1) is still too complex to solve. It is here that the density functional theory (DFT) provides a viable alternative to the many-body problem. DFT is an approach to transform the complex many-body Schrödinger equation into a set of single particle equations known as Kohn-Sham equations, which are easier to solve. These Kohn-Sham equations can be worked out with several numerical methods, such as linearized augmented-plane-wave, projector augmented wave, grids, etc. DFT can make the exact transformation from the many-body Schrödinger equation to Kohn-Sham equations without any loss of information, provided one knows a mathematical object, called exchange-correlation function. DFT demonstrates that such a mathematical object exists but does not represent what it looks like.

The main idea behind DFT is to use the particle density $n(r)$ as the key variable to calculate all the other observables. In other words, the knowledge of ground-state particle density implies knowledge of the wave function and the potential, and consequently, one can calculate all the observables.

### 2.2.1 Hohenberg-Kohn theorems

DFT is based on two mathematical theorems developed by Hohenberg and Kohn [92]:
**Theorem I:** For a system of interacting particles in the presence of external potential $V_{ext}(r)$, the potential $V_{ext}(r)$ is determined uniquely, except for a constant, by the ground-state particle density $n_o(r)$.
**Theorem II:** For any external potential $V_{ext}(r)$, a universal functional for energy $E[n(r)]$ can be defined. The density $n(r)$ that minimizes this functional is the exact ground-state density $n_o(r)$.

According to the above two theorems, there is a one to one mapping between ground-state particle density $n_o(r)$ and external potential $V_{ext}$, and vice versa. With the knowledge of $n_o(r)$, one can obtain $V_{ext}$, with which we can construct the Hamiltonian, which is used to determine the wave function; thus all the properties of the system can be determined based on the ground-state density. The total energy $E$ of the system can be expressed as a function of $n(r)$ as

$$\begin{aligned} E[n(r)] &= T_e[n(r)] + E_{int}[n(r)] + \int d^3r v_{ext}(r)n(r) \\ &= F[n(r)] + \int d^3r v_{ext}(r)n(r) \ , \end{aligned} \tag{2.4}$$

where $F[n(r)]$ is the unknown density dependent functional comprising the kinetic energy of the electrons ($T_e$) and the potential energy ($E_{int}$) of the interacting electrons. If the functional $F[n(r)]$ is known, $n(r)$ could be varied until we minimize the systems' total energy. Therefore, knowing $E[n(r)]$ is sufficient to calculate the ground-state electron density and energy. However, the Hohenberg-Kohn theorems do not provide information about $F[n(r)]$, which limits the usability of DFT in practical applications. This limitation has been overcome by the approach of Kohn and Sham, who constructed the famous Kohn-Sham ansatz [93]. This was one of the reasons that made DFT a popular tool for the calculation of electronic structure properties in condensed matter physics.

### 2.2.2 Kohn-Sham (KS) ansatz

The approach suggested by Kohn and Sham [93] is to have an exact transformation of the original many-body problem (coupled differential equations) into a single-particle equation (uncoupled) that can be solved easily. The main assumption of this approach is that the ground-state density of the interacting system is equal to some chosen non-interacting system. As a result, independent-particle equations for the non-interacting system can be exactly solvable with all the complex many-body terms incorporated into an exchange-correlation functional of the density. Thus the many-body Schrödinger equation is mapped on to auxiliary single-particle non-interacting Kohn-Sham equations, which is comprised of the usual electron kinetic energy term and a single particle local potential ($v_{eff}(r)$) acting on the electron at a location $r$ and given as:

$$\hat{H}_{KS}\phi_i = \epsilon_i\phi_i \tag{2.5}$$

$$\hat{H}_{KS} = -\frac{\nabla^2}{2} + \hat{V}_{KS} \tag{2.6}$$

in atomic units, where $\hbar = m_e = e = 1$. Here

$$\begin{aligned} \hat{V}_{KS} &= \hat{V}_{ext}(r) + \hat{V}_H(r) + \hat{V}_{XC}(r) \\ &= \hat{V}_{ext}(r) + \frac{\delta\hat{E}_H[n(r)]}{\delta n(r)} + \frac{\delta\hat{E}_{XC}[n(r)]}{\delta n(r)} \ . \end{aligned} \tag{2.7}$$

$N$-electron system exact ground-state density is given as

$$n(r) = \sum_{i=1}^{N} \phi_i^*(r)\phi_i(r) \ , \tag{2.8}$$

where the single-particle wave functions $\phi_i$ are the $N$ lowest-energy solutions of the Kohn-Sham equations. Equations 2.5, 2.7, and 2.8 are collectively known as the Kohn-Sham equations, which have to be solved self-consistently. Equation 2.4 is transformed in the following way:

$$\hat{E}_{KS}[n(r)] = \hat{T}_0 + \hat{V}_{ext} + \hat{E}_H + \hat{E}_{XC} \ , \tag{2.9}$$

where $T_0$ is the non-interacting independent particle kinetic energy given by

$$\hat{T}_0[n(r)] = -\frac{1}{2}\sum_{i=1}^{N} \int \phi_i^*(r)\nabla^2\phi_i(r)dr \ , \tag{2.10}$$

and $V_{ext}$ is the external potential due to the nuclei. We have split the term '$E_{int}$' in Equation 2.4 into $E_H$, known as the classical Coulomb self-interaction term or Hartree potential, given as

$$\hat{E}_H = \frac{1}{2}\int \frac{n(r)n(r')}{|r-r'|} d^3r d^3r', \tag{2.11}$$

and $E_{XC}$ is the exchange-correlation (XC) functional comprising all the many-body effects of exchange and correlation. Although, the KS approach is exact in theory, it is an approximation, since $E_{XC}$ is unknown. By comparing Equation 2.9 and Equation 2.4, $E_{XC}$ can be expressed in terms of the Hohenberg-Kohn functional as

$$\hat{E}_{XC} = (T_e[n(r)] - T_0[n(r)]) + (E_{int}[n(r)] - E_H[n(r)]) \ . \tag{2.12}$$

The above equation shows that $E_{XC}$ is the residue kinetic and potential energy in approximating the many-body interacting system as a system of independent-particles. This energy term is the only one which is unknown in the Kohn-Sham approach. To this extent, $E_{XC}$ has been reasonably approximated as a local or semi-local functional to describe the true exchange-correlation energy. Two famous approximation techniques for the XC potential are local-density approximation (LDA) and the generalized-gradient approximation (GGA). Even with such gross approximations, KS approach has much success in calculating ground-state properties of many-body electron systems.

In theory, the KS eigenvalues from Equation 2.5 have no physical meaning, due to the fact that we consider a set of non-interacting independent particles to describe a many-body system. These eigenvalues are not to be added to or subtracted from the interacting many-body system, because the total energy of the many-body system is not equal to the sum of each of the individual non-interacting eigenvalues in Equation 2.5. One exception in this regard is that the highest eigenvalue in a finite system, which is the negative of the ionization energy, "-$I$", has importance, because the asymptotic long-range density in a bound system is governed by the occupied state with the highest eigenvalue, which is assumed to be exact. Except for the KS highest-eigenvalue, all the others are not true.

Even though almost none of the KS eigenvalues have any physical meaning, they can be used to build physically meaningful quantities, for instance, developing perturbation expression for excitation energies using KS eigenvalues and eigenfunctions as a starting point. They have a definite mathematical meaning, normally called as Slater-Janak theorem, which states that the eigenvalue is the derivative of the total energy with respect to the occupation of the state, given as $\epsilon_i = dE_{tot}/dn_i = \int \frac{dE_{tot}}{dn(r)} \frac{dn(r)}{dn_i} dr$ .

### 2.2.3 Local (spin) Density Approximation (L(S)DA)

The KS ansatz successfully transforms the interacting many-body problem to a set of non-interacting single particle KS equations and simplifies the complexity. However, with unknown exchange-correlation functional $E_{XC}[n(r)]$, the KS equations cannot be solved. To overcome this hurdle, great progress has been made over the years to come up with reasonable approximations which can not only predict various properties of many-body systems reasonably well but also reduce the computational costs, making DFT the most preferable method for electronic structure calculations.

One such approximation is the widely used local (spin) density approximation or in short L(S)DA. In L(S)DA, the exchange-correlation energy $E_{XC}[n(r)]$ is just the integral over the space with exchange correlation energy density at a point '$r$' assumed to be same as in a homogeneous electron gas with that density at that point '$r$'. The exchange correlation energy $E_{XC}[n(r)]$ is given as

$$\begin{aligned} E_{XC}^{LSDA}[n^{\uparrow}(r), n^{\downarrow}(r)] &= \int n(r)\epsilon_{XC}^{hom}[n^{\uparrow}(r) + n^{\downarrow}(r)]dr \\ &= \int n(r)\left(\epsilon_x^{hom}[n^{\uparrow}(r) + n^{\downarrow}(r)]] + \epsilon_c^{hom}[n^{\uparrow}(r) + n^{\downarrow}(r)]]\right) dr \ . \end{aligned} \tag{2.13}$$

For unpolarized systems, LDA is calculated simply by setting $n^{\uparrow}(r) = n^{\downarrow}(r) = n(r)/2$. The exchange-

correlation potential $V_{XC}$ can be written as,

$$V_{XC}^{LSDA}(r) = \frac{\delta E_{XC}^{LSDA}[n^{\uparrow}(r), n^{\downarrow}(r)]}{\delta[n^{\uparrow}(r), n^{\downarrow}(r)]} \tag{2.14}$$

In LD(S)A approximation, the corrections related to the exchange-correlation energy due to inhomogeneities in the electron density at point '$r$' are ignored. Nevertheless, predictions using this approximation are reasonably accurate even in systems where the electron density changes rapidly. On the other hand, LDA underestimates the ground-state energies, ionization energies and the band gap of semiconductors, while overestimating the binding energies. Due to few shortcomings of this approximation, much work was done to improve the approximation with few modifications. As a result, generalized-gradient approximation (GGA) was introduced.

### 2.2.4 Generalized-Gradient Approximation (GGA)

As mentioned above, the corrections in the exchange-correlation energy due to inhomogeneity of the true electron density is ignored in LD(S)A, which could be different from the homogeneous electron gas. To overcome this limitation, work has been done to develop a new approximation, which is called generalized-gradient approximation (GGA), that takes the density gradient corrections and higher spatial derivatives of charge density into account. The exchange-correlation energy in GGA ($E_{XC}^{GGA}$) is given by

$$E_{XC}^{GGA}[n^{\uparrow}(r), n^{\downarrow}(r)] = \int n(r)\epsilon_{XC}^{hom}\left(n^{\uparrow}(r), n^{\downarrow}(r), |\nabla n^{\uparrow}(r)|, |\nabla n^{\downarrow}(r)|, ..\right) d^3r \ . \tag{2.15}$$

The most commonly used functionals in the framework of GGA were developed by Becke [94], Perdew and Wang [95], and Perdew, Burke, and Ernzerhof [96]. The advantage of GGA over LD(S)A is that it works very well in predicting properties such as, but not limited to total energy, bond length, and crystal lattice constant, especially in systems where the charge density is not homogeneous. However, in some cases, it overestimates the ionic crystal lattice constant. In this study, I have used either LDA or GGA approximation that is suitable and adequate for respective system of interest.

### 2.2.5 Pseudopotentials

It is a well-known phenomenon that most physical and chemical properties of atoms are determined by the structure and dynamics of valence electrons which are far from the core of the nucleus. This is particularly true for the formation of chemical bonds. The main idea of application of pseudopotential in electronic structure calculation is to replace the effects of the Coulomb potential of the nucleus and the effect of tightly bound core electrons by an effective ionic potential on the valence electrons.

Due to the Coulomb potential generated by the nucleus, the wave function of valence electrons oscillates in the region around the core of the nucleus. On the other hand, in the regions away from the core, the oscillations in the electronic wave function are absent. The wave function oscillations in the core region do not contribute to the physical properties of the system and are computationally expensive to deal with. The aim of the pseudopotential theory is to replace the actual potential with one which has desirable characteristics, and still contains the true potential outside of the core region of the nucleus. Beyond a radial distance $r_c$, known as cut-off radius, the pseudo wave function and the all-electron wave function are identical. There are mainly two kinds of pseudopotentials, namely, norm-conserving and ultrasoft pseudopotentials.

The use of pseudopotentials has two main advantages. The first one is to have fewer electrons to solve the Schrödinger equation, as we assume that the core electrons can be neglected since they do not take part in chemical bonding. Secondly, the true description of the valence electron wave function is not required near the nucleus core, where the oscillations of the wave function are strong and contains multiple nodes. As a consequence, the size of the basis set needed to accurately describe the valence electron wave function is reduced.

## 2.3 Time-dependent density functional theory (TDDFT)

To study the excited-state properties of a system subjected to a time-dependent external potential, DFT has to be extended beyond the static potential. An effective and potent approach to address this situation is through the use of time-dependent density functional theory (TDDFT), which can be seen as an extension of the conventional ground-state DFT to calculate time-dependent external perturbations. A way to resolve this issue is to calculate the excitations, as the time dependent external potential excites the material from its ground-state to a higher energy state. TDDFT, coupled with linear response theory, can be employed to calculate these excitation energy levels. The mathematical foundation of TDDFT was laid down by Runge and Gross [97], and its proof is more rigorous than that of the Hohenberg-Kohn theorem, and its explanation is beyond the scope of this dissertation. Runge and Gross demonstrated that if two different time-dependent (TD) external potentials, $\upsilon(\mathbf{r},t)$ and $\upsilon'(\mathbf{r},t)$ differ by more than just a time-dependent function *b(t)*, they cannot produce the same time-dependent density $\rho(\mathbf{r},t)$. Because of the uniqueness and one-to-one correspondence between the potential and density, one can consider the KS non-interacting electrons' density to be equal to the interacting density of the real system. The TD KS electrons obey the time-dependent Schrödinger equation called time-dependent Kohn-Sham (TDKS) equations

$$i\frac{\partial}{\partial t}\phi_j(\mathbf{r},t) = \Big[-\frac{\nabla^2}{2} + \upsilon_{KS}(\mathbf{r},t)\Big]\phi_j(\mathbf{r},t)\ . \tag{2.16}$$

The first term on the right hand side of Equation 2.16 is the kinetic energy operator.

$$\upsilon_{KS}(\mathbf{r},t) = \upsilon_{ext}(\mathbf{r},t) + \upsilon_H(\mathbf{r},t) + \upsilon_{\mathrm{XC}}(\mathbf{r},t), \tag{2.17}$$

$$= \upsilon_{ext}(\mathbf{r},t) + \int \frac{\rho(\mathbf{r}',t)}{|r-r'|}d\mathbf{r}' + \upsilon_{\mathrm{XC}}(\mathbf{r},t) \tag{2.18}$$

$\upsilon_{ext}(\mathbf{r},t)$ is the external potential including the external laser field and the Coulomb interaction between the electron and the nuclei, which is defined in the pseudopotentials. $\upsilon_H$ is the Hartree electrostatic interaction between the electrons. $\upsilon_{XC}$ is the time-dependent exchange-correlation potential including all the non-trivial many-body effects. The density of the interacting system is obtained from the orbitals $\phi_j$ by

$$\rho(\mathbf{r},t) = \sum_j^N |\phi_j(\mathbf{r},t)|^2\ , \tag{2.19}$$

where the summation is over all the occupied states. Appropriate approximations for $\upsilon_{XC}$ and strategies to practically address TDDFT problems are discussed in the following sections.

### 2.3.1 Adiabatic approximation

As mentioned in reference [98], similarly to ground-state DFT, the practical application of TDKS Equation 2.16 requires an appropriate approximation for the XC potential. The exact $\upsilon_{XC}$ is not only non-locally dependent on the density in the spatial variables but also depends in the time variables (memory dependence) [98]. Fortunately, in many cases, neglecting this time dependence led to an approximation that is quite effective and has been successfully utilized. This approach is known as adiabatic exchange-correlation approximation (AXCA), given as [98]

$$\upsilon_{XC}^{adia}[n](\mathbf{r},t) = \upsilon_{XC}^{GS}[n(t)](r)\ , \tag{2.20}$$

where $\upsilon_{XC}^{GS}$, representing the ground-state (GS) XC functional, is computed based on the instantaneous density $n(t)$. The AXCA becomes exact, when the true XC ground-state functional is known. The outcomes are influenced by inaccuracies in the ground-state approximations, like the absence of spatial non-locality of LDA or GGA. Nonetheless, in spite of this crudeness of AXCA, excited state properties such as optical spectra obtained within this approximation sometimes are as accurate as the results

obtained using more demanding many-body approaches [99].

### 2.3.2 Implementation of TDDFT: Real-time propagation

A practical method to solve TDDFT equations is briefly discussed in this section, which is explained in detail in reference [98]. As an initial step to our calculation, we can select the TDKS Equation 2.16 and directly integrate them. Commencing from the ground-state at time $t = 0$, at a subsequent time $t = t'$, it is possible to compute the density $n(\mathbf{r}, t')$ through the propagation of the occupied ground-state KS orbitals.

$$\phi_\upsilon(\mathbf{r}, t') = \hat{U}(t', 0)\phi_\upsilon(\mathbf{r}) \ , \tag{2.21}$$

where $\hat{U}$ is the time evolution operator

$$\hat{U}(t', 0) = \hat{\mathcal{T}} \exp\Big[ -i \int_0^{t'} \hat{H}(\tau) d\tau \Big] \ , \tag{2.22}$$

here $\hat{\mathcal{T}}$ represents the time ordering operator. Employing this method, the density at time $t = t'$ can be expressed as $n(\mathbf{r}, t') = \sum_\upsilon |\phi_\upsilon(\mathbf{r}, t')|^2$. In practical applications, the time evolution is accomplished by dividing the time interval from $t = 0$ to $t = t'$ in to small increments $\delta t$, making use of the property $\hat{U}(t_2, t_1) = \hat{U}(t_2, t_3)\hat{U}(t_3, t_1)$:

$$\phi_\upsilon(\mathbf{r}, t + \delta t) = \hat{U}(t + \delta t, t)\phi_\upsilon(\mathbf{r}, t) \ . \tag{2.23}$$

Selecting suitable approximations for the time evolution operator $\hat{U}(t+\delta t, t)$ is of utmost significance in practical computations, taking into consideration both numerical precision and computational efficiency. Regardless of the chosen approximation, they should all accurately reproduce the exact properties of $\hat{U}$, such as unitary, which is important for ensuring the total charge convergence during the propagation. The simplest method is the midpoint rule, where the propagator is approximated as the exponential of the Hamiltonian computed at time $t + \delta t/2$, as follows

$$\hat{U}(t + \delta t, t) = \exp\Big[ -i\hat{H}(t + \frac{\delta t}{2})\delta t \Big] \ , \tag{2.24}$$

here $\hat{H}(t + \frac{\delta t}{2})$ is calculated self-consistently with the predictor corrector method [100]. To compute the exponential in Equation 2.24, it is necessary to expand it into a Taylor series up to a specified order. Hence, Equation 2.23 can be written as

$$\phi_\upsilon(\mathbf{r}, t + \delta t) = \Big[1 - i\hat{H}(t + \frac{\delta t}{2})\delta t - \frac{1}{2}\hat{H}^2(t + \frac{\delta t}{2})\delta t^2 + ...\Big]\phi_\upsilon(\mathbf{r}, t) \ . \tag{2.25}$$

The above equation shows that the Hamiltonian can be repeatedly applied to the orbital. A similar process is required for iterative ground-state DFT calculations, and thus, TDDFT can benefit from already established methods for conventional static DFT. This approach offers several advantages. Firstly, it is sufficient to compute the occupied states of the ground-state Kohn-Sham Hamiltonian, which is particularly beneficial when employing a large basis set. Secondly, it allows for the calculation of the response function across a broad range of frequencies in a single propagation. In practice, there exists a relationship between the time step utilized and the maximum achievable frequency, specifically $\omega_{max} = 1/\delta t_{max}$.

The numerical stability of the calculation depends on the choice of the time step. The computational time required by this method is connected to the choice of the time propagation operator $\hat{U}$ and the total number of time steps required for the calculation to attain the end result. As shown in Equation 2.25, every step of the evolution needs several applications of the Hamiltonian to a number of orbitals equivalent to the occupied states. This iterative procedure is identical with that required for the calculation of the ground-state problem. Thus, the numerical scalability of this method is akin to the ground-state problem and is suitable for large systems [98].

### 2.3.3 Absorbing boundary conditions

TDDFT has a unique property whereby the obtained TD wave functions preserve their norm over time, as expressed by $\int d^3r\rho(\mathbf{r},t) = N$, where N refers to the norm or the number of particles. Essentially, this means that the probability density cannot be created or destroyed. In situations where a system is perturbed by an intense electric field, ionization occurs, hence, boundary conditions need to be implemented at the edges of the simulation box. In other words, while calculating the dynamics of a system under the influence of strong electric field within TDDFT, the outgoing wave functions that are driven by the field, will infact return to the initial position if the boundary conditions are reflective, which is unphysical. However, absorbing boundary conditions can be applied at the edges of the simulation box in order to prevent the reflections of the wave function. This is implemented by including a negative short range complex valued potential to the total potential at the region, which exists far away from the ionized system. If the outgoing wave function reaches the absorbing boundary and is absorbed, the norm of the wave function is no longer conserved and the fraction of the outgoing wave function is considered to describe ionization.

## 2.4 Two-temperature model (TTM)

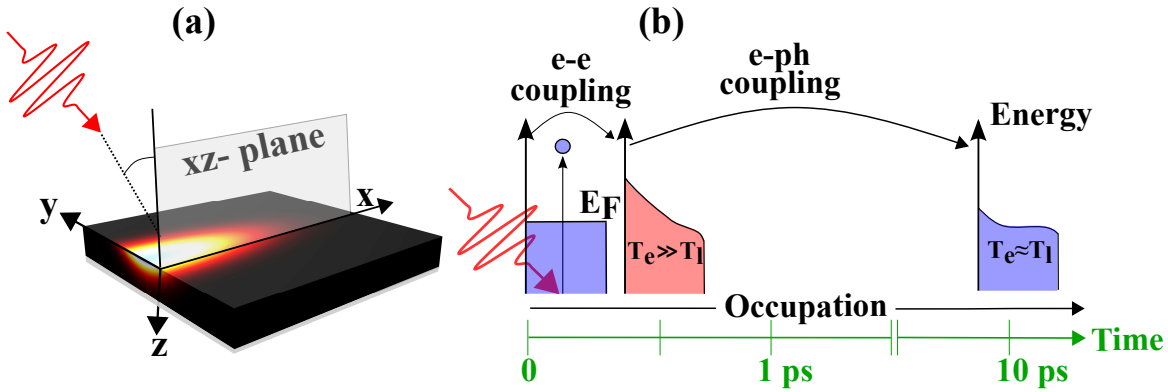


Figure 2.1: (a) Schematic representation of the 3D irradiation setup involving the focusing of an ultrashort laser pulse onto a metal film. The pulse is incident onto the surface plane $x-y$ at an angle with respect to the $z$ axis. (b) Illustration of the ultrafast thermalization processes time scales of both the electrons and lattice, characterized by the temperatures $T_e$ and $T_l$, respectively. These temperatures are perturbed from equilibrium due to the influence of the laser pulse, operating on ultrafast time scales.

Experimentally, a femtosecond laser pulse with suitable polarization is aimed onto the specified material surface at a predetermined incidence angle. The spatio-temporal profiles of the laser pulse, the focusing arrangement, and the inherent material properties all exert significant influence on the ensuing interaction. Additionally, the material characteristics, which vary with temperature, dynamically evolve during the interaction and must be integrated in a self-consistent manner within the process description. From such thermally dominant interactions, observables such as transient reflectivity [101–104], ablation threshold [105–108], or thermionic electron emission yield [109, 110] are extracted, and are dependent on the time-dependent material features. In the presence of a finite laser focal spot size, both the thermal changes and the material parameters that are temperature-dependent exhibit spatial variations, necessitating a thorough 3D analysis of the interaction. Consequently, to model the dynamic energy deposition on the surface of a metal and the subsequent thermal processes, we employ a suitable, dynamic 3D framework.

The irradiation setup is illustrated in Figure 2.1(a). The Cartesian coordinate system $(x, y, z)$ is arranged so that the $(x, y)$ plane corresponds to the surface that is irradiated, while $z$ is normal to this surface, i.e. defined by the $(x, y, 0)$ plane. Origin $(x = 0, y = 0, z = 0)$ is positioned on the target

surface, which receives the maximum laser fluence. The laser pulse is focused onto the surface at an incidence angle $\theta$, with the incidence plane being $xz$. The laser polarization is either oriented within the incidence plane (P) or perpendicular to it (S). Under the influence of an ultrafast, moderately intense laser pulse (peak laser intensity $I_0$ ranging from $10^9$ to $10^{14}$ $Wcm^{-2}$ and durations within the range of a few hundred to a thousand femtoseconds, denoted by $t_p \in [100, 1000]$ $fs$), a metal surface showcases distinct thermal reactions within its electronic and lattice systems. Each of these processes operates on different timescales [Figure 2.1(b)] and directly impact the underlying energy redistribution dynamics. When a femtosecond laser pulse is incident on a metallic film, most of the energy from the laser pulse is absorbed by the conduction-band electrons within a few femtoseconds. At first, the high energy electrons couple with each other via electron-electron (e-e) collisions and attain thermal equilibrium at a time scale of $\tau_{ee} < 100$ fs, which is termed as "internal thermalization". In this condition, the electron energy distribution is momentarily deviated from the Fermi-Dirac distribution [101, 111, 112]. As a result, two different temperatures exists between electrons and lattice, where the change in temperature of lattice is minimal (nonequilibrium condition), which was first described by Anisimov and coauthors [65].

Ultimately, through the process of electron relaxation dynamics, over a duration of $\tau_{ee}$, the electrons reestablish the Fermi-Dirac distribution. In our work, we consider the pulse duration $t_p$ (represented by the intensity full width at half maximum or FWHM) to be 200 $fs$. Consequently, upon laser excitation, the electron subsystem rapidly attains local thermal equilibrium, leading to an elevation in the electron subsystem's temperature $T_e$. This elevation takes place as the electron subsystem deviates from equilibrium with the phonon background (i.e., the lattice subsystem characterized by temperature $T_l$). The consequent dynamics in space and time is described by two distinct temperatures analogous to the electron ($e$) and lattice ($l$) sub-systems. These temperatures are interlinked via the electron-phonon ($e-ph$) coupling, depicted schematically in Figure 2.1(b). Ultimately, at a higher temperature, typically on a time span of several picoseconds ($ps$) the equilibrium between the electron and lattice sub-systems is reestablished (termed as "external thermalization"). This phenomenon can often be addressed by the classical TTM, which describes the temporal evolution of the temperature of both the electronic and the lattice sub-systems due to the absorption of the laser pulse energy within the material and is applied to model physical phenomena such as energy transfer between electrons and lattice during the laser-matter interaction period.

The importance of the 3D TTM lies in its ability to provide more accurate predictions of the behavior of materials under intense laser irradiation. By accounting for the three-dimensional distribution of temperature, the model can better capture the complex spatial and temporal dynamics of ultrafast laser-matter interactions. This is particularly important for understanding phenomena such as laser ablation, where material is removed from a surface by a laser pulse. The 3D TTM can also be used to study the formation of laser-induced periodic surface structures (LIPSS) [113] and other laser-induced material modifications. The 3D TTM is applied to model the spatio-temporal evolution of temperature and energy exchange among the electrons $T_e(x, y, z, \Delta t)$, lattice $T_l(x, y, z, \Delta t)$ of the solid, and the substrate $T_s(x, y, z, \Delta t)$, driven by a single Gaussian femtosecond laser source $Q(x, y, z, t)$, by considering the following 3D non-linear coupled parabolic equations, which are given as [101]

$$C_e(T_e)\frac{\partial T_e(x,y,z,t)}{\partial t} = \nabla.\big(k_e(T_e,T_l)\nabla T_e(x,y,z,t)\big) - G\big(T_e(x,y,z,t) - T_l(x,y,z,t)\big) + Q(x,y,z,t) - S_{es}(T_e,T_s), \tag{2.26a}$$

$$C_l\frac{\partial T_l(x,y,z,t)}{\partial t} = \nabla.\big(k_l\nabla T_e(x,y,z,t)\big) + G\big(T_e(x,y,z,t) - T_l(x,y,z,t)\big) - S_{ls}(T_l,T_s), \tag{2.26b}$$

$$C_s\frac{\partial T_s(x,y,z,t)}{\partial t} = \nabla.\big(k_s\nabla T_s(x,y,z,t)\big) + S_{ls}(T_l,T_s) + S_{es}(T_e,T_s), \tag{2.26c}$$

where $C_e/C_l$ ($C_s$) and $k_e/k_l$ ($k_s$) denote specific heat capacity and thermal conductivity of the electrons/lattice (substrate), respectively. $G$ is electron-lattice coupling factor. $S_{es/ls}$ is the boundary interface heat exchange between solid electrons/lattice and the substrate, given as $S_{es/ls} = G_{es/ls}(T_{e/l} - T_s)$, where $G_{es/ls}$ is the corresponding thermal boundary conductance. Equation 2.26a describes the energy absorption of the electron subsystem from the laser pulse, the heat diffusion among the electrons, and heat transfer to the lattice. The Equation 2.26b is for the lattice subsystem, and contains a heat diffusion term, and energy input term due to coupling with the electrons. Equation 2.26c is for the substrate system which contains the diffusion term and the boundary interface heat transfer between the metal electrons/lattice and the glass substrate. The laser power density is denoted by $Q(x, y, z, t)$, which is the source of energy input into the electron subsystem and is considered as a Gaussian pulse, in time and space [114], directed at an angle $\theta$ (w.r.t normal of the sample) onto the 3D volume surface.

The electric field $E(x, y, t)$ is obtained by transforming the incident laser field to the sample coordinate system ($x$,$y$) and thus the subsequent distribution of intensity on the surface of the target is attained and given as $I(x, y, t) = \epsilon_0 c/2|E(x, y, t)|^2$, where $\epsilon_0$ represents the permittivity of vacuum and $c$ denotes the speed of light in vacuum. Nonetheless, when the laser is incident at an oblique angle, to conserve the energy that is deposited and spread out over an area larger than that of normal incidence, the intensity is scaled by a factor of $1/\cos\theta$. But, in this work, since we are conserving the intensity, $1/\cos\theta$ factor is not necessary to include. Thus, the effective intensity '$I_{\text{eff}}$' can be written as $I_{\text{eff}}(x, y, t) = \epsilon_0 c/2\ |E(x, y, t)|^2$. Additionally, it is also necessary to include a suitable model for laser absorption at the areas near to the metal surface, taking into account the dynamic reflectivity $R_{s,p}(x, y, t)$, where $s$ and $p$ denotes the polarization of light that is perpendicular and parallel to the plane ($x$,$z$), respectively (see Figure 2.1a), which is explained later. The decay of $Q$ as a function of $z$ follows an exponential trend, in accordance with the physical principles that regulate the penetration of the pulse into the target.

$$Q\,(x, y, z, t) = \frac{I_{abs}(x, y, t)}{(\delta + \delta_b)(1 - \exp\,(-d/(\delta + \delta_b)))} \exp\left(-\frac{z}{(\delta + \delta_b)}\right), \tag{2.27}$$

here $I_{abs}$ represents the laser intensity absorbed by the sample at a point ($x$,$y$), which is given by $I_{\text{abs}}(x, y, t) = (1 - R_{s,p}(x, y, t))I_{\text{eff}}(x, y, t)$. Thickness of the target material is denoted with $d$, $\delta$ is the laser penetration depth, which depends on the wavelength and electron temperature, and is given as $\delta = 1/\alpha$ [115], where $\alpha = (4\pi Im(n_2))/\lambda$ is the absorption coefficient, imaginary part of the refractive index ($n_2$) is denoted by $Im(n_2)$, explained later. $\lambda$ denotes the laser wavelength. To consider the effects of both diffusion and ballistic motion of hot electrons, the electrons' ballistic range, $\delta_b$ is considered to be 105 $nm$ [116], and is included along with the optical penetration depth $\delta$.

We have calculated the temperature-dependent electron-lattice coupling factor, denoted as $G$, using the analytical expression given as [117] $G(T_e, T_l) = G_{RT}\left[A_e/B_l(T_e + T_l) + 1\right]$. Here, $G_{RT}$ is the electron-lattice coupling factor at room temperature and is equal to $2.2 \times 10^{16}\ Wcm^{-2}$ . The material constants $A_e = 1.2 \times 10^7\ K^{-2}s^{-1}$ and $B_e = 1.23 \times 10^{11}\ K^{-1}s^{-1}$ are considered. For this study, we assume the following constant values: $C_l = 2.45 \times 10^6\ Jm^{-3}K^{-1}$ [118], $C_s = 1.848 \times 10^6\ Jm^{-3}K^{-1}$ [101], and $k_s = 0.8\ Wm^{-1}K^{-1}$ [119]. The temperature-dependent parameters are defined as follows: $C_e(T_e) = \gamma T_e$ and $k_e(T_e, T_l) = k_0(T_e/T_l)$, where $\gamma = 71\ Jm^{-3}K^{-2}$ and $k_0 = 317\ Wm^{-1}K^{-1}$ [120]. Additionally, $k_l = k_{eq} \times 0.01\ Wm^{-1}K^{-1}$ [121, 122], where $k_{eq}$ represents the thermal conductivity at equilibrium and is given by the equation $k_{eq} = 320.973 - 0.0111\ T_l - 2.747 \times 10^{-5}\ T_l^2 - 4.048 \times 10^{-9}\ T_l^3$ [123]. The heat transfer at the boundary interface between the metal electrons/lattice and the glass substrate is expressed as $S_{es/ls} = G_{es/ls}(T_{e/l} - T_s)$. The thermal boundary conductance values are given as $G_{es} = (96.12 + 0.189\ T_e)\ MWm^{-2}K^{-1}$ and $G_{ls} = 141.5\ MWm^{-2}K^{-1}$ [124], respectively.

### 2.4.1 Temperature Dependent refraction index

As discussed earlier, during the laser-target interaction, absorbed intensity ($I_{abs}$) in Equation 2.27 is computed from the reflectivity, which is modeled using Fresnel equations for S ($R_s$), and P-polarized

light ($R_p$) [125]:

$$R_{\mathrm{s}}(x,y,t) = \left| \frac{n_1 \cos\theta - n_2 \sqrt{1 - \left(\frac{n_1}{n_2}\sin\theta\right)^2}}{n_1 \cos\theta + n_2 \sqrt{1 - \left(\frac{n_1}{n_2}\sin\theta\right)^2}} \right|^2 , \tag{2.28a}$$

$$R_{\mathrm{p}}(x,y,t) = \left| \frac{n_1 \sqrt{1 - \left(\frac{n_1}{n_2}\sin\theta\right)^2} - n_2 \cos\theta}{n_1 \sqrt{1 - \left(\frac{n_1}{n_2}\sin\theta\right)^2} + n_2 \cos\theta} \right|^2 , \tag{2.28b}$$

here refractive index of the ambient medium is denoted by $n_1$, considered to be unity (because it corresponds to vacuum), sample's refractive index $n_2 = n + ik = \sqrt{\epsilon_{DCP}(\omega)}$), where the real and imaginary parts of the refractive index are denoted by $n$ and $k$, respectively. Gold's complex dielectric constant is denoted by $\epsilon_{DCP}$.

The refractive index of a material is wavelength-dependent, but it can also undergo significant changes during interactions with extreme temperature variations. For metals, the widely used permittivity calculation follows the Drude-Lorentz model, but for improved accuracy, especially with metals such as silver and gold, the Drude-critical points model (DCP) has been found to be more effective [126]. Therefore, in our calculations, we adopt the gold's electric permittivity model $\epsilon_{DCP}$ proposed in existing literature [126–128]. Considering the influence of lattice and electron temperatures on the permittivity, we aim to create a refractive index model that is temperature-dependent. To achieve this, we used temperature-dependent electron relaxation times from the work of Block et al. [101] and combined it with the Drude-critical points model. The model considered by Vial combines the Drude intraband contributions to permittivity with two-critical points model that account for interband transitions, given as [126]

$$\epsilon_{\mathrm{DCP}}(\omega) = \epsilon_\infty - \frac{\omega_P^2}{\omega^2 + i\gamma\omega} + \sum_{p=1}^{2} A_p \Omega_p \left( \frac{e^{i\phi_p}}{\Omega_p - \omega - i\Gamma_p} + \frac{e^{-i\phi_p}}{\Omega_p + \omega + i\Gamma_p} \right) . \tag{2.29}$$

In Equation 2.29, the right-hand side consists of three terms, each with specific contributions to the model. The first two terms represent the standard Drude model [129], where $\epsilon_\infty$ is the high-frequency limit dielectric constant, $\omega_P$ denotes the plasma frequency, and the damping term is denoted by $\gamma$. The third term accounts for two interband transitions and employs the two-critical points transition model as explained in the reference [130]. $\phi_p$ denotes the phase, $\Omega_p$ signifies the energy of the gap, $A_p\Omega_p$ represents the dimensionless amplitude, and $\Gamma_p$ represents the broadening, which is given as $\Gamma_p = A_{\Gamma p} T_e^2 + B_{\Gamma p} T_l + \gamma_p$. The Permittivity in Equation 2.29 is given as a function of driving laser frequency. Vial [126] obtains the constants $A_p$, $\Omega_p$, $\Gamma_p$, $\gamma$, $\phi_p$, and $\omega_D$ by fitting the model to experimental data, room-temperature data from Johnson and Christy [131]. In the earlier works [127, 128], the fit with all the free parameters produced $\phi_1 \sim \phi_2 \sim -\pi/4$. To simplify the parameter space and improve convergence of the other parameters, we constrained the two phases to be the same and equal to $-\pi/4$, effectively reducing the number of independent parameters.

However, this model lacks temperature dependence. To address this limitation, we introduced modifications to the model. First, we considered $\gamma$ to be temperature dependent, following the approach used by Block et al. [101]. Additionally, we made $\Gamma_p$ temperature-dependent as well. We then fitted our modified model to Johnson and Christy data [131]. Considering only the Drude model term, both the plasma frequency $\omega_P$ and the electron relaxation rate $\gamma$ exhibit temperature-dependent variations. For instance, at moderate lattice temperatures, the gold lattice contains one conduction band (free) electron per nucleus. However, the lattice may experience thermal expansion and a density change if it melts. The plasma frequency can be expressed as $\omega_P = \sqrt{\frac{e^2 n_e(T_0)}{\varepsilon_0 m_{eff}} \frac{1}{(1+\beta\Delta T_l)}}$, where $e$ is the charge of an electron, the ambient temperature is denoted by $T_0$, free electron density is denoted by $n_e(T_0)$ that is

| Parameter | Value |
|---|---|
| A $[K^{-2}s^{-1}]$ | 1.2 $\times 10^{7}$ |
| B $[K^{-1}s^{-1}]$ | 4.428703071 $\times 10^{11}$ |
| $\Omega_1$ $[rad\ s^{-1}]$ | 4.01772608$\times 10^{15}$ |
| $A_{\Gamma 1}$ $[K^{-2}s^{-1}]$ | 1.2 $\times 10^{7}$ |
| $B_{\Gamma 1}$ $[K^{-1}s^{-1}]$ | 1.14681587030 $\times 10^{11}$ |
| $\gamma_1$ $[rad\ s^{-1}]$ | 7.9 $\times$ $10^{14}$ |
| $\phi_1$ | $-\pi/4$ [127, 128] |
| $A_{\Gamma 2}$ $[K^{-2}s^{-1}]$ | 1.2 $\times 10^{7}$ |
| $B_{\Gamma 2}$ $[K^{-1}s^{-1}]$ | 6.094240955631399 $\times 10^{11}$ |
| $\gamma_2$ $[rad\ s^{-1}]$ | 1.9 $\times$ $10^{15}$ |
| $\phi_2$ | $-\pi/4$ [127, 128] |
| $\Omega_2$ $[rad\ s^{-1}]$ | 5.56883141$\times 10^{15}$ |
| $A_1$ | 0.917783355 |
| $A_2$ | 1.52288304 |
| $\epsilon_\infty$ | 1.197 |

Table 2.1: Parameters in Equation 2.29 calculated by fitting to Johnson and Christy data [131].

equivalent to $5.9 \times 10^{28}\ m^{-3}$, $\varepsilon_0$ is the vacuum dielectric permittivity, $m_{eff}$ is the effective mass of an electron ($\sim 1.094 \times m_e$, the mass of an electron [127]), and $\beta$ is the volume thermal expansion coefficient of gold, which is approximately $4.23 \times 10^{-5}\ K^{-1}$ [132]. However, modeling $\gamma$ with a constant value is not suitable for a material that has highly varying temperatures. The electron collision rate term $\gamma$ can be separated into two components: electron-electron collision rate $\gamma_{e-e}$ and electron-phonon collision rate $\gamma_{e-ph}$, where the overall rate is given by $\gamma = \gamma_{e-ph} + \gamma_{e-e}$, with $\gamma_{e-e} = AT_e^2$ and $\gamma_{e-ph} = BT_l$ [101, 133]. The analytical estimation of both terms is provided by Fisher et al. [134]. The parameters for Equation 2.29 resulting from the fit are displayed in Table 2.1.

Therefore, by knowing $T_e(x, y, t)$ and $T_l(x, y, t)$ at the interface plane, along with the incident laser parameters, it is possible to calculate the reflectivity $R_{s,p}(x, y, t)$. The calculations can be expanded and applied to any laser polarization orientations in a general manner. This is achieved by breaking down the laser electric fields on the surface into perpendicular S and P components, and then combining the reflection coefficients for each polarization separately.

# Chapter 3

# Thermionic/photo-thermionic emission from metal nanotargets and its dependence on coatings

The emission of electrons from a material refers to the process of the carriers escaping the surface barrier. This phenomenon has a wide range of applications, including the construction of bright electron sources for high-resolution electron microscopy [135]. Important properties such as good mechanical and chemical stability [136], appropriate surface morphology [137], and high electron emission probabilities [138] are the basic criterion to achieve efficient electron emission from a material. In this regard, cladding (the application of one material over another to provide a layer) on a metal surface is highly effective, particularly for practical usage, commercialization, and efficient installation in devices. Hence, different surface treatment methods for films are gaining considerable attention in the materials engineering community as a viable approach for further enhancing the target's emission properties. Surface engineering methods [139, 140], including ion-beam bombarding, hydrogen etching, and metal coating, are rapidly advancing towards improved properties and performance.

One common method to improve the electronic properties of surfaces involves modifying the effective barrier height or work function to increase the emission flux. This can be achieved through various means, such as substrate effects [40], doping [141], or introducing defects [142]. In a recent study [143], cesium combined with an appropriate proportion of oxygen was deposited on graphene to lower its work function. The study also suggests that the work function could be further reduced by electrostatic gating obtained through suitable doping of the parent material, thereby adjusting the interlayer interaction with the coating. The interaction at the interface between the target and the coating material depends on the effective interface thickness, which is also related to the thickness of the coating material. Hence, key contributions from (i) coating thickness, (ii) thickness and type of each material layer, and (iii) the interface region necessitates a thorough investigation.

However, there is a lack of understanding regarding the influence of coating thickness on effective flux, which necessitates a thorough investigation. Recent observations indicate that the surface material's dimensionality significantly impacts the characteristics of effective field emission [144], emphasizing the importance of coating thickness in determining the emission current. Even monoatomic layers (i.e., few angstroms) of coating thickness, as demonstrated in the study by Khalid et al. [145], can be effective in enhancing field emission properties from metal surfaces. In this context, first we develop an analytical model to examine the electron emission processes from metal nanotargets, to evaluate the impact of surface coating on electron emission properties of a coated target and to establish a suitable parameter range for its efficient operation. According to experimental findings [146], the stability and efficiency of field-emission can be significantly enhanced based on the microstructure and surface morphology of the surface coating, as compared to the films that are not coated. It is an important question to explore how the properties of the material, such as the work function and the Fermi level of the surface coating compared to its inner bulk counterpart, influence the overall performance of field emitters. In this

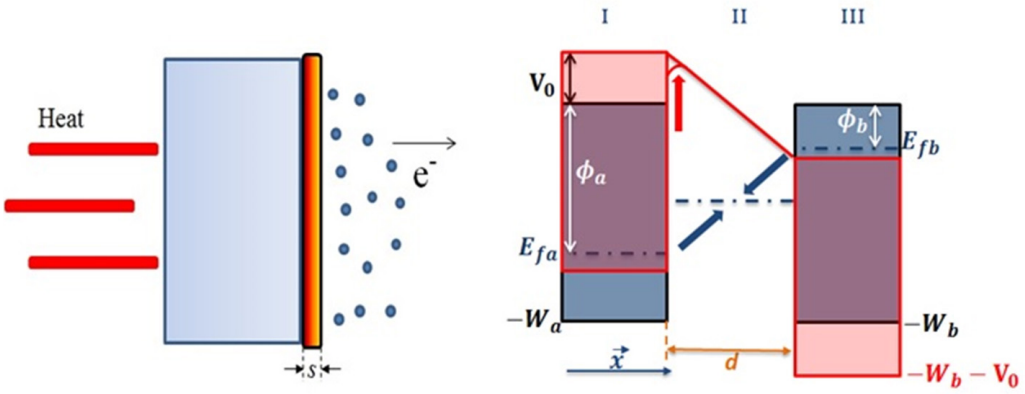


Figure 3.1: Schematic representation of heat induced thermionic electron emission from a thin coating with width $s$ over a metal target (left panel). The schematic representation of energy levels in composite materials is shown in the right side panel. All energy levels are calculated from the vacuum surface. The three different regions I, II, and III correspond to the target material, interface (thickness $d$) formed due to the coating material and the target material, respectively. The shaded blue and red regions refer to the energy levels of the target and the coating material when kept isolated and in contact, respectively. The transfer of electron population to achieve dynamic equilibrium is denoted with blue arrows.

chapter, we propose an analytical model to investigate electron emission from a coated metal surface, subject to a DC electric field. Additionally, we examine the effective emission properties for varying thicknesses of the coating layer, with the aim of identifying a straightforward approach to improving the field emission efficiency from coated metal targets.

## 3.1 Electron energy analysis

In this study, we investigate the electron transport properties in the context of electron emission from surfaces coated uniformly with a low work function material onto a planar bulk metal target. This system can be visualized as a uniform metal or semiconductor surface in contact with a bulk material. When brought into contact, the free electrons transfer from the lower work function coating layer to the higher work function parent surface, resulting in the equilibration of the respective Fermi levels at a common potential (as in Figure 3.1). This leads to the development of a finite potential ($2V_0$) equivalent to the difference between their work functions across the interface region (thickness $d$) between the two surfaces, resulting in an electric field inwards to the parent surface. As a result of this potential/field structure, the electrons inside the parent metal available for emission must overcome the Schottky reduced triangular potential barrier, while the electrons related to the outer coating surface must overcome the enhanced step potential barrier for emission. The energy diagram of the system is shown in Figure 3.1, where all the energy levels are measured from the vacuum level. The Fermi level, bottom of the conduction band (barrier height), and work function are represented by $E_f$, $W$, and $\phi$, respectively, while the additional subscripts '$a$' and '$b$' denote the properties associated with the parent and coating materials. The additional potential $V_0$ represents the rise/drop in the energy levels of the parent/coating material due to the transfer of the electron population in achieving dynamic equilibrium of the Fermi levels, shown by broken blue lines in Figure 3.1. The Schottky reduced potential barrier is shown in the figure with a red arrow. By estimating the electron emission flux from the coated surfaces, we evaluate the coefficient of tunneling for the electron populations associated with the parent target and coated surfaces using this electronic energy level description, which is further used to investigate the electron emission currents.

## 3.2 Estimation of the tunneling coefficient

In order to calculate the tunneling coefficient of electrons from a coated surface, we analyze the energy configuration in two steps. First, we consider the tunneling of electrons from the inner parent material at a negative potential with a Schottky reduced triangular potential barrier. Second, we examine the effective tunneling of electrons from the coating surface, which offers an enhanced step potential barrier. A graphical illustration of both cases is depicted in Figure 3.1. The electron occupancy in the potential structures is typically described by the Schrödinger wave equation. The time-independent Schrödinger wave equation for electrons can be expressed as [147]

$$\frac{d^2\psi}{dx^2} + \frac{2m}{\hbar^2}\Big[E_x - V(x)\Big]\psi = 0 \ , \tag{3.1}$$

here $E_x$ and $V(x)$ refers to the normal and potential energy of electrons in the potential structure, respectively, while $m$ is the electronic mass and $\hbar$ is the reduced Planck constant.

Using the respective energy structure, for the inner parent material (Figure 3.1), the potential energy $V(x)$ in the three different regions could be given as [148–150]

$$V(x) = V_0, \qquad x < 0 \tag{3.2a}$$
$$V(x) = V_0(1 - 2x/d), \qquad 0 \le x \le d \tag{3.2b}$$
$$V(x) = -V_0 \qquad x > d \tag{3.2c}$$

By substituting the above potential energy expressions in Equation 3.1, corresponding Schrödinger wave equation can be written as,

$$\psi^{''}(\zeta) + k_1^2\psi = 0, \qquad \zeta(= x/d) < 0 \tag{3.3a}$$
$$\psi^{''}(\zeta) + (k_2^2 + k_p^2\zeta)\psi = 0, \qquad 0 \le \zeta \le 1 \tag{3.3b}$$
$$\psi^{''}(\zeta) + k_3^2\psi = 0, \qquad \zeta > 1 \tag{3.3c}$$

where $\varepsilon_x = E_x/V_0$, $k^2 = (2mV_0d^2/\hbar^2)$, $k_2^2 = k_1^2 = k^2(\varepsilon_x - 1)$, $k_3^2 = k^2(\varepsilon_x + 1)$, $k_p^2 = 2k^2$. Considering the wave solution in these regions, the solutions of the set of Equations 3.3 can be expressed as

$$\psi \equiv \psi_1 = \exp ik_1\zeta + b\exp -ik_1\zeta, \qquad \zeta < 0 \tag{3.4a}$$
$$\psi \equiv \psi_2 = cA_i\Big[-(k_2^2 + k_p^2\zeta)/(ik_p)^{4/3}\Big] + dB_i\Big[-(k_2^2 + k_p^2\zeta)/(ik_p)^{4/3}\Big], \qquad 0 \le \zeta \le 1 \tag{3.4b}$$
$$\psi \equiv \psi_3 = f\exp ik_3\zeta \qquad \zeta > 1 \tag{3.4c}$$

The solutions described above show that Equation 3.4a represents the incident (first term) and reflected (second term) waves in the first region ($\zeta < 0$), while Equation 3.4c corresponds to the wave transmitted to the third region ($\zeta > 1$). The coefficients $b$ and $f$ denote the amplitude of the reflected and transmitted waves in the first and third regions, respectively. The solution for the second region (Equation 3.4b) represents growing (first term) and decaying (second term) waves. The transmission and reflection coefficients are obtained by applying the continuity of the wave function and its derivatives at the boundary layers. By using this method and performing some algebraic manipulations, coefficient $f$, which represents the transmission of the wave in the third region, can be expressed as

$$f = \frac{f_n}{f_{d1} - f_{d2}} \ . \tag{3.5}$$

With

$$f_n = 2(i/k_3)(ik_p)^{2/3}\left[A_i^{'}(c_1)B_i(c_1) - A_i(c_1)B_i^{'}(c_1)\right]\exp\left(-ik_3\right) ,$$
$$f_{d1} = \left[B_i(c_0) - (i/k_1)(ik_p)^(2/3)B_i^{'}(c_0)\right]\left[A_i(c_1) + (i/k_3)(ik_p)^(2/3)A_i^{'}(c_1)\right] ,$$
$$f_{d2} = \left[A_i(c_0) - (i/k_1)(ik_p)^(2/3)A_i^{'}(c_0)\right]\left[B_i(c_1) + (i/k_3)(ik_p)^(2/3)B_i^{'}(c_1)\right] ,$$
$$c_0 = -k_2^2/(ik_p)^{4/3} \; and \; c_1 = -(k_2^2 + k_p^2)/(ik_p)^{4/3} .$$

The coefficient of the tunneling of electrons into the third region can be represented as $T_a = |(k_3/k_1)ff^*|$, where $f^*$ refers to the complex conjugate of coefficient $f$. This equation provides information about the likelihood of the electrons having a certain energy to approach the top layer, which adds to the electron population on the coated surface and influences electron emission. Referring to the potential structure for the outer coated surface in Figure 3.1 (region III), the coefficient of tunneling related to the enhanced step potential barrier (by $V_0$) can be represented as [150]

$$T_b = \frac{4\varepsilon_x^{1/2}(\varepsilon_x + w_b + 1)^{1/2}}{\left[\varepsilon_x^{1/2} + (\varepsilon_x + w_b + 1)^{1/2}\right]^{1/2}} , \tag{3.7}$$

where $w_b = W_b/V_0$. After determining the tunneling coefficient of electrons, the subsequent step is to calculate the emission flux from the coated surfaces.

## 3.3 Evaluation of the emission current

Due to the bulk nature of the inner surface, the electrons in the conduction layer (Fermi sea) exhibit a parabolic dispersion relation of the form $E = \hbar^2k^2/2m$. When carriers approach the interface, image charges are induced, causing a slight reduction in the effective barrier height. To account for this "Schottky barrier" effect, we incorporate the induced electric field due to the contact potential in our analysis, which elevates the electron statistical distribution level to a higher energy state and affects the evaluation of the emission flux. Following Fowler's approach to the statistical distribution for bulk metallic materials, the total number of electrons impinging the surface normally (for the parent surface) per unit area per unit time, with normal and parallel energy components in the range of ($E_x$ and $E_x + dE_x$) and ($E_t$ and $E_t + dE_t$), can be expressed as

$$d^2n_a = (A_0/e)T^2[T_a(e_x)F(e_x + e_t + \varphi_a - \upsilon_0 - \upsilon_{sc})]de_xde_t , \tag{3.8}$$

where $A_0 = 4\pi emk_B^2/h^3 \sim 117A/cm^2K^2$, $e_{x,t} = E_{x,t}/k_BT$, $\varphi_a = e\phi_a/k_BT$, $\upsilon_0 = eV_0/k_BT$, and $(A_0/e)$ represents the flux associated with the Richardson constant ($A_0$). The term $\upsilon_{sc} = (e^3\mu)^{1/2}/k_BT$ accounts for the lowering of the potential barrier due to the Schottky effect, which causes a rise in particle energy. The parameter $\mu = 2V_0/d$ represents the electric field strength. The function $F(E)$ corresponds to the electron energy distribution, and $T$ represents the surface temperature. The Boltzmann constant is denoted as $k_B$. In the present calculations, we use Fermi-Dirac (FD) statistics for the energy distribution of electrons, denoted by $F_{FD} = [1 + \exp(E/k_BT)]^{-1}$. At higher temperatures, the electron energy distribution approaches a Maxwellian distribution ($M$), denoted by $f \equiv f_M = \exp(-E/k_BT)$. After applying the appropriate particle distribution, such as $FD$ or $M$, the Equation 3.8 can be simplified by integrating over the $e_t$ space, which ranges from 0 to infinity. The resulting expression is given as

$$dn_{a,FD} = (A_0/e)T^2[T_a(e_x)\ln\left[1+\exp\left(\upsilon_0+\upsilon_{sc}-\varphi_a-e_x\right)\right]]de_x\ , \tag{3.9a}$$

$$dn_{a,M} = (A_0/e)T^2[T_a(e_x)\exp\left(\upsilon_0+\upsilon_{sc}-\varphi_a-e_x\right)]de_x\ . \tag{3.9b}$$

The set of Equations 3.9 are used to calculate the flux of electrons that can surpass the triangular barrier present at the interface region. This results in an increase in the electron population density for emission, in addition to the existing electrons in the top coating layer. This is achieved by the enhanced step potential barrier at the outer surface.

It is worth taking into account the width of the coating, as it plays a critical role in determining the concentration of charge carriers (electrons) within the coated region, which, in turn, impacts the electrical conductivity. To calculate the electron population density within the coating material, we employ a non-parabolic energy dispersion relation that is dependent on the thickness, similar to that of 2D graphitic heterostructures [151]. The parallel dispersion relation for the top layer of the coating, with thickness ($s$), can be described as [151]

$$k_t dk_t = \left(\frac{\pi\hbar}{k_B}\right)(2A_0T/e)\left(\frac{e_h^{-2a_0/s}}{s/a_0}\right)(E-E_x)^{(2a_0/s)-1}dE. \tag{3.10}$$

The total energy of electrons inside the layer is given by $E = (E_x + E_t)$. The hopping parameter between consecutive atomic layers is denoted by $e_h$, while $a_0$ represents the interatomic mean distance. It is important to note that the constant term in the dispersion relation is adjusted to ensure that the final expression for thermionic flux is consistent with the Richardson-Dushman relation in the limiting case where the thickness of the layer approaches infinity. By using the above dispersion relation, the number of electrons hitting the top coated layer from inside with a total energy between $E$ and $(E+dE)$ and a normal energy between $E_x$ and $(E_x+dE_x)$ per unit area per unit time can be expressed as [7, 152, 153]

$$d^2n_b = (2A_0/e)T^2\left[e_h^{'-2a_0/s}/(s/a_0)\right](e-e_x)^{(2a_0/s)-1}F(e+\varphi_b+\upsilon_0)de\ de_x\ , \tag{3.11}$$

By integrating the distribution over the total energy range $(e_x,\infty)$ and simplifying it further, the electron distribution with $FD$ and $M$ statistics for normal energy can be expressed as

$$dn_{b,FD} = (2A_0/e)T^2\left[\frac{e_h^{'-2a_0/s}}{(s/a_0)}\right]\Gamma(2a_0/s)\left[\text{-Polylog}[2a_0/s,-\exp\left[-(e_x+\varphi_b+\upsilon_0)\right]]\right]de_x\ , \tag{3.12a}$$

$$dn_{b,M} = (2A_0/e)T^2\left[\frac{e_h^{'-2a_0/s}}{(s/a_0)}\right]\Gamma(2a_0/s)\exp\left[-(e_x+\varphi_b+\upsilon_0)\right]de_x\ . \tag{3.12b}$$

The total normal electron flux available for emission from the top layer with thickness $s$ can be determined by combining the contributions from both the inner parent metal as given in Equation 3.9 and the outer surface layer population as given in Equation 3.12, and can be written as

$$dn_{FD} = dn_{a,FD} + dn_{b,FD}\ , \tag{3.13a}$$

$$dn_M = dn_{a,M} + dn_{b,M}\ . \tag{3.13b}$$

To obtain the total electron flux emitted from the coated surface, we need to integrate the normal flux obtained from the tunneling probability of the outer region's enhanced step barrier over the appropriate normal energy space, that is $e_x \equiv (0,\infty)$ as

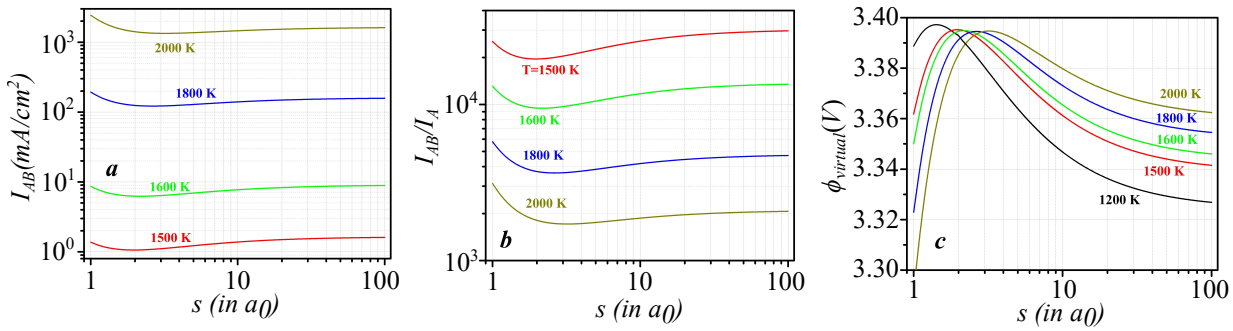


Figure 3.2: (a) Emission current ($I_{AB}$), enhanced current (b) due to coating ($I_{AB}/I_A$) and (c) the virtual work function ($\phi_{virtual}$) with respect to the width of the coating material operating at various temperatures ($T$). The results correspond to cesium (Cs) coating on a silver target material with $\phi_{Ag} = 4.5\ V$, $W_{Ag} = 10\ V$, $\phi_{Cs} = 1.95\ V$, $W_{Cs} = 3.54\ V$, $d = 5a_0$ and $e_h = 0.2\ V$.

$$n_{FD} = \int_0^\infty T_b(e_x)(dn_{a,FD} + dn_{b,FD})de_x \ , \tag{3.14a}$$

$$n_M = \int_0^\infty T_b(e_x)(dn_{a,M} + dn_{b,M})de_x \ . \tag{3.14b}$$

One can easily confirm that when the coating thickness ($s$) approaches zero (i.e. in the absence of coating), using Equation 3.9 along with $\upsilon_0 = \upsilon_{sc} = dn_{b,M} = 0$ (corresponding to $s = 0$), and simplifying $T_b = T_a = 1$, Equation 3.14b reduces to the well-known Richardson Dushman law [147–150, 154], viz. $n_M \sim (A0/e)T^2 \exp(-\psi_a) = (A0/e)T^2 \exp(-e\psi_a/k_BT)$. The set of equations presented in Equation 3.14 has been numerically analyzed for a parametric study.

## 3.4 Numerical results and discussion

In this section, we use numerical analysis to investigate the impact of surface coating (specifically, substrate material and width) on the electron emission flux, or current, from surfaces operating at finite temperatures, based on the derivations presented above (3.3). For illustration purposes and numerical appreciation of the analysis, we consider silver (Ag, with $\phi_{Ag} = 4.5\ V$ and $W_{Ag} = 10\ V$) as the inner parent metal (target, $a$), and cesium (Cs, with $W_{Cs} = 3.54\ V$ and $\phi_{Cs} = 1.95\ V$), barium (Ba, with $\phi_{Ba} = 2.52\ V$ and $W_{Ba} = 6.16\ V$), and lithium (Li, with $\phi_{Li} = 2.93\ V$ and $W_{Li} = 7.67\ V$) as three independent coating materials (substrate, $b$) for three separate sets of parametric evaluations. Other parameters used for computations are $e_h = 0.2\ V$, $d = 5a_0$ and $a_0 = 600\ nm$, which are physically plausible values for real systems [150, 151, 154]. The effect of individual parameters on the emission current is analyzed by varying them over a wide range while keeping other factors constant. The emission flux of electrons ($I_{AB}$), relative enhancement in emission current ($I_{AB}/I_A$), and the effective work function ($\phi_{virtual}$) of the coated surface are evaluated using the analytical framework and shown as functions of surface temperature ($T$), coating thickness ($s$), width of the interface region ($d$), and base work function ($\phi_A$). Note that the width of the interface region ($d$) characterizes the mutual interatomic interaction between the parent and the surfaces of the coating material, which eventually affects the electron emission flux via efficient tuning of the effective material work function. Since the half-width of the interface region ($d/2$) should not exceed the coating width ($s$), we assume that $d \equiv 2s$ for $s \leq d/2$ and $d \equiv d$ for $s > d/2$. This means that a high transition field occurs in the former case (thin coating), which may lead to a higher emission flux.

Figure 3.2 shows the impact of coating thickness on emission flux ($I_{AB}$), current enhancement ($I_{AB}/I_A$), and virtual work function ($\phi_{virtual}$). The minimum value of the electron emission current associated with the coating surface ($I_{AB}$, Figure 3.2a) is observed to occur at $s = d/2 \sim 2.5a_0$. As

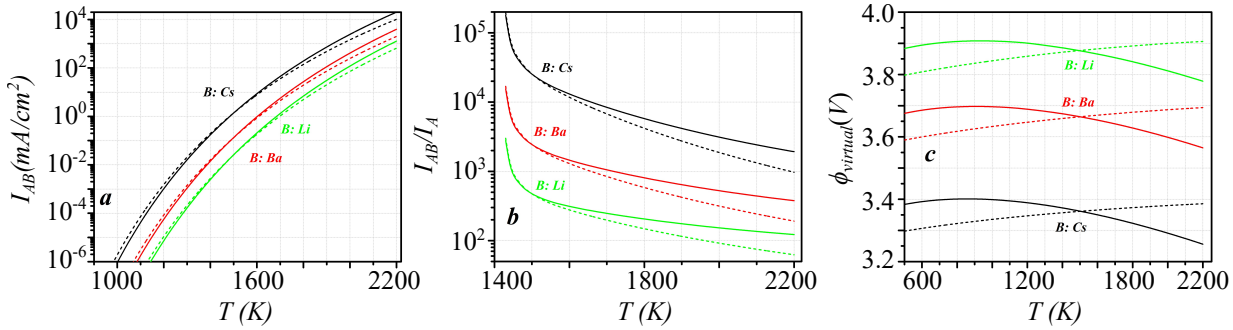


Figure 3.3: (a) Emission current ($I_{AB}$), enhanced current (b) due to coating ($I_{AB}/I_A$) and (c) the virtual work function ($\phi_{virtual}$) as a function of the operating temperature ($T$) for various coating materials. The curves correspond to a silver (Ag) target ($\phi_{Ag} = 4.5\ V$, $W_{Ag} = 10\ V$), coated with Cs ($\phi_{Cs} = 1.95\ V$, $W_{Cs} = 3.54\ V$), or Ba ($\phi_{Ba} = 2.52\ V$, $W_{Ba} = 6.16\ V$), or Li ($\phi_{Li} = 2.93\ V$, $W_{Li} = 7.67\ V$). $e_h = 0.2\ V$ and $d = 5a_0$. The solid and broken lines correspond to the coating width $s = a_0$ and $s = 10a_0$, respectively.

the coating thickness increases beyond this minimum, the emission current increases, with a more pronounced effect in the region $s > 2.5a_0$ due to an increase in electron population within the coated sheet. In the region $a_0 \leq s \leq 2.5a_0$, the high electric field in the interface region enhances the tunneling coefficient, increasing the diffusion flux of electrons from the base material to the coating sheet and thereby increasing the electron population available for emission. The emission flux is observed to saturate at a finite value with increasing coating thickness, and the Schottky effect is less pronounced for the parameters considered in this study. A rise in temperature also increases the emission current due to an increase in the high-energy electron population in the energy distribution tail. Coating the metal base with a suitable material can efficiently enhance the emission flux, as illustrated in Figure 3.2b, where the flux increases by more than three orders of magnitude. The suitable choice of coating materials and thickness provides flexibility to tune the emission current. The effective work function of the composite system can be estimated by comparing the outcoming flux from the coating surface with the thermionic emission flux associated with the Richardson-Dushman law ($\sim A_0 T^2 \exp(-\phi_{virtual}/k_B T)$). Figure 3.2c shows that the appropriate coating of the substrate over the base metal efficiently reduces the work function ($\phi_{virtual}$), with Ag work function reduced to $\sim 3.4\ V$ due to Cs coating. The dependence of $\phi_{virtual}$ on coating thickness ($s$) is a consequence of the emission current's dependence on $s$.

Figure 3.3 presents a comparison of the emission flux ($I_{AB}$), current enhancement ($I_{AB}/I_A$), and virtual work function ($\phi_{virtual}$) for different coating substrates (Cs, Ba, and Li) at two distinct coating thicknesses, $s = a_0$ and $s = 10a_0$, as a function of the operating temperature ($T$). As shown in Figure 3.3a, the emission current ($I_{AB}$) increases with a rise in surface temperature, which can be attributed to the larger population of high-energy electrons available for emission in the composite coated surface. The emission flux decreases with increasing work function of the coating materials, i.e. Cs, Ba, and Li. For a thinner coating ($s = a_0$), the electron emission is pronounced at high operating temperatures, whereas for a thicker coating ($s = 10a_0$), the emission is more effective at lower temperatures, indicating reduced field emission contribution. At lower temperatures (around 1400 $K$), the emission current is dominated by the electron population density, which is higher for $s = 10a_0$ than for a monolayer coating ($s = a_0$). At an operating temperature of around 1500 $K$, the two coating thicknesses meet, implying a similar virtual work function. The temperature dependence of the current enhancement factor ($I_{AB}/I_A$, Figure 3.3b) and virtual work function ($\phi_{virtual}$, Figure 3.3c) can be explained by the varying work function of the coating materials and the temperature dependence of the emission current ($I_{AB}$, Figure 3.3a).

The influence of the varying parent (target) material's work function ($\phi_a$) for a particular coating material (Cs coated surface) operating at different temperatures for two extreme choices, i.e. $s = a_0$ and $s = 10a_0$, on the virtual work function ($\phi_{virtual}$) and emission current ($I_{AB}$) are illustrated in

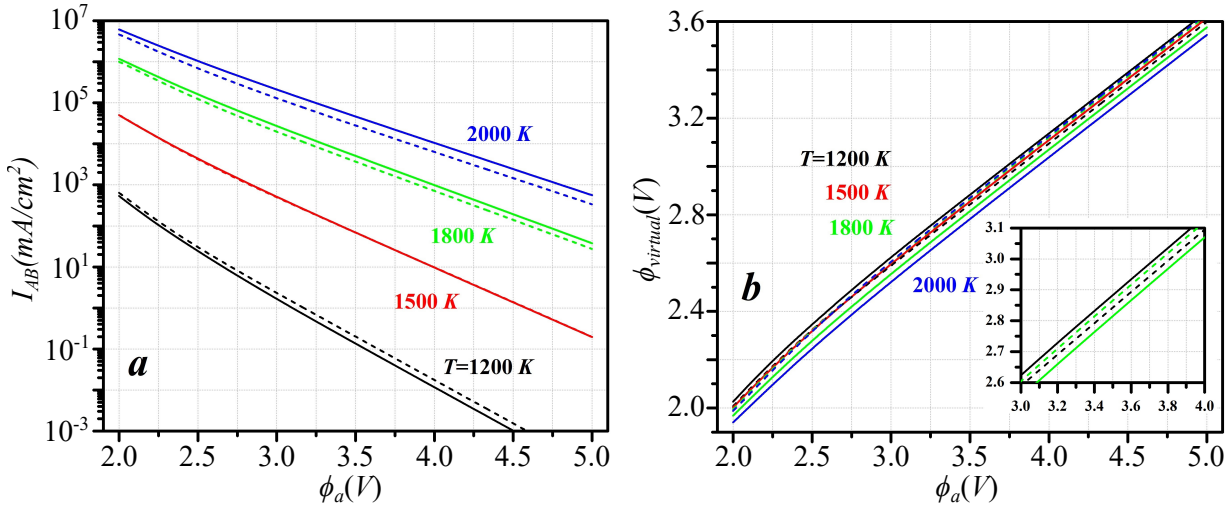


Figure 3.4: (a) Emission current ($I_{AB}$) and (b) the virtual work function ($\phi_{virtual}$) as a function of work function of the base material ($\phi_a$) operating at various temperatures ($T$). The curves correspond to cesium (Cs) coating ($\phi_{Cs} = 1.95\ V$, $W_{Cs} = 3.54\ V$), $W_a = 10\ V$, $e_h = 0.2\ V$, and $d = 5a_0$. The solid and broken lines correspond to the width of the coating metal $s = a_0$ and $s = 10a_0$, respectively. The inset in (b) depicts enlarged representation in $\phi_a$ range of $3 - 4\ V$.

Figure 3.4. As $\phi_a$ increases, the barrier height for electron diffusion via interface region III increases, resulting in a decrease in effective emission flux. At temperatures below 1500 $K$, the thicker coating yields a higher emission current $I_{AB}$ for a specific $\phi_a$ value, while at temperatures above 1500 $K$, the emission current $I_{AB}$ increases as the coating thickness decreases (as indicated by the position of the broken lines relative to their corresponding solid lines for $T = 1200\ K$ and 1800 $K$ in Figure 3.4a). The change in thickness dependence of current is more distinctly observable in the inset of Figure 3.4b. The efficient current in the case of thinner coating at high temperature is also visualized here, as discussed before in case of Figure 3.3a. Figure 3.4b provides an estimation of the virtual work function, corresponding to that shown in Figure 3.4a.

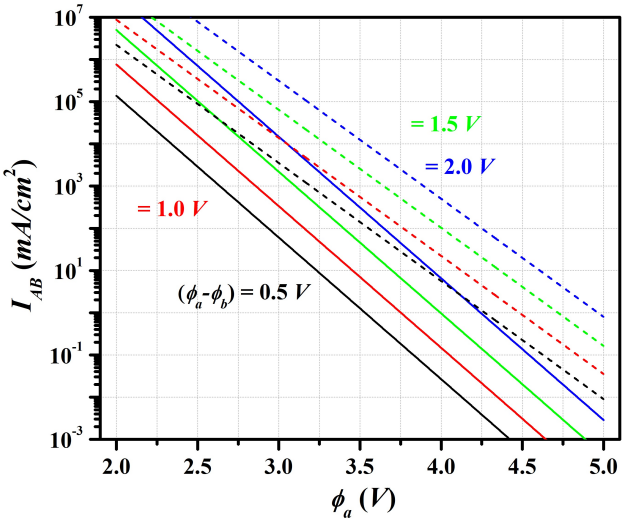


Figure 3.5: Emission current ($I_{AB}$) as a function of the target material's work function ($\phi_a$) for different values of ($\phi_a - \phi_b \equiv 2V_0$). The curves correspond to $W_a = 10\ V$, $W_b = 7\ V$, $e_h = 0.2\ V$, $s = 10a_0$ and $d = 5a_0$. The solid and broken lines correspond to the surface temperature $T = 1500\ K$ and $T = 1800\ K$, respectively.

The estimation is based on the equivalence between the net emission current calculated using the

present formulation and the Richardson-Dushman (RD) relation. The figure indicates that the effective reduction in work function due to the coating is more significant for larger $\phi_a$. This can be explained by the higher electrostatic potential (field) across the interface region, which results in a higher emission current. A significant enhancement in the emission current is noticed when both $\phi_a$ and $\phi_b$ are low but $(\phi_a - \phi_b)$ is substantially large, as evidenced by Figure 3.5. From the slope of the $I_{AB}$ against $\phi_a$ curves shown in Figure 3.5, we understand that the lower the operational temperature, the stronger the dependence of $I_{AB}$ on $\phi_a$. The set of figures in 3.6 shows the relationship between the width of the transition layer $d$ (which implies the strength of the field) and the emission flux, as well as the corresponding virtual work function for Cs-coated surfaces. The reason for the rise in the emission current as $d$ decreases can be attributed to the efficient electron flux due to the intense electric field across the interface region. This behaviour is displayed in Figure 3.6a. As illustrated in Figure 3.6b, the virtual work function associated with the coated surface is found to decrease significantly with a decrease in the width of the interface region ($d$). The observed behavior is a result of the emission current increasing in proportion to the RD emission law. It is worth noting that while the illustration is specific to a particular combination of parent and coating materials, the underlying concept can be applied to any general case.

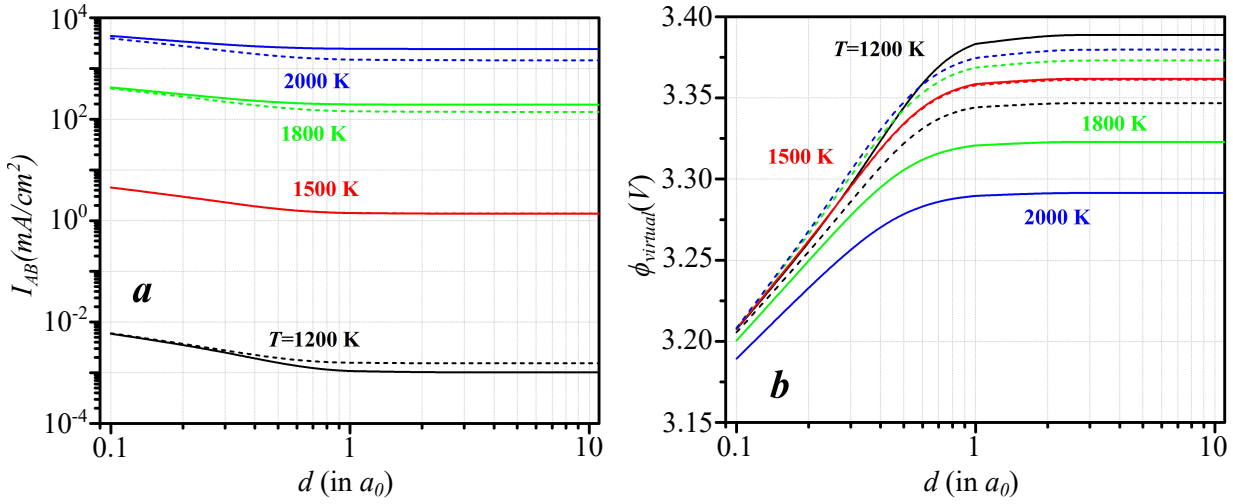


Figure 3.6: (a) Emission current ($I_{AB}$) and (b) virtual work function ($\phi_{virtual}$) as a function of interface width ($d$) for different operating temperatures ($T$). The curves correspond to cesium (Cs) ($\phi_{Cs} = 1.95\ V$, $W_{Cs} = 3.54\ V$) coated silver (Ag) target ($\phi_{Ag} = 4.5\ V$, $W_{Ag} = 10\ V$), $e_h = 0.2\ V$, and $d = 5a_0$; the solid and broken lines refer to the coating width $s = a_0$ and $s = 10a_0$, respectively.

## 3.5 Conclusions and outlook

To summarize, in this study, we investigated electron emission from coated surfaces at finite temperatures and explored the impact of different coating substrates in terms of various materials and thickness. The coating creates a high electric field interface with the parent metal target, leading to enhanced electron emission flux. To analyze this emission, a formalism based on Fowler's treatment of electron emission and FD statistics for estimating the total density of states was established. This formulation is applicable to any metal/semiconductor combination [155, 156]. The electron emission flux from coated surfaces was derived as a function of material specifications and coating thickness, and numerical calculations were performed to quantitatively understand the conceptual basis within specific parametric regimes. A significant finding is that the electron emission flux from coated surfaces is sensitive not only to the materials but also to the coating thickness, which can be utilized to tune the electron emission at a desired operational temperature.

While surface nano-structuring is being considered as a promising approach to tune electron emission [157] and some surface coatings are known for their high reactivity, it seems that the simple

modulation of the coating thickness can provide an easy and effective means to control the emission current. The study reveals that the electron emission flux is more pronounced in the high-temperature regime (above 1500 $K$) for thin coatings, while thicker coatings result in more efficient emission at lower temperatures. The analysis suggests that the electron emission flux can be fine-tuned by selecting appropriate physical parameters of the coating substrates and base material. This insight into the electron emission phenomenon, the formulation, and flux estimates in relation to coating surfaces could be practically useful in developing efficient and tunable field emitters and thin-film devices.

In summary, we have developed a numerical model to study the photo-assisted thermionic emission under a DC electric field, from coated metal targets, as often required for such films in the laser industry [158, 159]. However, for such advanced applications, ultrafast laser pulse is used in most modern-day experiments. To capture such delicate light-matter interactions in laboratory conditions, one essential condition is to have an improved description of the material. For this, in the next chapter, we use *ab initio* DFT formalism to obtain the ground state properties of an emerging 2D material, known as phosphorene.

# Chapter 4

# Photothermionic electron emission from 2D nanostructures

As we understood from the previous Chapter 3, electron emission processes are highly sensitive to the surface chemistry, surface morphology and electronic properties, such as, work function, Fermi energy of each layer in a coated metallic targets. To utilize and extend such understanding for device functionalities, it is important to go beyond metal nanotargets and understand semiconducting nanostructures, which are the pillars of modern nanotechnology. Materials such as semi-metallic graphene, or wide band-gap $MoS_2$, to name a few, are utilized in the study of state-of-the-art light-matter interactions and explored their strong-field features [160, 161]. Phosphorene, a relatively new member in the family of 2D materials, is an atomically thin 2D semiconducting material, with an immense band-gap tunability, with a band gap intermediate between graphene and transition metal-dichalcogenides (TMDs), with a sufficiently large electronic band gap and high carrier mobility, making it ideal for wide-ranging optoelectronic applications and as a functional component for heterostructure synthesis. With the recent successful experimental exfoliation of phosphorene from its layered bulk counterpart, phosphorene has been considered a unique addition to the list of emerging 2D materials with many potential applications in nanophotonics and nanoelectronics.

Extensive experimental and theoretical studies have revealed its electronic properties, and it has demonstrated high on-off ratios in field effect transistors, with applications in energy conversion and storage devices, spintronics, biosensor design, and optoelectronics. It has also been identified as a good thermoelectric material, with a predicted figure of merit of $0.2 - 0.7$ in doped phosphorene at low temperatures, reaching up to 2.5 at 500 $K$. While various aspects of phosphorene have been extensively studied, its potential as a photo-thermionic emitter has yet to be explored. However, the relationship between thermoelectric properties and thermionic signatures in solid state devices suggests that phosphorene may have promising thermionic features. Therefore, it is worth investigating whether phosphorene can serve as a new 2D material for efficient thermionic emission, a concept previously demonstrated in graphene. Moreover, graphene's emission flux has been enhanced with photon irradiation, indicating its potential for photo-thermionic conversion. Although no such precedents exist for phosphorene, its strong absorption features suggest that it is a promising candidate for further exploration.

This study presents the first demonstration of black phosphorene's potential as an effective thermionic emitter and shows that its performance can be improved by photon irradiation. We use density functional theory calculations to determine the electronic bands and the location of band edges in phosphorene, followed by the establishment of a suitable dispersion relation using the tight-binding model. The study then develops a formalism to examine coexisting thermionic and photo-thermionic emission from illuminated phosphorene structures, by considering the effect of electron energy redistribution due to thermal agitation via incident radiation. Using Fowler's approach for electron emission and incorporating the Fermi-Dirac statistics for electrons, the expressions for the photo-thermionic and thermionic emission flux are derived. The cumulative emission flux is found to be highly sensitive to the parametric tuning of the incident radiation and material specifications, with

the photo-thermionic flux dominating over the thermionic emission flux at lower surface temperatures and incident wavelengths, according to the parametric analysis.

In this work, our main objective is threefold, i.e., to investigate the electron emission from phosphorene (i) via manipulating its work function, (ii) as a function of incident photon energy, and (iii) with respect to different operating temperatures. Furthermore, we benchmark our analytical estimates of emission current against the experimental data to justify the validity of our model.

## 4.1 *Ab initio* based approach to define tight binding parameter space for 2D phosphorene

As discussed in Section 2.2, *ab-initio* DFT based approaches can be efficiently used to analyze the atomic and electronic structures of a material. We employ this state-of-the-art approach, which determines the properties of a many-electron system using the spatially dependent electron density obtained from Kohn-Sham equations to explore the electronic bands, band edges location of 2D phosphorene and estimates its work function and Fermi level. In our numerical simulations, the valence states are represented using ultrasoft pseudo-potentials within the GGA (see Section 2.2.4) scheme proposed by Perdew, Burke, and Ernzerhof (PBE), as implemented in the QE package. These pseudopotentials have been tested and found to be suitable for this system and many other 2D materials. While Heyd-Scuseria-Ernzerhof (HSE) hybrid functional calculations provide a better band gap, PBE results are efficient descriptors for more expensive HSE calculations and the trends suggested by experimental results since HSE band gaps scale linearly with PBE band gaps [162].

The total energy of electrons is evaluated for convergence with respect to k-points, energy cutoff, and other significant parameters. A basis set using plane waves with an energy cutoff of 60 $Ry$ is chosen, and the crystal structure is fully relaxed until the final force on each atom is less than 0.001 $eV/$Å, and the electronic energy convergence threshold of $10^{-6}$ $eV$ is achieved. The k-point sets generated by the $12 \times 12 \times 1$ Monkhorst-Pack mesh are used for the Brillouin zone integration. The electronic bands are plotted along the high symmetry directions $\Gamma \rightarrow$Y $\rightarrow$ L $\rightarrow \Gamma \rightarrow$ X $\rightarrow$ L, and the puckered honeycomb structure of monolayer black phosphorene is simulated with an in-plane rectangular unit cell (Figure 4.1a). A fairly large vacuum of 16 Å is created along the z-direction to prevent unphysical interactions between one unit cell and its successive periodic images. Overall, our DFT-based results accurately represent the relaxed structure of phosphorene and reproduce important features and trends in its band structure.

Although DFT calculations offer a complete band structure for the relaxed system, simplified analytical relations for energy dispersion relations are often more practical and provide insight into parametric trends. TB models are often utilized to achieve this purpose, as they are stationary approximations to self-consistent DFT calculations. However, TB models have limitations and are not suitable for representing complex systems like structures with impurities or strongly correlated materials with highly localized electrons. Nevertheless, it has been shown that this method can reasonably describe the bands around the Fermi level for pristine phosphorene if the TB parameters are obtained directly from the DFT band structure. Therefore, a suitable TB model, incorporating the DFT results for phosphorene, can be efficiently used to estimate emission currents in our case.

The tight-binding Hamiltonian of a pristine, planar monolayer phosphorene can be expressed using the effective model as

$$H = \sum_{(i,j)} t_{ij} c_i^{\dagger} c_j = \sum_i \epsilon_i + \sum_{i \neq j} t_{ij} c_i^{\dagger} c_j \ . \tag{4.1}$$

The summation is taken over all the lattice sites in the unit cell of phosphorene, where $\epsilon_i$ denotes the on-site total energy of valence electrons at site $i$, $t_{ij}$ represents the electron transfer energy (hopping parameter) between $i^{th}$ and $j^{th}$ sites, and $c_i$ ($c_j$) is the creation (annihilation) operator of electrons on the site $i(j)$. Electrons in phosphorene are confined by the parallel energy dispersion $E_t(k_x, k_y)$ in the 2D $x$-$y$ plane. For monolayer phosphorene, it is reasonable to only consider in-plane hopping parameters

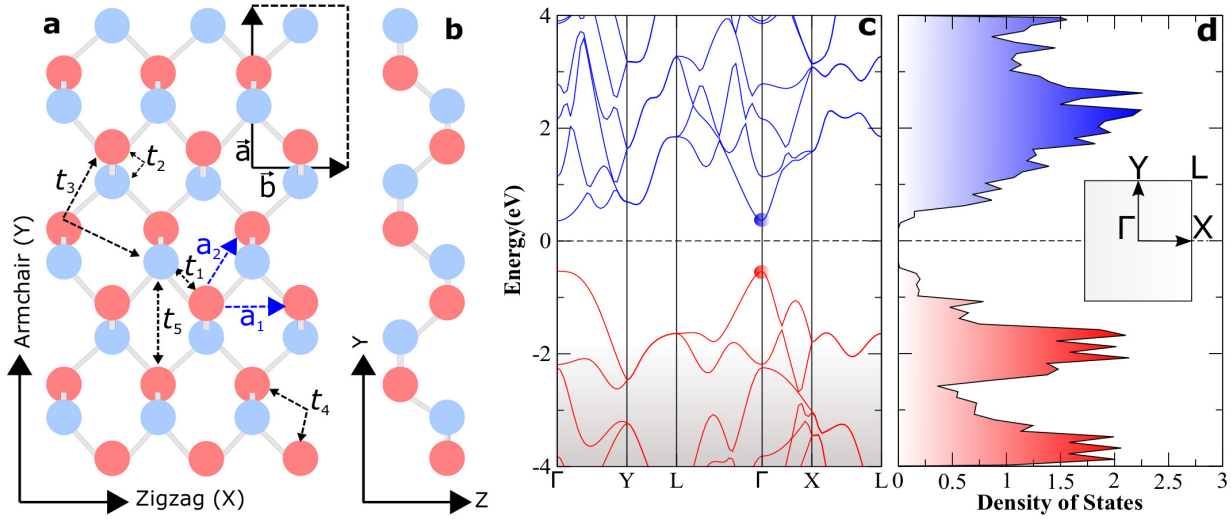


Figure 4.1: (a) Top view of the atomic structure of monolayer phosphorene with different tight binding hopping energies $t_i$, and its side view (b). The red and blue balls correspond to phosphorous atoms in two different planes. The unit cell structure is represented by the black rectangular box. (c) Electronic band structure, and (d) corresponding densities of electronic states of phosphorene. The inset shows irreducible Brillouin zone with high symmetry points of phosphorene. Fermi level $E_f$ is shifted to 0 in this figure.

and neglect the out-of-plane ones. Since phosphorene has four atoms per unit cell (Figure 4.1a), a four band model is sufficient to describe the energy dispersion within the tight-binding framework. Rudenko et al. proposed a five hopping integral model ($t_1, t_2, t_3, t_4$, and $t_5$) to the nearest and next-nearest neighbors (as illustrated in Figure 4.1a) to describe the energy band structure of phosphorene in the region 0.3 $eV$ above and below the band gap. The tight binding parameters are presented with a single index (1-5) for simplicity, and taking into account the $C_{2h}$ point group invariance, the Hamiltonian can be reduced to a simpler $(2 \times 2)$ block matrix in the momentum space through a unitary transformation, which can be written as

$$H = \sum_k c^\dagger(\mathbf{k}) \hat{H}'_k \; c(\mathbf{k}) \; , \tag{4.2}$$

where

$$\hat{H}'_k = \begin{pmatrix} T^4(\mathbf{k}) & T^0(\mathbf{k}) \\ T^{0*}(\mathbf{k}) & T^4(\mathbf{k}) \end{pmatrix} \; , \tag{4.3}$$

$T^0(\mathbf{k})$, and $T^4(\mathbf{k})$ in momentum-space can be expressed as

$$T^0(\mathbf{k}) = t_1(1 + e^{-i\mathbf{k}\cdot\mathbf{a}_1}) + t_2 e^{-i\mathbf{k}\cdot\mathbf{a}_2} + t_3(e^{-i2\mathbf{k}\cdot\mathbf{a}_2} + e^{i\mathbf{k}\cdot\mathbf{a}_1 - i2\mathbf{k}\cdot\mathbf{a}_2}) + t_5 e^{-i\mathbf{k}\cdot\mathbf{a}_1 + i\mathbf{k}\cdot\mathbf{a}_2} \; , \tag{4.4}$$

$$T^4(\mathbf{k}) = 2t_4[\cos\mathbf{k}\cdot\mathbf{a}_2 + \cos\mathbf{k}\cdot(\mathbf{a}_1 - \mathbf{a}_2)] \; . \tag{4.5}$$

The real space lattice vectors $\mathbf{a}_1$ and $\mathbf{a}_2$ are depicted in Figure 4.1(a). By diagonalizing the Hamiltonian in Equation 4.2, the energy eigen spectrum $E(\mathbf{k})$ can be obtained analytically from the solutions of the characteristic equation:

$$\begin{vmatrix} E(\mathbf{k}) - T^4(\mathbf{k}) & T^0(\mathbf{k}) \\ T^{0*}(\mathbf{k}) & E(\mathbf{k}) - T^4(\mathbf{k}) \end{vmatrix} = 0 \; , \tag{4.6}$$

$$\text{i.e. } E_\pm(\mathbf{k}) = T^4(\mathbf{k}) \pm \; |T^0(\mathbf{k})| \; . \tag{4.7}$$

These solutions represent the energy bands of phosphorene in the vicinity of the Fermi level and are used to compute electron emission from phosphorene. If $t_4 = 0$, the solution is symmetric, indicating

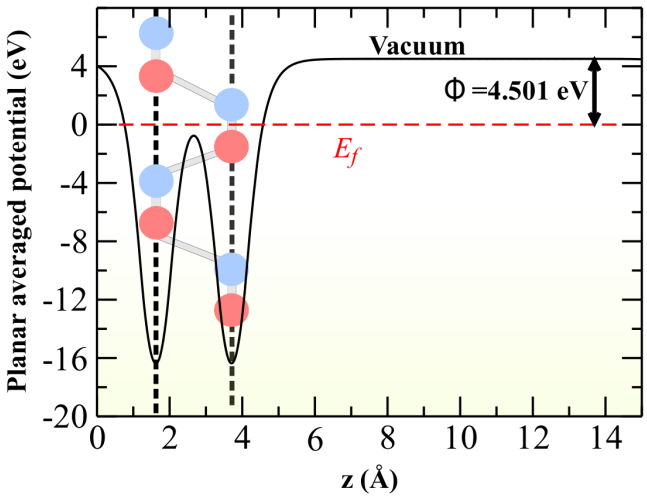


Figure 4.2: In-plane ($x$-$y$ plane) averaged potential as a function of height $z$ from the phosphorene surface (along out-of-plane direction). Side view of the phosphorene is overlaid on the same result to highlight that the location of the dips of the average potential curve (black dashed lines) coincides with the positions of the atomic planes along $z$. The average potential asymptotically approaches the constant vacuum value. The difference between asymptotic vacuum potential and the Fermi level (marked by the horizontal red dashed line) yields work function of phosphorene from this analysis. Fermi level $E_f$ is shifted to 0 in this figure.

that spectral asymmetry in the energy spectrum of phosphorene arises from non-zero hopping $t_4$, which breaks the electron-hole symmetry of the energy spectrum and induces crystal anisotropy.

## 4.2 Electronic structure properties and work function

The in-plane projection of the lattice of black phosphorene is a hexagonal honeycomb structure, with two parallel planes each having two atoms resulting in four phosphorous atoms per unit cell. This leads to a puckered honeycomb structure where each phosphorous atom is bonded to three adjacent atoms as shown in Figure 4.1(a) (corresponding side view is shown in Figure 4.1b), creating an anisotropic crystal structure. The optimized lattice constants $a = 4.62$ Å, and $b = 3.29$ Å are consistent with previous theoretical [163, 164] and experimental [165] works. The electronic band structure and density of states exhibit a direct band gap of $\sim 1\ eV$ at Γ point [Figure 4.1(c,d)], with the upper part of the valence bands consisting of bonding $3p$ orbitals and the lower part of the conduction bands consisting of anti-bonding $3p$ orbitals primarily with $p_z$ contribution and to a small extent from $3s$ states at Γ point. The reciprocal lattice and high symmetry points are shown in the inset of Figure 4.1(d). The phosphorene band structure obtained from DFT is used to compare and tune the tight-binding parameters and to calculate the work function of the material.

The energy required to transfer an electron from the Fermi level to the vacuum level, known as the work function, is determined for monolayer phosphorene. This is achieved by creating an infinite array of 2D periodic slabs of phosphorene monolayer separated by a wide vacuum spacing of 16 Å to eliminate any electrostatic interactions between the slabs. The electrostatic potential is calculated by averaging the effective spatial distribution of the potential in the planes parallel to the surface, which yields the potential in vacuum and hence the work function. The calculated effective work function is 4.501 $eV$ (Figure 4.2), which matches well with a previously calculated work function of 4.5 $eV$. In monolayer phosphorene, the potential exhibits two minima, each corresponding to an atomic plane, and it saturates to a positive asymptotic value at a distance of approximately 3 Å above the second atomic plane. This information is crucial for tuning the tight-binding parameters of the electronic

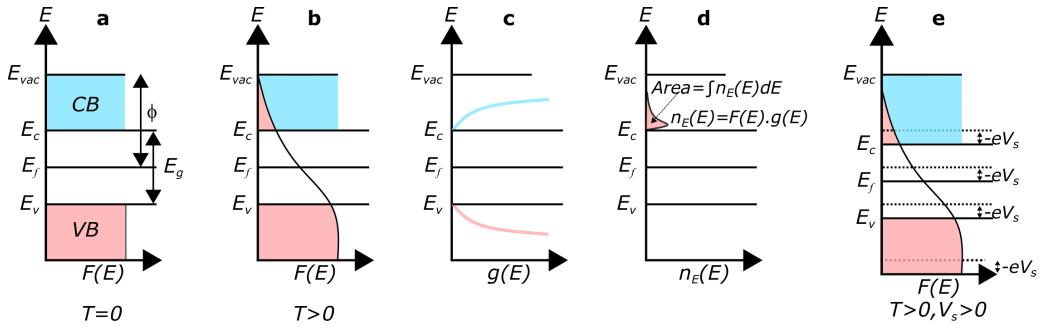


Figure 4.3: Schematic representation of the Fermi-Dirac distribution and the effective number of available electrons at various temperature and biasing conditions. (a) At absolute zero, the Fermi-Dirac distribution consists of completely filled valence bands (VB), while the conduction bands (CB) remain empty. The maximum energy of the valence band is represented with $E_v$, and the minimum energy of the conduction band is represented with $E_c$. $E_f$ is the Fermi level, and $E_g(= E_c - E_v)$ is the band gap energy. Moreover, $\phi$ represents the energy required for an electron to escape from the $E_f$ to the vacuum energy level ($E_{vac}$), and an electron with energy above this level is considered free. (b) As the temperature increases (finite temperature $T$), the Fermi-Dirac distribution is modified, and the distribution tail extends into the CB (pink shade). This modification results in a fraction of electrons in the VB gaining energy and moving to populate the CB. (c) The density of states (DOS) $\mathbf{g}(E)$ near the band edges is depicted. (d) The probabilistic occupancy of the total number of electrons in the CB. (e) When a finite positive surface potential ($\mathrm{V}_s \geq 0$) is applied, all energy bands are downshifted by -e$\mathrm{V}_s$, causing an enhancement in the electron population in the CB compared to the scenario shown in (d) at the same temperature.

bands of phosphorene.

## 4.3 Electron emission from 2D phosphorene: a semi-analytical approach

The study of electron thermionic emission in low-dimensional materials has gained significant attention in recent years, with various models proposed for graphene, including those that assume non-conservation of electron momentum in the lateral emission direction and those that assume conservation of momentum. These models have helped identify universal analytical characteristics in thermionic transport in 2D materials. In this work, we present a semi-analytical approach that incorporates results obtained from *ab initio* DFT calculations to examine the behavior of photon-assisted thermionic emission in phosphorene.

Upon examining the energy spectrum of the two band model (Equation 4.7), it becomes evident that the energy of bands associated with $E_+(\mathbf{k})$ is lower than those associated with $E_-(\mathbf{k})$. The $E_+(\mathbf{k})$ bands accurately describe the primary electron and hole bands near the Fermi level and are therefore selected for electron emission analysis. As a result, the parallel dispersion $E_t(\mathbf{k})$ can be further simplified to the two band energy spectrum (Equation 4.7), which becomes

$$E_t(\mathbf{k}) = E_+(\mathbf{k}) = T^4(\mathbf{k}) + |T^0(\mathbf{k})| \ . \tag{4.8}$$

By comparing the DFT band structure with the TB bands, we determine revised values of the TB parameters: $t_1 = -1.22\ eV$, $t_2 = 3.665\ eV$, $t_3 = -0.205\ eV$, $t_4 = -0.105\ eV$, and $t_5 = -0.055\ eV$. These $t_i$ parameters are then utilized in the analytical formalism to study thermionic and photon-assisted thermionic emissions from an irradiated phosphorene surface.

The incident radiation flux on the surface of phosphorene has a dual effect: a portion of the absorbed energy causes surface heating through collision, while the remaining photon flux induces direct electron photoemission. The electrons in the valence and conduction bands of phosphorene

follow the Fermi-Dirac distribution. Figure 4.3(a-e) illustrates the different scenarios under this scheme. At absolute zero temperature ($T = 0\ K$) and unbiased surface, electrons fill the valence band up to its maximum, and the work function ($\phi$) is the barrier height for electron emission (Figure 4.3a). At finite temperatures ($T > 0\ K$), the high energy tail of the electron population extends beyond the Fermi energy ($E_f$), and electrons with energy greater than the barrier height are emitted (Figure 4.3b). Density of states near the band edges are shown in Figure 4.3(c). The probability of electron occupation in the available states depends on the electron energy distribution and DOS. This scenario is represented in Figure 4.3(d). The surface can be biased by applying an external potential or due to continuous electron emission and recollection equilibrium. This bias is represented by potential $V_s$, which tunes the effective barrier height for electron emission as $V_T = \phi + V_s$. Under the influence of a finite positive potential, the energy structure drops down by energy $-eV_s$ as represented in Figure 4.3(e). The effects of temperature appear through the tuning of the Fermi-Dirac distribution. We can express the distribution of momentum of the electron flux that approaches the top layer surface of phosphorene perpendicularly (at $z = 0$) from the inside and is available for emission, with a total energy between $E_t$ and $(E_t + dE_t)$ and a normal energy (along the $\hat{z}$ axis, normal to the surface) between $E_z$ and $(E_z + dE_z)$ as

$$d^3n = \left(\frac{\hbar k_z}{m}\right)\left(\frac{1}{2\pi^2}\right)F(E)dk_xdk_ydk_z = \left(\frac{k_BT}{2\pi^2\hbar a_0^2}\right)F(E)dk_xdk_ydk_z\ , \tag{4.9}$$

where $F = F_{FD} = [1 + \exp[\epsilon_z + \epsilon_t - \epsilon_f]]$ refers to FD distribution of electrons, $k = ka_0$, $\epsilon_t = E_t/k_BT$, $\epsilon_z = E_z/k_BT = \hbar^2k_z^2/2mk_BT$, $\epsilon_f = E_f/k_BT$, $E_f$ refers to the Fermi energy level, $a_0$ is the interatomic distance between consecutive layers, $\hbar$ and $k_B$ are the reduced Planck's and Boltzmann's constants, respectively, and $T$ is the temperature of the electron emitting surface. The substitution of $(\hbar k_z/m)dk_z$ by $\hbar^{-1}dE_z$ has been made using the group velocity relation $\hbar k_z/m = dE_z/dk_z$ in order to obtain Equation 4.9.

Suppose a uniform radiation flux with photon frequency $\nu$ and normalized energy $\epsilon_\nu = h\nu/k_BT$ illuminates the phosphorene sheet. The incident photon flux is given by $\Lambda(\nu) = I_{in}/h\nu$, where $I_{in}$ is the incident light intensity. According to Fowler's theory, when an electron hits the surface, it has a probability $\beta(\nu)\Lambda(\nu)$ per unit time of enhancing its normal energy $\epsilon_z$ by absorption of a photon, assuming $\Lambda(\nu)$ photons are incident per unit time per unit surface area. The total electron flux available for enhancement of normal energy $n_t$ can be obtained by integrating Equation 4.9 over the energy space with normal energy $\epsilon_z$ up to the Fermi level $(0,\ E_f)$ in the quasi-continuum model. From the incident radiation flux, an absorbed fraction $\alpha$ goes into $\beta(\nu)\Lambda(\nu)$ fraction of the electron flux available for emission. The parameter $\beta(\nu)$ that leads to the redistribution of the electrons to the higher energy states can be calculated by equating the $\beta(\nu)\Lambda(\nu)$ factor of the total electron flux $(n_t)$ available for the emission with the absorbed incident photon flux as $\beta(\nu)n_t = \alpha$. A fraction $\mu$ of the absorbed energy is consumed in lattice thermalization to increase its surface temperature, while the rest (fraction 1 - $\mu$) is utilized in the process of electron emission. Therefore, the $f_P \equiv (1-\mu)\beta(\nu)\Lambda(\nu)$ fraction of the electron flux contributes to photoemission, while the remaining fraction $f_T \equiv 1-(1-\mu)\beta(\nu)\Lambda(\nu)$ leads to the thermionic emission of electrons.

We will now examine the two aforementioned scenarios separately. In the case of conventional thermionic emission (where $\epsilon_z > \epsilon_c$ with $\epsilon_t$ replaced from Equation 4.8), the momentum distribution of the electrons within the sheet can be represented as follows:

$$d^3n_{Th} = f_T\left(\frac{k_BT}{2\pi^2\hbar a_0^2}\right)\left[1 + \exp\left(\epsilon_z - \epsilon_f\right)\exp\left[\Gamma^4(\mathbf{k}) + Abs[\Gamma^0(\mathbf{k})]\right]\right]^{-1}dk_xdk_ydk_z\ , \tag{4.10}$$

where $n_{Th}$ is the thermionic emission flux. The momentum distribution of the electrons, which have absorbed a photon and have normal energy $\epsilon_z' = \epsilon_z + \epsilon_\nu$ and transverse momenta $k_x' = k_x$, $k_y' = k_y$ can be obtained by expressing $\epsilon_z, k_x, k_y$ in Equation 4.10 in terms of $\epsilon_z', k_x', k_y'$. The resulting distribution can be written as

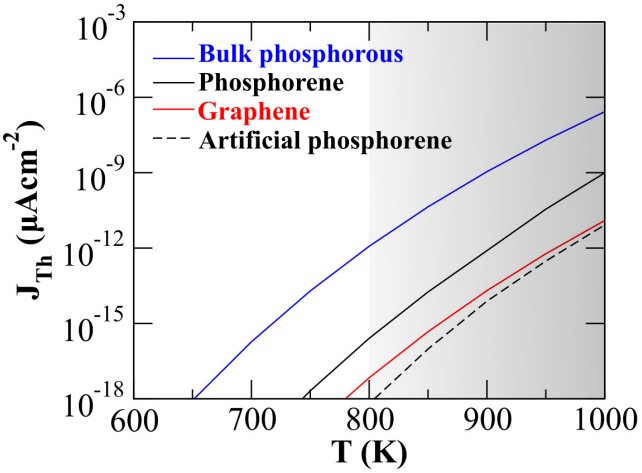


Figure 4.4: Thermionic emission current from different systems as a function of surface temperature. The blue curve represents the typical bulk material with a parabolic dispersion relation. The red curve corresponds to a 2D graphene material with a linear parallel dispersion relation. The black curve shows 2D phosphorene with an anisotropic parallel dispersion relation, while the broken black curve illustrates the 2D isotropic dispersion of phosphorene. The shaded region indicates the temperature range where the sublimation process in phosphorene becomes significant

$$d^3n_{Ph} = f_P\left(\frac{k_BT}{2\pi^2\hbar a_0^2}\right)\left[1+\exp\left(\epsilon_z-\epsilon_f-\epsilon_\nu\right)\exp\left[\Gamma^4(\mathbf{k})+Abs[\Gamma^0(\mathbf{k})]\right]\right]^{-1}dk_xdk_ydk_z\ , \tag{4.11}$$

where $n_{Ph}$ is the photo-thermionic emission flux. We have simplified Equation 4.11 by removing the primes. To obtain the flux resulting from the thermionic/photo-thermionic emission, we need to integrate the expressions (Equation 4.10, and Equation 4.11) over appropriate boundaries in **k**-space and the effective surface potential barrier ($\epsilon_z$). Since the lattice vectors in parallel dispersion are periodic, we can choose integration limits over **k** so that it covers the maximum dimension along the X and Y directions in **k**-space, for instance, $\mathbf{k} = 2\pi/(\mathbf{a}_1, \mathbf{a}_2)_{min}$.

To exclude tunneling effects and focus solely on the photo-thermionic effects of a suspended phosphorene layer (under dynamic equilibrium), a positive surface potential ($V_s \geq 0$) is chosen. Under this condition, the thermionic/photo-thermionic emission takes place only when $\epsilon_z > \epsilon_c - \upsilon_s$, where $\upsilon_s = -eV_s/k_BT$. The resulting net thermionic/photo-thermionic flux can be written as:

$$n_{Th,Ph} = \int d^3n_{Th,Ph} = \int_{\epsilon_c-\upsilon_s}^{\infty}\left(\int_{-k_{x0}}^{k_{x0}}\int_{-k_{y0}}^{k_{y0}} d^3n_{Th,Ph}dk_xdk_y\right)d\epsilon_z. \tag{4.12}$$

Therefore, the current density associated with thermionic/photo-thermionic emission can be calculated from the flux presented in Equation 4.12 as $J_{Th,Ph} = en_{Th,Ph}$. To obtain the thermionic/photo-thermionic emission flux from an unbiased surface, the surface potential barrier $\nu_s$ is set to 0 in Equation 4.12.

## 4.4 Results and Discussion

### 4.4.1 Evaluation of thermionic current density and its dependence on anisotropy

Figure 4.4 presents a comparison of the thermionic emission flux from black phosphorene, its bulk counterpart, and graphene, at temperatures ranging from $600-1000\ K$. The three cases have different dispersion relations. The work function of the phosphorene bulk counterpart ($\phi = 4.03\ eV$), which is considered as stacking of phosphorene multilayers, is taken from recent experimental work. Neglecting

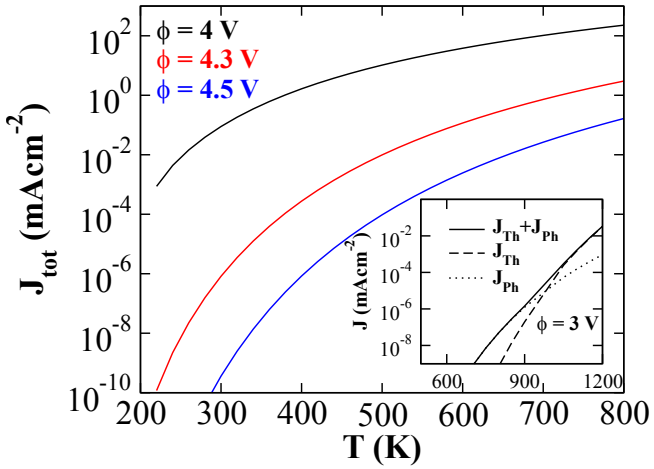


Figure 4.5: Total emission flux $J_{tot}(= J_{Th} + J_{Ph})$ plotted against surface temperature for various work function values, 4 $V$ (black curve), 4.3 $V$ (red curve), and 4.5 $V$ (blue curve). The irradiated photon has a wavelength of 300 $nm$. In the inset, a comparison is shown for the total current (solid curve), thermionic emission current (dashed curve), and photoelectric emission current (dotted curve) as a function of surface temperature. The calculations are performed with a work function of 3 $V$ and a wavelength of the irradiated photon set at 800 $nm$.

the anisotropy of phosphorene structure (assuming $t_4 = 0$, and therefore a symmetric energy spectrum) results in a significant reduction in the emission current, as indicated by the black dashed line, by almost two orders of magnitude. Therefore, anisotropy is expected to be a crucial factor. Compared with monolayer graphene (considering linear parallel dispersion), which is a well-known material used for efficient thermionic conversion, anisotropic phosphorene produces a higher thermionic current, particularly at higher temperatures. This anisotropy feature can be utilized in the development of efficient phosphorene-based cathodes in thermionic conversion schemes. As the surface temperature rises, the fraction of high-energy electrons in the population density distribution function increases, resulting in an increase in the emission current in all cases (Figure 4.4). The stability of thin layers of black phosphorus (BP) depends on the oxidation conditions in the surrounding environment and the operating temperature. Oxidation can be avoided entirely in vacuum experiments, but in the presence of ambient nitrogen, sublimation of few-layer thin BP occurs at a lower temperature. Experimentally, thermal degradation of phosphorene starts around 700 $K$ in vacuum in contrast to 883 $K$ for bulk BP sublimation temperature. However, several mitigation strategies can be employed to overcome phosphorene degradation under ambient conditions without significantly affecting its properties [166]. Moreover, the operating temperature and thermal stability can be enhanced through various means, such as forming heterostructures with graphene. Thus, we have calculated the thermionic emission flux up to temperatures beyond the current thermal tolerance of BP, shown in the shaded region in Figure 4.4. Although our model predictions are relevant within the unshaded region in Figure 4.4, the shaded region allows us to verify the consistency of our theoretical prediction. We have found that the results for graphene and artificial phosphorene approach each other with increasing temperature, and the overall thermionic contribution for phosphorene remains higher.

### 4.4.2 The effect of work function on emission current

In Figure 4.5, for phosphorene, we present the variation of total emission flux $J_{tot}$ $(= J_{Th} + J_{Ph})$ for $\lambda = 300$ $nm$ with changing surface temperature. To compare, we have considered three different work function values. As the work function decreases, the flux increases because less energy is required for electron emission. The photo-thermionic emission flux dominates over the thermionic flux and $J_{Th}$ becomes comparable to $J_{Ph}$ only at higher temperatures, as shown in the inset of Figure 4.5. It is important to note that the temperature at which this transition is predicted to occur (inset of Figure

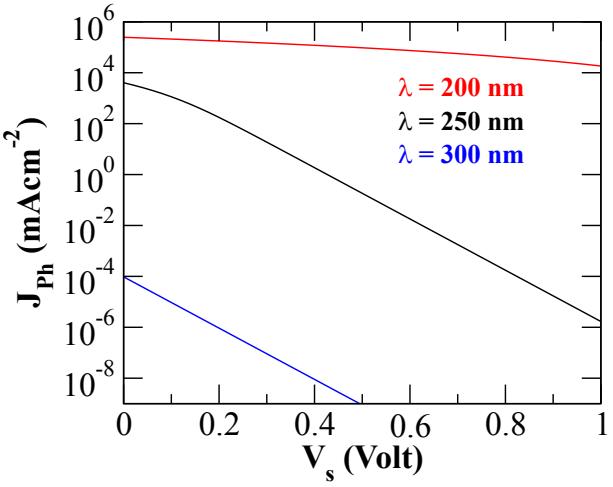


Figure 4.6: The graph illustrates the photo-thermionic emission current from irradiated phosphorene at a temperature of 500 $K$, with varying positive potential. For comparison, three different incident light wavelengths are considered: 200 $nm$ (red curve), 250 $nm$ (black curve), and 300 $nm$ (blue curve).

4.5) is also the point where sublimation of pristine phosphorene begins, as previously discussed. This implies that for practical purposes, photo-thermionic processes dominate.

The photo-thermionic effect is described as a combination of thermionic and direct photoemission processes, influenced by thermal agitation of electron momentum distribution function. As the wavelength of incident radiation decreases, the direct photoemission becomes dominant over the other process. At lower temperatures ($200 - 500$ $K$), the photo-thermionic flux is significant, making photon-irradiated phosphorene a viable candidate for moderate temperature waste utilization. The magnitude of the fluxes depends on the work function, which can be adjusted through materials engineering, and is more pronounced for lower work function values.

### 4.4.3 Dependence of photo-thermionic emission flux on surface bias

We then investigate how a finite positive potential affects the photo-thermionic emission, as shown in Figure 4.6. The photoemission flux is found to decrease with increasing wavelength, which can be attributed to a small shift in the momentum distribution of the agitated electron population available for emission. While it has been demonstrated that changing the wavelength of light from 280 $nm$ to 1050 $nm$ can reduce the stability of thin BP layers under ambient air conditions due to reactive oxygen species, this is not a concern when operating in a vacuum. However, the positive potential over the surface leads to an enhanced potential barrier for the emitting electrons due to Coulomb attraction, resulting in a reduced flux. Figure 4.7(b) illustrates that the photo-thermionic flux ($J_{Ph}$) is significantly stronger than the thermionic flux ($J_{Th}$) by several orders of magnitude over a range of tuned barrier heights (effective work function). The dominance of $J_{Ph}$ over $J_{Th}$ increases steadily with increasing barrier height $\phi$ for $\lambda = 300$ $nm$. However, at higher operating temperatures $T$, a greater population of electron density is available for thermionic emission, leading to a decrease in the ratio of $J_{Ph}$ and $J_{Th}$ with increasing $T$ (as shown in Figure 4.7b). For larger barrier heights, both constituent currents are significantly reduced due to the low availability of high energy electron population near the vacuum level ($V = 0$, as shown in Figure 4.3), resulting in a marginal change in their ratio. Additionally, the ratio of $J_{Ph}$ and $J_{Th}$ is sensitive to incident $\lambda$ for different operating temperatures and effective barrier heights $\lambda$. As the incident energy increases (reducing $\lambda$), more electrons emit through the photo-thermionic mechanism, thereby enhancing the ratio of $J_{Ph}$ to $J_{Th}$. Direct photoemission becomes significant for $\lambda \approx 500$ $nm$ radiation with respect to thermionic flux (ratio of $J_{Ph}$ to $J_{Th}$ $\approx$ $10^{10}$ ), while for higher $\lambda$, photon aided thermionic flux is prominent at $T = 500$ $K$ .

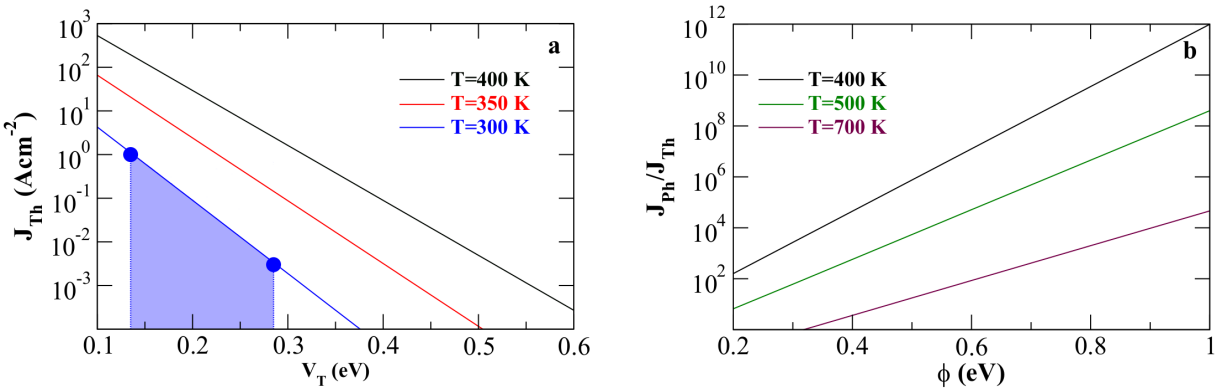


Figure 4.7: The graph shows a comparison between analytical estimates of emission current and experimental data. In (a), the current is plotted against the tuned barrier height, and the experimental data points are represented by blue dots. In (b), the ratio of photo-thermionic current ($J_{Ph}$) to thermionic current ($J_{Th}$) is plotted as a function of the effective barrier height (or tuned work function) $\phi$. The wavelength of the irradiated photon is fixed at 300 $nm$.

### 4.4.4 Comparison with experiments

Experimental studies on few-layer phosphorene [167] offer an opportunity to validate our analytical model's predictions against actual measured values. These studies have primarily focused on phosphorene-based field-effect transistors (FETs) and their electronic transport characteristics, but they also provide insight into thermionic emission phenomena. For example, Fig. 1b in Das et al. [167] shows the transfer characteristics of a monolayer phosphorene flake operating at room temperature (300 $K$) under flat band condition ($|V_F| > |V_{BG}|$), where the measured device current ($I_{DS}$) is purely thermionic in a specific voltage range and displays a log-linear dependence on the gate bias voltage ($V_{BG}$). It is shown that this dependence is valid in the current voltage range of $(V_F, I_F)$ to $(V_M, I_M)$, where the subscripts $F$ and $M$ are the flat band condition and the minimum current points, respectively. The measured values in Das et al. [167] for $(I_M, I_F)$, and corresponding voltage values $(V_M, V_F)$ are approximately $(0.0003 - 0.1)$ $\mu A/\mu m$ and (0, 1.8) $V$, respectively. The slope ($\gamma = \Delta \ln(I_{DS})/\Delta(V_{BG}/\beta)$) of the dependence is approximately 25, where $\beta$ is the band movement factor (≈15 in this operating regime [167]) that determines the band movement due to applied gate voltage as $\Delta\phi = (V_F - V_M)/\beta \approx 0.12$. Even though these results are obtained in the FET mode of operation, the fact that both the current ($I_F$) and the slope ($\gamma$) are only weakly dependent on drain bias $V_{DS}$ makes it possible to directly compare with the thermionic flux calculated using Equation 4.12. With the lateral cross section ($\sigma \approx 2 \times 10$ $\mu m$) and channel width $l \approx 2$ $\mu m$ taken into account, the estimated current can be expressed as $(l \times I/\sigma) \approx (0.003 - 1.0)$ $Acm^{-2}$. Figure 4.7(a) illustrates the calculated thermionic emission current from an uncharged monolayer phosphorene surface as a function of tuned barrier height ($V_T$) for different operating temperatures. The shaded region in Figure 4.7 corresponds to the experimental conditions mentioned above, where $T = 300$ $K$. The calculated slope $\gamma \approx 21$, which is in reasonable agreement with the experimental measurement. Additionally, we calculate the rigid band movement corresponding to $(I_M, I_F)$, i.e. $V_T(I_F) - V_T(I_M) = 0.14$ $V$, which correctly reproduces the measured $\Delta\phi$. These results suggest that our approach is valid for estimating the electron emission flux from phosphorene.

We would like to point out that in 2D materials with external contacts, additional effects may be significant depending on the operational conditions. For instance, in mechanically exfoliated $MoS_2$ crystals, vertical charge conduction mechanism using Fowler-Nordheim formulation has been successfully employed. In contrast, in chemical vapor deposition grown pyramidal-structured $MoS_2$ flakes, the Richardson-Schottky effect has been shown to play a role, which is the lowering of interface potential maximum due to the presence of image charge effect. In future studies, it is crucial to investigate the role of such effects in phosphorene, which has exhibited promising results as a photo-thermionic

emitter in this study. Our emission current equations (Equation 4.10 and Equation 4.11) do not explicitly include the exact Schottky barrier profile or the image charge effects. However, we implicitly consider such effects lumped within the potential $V_s$ when evaluating the currents, which provides a tuned barrier height for emission, $V_T = \phi + V_s$ (as shown in Figure 4.7(a) for comparison with the experiment).

## 4.5 Conclusions and outlook

In this chapter, I showcase the potential of the 2D material phosphorene as a photo-thermionic electron emitter. We develop a theoretical procedure to calculate the appropriate emission current, based on semi-analytical modeling to calculate the thermionic emission flux. Our model is valid for dynamical equilibrium conditions and is verified against experimental observations. Our findings demonstrate that the anisotropic energy dispersion of phosphorene leads to a higher emission flux and superior emission current compared to those of graphene, making it a highly efficient candidate for photo-thermionic emission and thermionic emission-based energy conversion technology. Our calculations are based on adiabatic or continuous irradiation conditions, which are sufficient to highlight the main features of the process and relevant to many experimental scenarios. Our approach offers a fundamental understanding of the photo-thermionic behavior of 2D phosphorene with signature features that match remarkably well with experimental results.

The subsequent objective is to modify the methodology to accommodate laboratory scale high-intensity optical drivers, which are abundant in spatio-temporal features and offer complex interaction scenarios. However, dealing with these non-adiabatic spatio-temporally dependent aspects is theoretically challenging and would require the inclusion of higher-order complexity in our approach, which is our next goal and discussed in next chapter. The emergence of state-of-the-art ultrashort laser facilities like ELI ALPS presents new prospects for potential high-yield ultrafast emissions using materials such as phosphorene. This study lays the groundwork for exploring this direction. While phosphorene is considered as a test case, our approach is generally valid for any nanomaterial for which its crystal structure and electronic properties can be calculated, to use them further in our model for photo-thermionic emission, for an accurate estimate of coexisting thermionic and photo-thermionic currents from low dimensional nanostructures.

# Chapter 5

# Femtosecond laser induced ultrafast electron emission processes in metallic films

From Chapter 4, it is now clear that an improved description of material's atomic and electronic properties can play a significant role in evaluating the thermionic and photo-induced thermionic emission processes. However, in light-matter interactions, it is not just the material, but also a suitable description of external applied laser field plays a crucial role in correctly determining the light induced electron emission processes. Since the advent of intense laser pulses ranging from the femto- to the pico-second timescales, the interest in laser-matter interaction studies has considerably increased. Ultrafast laser pulses provide a precise control of material processing, without causing damage to the areas surrounding the laser-matter interaction region. Laser processing involves different aspects of physics, for instance, thermodynamics, optics, quantum mechanics and materials science, to name a few. Hence, numerical modeling is essential in order to understand and optimize the laser induced processes in materials. In this chapter, we investigate the laser induced non-equilibrium dynamics of the electrons and lattice in gold coated glass substrate using two temperature model (TTM) developed by Anisimov et al. [65], which is an efficient numerical model to predict the dynamics of electrons, lattice under the influence of ultrafast laser fields.

## 5.1 Introduction

Ultrafast electron pulses using various techniques such as crystallography, microscopy, and ultrafast electron diffraction [168] are able to provide ultrafast time-resolved characterization of the underlying processes in physics, chemistry and biology [169–172]. In order to probe the microscopic structural dynamics of atoms and molecules, an in-depth understanding and control over the spatio-temporal characteristics of ultrafast electron pulse is needed to interpret the time-resolved atomic-scale images. Over the years, there has been several debates on the process of ultrafast laser induced electron emission, which comprises of various phenomena, such as multiphoton field emission [173], optical field emission [174], and multiphoton absorption followed by over the barrier emission [175]. It is important to have an in-depth knowledge of the emission process to understand the sub-cycle, electron pulse which is shorter than the duration of the laser pulse.

Intense femtosecond laser pulses can rapidly heat materials through ultrafast laser heating, leading to nonequilibrium energy transport. This phenomenon finds diverse applications in X-ray lasers, laser-driven ultrafast electron switches, ultrafast transmission electron microscopy, and other fields [176–179]. When subjected to femtosecond laser irradiation, metals exhibit a intricate interaction between electron and lattice [64], resulting in the change of electron and lattice temperatures as a function of time within the material [65–67] and associated fluctuations in carrier density and equilibration dynamics. Although direct imaging of internal structures during such ultrafast and irreversible transitions is

challenging, energy deposition and equilibration dynamics offer crucial insights into the atomic-level processes occurring within the material.

In this chapter, a nonequilibrium model, i.e. TTM will be utilized to describe the temporal evolution of electronic temperature, lattice temperature, electron thermalization duration, and electron-lattice thermalization duration along with the electron emission process from a metallic surface driven by an ultrafast laser pulse. First, we employ an enhanced 3D TTM that incorporates a nonlinear heat equation and laser interactions in all the three dimensions $(x,y,z)$. This model enables the comprehensive evaluation of both spatio-temporal electron and lattice temperature profiles in a gold-coated glass substrate under the influence of a Gaussian femtosecond pulse. Our implementation facilitates the investigation of effects arising from any laser incidence, the role of laser polarization, and the effects of focal spot size of the laser. Then 3D TTM and an appropriate thermionic emission description is self-consistently coupled. Through this, we compute the laser-induced energy deposition and subsequent energy absorption within the gold-glass film. Additionally, we demonstrate the significant modifications in thermionic currents induced by space-charge effects. While the electron and lattice temperature, and the duration of the electron-lattice thermalization are calculated using the TTM, we investigate the thermionic emission properties from gold films under ultrashort laser excitation using suitable modification of the Richardson-Dushman equation, accounting for the dynamic impact of space-charge phenomena and temperature dependent chemical potential. We demonstrate the clear dependence of the thermionic current and duration of emission on the dynamics of electron-lattice thermalization, a feature which is not yet published by anyone else. Our comprehensive analysis suggest potential ways to enhance the duration of the thermionic current, a critical characteristic for applications in thermionic electron emitters.

## 5.2 Results and discussion

### 5.2.1 Initial and boundary conditions and semi-analytical approach for laser driven thermionic emission rate

In order to solve the set of Equations 2.26, the initial electronic $(T_e)$, lattice $(T_l)$, and substrate $(T_s)$ temperatures are assumed to be equal to room temperature, i.e. $T_e(x,y,z,-4t_p) = T_l(x,y,z,-4t_p) = T_s(x,y,z,-4t_p) = 300^\circ\ K$, where $t_p$ is the pulse duration at full width at half maximum (FWHM) of the intensity temporal envelope, and time $t = -4t_p$ refers to the moment when the numerical solution starts and the laser-target interaction is about to start. The laser pulse's maximum intensity is reached at the surface of the metal at $t = 0$. In our framework, at each time increment, we account for space-charge limited thermionic emission as the boundary condition for heat loss by surface electrons on the irradiated sample surface [180–182]. This condition is represented as $k_e \frac{\partial T_e}{\partial z}\Big|_{z=0} = -(eE_f + e\phi)\dot{N}_{sc}\Big|_{z=0}$, where $z = 0$ denotes the irradiated surface of the sample, $e$ represents the electron charge, $E_f$ denotes the Fermi energy, $\phi$ is the work function, and $\dot{N}_{sc}$ represents the rate of space-charge limited thermionic emission per unit area (number/$m^2 s$). On the other hand, the boundary conditions on the un-irradiated surfaces are considered in such a way that these surfaces are assumed to be thermally insulated from the ambient environment. During each time increment, the set of equations (presented in Equation 2.26) are advanced using the initial and boundary conditions outlined earlier and the thermionic electron emission rate $(\dot{N}_{sc})$ is determined in a self-consistent manner from a modified Richardson-Dushman equation.

By utilizing the well-established Richardson-Dushman equation, the rate of thermionic emission, denoted as $\dot{N}_1$, can be derived by assuming that the Fermi energy $E_f$ (5.53 $eV$ for gold [183]) is approximately equivalent to the chemical potential $(\mu)$ of free electrons, a valid assumption when $k_B T_e$ is less than 1 $eV$. The Richardson-Dushman equation [44] for the thermionic emission rate is as follows:

$$\dot{N}_1 = (A_0/e)T_e^2 \exp\left((-e\phi)/(k_B T_e)\right) , \tag{5.1}$$

where $A_0 = 1.2 \times 10^6\ Am^{-2}K^{-2}$, $e$ represents the charge of an electron, $\phi$ denotes the work function of

the metal (with a value of 5.17 $eV$ for gold [184]), and $k_B$ represents the Boltzmann constant. As the evolution of electron temperature begins the process of thermionic emission, the emitted electrons leave a positive residual charge on the metal surface. This charge has an impact on the subsequent evolution of the emission current. Particularly under femtosecond laser irradiation conditions, these effects, known as space charge effects, can become nontrivial [185]. Having the knowledge of the magnitude of space charge effects is pivotal for accurate estimation and analyzing laser-induced electron emission. While time-integrated total thermionic emission yields from numerous existing experiments have been employed to assert strong suppression of space charge, the dynamic alterations in the Gaussian contour of the focal spot and the resulting ultrafast temporal fluctuations in emission current have not been investigated in previous works. Given the advancing capabilities to resolve and detect electron emissions at an ultrafast timescale through cutting-edge experiments [8, 186–189], a precise evaluation of the space-charge potential becomes crucial for predicting the temporal and spatial characteristics of the emitted electrons.

At elevated temperatures, the chemical potential $\mu$ deviates from its value ($E_f$) at absolute zero. Hence, it becomes necessary to incorporate a suitable temperature-dependent form of $\mu$. Additionally, during thermionic emission, the electrons emitted from the metal surface form a cloud of unbound electrons with a negative charge [109]. This electron cloud contributes to the space-charge phenomenon, which arises due to the Coulomb interaction among the escaping electrons. Therefore, we use a modified Richardson-Dushman equation that account for temperature-dependent chemical potential $\mu(T_e)$ and the effects of space-charge resulting from the thin disk of electrons near the solid surface, for calculating $\dot{N}_{sc}$:

$$\dot{N}_{sc} = C(k_B T_e)^2 \exp\left( - \frac{eE_f - \mu(T_e) + e\phi + \phi_{sc}}{k_B T_e} \right), \tag{5.2}$$

where $c = 4\pi m/h^3$, $c$ is the speed of light in vacuum, $m$ is the electron mass, $h$ is the Planck constant, and $\phi_{sc}$ is the space-charge potential. $T_e$ refers to the surface electron temperature $T_e(x, y, z = 0, t)$.

### 5.2.2 Impact of the polarization of the laser and its angle of incidence on the temporal evolution of electron and lattice temperature

To optimize and control the thermal response and to understand the dependence of it on the laser polarization and angle of incidence, numerical calculations are done. In our simulations, the input parameters include a 500 $nm$ thick Au sample, a 200 $fs$ laser pulse duration at FWHM of the intensity temporal envelope, a central wavelength of 800 $nm$, a peak intensity of $4 \times 10^{11}$ $Wcm^{-2}$, a beam waist size of 9 $\mu m$ at FWHM of the intensity temporal envelope, and a 500 $nm$ thick glass substrate, unless stated otherwise. Figure 5.1(a) and 5.1(b) display the change of surface electron and lattice temperatures as a function of time at the central region of the laser-irradiated area for S and P polarized pulse cases, respectively. For the S polarized case, it is evident from Figure 5.1(a) and 5.1(b) that the peak electron temperature ($T_e^{max}$) decreases with increasing laser incidence angle from 0° to 80°, whereas for the P polarized case $T_e^{max}$ increases under the same conditions. For all the non-zero laser incidence angles, the peak electron temperature is higher in the P polarized case compared to that in the S polarized case. The lattice peak temperature show same dependency on the laser incidence angle. Furthermore, we show that the duration of electron-lattice (e-l) thermalization (the time required to attain thermal equilibrium between the electrons and lattice sub-systems) increases as $T_e^{max}$ rises. Hence, as shown in Figure 5.1(a) and 5.1(b), a rise in the laser angle of incidence decreases the duration of the e-l thermalization in the S polarized case. Conversely, the e-l thermalization duration rises with $\theta$ from 0° to 80° in the case of P polarized pulse. In Figure 5.1(c), $T_e^{max}$ is presented for S (black curve) and P polarized (red curve) cases against the angle of incidence. We calculated the difference ($\Delta^{max}$) (green curve) between $T_e^{max}$ in S and P polarized cases, and observed that the maximum value of $\Delta^{max}$ occurs at an incidence angle of $\theta = 79°$.

To emphasize the impact of laser polarization and select an experimentally feasible laser incidence angle, the remaining results in this chapter are calculated for $\theta = 45°$, unless stated otherwise. Figure

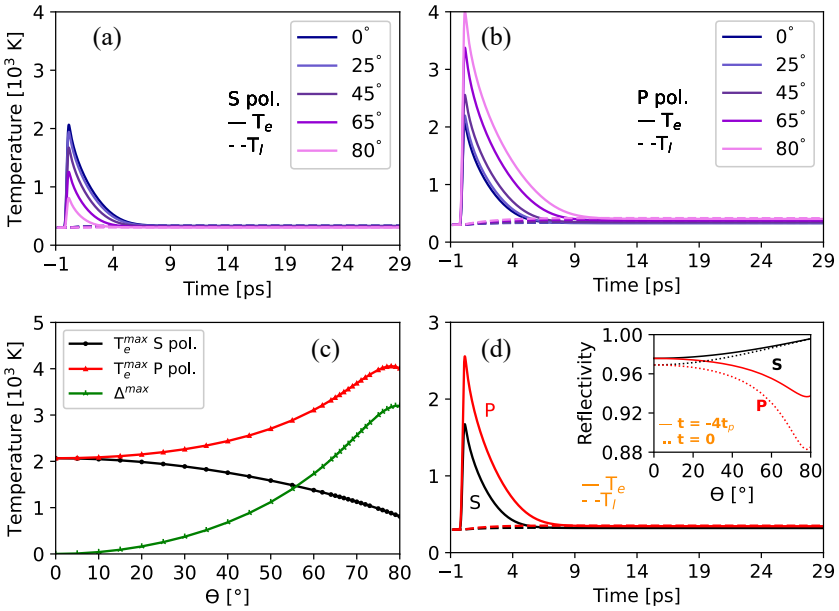


Figure 5.1: Temporal evolution of the surface electron temperature of electron ($T_e$) (solid lines) and lattice temperature ($T_l$) (dashed lines) at the central region of the laser-irradiated area for the (a) S and (b) P polarization against the angle of incidence of the laser ($\theta$). (c) The maximum electron temperature ($T_e^{max}$) as a function of $\theta$ for S (in black), P (in red) polarization and their difference ($\Delta^{max}$) (in green). (d) The temporal evolution of the surface $T_e$ (solid lines) and $T_l$ (dashed lines) for the S (in black) and P polarization (in red) for $\theta = 45°$. The inset in (d) shows the reflectivity as a function of $\theta$ for the S (in black) and P polarization (in red). The solid lines denotes $R_{s,p}(T_e = 300\ K)$ and the dotted lines denotes $R_{s,p}(T_e = T_e^{max})$. The reflectivity minima are observed at 79° near the Brewster's angle. The input parameters used are: peak laser intensity $I_0 = 4 \times 10^{11}\ Wcm^{-2}$, pulse duration $t_p = 200\ fs$ (intensity full width at half maximum), central wavelength of the laser $\lambda = 800\ nm$, and gold thickness $d = 500\ nm$.

5.1(d) illustrates the change of the surface electron and lattice temperature as a function of time at the central region of the laser-irradiated area for both S and P polarized cases. In the case of S polarization, the peak electron temperature reaches 1674 $K$ at 0.14 $ps$, while the lattice temperature reaches 324 $K$. Furthermore, in the P polarized case, the maximum electron temperature is 2557 $K$ attained at 0.15 $ps$, and the maximum lattice temperature is 352 $K$. Consequently, the duration of electron-lattice (e-l) thermalization is approximately 6 $ps$ for the S polarized case, which is shorter compared to 8 $ps$ in the case of P polarization.

The role of laser polarization on $T_e^{max}$ and its dependence on incidence angle of the laser can be explained in terms of the amount of laser energy absorption into the gold-glass film. As it is evident that the decrease in reflectivity yields in more energy transfer from the laser to the electron subsystem within the skin depth of the gold sample, resulting in increased $T_e^{max}$. In order to highlight the significance of temperature dependent reflectivity, the inset in Figure 5.1(d) illustrates the reflectivity for both the S (black curves) and the P polarized (red curves) cases against angle of incidence of the laser obtained at two distinct time points: (i) at room temperature, i.e. at $t = -4t_p$ (solid curves), and (ii) at the peak of the laser intensity, i.e. at $t = 0$ (dotted curves). In both the temperature dependent cases, the reflectivity minimum could be treated as Brewster's angle, which occurs at $\theta = 78°$. Our findings demonstrate that reflectivity is lower for the P polarized case, resulting in a higher deposition of laser energy on the sample's surface. Consequently, for every non-zero $\theta$ value, except $\theta = 0°$ (where the S and P polarized lasers are identical), the surface electron temperature is higher in the P polarized case compared to the S polarized scenario. Furthermore, self-consistently including the temperature dependence in reflectivity yields higher electron temperature.

Therefore, in our calculations, we incorporated the material's temperature-dependent reflectivity

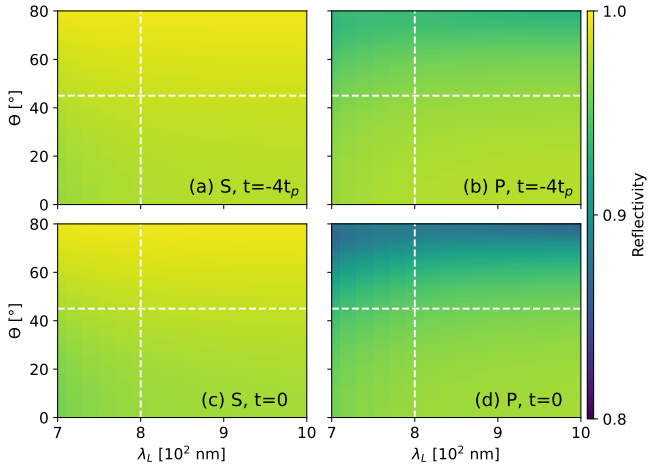


Figure 5.2: (a,b) Gold reflectivity against angle of incidence ($\theta$) and laser wavelength ($\lambda_L$) for S and P polarized laser at time $t = -4t_p$, i.e. $R_{s,p}(T_e = 300\ K)$ and (c,d) at time $t = 0$, i.e. $R_{s,p}(T_e = T_e^{max})$. The input parameters used are: peak laser intensity $I_0 = 4 \times 10^{11}\ Wcm^{-2}$, intensity FWHM pulse duration $t_p = 200\ fs$, and gold thickness $d = 500\ nm$.

to accurately assess its thermal response when subjected to an ultrashort laser pulse. Figure 5.2 illustrates the variation of gold's reflectivity under different laser incidence angles as a function of laser wavelength. Figure 5.2(a) and (b) depicts the reflectivity calculated at room temperature (300 $K$, i.e., at $t = -4t_p$) for S polarized and P polarized lasers, respectively. On the other hand, Figure 5.2(c) and (d) display the results at time $t = 0$ (i.e., at the peak intensity of the laser) for the S and P polarized case, respectively. These figures clearly indicate that reflectivity is influenced by both $T_e$ and $T_l$, which are spatial and temporal dependent. Consequently, considering a temperature reflectivity value provides a more realistic approach when determining the spatio-temporal thermal response of a material. In Figure 5.2, the laser wavelength and incidence angle selected for the rest of the simulations in this chapter are denoted by vertical and horizontal white dashed lines, respectively. Note that for 200 $fs$ pulse centered at 800 $nm$ is almost flat within the bandwidth and does not show any features of interband transitions [190] in our case. Hence, without losing any generality, in our simulations, we are allowed to use the temperature-dependent reflectivity for 800 $nm$.

### 5.2.3 Evolution of spatio-temporal surface electron temperature distribution

We determined the spatial distribution of the surface electron temperature for both the S and P polarized cases at specific time intervals just before and after the peak intensity of the laser pulse (occurring at $t = 0\ ps$) (Figure 5.3). The top row in Figure 5.3 is obtained with S polarized laser pulse, while the bottom row is with P polarized pulse. In all panels of Figure 5.3, the difference in electron temperature between the S and P polarized cases is evident. The asymmetry of the hot spot along x and y direction is evident in this figure. The Gaussian profile of the focal spot is reflected at oblique incidence from the sample surface. The elongation of the hot spot in the x-direction signifies the elongated energy deposition feature resulting from the oblique angle of incidence. To emphasize this feature, we have highlighted the $T_e(x, y, z = 0) = 500\ K$ isocontour in red in each of the panels in Figure 5.3. Beyond $t = 0\ ps$ (at the peak laser intensity), the electron temperature continues to increase until $t = 0.15\ ps$, after which it starts to decrease. This behavior is consistent with the findings presented in Figure 5.1(d), where $T_e$ exhibits a sharp rise until 0.15 $ps$, while its decline beyond 0.15 $ps$ is comparatively slower. The temperature profile at the focal spots in Figure 5.3(c) and (g) clearly exhibits a significant difference in $T_e^{max}$ between the S and P polarized cases, which is consistent with Figure 5.1. This difference is due to the distinct reflectivity conditions for the S and P polarized lasers.

To study the evolution of the lateral dimensions of the laser-induced hot spot, we extract line-out profiles along the $x$ and $y$ axes from the surface electron temperature profile at various time instants.

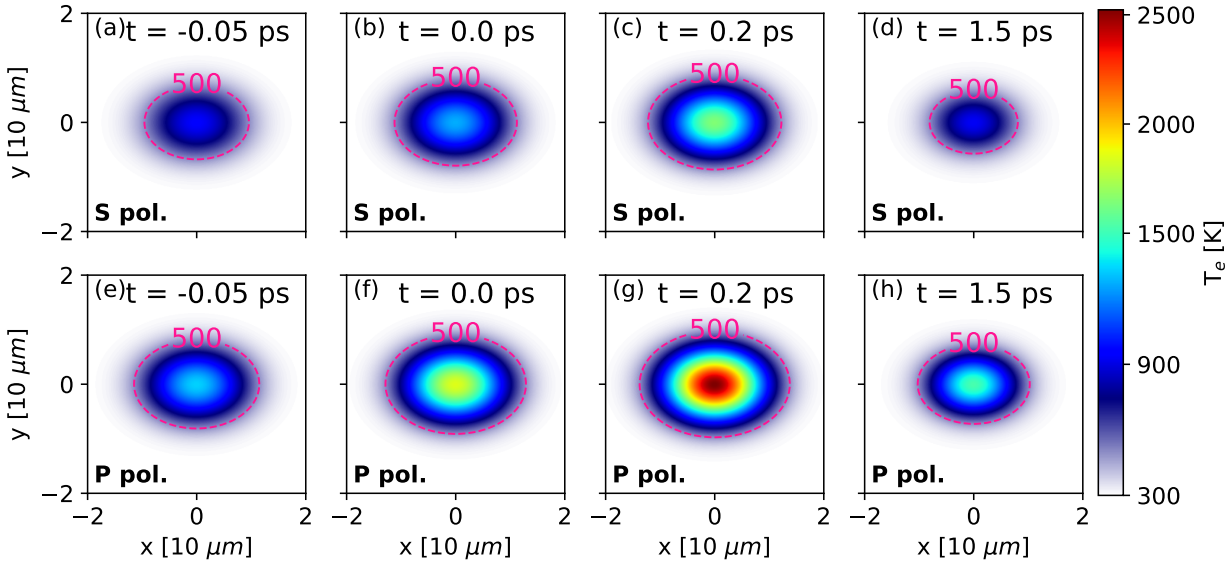


Figure 5.3: The spatial distribution of the surface electron temperature at specific time instants for the S (a-d) and P polarized (e-h) laser pulses incident at $\theta = 45°$ onto the sample. The pink iso-temperature line denotes $T_e = 500\ K$. The simulation parameters are same as given in Figure 5.1.

Figure 5.4 presents the corresponding line-outs at the center of the focal spots of the $T_e$ profiles in Figure 5.3. Figure 5.4(a) and (c) show the variation of $T_e$ along the $x$ with $y = 0$ for the S polarized pulse case, while Figure 5.4(e) and (g) display the variation along $y$ with $x = 0$ for the P polarized case. To evaluate the width of the electron temperature (Gaussian-like) profile, we calculated the half-width at half maximum (HWHM) lengths along the $x$ direction (denoted as $R_1$) and $y$ direction ($R_2$) at each time point $t$. These calculated values are presented in Figure 5.4(b) and (d) for the S polarized case, and in Figure 5.4(f) and (h) for the P polarized case. The color map displayed in Figure 5.4 denotes the time scale, and the colored circles depicted in the right column panel correspond to the respective colored curves seen in the left column. The temporal evolution of the surface hot spot size show the same behavior for both S and P polarization, aligning qualitatively with the dynamics of $T_e$ as illustrated in Figure 5.1(d). In each scenario, the hot spot size initially increases rapidly within a sub-picosecond time scale immediately following laser excitation to its peak value. This size then gradually decreases over the course of several picoseconds, eventually stabilizing at a constant value once electron-lattice thermalization is finished. Notably, it is observed that the maximum hot spot size attained in each case ($2R_2 \sim 10 - 11\ \mu m$) at the peak of the electron temperature surpasses the focal spot size (FWHM $= 9\ \mu m$), yet $R_2$ decreases to $\sim 6 - 7\ \mu m$ over the course of several picoseconds. Such estimations, deducted from these calculations, hold crucial significance in both the design of experiments aimed at investigating heat dynamics in plasmonics [191] and in applications involving pump-probe thermoreflectance [192] configurations.

### 5.2.4 Evolution of the thermionic current density in space and time

We calculate the thermionic emission current density resulting from the thermal changes in the laser-heated metal surface, utilizing the modified Richardson-Dushman equation (MRD) as given in Equation 5.2, self-consistently together with the TTM at each time increment, using the specified initial and boundary conditions. For the initial state of $\dot{N}_{sc}$, we assume an absence of electron emission from the gold surface prior to laser excitation. In this study, we examine the thermionic current based on a MRD, which takes into account the influence of the space-charge field generated by the electron cloud near the laser-induced focal spot on the metal surface. Additionally, we incorporate the temperature-dependent chemical potential. Before delving deeper into the results, we discuss the intricate terms, such as the potentials $\phi_{sc}$ and $\mu(T_e)$ within the exponential of the MRD equation.

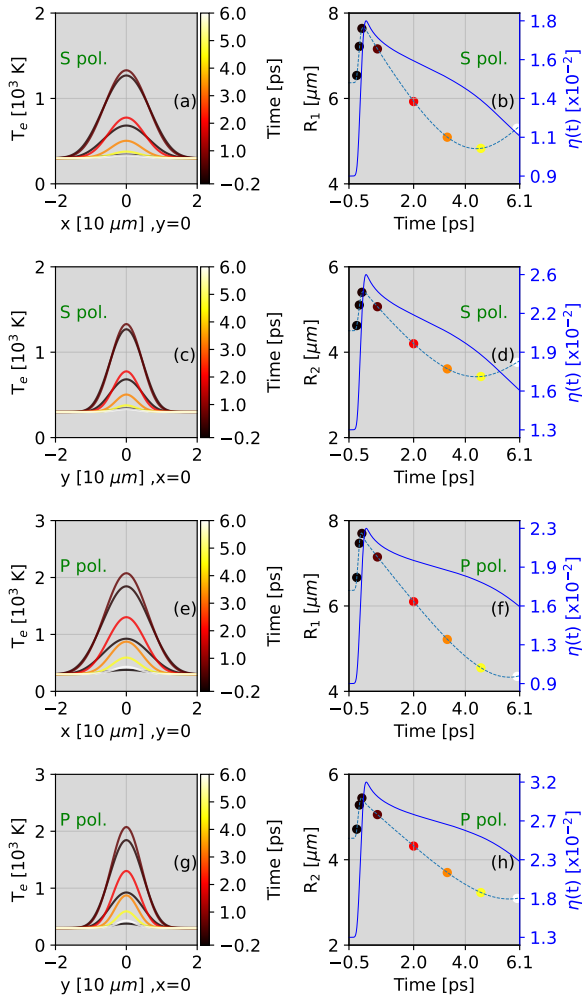


Figure 5.4: Evolution of the $x$ and $y$ line-outs of the surface electron temperature ($T_e$) at specific time instants for S (first and second row) and P polarized (third and fourth row) laser pulse incident on to the sample at $\theta = 45°$. Corresponding half-width at half maximum (HWHM) of the $T_e$ distribution (Gaussian-like) along the $x$ and $y$ directions, denoted as $R_1$ and $R_2$, respectively, are displayed in the second column. The right axes (in blue) in the second column denotes $\eta(t)$ (expressed in Equation 5.3) for the validity regime of the space charge model. The input parameters are same as mentioned in Figure 5.1.

### Role of dynamic space charge effects and corresponding validity regime of the model

Thermionic emission occurs following the laser-induced heating of the metal surface. As this ultrafast thermionic emission takes place, a thin disk of emitted electrons emerges parallel to the metal surface, resulting in the space charge barrier. Hence, it becomes important to appropriately account for the implications of laser-induced space-charge effects. The influence of the space charge field, as a rule, is complicated [193, 194]; not all emitted electrons are uniformly impacted by the barrier, and thus, representation of $\phi_{sc}$ as an effective potential is not universally applicable. The most rigorous approach for handling space charge effects involves N-body numerical simulations, entailing calculations of Coulombic forces and the solution of equations of motion through advanced numerical techniques [195–197]. However, in the context of ultrafast emissions, such as those induced by femtosecond laser irradiation, the emitted electrons exhibit strong spatial localization and are released early in the interaction, permitting simplifications [109, 198].

If the duration of the laser pulse is short enough, a thin charged disk composed of escaped electrons forms near the metal surface, with a spatial width denoted as $\Delta x$ parallel to the gold surface. In order to investigate further, we consider a square-wave temperature pulse of duration $\tau$ and a peak electron

temperature $T_e$ and consider the emitted electrons that remain above the surface. If $\tau$ is also the emission duration, then the maximal width of the emitted electron disk becomes $\Delta x = \sqrt{3k_BT_e/m}\tau$, where $\sqrt{3k_BT_e/m}$ represents the root mean square speed, and the maximum lateral width can be approximated as $max(2R_1, 2R_2) = 2R_1$. Consequently, we introduce the temperature-dependent ratio as a criterion for determining whether the emitted hot electrons can be approximated by a thin disk or not, given as

$$\eta(t) = \frac{\Delta x\big(T_e(t)\big)}{2R_{1,2}\big(T_e(t)\big)} = \frac{\sqrt{3k_BT_e/m}\tau}{2R_{1,2}\big(T_e(t)\big)} \ . \tag{5.3}$$

Hence, when $\eta(t) \ll 1$, the electrons emitted through the thermionic process can be accurately represented by a thin disk.

In the existing literature [109, 199], the disk model validity was tested by considering $\tau$ to be 1 $ps$ and a single temperature for the emitted electrons was considered, resulting in a space-charge barrier potential, given as $\phi_{sc} \approx aN_{yield}e^2/R_1$, where $N_{yield}$ represents the analytical expression for the total yield. The total yield is obtained by solving Equation 5.2 for a square-wave temperature pulse with a duration of $\tau$ [109, 180, 181]. The expression for $N_{yield}$ is given by $N_{yield} = (k_BT_e)/(ae^2/R_1)\log\big[1 + C\tau\pi R_2 ae^2 k_BT_e \exp\big(-(eE_f - \mu(T_e) + e\phi)/(k_BT_e)\big)\big]$, here $R_1$ and $R_2$ denotes the semi-major and semi-minor axes lengths of the elliptical electron charge disk, and $a$ is a constant dependent on the geometry of the escaping electron cloud. For a uniform thin disk, the value of $a = 16/(3\pi) = 1.7$ [109].

Based on the approach given in [109], under the thin disk condition, the space charge model remains valid if $\eta(t) \ll 1$, where $2R_{1,2}$ denotes the lateral spatial extent corresponding to the direction under consideration. In the x-direction, $2R_{1,2}(T_e(t))$ is represented by $2R_1$, while in the y-direction, it corresponds to $2R_2$ as illustrated in Figure 5.4. Hence, the parameter $\eta(t)$ provides the temporal trend in space charge evolution and defines the regime within which the space charge model remains valid. The fluctuations of $\eta(t)$ over time, calculated from our simulations for both S and P polarized laser fields, are depicted as the blue solid curves in Figure 5.4(b),(d),(f), and (h). In all scenarios, $\eta(t)$ remains two orders of magnitude below 1, thereby confirming the applicability of the space charge model integrated thermionic emission in our specific case.

In our approach, we extend the space charge model by including the spatial (and temporal) dependence of $\phi_{sc}$, via the calculated surface temperature profile. We calculate $\phi_{sc}$ based on the emitted electrons from the surface of the sample. Therefore, in our formulation, $\phi_{sc} = aN_{yield}e^2/R_1(t)$, which provides the dynamic variation of the space charge. The total number of thermionic electrons emitted per unit area, denoted as $N_{sc}$ (number/m$^2$), is numerically calculated and given as

$$N_{sc} = \int_{t_i}^{t_f} \dot{N}_{sc}\ dt \ , \tag{5.4}$$

where $t_i$ and $t_f$ are the initial and final times of the numerical simulation, respectively. $N_{yield}$ is given as $N_{yield} = \sum N_{sc}\delta x\delta y$, where $\delta x$ and $\delta y$ are the grid size along the $x$ and $y$ direction, respectively.

The configuration of the pulse profile, laser polarization, angle of incidence, and focal spot size collectively influence the thermal distribution across the target surface, consequently changing the accumulated space charge over the metal surface. Consequently, when computing the thermionic emission rate ('$\dot{N}_{sc}$'), we account for this variable contribution in a time-dependent manner. Rather than adopting a static rectangular $T_e$ temporal profile, we consider its profile self-consistently.

**Temperature dependent chemical potential**

In accordance with the Fermi-Dirac distribution, as temperature reaches absolute zero, single-particle states with lower-energy are filled up to the Fermi energy ($E_f$), adhering to the Pauli exclusion principle. Conversely, states beyond $E_f$ remain unoccupied. With increase in temperature, the system's total internal energy increases, leading to electron excitations and the population of higher-energy states beyond $E_f$. Consequently, a greater number of previously occupied lower-energy states become unoccupied, resulting in a decrease in the energy of the lowest-lying states. This, in turn, leads to a

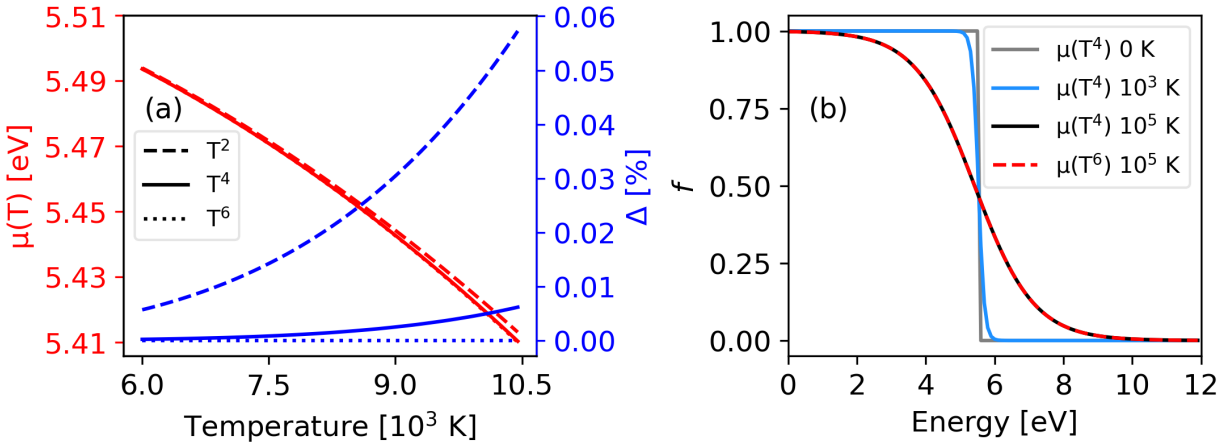


Figure 5.5: (a) The Variation in the chemical potential $\mu(T)$ as a function of temperature $T$ considering the terms up to the order of $T^2$ (dashed), $T^4$ (solid), and $T^6$ (dotted) in Equation 5.5. The percentage change $\Delta$ of $\mu(T)$ for each of these scenarios is shown on the right-hand side in blue. (b) Dependence of Fermi-Dirac distribution functions for gold on $\mu\big(\mathcal{O}(T^p)\big)$ at different temperatures, where, $p = 4$ or 6.

decrease in the chemical potential $\mu$. Therefore, it is necessary to consider the temperature-dependent chemical potential in the calculations of $\dot{N}_1$ (Equation 5.1).

This Fermi-Dirac energy distribution of electrons is given as $f_i^N = 1/\big(\exp\big((\epsilon_i - \mu)/(k_B T)\big) + 1\big)$, where $\mu$ represents the chemical potential, $k_B$ is the Boltzmann constant, $T$ denotes the temperature, and $f_i^N$ denotes the mean number of electrons in the one-electron level $i$. The total number of electrons $N$ is determined by summing the mean numbers from all levels. The temperature dependence of the chemical potential can be calculated using the Sommerfeld expansion applied to the integral forms [132], given as

$$\mu(T_e) = eE_f\left[1 - \frac{\pi^2}{12}\left(\frac{k_B T_e}{eE_f}\right)^2 - \frac{3\times 7\pi^4}{8\times 360}\left(\frac{k_B T_e}{eE_f}\right)^4 - \frac{31\times 105\pi^6}{15120\times 32}\left(\frac{k_B T_e}{eE_f}\right)^6\right], \tag{5.5}$$

where $E_f$ is the Fermi energy.

The influence of higher-order terms (up to $T^6$) on the chemical potential ($\mu$) is evaluated and depicted in Figure 5.5. The results clearly demonstrate that considering terms up to $T^2$ and up to $T^4$ leads to different outcomes. Conversely, there is no significant distinction between the results obtained for $T^4$ and $T^6$ (indicated by the red curves). Furthermore, Figure 5.5(a) presents the percentage variation $\Delta[\%]$ of $\mu(T_e)$ (represented by the blue curves) using the expression $\Delta = (\mu(T^p) - \mu(T^6))/\mu(T^6)$, where $p$ corresponds to 2, or 4, or 6. The calculations reveal a percentage variation of less than 0.01% when high-order terms up to $T^4$ are included. Hence, higher-order terms ($> \mathcal{O}(T^4)$) are disregarded in Equation 5.5. Another justification for neglecting higher-order terms $> \mathcal{O}(T^4)$ is depicted in Figure 5.5(b). The Fermi distribution $f$, which depends on $\mu(T_e)$, is plotted as a function of energy. Even when considering very high electron temperatures, such as $T_e = 10^5\ K$ in $\mu(T_e)$, no significant change in the Fermi distribution is observed for both cases of $\mu(T^4)$ and $\mu(T^6)$ (as shown in Figure 5.5(b)). Thus, higher order terms ($> \mathcal{O}(T^4)$) are neglected in Equation 5.5.

### Time-dependent evolution of the thermionic current and charge

For the same input parameters shown in Figure 5.1(d), we calculate the temporal evolution of the thermionic emission rate ($\dot{N}_{sc}$, number/m$^2$s) at the central region of the laser-irradiated area using Equation 5.2. The results are presented in Figure 5.6(a). Furthermore, we obtain the temporal evolution of the total number of emitted electrons ($N_{sc}$, number/m$^2$) from the central region of the laser-irradiated area using Equation 5.4, as shown by the blue curves in Figure 5.6(a). It is evident that the evolution of $\dot{N}_{sc}$ exhibits differences between the S and P polarized cases. These differences can be

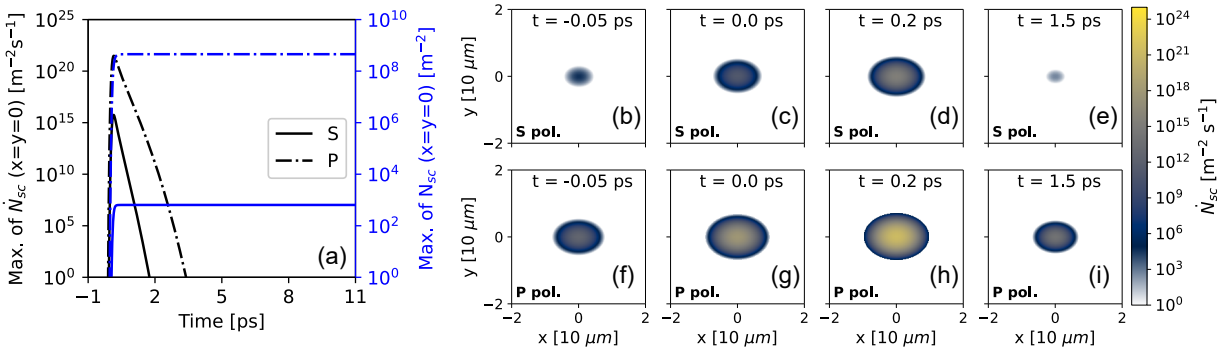


Figure 5.6: The change of thermal processes in gold under the influence of a laser: (a) depicts the time-dependent changes in the thermionic emission rate $\dot{N}_{sc}$ (in black) which is maximum at the central region of the irradiated surface ($x = y = 0$) obtained for S (solid line) and P (dash dot line) polarization, computed using Equation 5.2. consequently, the total number of thermionic electrons $N_{sc}$ emitted per unit area which is maximum at the central region of the irradiated area ($x = y = 0$) (blue curves) calculated using Equation 5.4 for S (solid curve) and P (dash dot curve) polarization. Snapshots of $\dot{N}_{sc}$ are presented for the S (b-e) and P polarized laser (f-i) at different time steps. The simulation parameters are same as specified in Figure 5.1.

explained by the rapid increase in electron temperature during the laser interaction period and the slow thermal relaxation during e-l thermalization, due to the low electronic heat capacity. This indicates that the thermionic emission tail is extended in the case of the P polarized laser, with the rise duration from $10^0$ $m^{-2}$ $s^{-1}$ to the maximum value of 0.24 $ps$, followed by a drop duration of 2.8 $ps$ from the peak. In contrast, in the case of S polarization, the duration of rise and drop are 0.2 $ps$ and 1.6 $ps$, respectively. As a result, $N_{sc}$ is higher for the case of P polarization compared to the S polarized case.

As depicted in Figure 5.6(a), $N_{sc}$ experiences a rapid increase during laser irradiation, but eventually saturates by the end of the laser pulse. Moreover, $N_{sc}$ is higher for the P polarized case compared to the S polarized case. This behavior is directly linked to $\dot{N}_{sc}$; due to the longer duration of thermionic emission in the case of the P polarized laser compared to the S polarized laser, a larger number of electrons are available for emission from the sample's surface. Therefore, $N_{sc}$ is higher for the P polarized case compared to the S polarized case. To highlight the role of laser polarization, the spatial distribution of $\dot{N}_{sc}$ at certain time instants near the peak of the laser intensity is calculated (see Figure 5.6(b-i)). Due to the low electron temperature in the S polarized case (see Figure 5.1(d)), the thermionic emission rate is smaller compared to that in P polarized case.

The role of both the S polarization and P polarization light on the electron-lattice thermalization duration ($\tau_{el}$) and duration of the thermionic emission ($\tau_{em}$) was analyzed as a function of the laser incidence angle and is illustrated in Figure 5.7. The variation between the surface electron and lattice temperatures ($T_e - T_l$) at the central region of the laser-irradiated area for the S and P polarized lasers was computed with respect to laser incidence angle and is presented in Figure 5.7(a) and (b), respectively. To determine $\tau_{el}$ for each laser incidence angle, two time instants were selected at which $T_e - T_l = 10$ $K$ (indicated by circles in Figure 5.7(a, b)). The time difference between these selected values provided $\tau_{el}$ for both the S and P polarized lasers, as depicted in Figure 5.7(c). As the laser incidence angle increased, $\tau_{el}$ decreased for the S polarized laser but increased for P polarized laser. This behavior is due to the fact that as the electron temperature increases, more time is needed for energy transfer from the excited electrons to the lattice. The higher $T_e^{max}$ in the case of the P polarized laser, shown earlier in Figure 5.1(c), explains the longer $\tau_{el}$ for the P polarized case (Figure 5.7(c)). This phenomenon is supported by the reflectivity results shown in the inset of Figure 5.1(d), where it is evident that the reflectivity decreases for P polarized laser, indicating higher energy absorption by the sample and resulting in a higher $T_e$. The opposite trend is observed for the S polarized pulses, leading to a higher surface electron temperature compared to the S polarized case. Similar trends are observed in the thermionic emission duration $\tau_{em}$ shown in Figure 5.7(d-f).

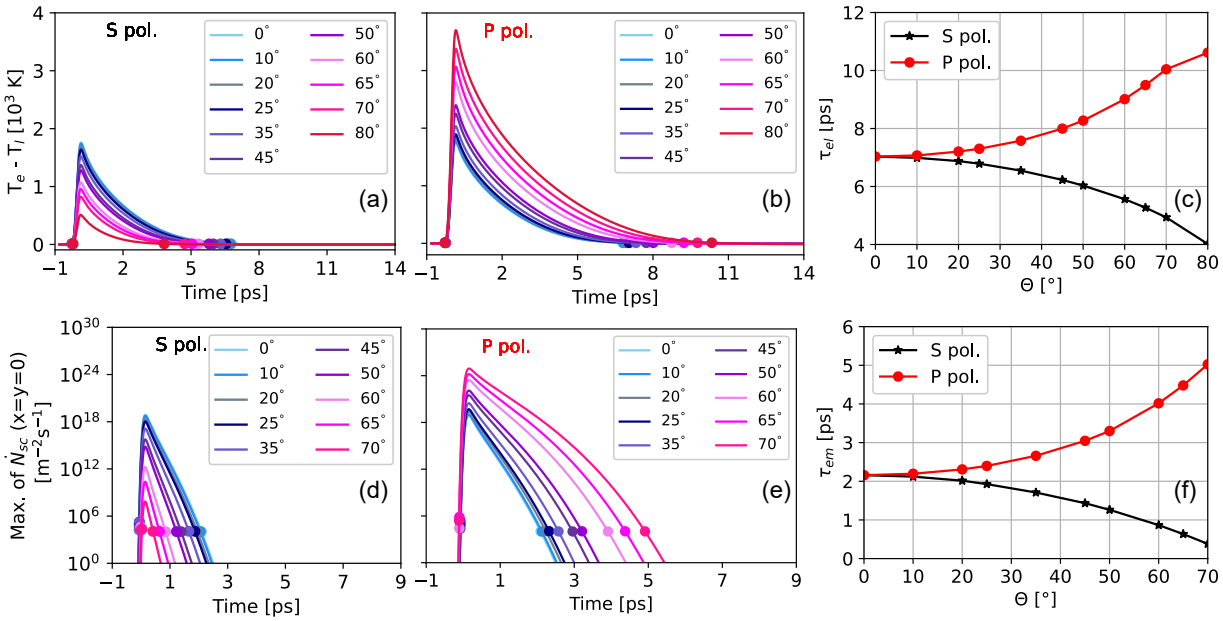


Figure 5.7: The variation in surface electron $T_e$ and lattice temperature $T_l$ at the central region of the laser irradiated area is examined for different incident angles of the laser, both for the (a) S polarized and (b) P polarized laser pulses. The time interval between the two circular markers (located when $T_e - T_l = 10\ K$) is designated as the electron-lattice thermalization duration denoted as '$\tau_{el}$', represented in (c) for both S (in black) and P (in red) polarized laser pulses. The maximum thermionic emission rate ($\dot{N}_{sc}$) at the central region of the laser irradiated area for various incident angles of the laser for the S (d) and P (e) polarized laser pulse. The time interval between the two circular markers is considered as the thermionic emission duration denoted as $\tau_{em}$, and depicted in (f) for the S (in black) and P (in red) polarized laser pulse.

The difference in peak electron temperature between the S polarized laser and the P polarized case (see Figure 5.1(c)) leads to distinct behaviors in thermionic emission duration. For the S polarized laser case, where the peak electron temperature is lower, hot electrons transfer their energy to the lattice more quickly, resulting in a decrease in their temperature and consequently leading to a shorter thermionic emission duration (Figure 5.7(d)). Conversely, in the P polarized case with a higher peak electron temperature, hot electrons take more time to transfer their energy to the lattice, leading to an extended thermionic emission duration (Figure 5.7(e)). This effect causes the thermionic emission duration ($\tau_{em}$) to increase for the P polarized case and decrease for the S polarized case as a function of the laser incidence angle (Figure 5.7(f)). To calculate $\tau_{em}$, two time instants were considered when the peak of $\dot{N}_{sc}$ (the surface electron emission rate) reached $10^4\ m^{-2}\ s^{-1}$, as indicated by filled circles in the Figure 5.7(f). The time interval between these two circular markers represents the thermionic emission duration $\tau_{em}$.

## 5.3 Conclusions and outlook

Gold, classified as a noble transition metal [200], has a wide range of versatile applications, spanning from flexible integrated electronics [201], biomedical [202], to the emerging field of twistronics [203]. Furthermore, gold-coated mirrors play a significant role in ultrafast laser optics. In the realm of research encompassing all these applications, the ultrafast thermal management and electron emission from metal nanofilms are significant. In this work, we have employed and used numerical simulations to investigate the role of polarization on the ultrafast thermionic emission originating from a nanoscale gold film coated on a glass substrate, subject to the obliquely focused femtosecond laser pulse irradiation. We have employed an enhanced TTM that efficiently computes the 3D heating incorporating temperature-

dependent optical and material properties. Additionally, we have utilized the modified Richardson-Dushman equation for the computation of thermionic emission profiles.

We investigated the change of electron and lattice temperatures as a function of time at various laser incidence angles. Our results revealed that around the Brewster angle of incidence, polarization of the laser can be changed from S to P in order to tune and enhance the laser-spot size, the surface electron temperature, and the subsequent thermionic emission rate. Our finding reveal that for each of the incidence angles, the duration of the thermionic current pulse shows a strong relationship with the intrinsic electron-lattice thermalization duration of gold. As the electron-phonon coupling strength increases, it results in a decrease in the time required for electron-lattice thermalization. Our findings suggest that through suitable selection of the metal coating, it becomes feasible to tune the duration of the thermionic current pulse while simultaneously preserving its peak brightness. Considering the recent advancements in experimental capabilities, which permit to resolve and detect the electron emissions on ultrafast timescales [186–189], these insights open up new avenues for exploration. Moreover, this holds considerable promise for advancing the creation of high-intensity, ultrafast electron imaging instruments.

It's worth mentioning that there have been recent significant advancements in the efficiency of thermophotovoltaic power generation [204], especially in high-temperature emitter scenarios [205]. In some instances, these systems incorporate a reflective metal-dielectric structure [206]. These methods hold important implications for energy harvesting applications. Furthermore, thermionic emission based on solar concentrators [207, 208], along with thermionic energy converters [209] often employ metal-based architectures. However, it's worth noting that most of these investigations are typically conducted under conditions of steady-state thermal equilibrium. The introduction of ultrafast laser-induced thermal management and its consequent impact on thermionic processes would introduce dynamic elements into these experiments. This dynamic perspective has the potential to uncover novel insights, enriching our current knowledge of these topics within applied surface science. Importantly, the methodology and findings reported in our work could offer valuable insights for interpreting results and designing experiments in these areas.

However, in a scenario where the electron temperature approaches or exceeds the Fermi temperature, the TTM necessitates the incorporation of full quantum mechanical calculations [210]. Moreover, in the case of semiconductors, an extended version of the TTM is required [211]. For studying much longer timescale dynamics and obtaining extensive details, one can resort to computationally intensive molecular dynamics simulations combined with a 3D TTM [212–214]. In a scenario where a femtosecond laser pulse of duration less than 100 $fs$ interacts with a metal, the e-e collisions are not fast enough to reach internal thermalization during the laser pulse. In such cases, for a more rigorous study of laser-matter interactions, an alternative to the TTM model is the use of *ab-initio* time-dependent density functional theory. This approach provides a more accurate description of the system's behavior under the influence of ultrashort laser pulses, and is particularly advantageous when a higher level of precision is desired. This theoretical approach is used to investigate the electron dynamics laser driven atom and 2D material in the later chapters.

# Chapter 6

# Addressing the ultrashort laser induced sub-cycle dynamics: HHG in atoms irradiated by linear and bi-circular counter-rotating laser fields

In laser excited materials, while the electrons and lattice elevated temperature results in strong thermionic emission, within a laser pulse cycle, sub-cycle electron dynamics follows the pulse shape that results in change of the transient response of the elevated electrons. Monitoring and understanding this process is critical to have a complete picture of ultrafast electron dynamics, that occurs at femtosecond timescale. Ultrashort pulses which are obtained by HHG mechanism can enable the study and helps in understanding the ultrafast electron dynamics processes at the atomic and molecular level. Ultrashort pulses have wide range of applications, to name a few, (i) in laser ablation experiments, they are used for precise and controlled material removal, (ii) in laser-driven particle acceleration, they can accelerate charged particles (electrons, ions) to very high energies.

The ultrafast timescale of the new generation lasers can vary from less than 6 $fs$ to 75 $ps$ as available in the state-of-the-art ELI ALPS laser facility [215], which enables the observation and manipulation of electron motion within atoms, allowing researchers to probe electron excitation, ionization, and recombination with extraordinary precision. To study the electron dynamics under the influence of even shorter laser pulses ($\leq 100$ $fs$), two-temperature model, which was described in chapter 5 is no longer valid [216]. An alternative, more general approach to investigate excited state properties in ultrashort laser driven materials is the time-dependent density functional theory (TDDFT) method, which is particularly useful to capture electron dynamics in atoms, solids, and to study chirality of molecules, to name a few. Gold, being a periodic metallic system that has several discretized bands is computationally expensive to investigate using TDDFT approach. Hence, in this chapter, based on *ab-initio* calculation within TDDFT method, which is a more general approach, as a first step, we probe femtosecond laser-driven electron dynamics in atoms, by considering multi electron effects, aiming to shed light on the intricate mechanisms that govern high-order harmonic generation. First, we investigate the electron dynamics in an argon atom driven by a linear polarized (LP) laser field and discuss the underlying physical principles that describe electron behavior under the influence of an intense femtosecond laser field.

Bi-chromatic circular counter rotating (BCCR) laser fields are used to generate high harmonics with ellipticity ranging from linear to almost circular, which is a promising source of ultrashort XUV radiation at the attosecond timescale [217]. Such XUV radiation is useful for analysing the magnetic, electrical, structural properties of materials. The polarization or the ellipticity of the attosecond pulses can be tuned by changing the emitted harmonic's ellipticity, which can be tuned by changing the driver fields. The light sources generated using BCCR fields can be used to probe chiral-specific phenomena such as magnetic circular dichroism [218], among many others. To this extent, we study the time

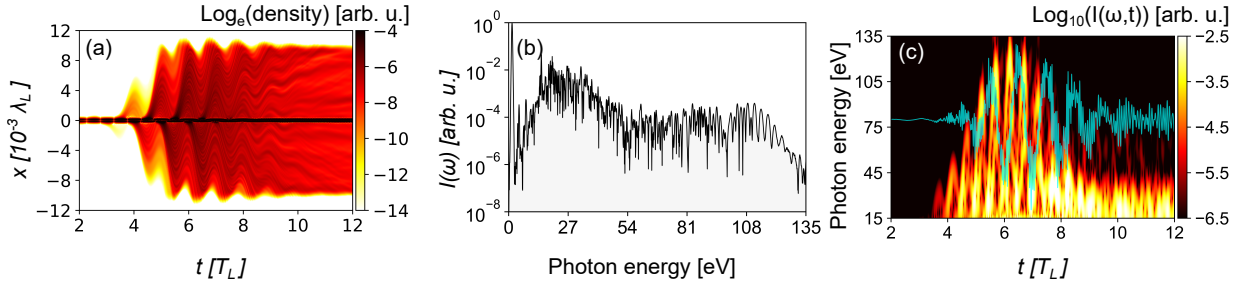


Figure 6.1: Electron dynamics in Ar atom driven by a linear polarized laser field with a peak intensity $I_0 = 5 \times 10^{14}\ Wcm^{-2}$. (a) Evolution of induced electronic density, averaged over the $y$-$z$ plane and taken along $x$-direction (laser polarization direction). (b) Harmonic spectrum of Ar showing main spectral features, such as, cooper minimum at $\sim 50\ eV$. (c) Time-frequency analysis of the harmonic emission. Cyan curve depicts the electric field after the interaction.

dependent electron dynamics in an argon atom driven by the BCCR laser fields and compare our results to the experimental findings.

## 6.1 Numerical method

The time-dependent electron dynamics in argon under the influence of LP and BCCR laser fields are investigated based on *ab-initio* calculation within TDDFT (as mentioned in Section 2.3) approach [97] in the real-time and real-space grids as implemented in the Octopus computational package [219, 220]. TDDFT within the GGA with exchange and correlations of PBE [96] is used in this work. In this approach, the evolution of electronic wavefunctions are performed on the basis of Kohn-Sham (KS) equation defined as in Equation 2.16. The nuclei motion is neglected, which is justified for ultrashort laser pulses, even in longer pulse, the effects are expected to be minimal [221–223]. Theoretical model involving linear polarized laser and BCCR laser fields are described in Section 6.2 and Section 6.3, respectively.

## 6.2 Non-linear response in linear polarized laser driven Ar atom

As mentioned earlier, in this chapter we use two different laser fields are used to investigate electron dynamics in argon atom. In this section, non-linear response of argon atom is investigated using a LP laser field. The driving laser field is linearly polarized along $x$ direction and is assumed to be spatially uniform, which is justified for the laser wavelengths larger than the size of Ar atom. Furthermore, the contributions from the magnetic component of the electromagnetic field and any other relativistic effects, such as spin-orbit coupling are neglected in this work. The driving field is given as

$$\boldsymbol{E}(t) = E_0 \exp\Big[-2\log(2)(t-2\tau)^2/\tau^2\Big] \cos\Big[\omega_0(t-2\tau)\Big]\boldsymbol{e_x}\ , \tag{6.1}$$

where $\omega_0$ is the carrier frequency, $\tau \simeq 8\ fs$ is the pulse duration at full width half maximum of the intensity temporal profile. $E_0$ is the peak field amplitude, defined in atomic units in terms of the peak intensity of the laser $I_0$ as: $E_0 = \sqrt{I_0/I_a}$, where $I_0 = 5 \times 10^{14}\ Wcm^{-2}$, $I_a = 3.51 \times 10^{16}\ Wcm^{-2}$ is the atomic intensity unit. The central wavelength of the laser is $\lambda = 800\ nm$, corresponding to $1.55\ eV$ photon energy. The carrier phase envelop is considered to be zero ($\phi = 0$). These field parameters are similar to those which can be achieved with SYLOS laser for GHHG at ELI ALPS facility [215, 224].

The initial states are derived from self-consistent solutions of wave functions at the DFT level. Subsequently, these states are propagated using the approximated enforced time-resolved symmetry method, using time steps of $\Delta t = 0.3$ atomic units. The Hamiltonian exponential is computed using the LANCZOS method described in Castro et al. [225]. The exchange-correlation potential is represented by the local density approximation [99, 226]. All calculations were performed employing fully relativistic

Hartwigsen, Goedecker, and Hutter pseudopotentials [227]. To investigate the multielectron dynamics of argon, a single Ar atom is placed in a parallelepiped simulation box with dimensions of 50 Bohr along $y$, $z$ direction and 360 Bohr along $x$ direction (laser polarization direction), which includes 40 Bohr of absorbing regions on both sides of the argon atom. This is a precautionary measure to prevent unphysical reflection of field-accelerated electrons at the border of the simulation box. The absorbing regions are treated using the complex absorbing potential (CAP) function [228], with a CAP height of $-1$ atomic units (a.u.). The real-space cell is sampled along all three directions with a grid spacing of 0.18 Å. The high harmonic spectrum $I(\omega)$ is calculated from the Fourier transform ($\mathcal{FT}$) of the time-dependent dipole acceleration $\boldsymbol{a}(t)$ as [229–231]

$$I(\omega) = \left|\mathcal{FT}[\boldsymbol{a}(t)]\right|^2 = \left|\mathcal{FT}[\ddot{\boldsymbol{d}}(t)]\right|^2 \tag{6.2}$$

where $\boldsymbol{d}(t) = \int n(\boldsymbol{r},t)\boldsymbol{r}d\boldsymbol{r}$ is the time-dependent dipole moment, $n(\boldsymbol{r},t) = \sum_{i=1}^{N}|\psi_i(\boldsymbol{r},t)|^2$ is the time-dependent electron density and $N$ is the number of Kohn-Sham orbitals given by $\psi_i(\boldsymbol{r},t)$.

Figure 6.1(a) shows the temporal evolution of induced electron density, averaged over the $y$-$z$ plane and projected along the $x$ direction, i.e. along the laser polarization direction. The excited electron density captures the subcycle dynamics, involving three-step-like processes [232]. These processes are distinctly visible, with ionization occurring near the peak of the driving pulse field, electron acceleration away from the atom in the light field, and eventual recollision near the zero crossing of the field in each half-cycle. This periodic recombination leads to the emission of high harmonics spectrum, as depicted in Figure 6.1(b), with harmonics reaching up to a cutoff energy of 110 $eV$.

Experimental observations, particularly in argon atoms, have shown the appearance of a local minimum in the high harmonic emission, specifically near 48 $eV$ [233]. This minimum is associated with the Cooper minimum, which arises from a complete cancellation of dipole moments between $p$ and $d$ ground state orbitals, leading to a null dipole moment, as seen in XUV photoionization of argon [234]. Remarkably, our TDDFT simulations in Figure 6.1(b) accurately reproduce this feature of the Cooper minimum in the argon HHG spectra, validating our approach to study non-linear response in atoms under the influence of intense laser fields.

The cyan curve in Figure 6.1(c) illustrates the dipole acceleration, $\boldsymbol{a}(t)$ along the laser polarization direction ($x$-axis). The slow variations of $\boldsymbol{a}(t)$ represent the transmitted part of the driving laser field, while the high-frequency modulations superimposed on it lead to the phenomenon of HHG. To validate the trajectories of the wave packet bundles, a time-frequency analysis of the harmonic emission in argon is performed using Gabor transformation, a type of time-windowed Fourier transformation [235, 236]. An optimal window size $\delta$ is considered for the analysis [237]. The Gabor transform $\left|G(\tau,\omega)\right|$ of the signal $s(t)$, which represents the time-domain reflected electric field in this case, is given as $G(\tau,\omega) = \int_{t_i}^{t_f} s(t)\frac{1}{\delta}\exp\big(-(t-\tau)^2/(2\delta)\big)^2\exp(i\omega t)dt$, where $t_i$ and $t_f$ are the initial and final simulation time $t$, respectively. $\tau$ corresponds to each element in the time array, representing the horizontal axis in the plot. The resulting colormap in Figure 6.1(c) depicts $\left|G(\tau,\omega)\right|^2$, which captures several intricate details, as follows:

(i) In the time-frequency analysis, the highest photon energy in the HHG spectra, or the cut-off harmonics, are emitted at times near the maxima of the short pulse envelope.

(ii) Furthermore, within each half cycle of the laser pulse, during the rising edge of the pulse (for instance, in the half cycle with $3.95 \leq t[T_L] \leq 4.45$ in Figure 6.1(c), the highest-energy photons are emitted near the zero crossings of the field.

(iii) Within each such laser half cycle, the lower-energy photons exhibit two different emission times, while the photons near the half cycle cut-off have a unique emission time (near the zero-crossing of the field).

(iv) This phenomenon is similar to the concept of short and long trajectories (short trajectory corresponds to electrons with the same return energy released just before the first zero-crossing of the field. Whereas, long trajectories corresponds to electrons released just after the peak of

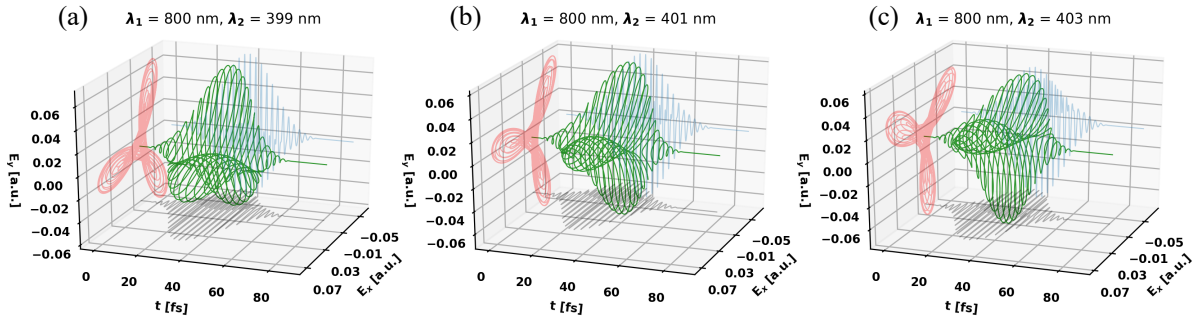


Figure 6.2: Bi-circular counter rotating electric fields with fundamental field having a central wavelength "$\lambda_1$" of 800 $nm$ and three different second harmonic field wavelengths "$\lambda_2$", i.e., (a) 399, (b) 401, and (c) 403 $nm$.

the laser field) within the simplified saddle point picture (as illustrated in Figures 7 and 8 in [232], for example). Specifically, the photons emitted before the cut-off energy display a positive chirp, while those emitted after the cut-off show a negative chirp, as seen from the curvature in the time-frequency map [238]. This intricate interplay results in the patterns observed in Figure 6.1(c).

## 6.3 Strong-field electron dynamics in bi-circular counter rotating laser driven argon atom

In the previous section, I have presented and discussed the linear polarized laser driven electron dynamics in argon atom. Our results matches well with the experimental findings of the significant features of argon HHG spectrum, such as the Cooper minimum, which validates our TDDFT approach for the studies of strong-field electron dynamics in multielectron systems. In this section, we go beyond linear polarized laser field. In order to generate highly energetic higher order harmonics and to exert control over the electron dynamics, BCCR laser fields are already in use [239, 240]. Until recently (2014), XUV light sources has only been available at large-scale X-ray facilities, like synchrotons. Recent experiments demonstrated bright, phase-matched, XUV circular polarized laser pulses generation using BCCR laser fields which is an important step towards the advancement of table-top systems that can be used for spectroscopy in chiral media and other magnetic materials with very high temporal and spatial resolution [241]. We investigate the non-linear response of argon under the influence of BCCR laser fields within TDDFT approach and compare our results with the experimental findings performed by our collaborators.

### 6.3.1 Field description and simulation parameters

The driving laser fields, as described in terms of an electric field, are polarized in the $x$-$y$ plane and are assumed to be spatially uniform, which is justified for the laser wavelengths larger than the argon atom size. In addition, the contributions from magnetic component of the electromagnetic field and any other relativistic terms, such as spin-orbit coupling are neglected. The combined electric field is a superposition of two counter rotating laser fields, and is given as

$$E(t) = \sum_{i=1,2} E_i \cos\left(\frac{(t-\tau_{\omega 1})}{\tau_{\omega i}}\right)^2 \Bigg[\cos\Big(\omega_i(t-\tau_{\omega 1})\Big)\boldsymbol{e_x} + a_i \sin\Big(\omega_i(t-\tau_{\omega 1})\Big)\boldsymbol{e_y}\Bigg], \tag{6.3}$$

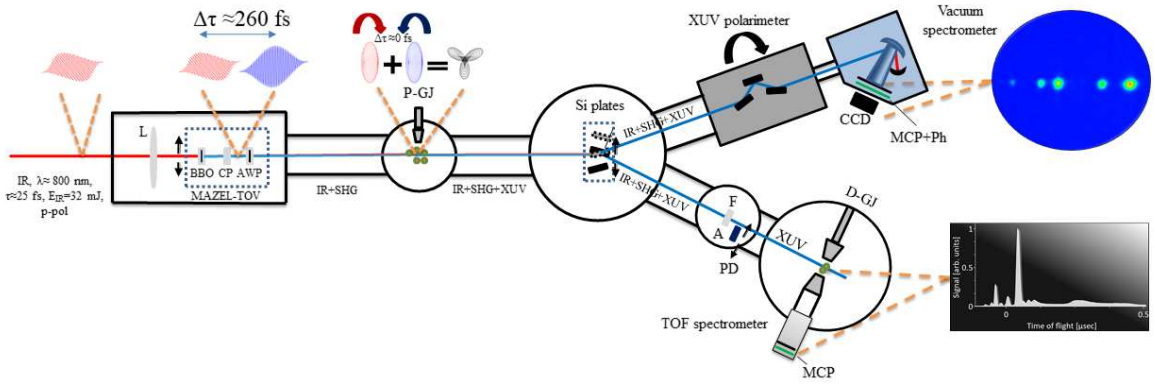


Figure 6.3: An experimental setup for the generation of tunable XUV radiation with high elliptical polarization. A compact (15 cm long) system, MAZEL-TOV-like device is positioned after a 3-meter focal length lens (L). The device include a BBO crystal, a calcite plate (CP), both independently mounted on precision rotatable stages, and a rotatable super-achromatic quarter waveplate (AWP). The system utilizes a two-color bi-circular field beam, which is focused onto a pulsed gas jet filled with argon (P-GJ). The resultant XUV radiation is directed towards a detection area using Si plates, which has two branches. The first branch accommodates a calibrated XUV photodiode (PD), a pulsed gas jet containing argon (D-GJ), and a $\mu$-metal shielded time-of-flight (TOF) spectrometer. In the second branch, there is a rotating in-vacuum polarizer followed by the XUV radiation diffraction through a spherical holographic grating and detected by a microchannel-plate (MCP) detector connected to a phosphor screen.

where $\boldsymbol{e_x}$ and $\boldsymbol{e_y}$ are the two mutually perpendicular unit vectors. In this work, we considered two counter rotating fields of $a_1 = -a_2 = 1$ with $E_1 = E_2 = E_0$. All the input laser parameters are experimental values. The peak field amplitude ($E_0$) is expressed in terms of peak laser intensity ($I_0$), in atomic units as $E_0 = \sqrt{I_0/I_a}$, where $I_0 = 10^{14}\ Wcm^{-2}$ and $I_a = 3.51 \times 10^{16}\ Wcm^{-2}$. Note that the peak laser intensity is lower than the one used in the previous section for atomic case. This is due to the fact that, mixing of two different laser fields (in the case of BCCR) would add up to yield higher peak intensity. $\cos\left((t-\tau_{\omega 1})/\tau_{\omega i}\right)^2$ denotes the envelope of the pulse, where $\tau_{\omega 1}$ is the total duration of the fundamental pulse, that may be defined in terms of full width at half maximum (FWHM) of intensity temporal profile, $\tau_p : \tau_{\omega 1} = \tau_p/(2\arccos(2^{-1/4}))$, where $\tau_p = 25\ fs$. $\tau_{\omega 2}$ is the pulse duration of the second harmonic field, which is defined as $\tau_{\omega 2} = \tau_{\omega 1}/\sqrt{2}$. A central wavelength $\lambda_1 = 800\ nm$ is used for the fundamental field and four different wavelengths are used for the second harmonic field, which are $\lambda_2 = 399,$ or $400,$ or $401,$ or $403\ nm$. The three different BCCR laser fields used in experiment and theory are shown in Figure 6.2.

The initial states are obtained from self-consistent solutions of wave functions at the DFT level. Later, those states are propagated by using the approximated enforced time-resolved symmetry method, with $\Delta t = 0.3$ a.u. time-steps. The exponential of the Hamiltonian is calculated using LANCZOS method [225] and the exchange-correlation potential is represented by the LDA [99, 226]. All the calculations were performed using fully relativistic Hartwigsen, Goedecker, and Hutter pseudopotentials [227]. To understand the multielectron dynamics of argon, its dipole interaction with external field and resulting HHG within the framework of TDDFT, single Ar atom is placed in a parallelepiped simulation box of size 40 Bohr along each of the three Cartesian ($x$,$y$,$z$) directions, which includes 4 Bohr of absorbing regions on either sides of the argon. The absorbing regions are treated using well-recognized mask function [242, 243], that ensures prevention of unphysical reflection of field-accelerated electrons at the border of the simulation box. The real-space cell was sampled along all the three directions by a grid spacing of 0.18 Å. In all our calculations, we test the convergence of parameters, such as the time step, grid spacing, absorbing regions. As mentioned before, using Equation 6.2, the harmonic spectral properties are calculated from the resulting dipole acceleration signal, which has components that are both parallel and perpendicular to the laser polarization.

### 6.3.2 Experimental setup

The experiments performed by our collaborators consists of a setup that employs a compact MAZEL-TOV-like scheme for producing elliptically polarized HHG spectra ([244]), as schematically shown in Figure 6.3, within the Attosecond Science and Technology Laboratory (AST) at FORTH-IESL. This setup consists of three sections: a focusing and MAZEL-TOV-like device chamber, a harmonic generation chamber, and detection chambers (as depicted in Figure 6.3). This setup results in the $\omega$ and $2\omega$ fields coinciding along the propagation axis, near a pulsed gas jet filled with argon. Under Gaussian optics, the intensity at the focus for both components of the bi-circular polarized field is estimated to be around $10^{14}\ Wcm^{-2}$. Beyond the gas jet, the produced XUV radiation co-propagates with the BCCR driving fields towards a pair of Si plates positioned at a 75° angle. These plates reduce the p-polarization component of the fundamental and second harmonic radiation while reflecting the harmonics towards the detection area.

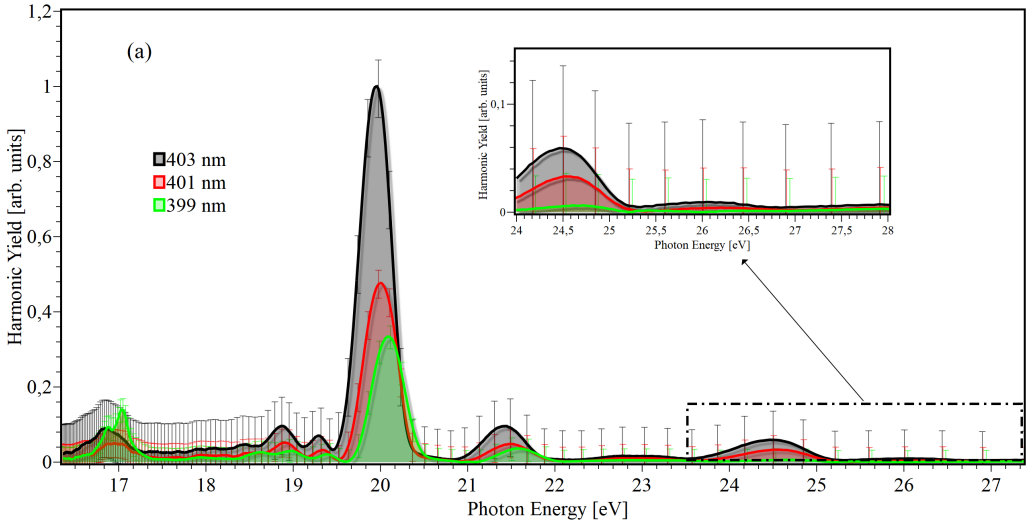


Figure 6.4: Highly-elliptical polarized HHG spectra for three different values of central SHG wavelength. The maximum shift in energy ($\Delta E$) observed is approximately 150 $meV$.

The detection area comprises two arms. The first arm, located just after the first Si plate, features two apertures to block the outer portions of the $\omega$ and $2\omega$ beams, allowing XUV radiation to pass through. A Sn filter is fixed to the second aperture, serving for spectral selection of the XUV. The spectral intensity distribution of the XUV radiation is determined by measuring single-photon ionization photoelectron spectra induced by XUV radiation with photon energy higher than argon's ionization energy. In the second arm, positioned after the Si plate, XUV radiation is diffracted by a spherical holographic grating and detected by a microchannel-plate detector.

### 6.3.3 Results and discussion

#### Spectral characterization and probing of ellipticity of emitted XUV radiation

To spectrally characterize the highly-elliptical XUV radiation, various photoelectron spectra were recorded by changing the angle ($\Delta\theta$) of the BBO crystal within the MAZEL-TOV-like device. Illustrated in Figure 6.4 are distinctive HHG spectra demonstrating the high ellipticity, displayed for three distinct $\Delta\theta$ positions. Notably, energy shift becomes apparent towards higher photon energies as the angle between the propagation axis of the IR driving field and the BBO crystal is increased. The maximum energy shift attained is $\Delta E \approx 150\ meV$. The ellipticity of the emitted higher order harmonics as a function of BBO angle is measured. Confirmation of the highly-elliptical polarization state within the HHG spectra was achieved through polarization measurements, revealing ellipticities reaching approximately 70% at around 22 $eV$, as depicted in Figure 6.5(a). Noticeably, no dependence on the central wavelength of the SHG was identified.

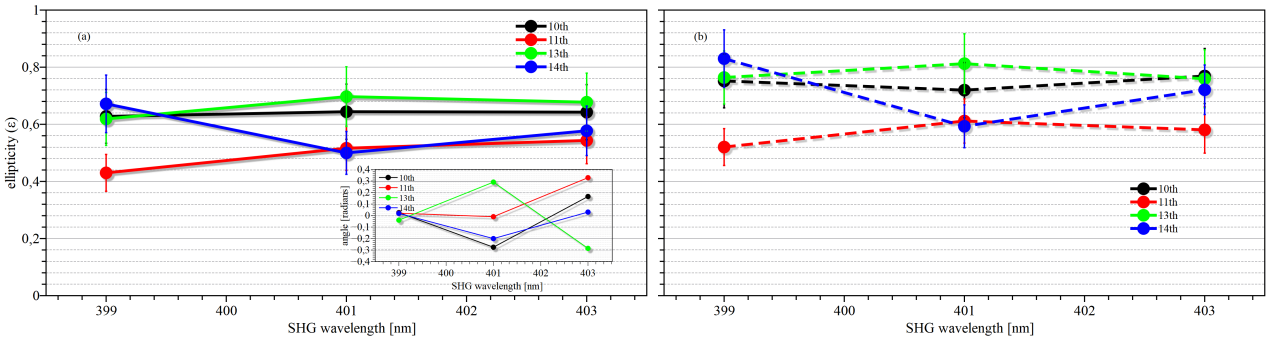


Figure 6.5: The role of central frequency of the SHG of the fundamental frequency on the ellipticity measured at the detection area (a) and reconstructed at the source (b).

The inset of Figure 6.5(a) illustrates the angle between the major axis of the ellipse and the vector perpendicular to the polarization axis of the linearly polarized field, determined through polarimetric measurements. The orientation of the ellipse manifests strong dependence on two factors: (i) the phase of the XUV radiation and the temporal delay between the counter-rotating two-color fields at constant second harmonic wavelength. The latter can be experimentally adjusted by manipulating the angle of the calcite plate within the MAZEL-TOV device and (ii) the angle of the BBO crystal while maintaining all other parameters constant. This yields in tuning two experimental parameters. Firstly, adjustments in the central wavelength and amplitude of the second harmonic field. Secondly, slight modifications in the temporal delay between the fundamental and second harmonic fields. Both of these adjustments result in a rotation of the rosette-like field pattern along the propagation axis. Simultaneously, changes in the harmonic phase occur due to the distinct energy ratios of the electric field components. Further details can be found in reference [245].

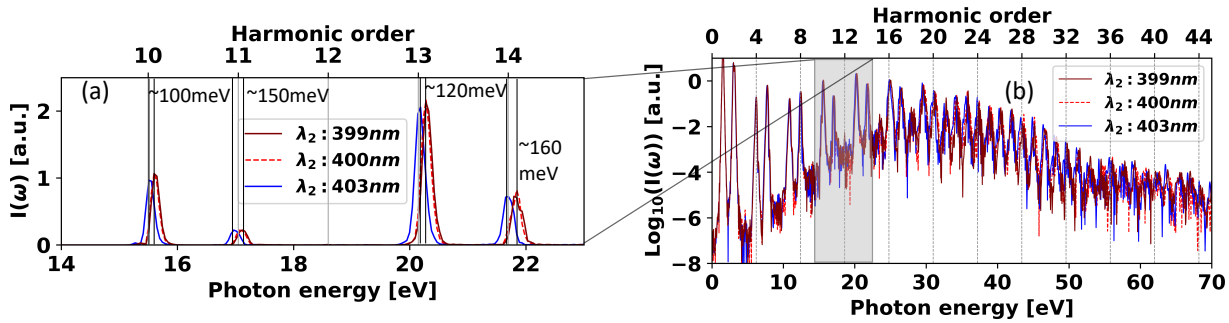


Figure 6.6: High-order harmonic spectra of an argon atom in linear scale (a) and logarithmic scale (b) obtained under the influence of BCCR laser field. A wavelength of $\lambda_1 = 800\ nm$ for the fundamental laser field is fixed and the wavelengths of the second harmonic field is varied, i.e. $\lambda_2 = 399, 400,$ and $403\ nm$. Energy shift in the high harmonic spectra as a function of second harmonic laser field's wavelength is shown in panel (a).

The current experimental setup utilized for characterizing harmonic ellipticity involves the incorporation of a Si plate, which serves to reflect the harmonic radiation towards the XUV polarimeter. This optical component exhibits slight variations in its reflectivity for the s and p polarization component of the XUV radiation, thereby influencing the measured ellipticity of the HHG radiation. By employing the appropriate Fresnel equations and utilizing refractive indices extracted from Palik et al. [246], the reflectivity of the Si plate can be computed for the two distinct polarization orientations. This calculation allows for the estimation of ellipticity values at the source for each harmonic component. The analysis revealed ellipticities reaching approximately 85% at around 22 $eV$, as depicted in Figure 6.5(b). The combined ellipticity values, along with the high energy of the XUV pulses, establish a source that is well-suited for various applications, such as manipulation and imaging of ultrafast

magnetism in magnetic materials [247–249], probing chiral matter dynamics in ultrafast experiments [250], and exploring circular dichroism in atomic systems [251–253], in which intense highly elliptical or circularly polarized XUV radiation is crucial for inducing nonlinear processes [252].

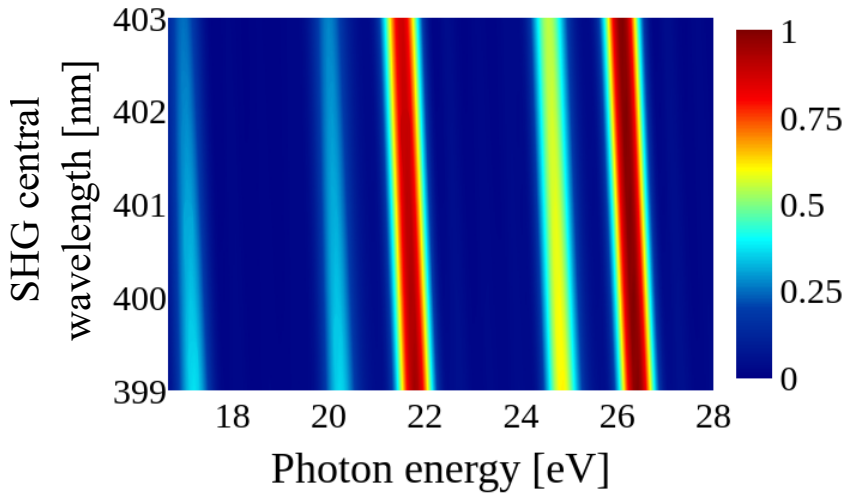


Figure 6.7: Harmonic spectra in Argon obtained as a function of the SHG central wavelength using SFA. The input parameters used were: peak intensity of fundamental ($I_\omega$) and second harmonic ($I_{2\omega}$) fields is $10^{14}$ $Wcm^{-2}$, central wavelength of the fundamental field is $\lambda_1 = 800$ $nm$ and the second harmonic central wavelength is varied between 399 $nm$ $\leq \lambda_2 \leq$ 403 $nm$ .

**Estimation of HHG spectrum and ellipticity of emitted harmonics using TDDFT simulations**

In our numerical simulations, we considered peak laser intensity of $10^{14}$ $Wcm^{-2}$ for both the fundamental and second harmonic fields. The overall electric field exhibits a trefoil pattern, as depicted in Figure 6.2(a-c) (highlighted in red). To achieve harmonic generation and control the photon energy of emitted harmonics in argon atom, we combine circularly polarized light at the fundamental frequency $\omega_1$ ($\lambda_1 =$ 800 $nm$) with its counter-rotating second harmonic $\omega_2$ ($\lambda_2 = 399$ $nm$ in Figure 6.2(a), and varying wavelengths of 400 $nm$, 401 $nm$, and 403 $nm$ in Figures 6.2(b) and (c)). The resulting harmonic radiation is represented as the sum of the absolute squares of the two polarization components ($x$ and $y$), as illustrated in linear and logarithmic scales in Figure 6.6(a) and Figure 6.6(b), respectively. Notably, the HHG spectrum in Figure 6.6(b) exhibits a distinctive structural peak within the $15-30$ $eV$ frequency range.

We determine that the emitted harmonic spectrum characteristics, such as HHG intensity and the polarization states of the harmonics, exhibit a substantial dependence on the wavelength and intensity ratio of the two driving field components in the BCCR field. Our TDDFT analysis reveals a notable correlation between the generated harmonic spectrum and the central wavelength of the second harmonic. This correlation aligns well with another theoretical calculations presented in Figure 6.7 obtained under the strong-field approximation (SFA). Furthermore, our findings demonstrate a significant central energy shift of approximately 150 $meV$ in the HHG spectrum, as depicted in Figure 6.6(a). This shift is a direct result of tuning the wavelength of the second harmonic and provides supporting evidence for the experimental results reported in 6.4.

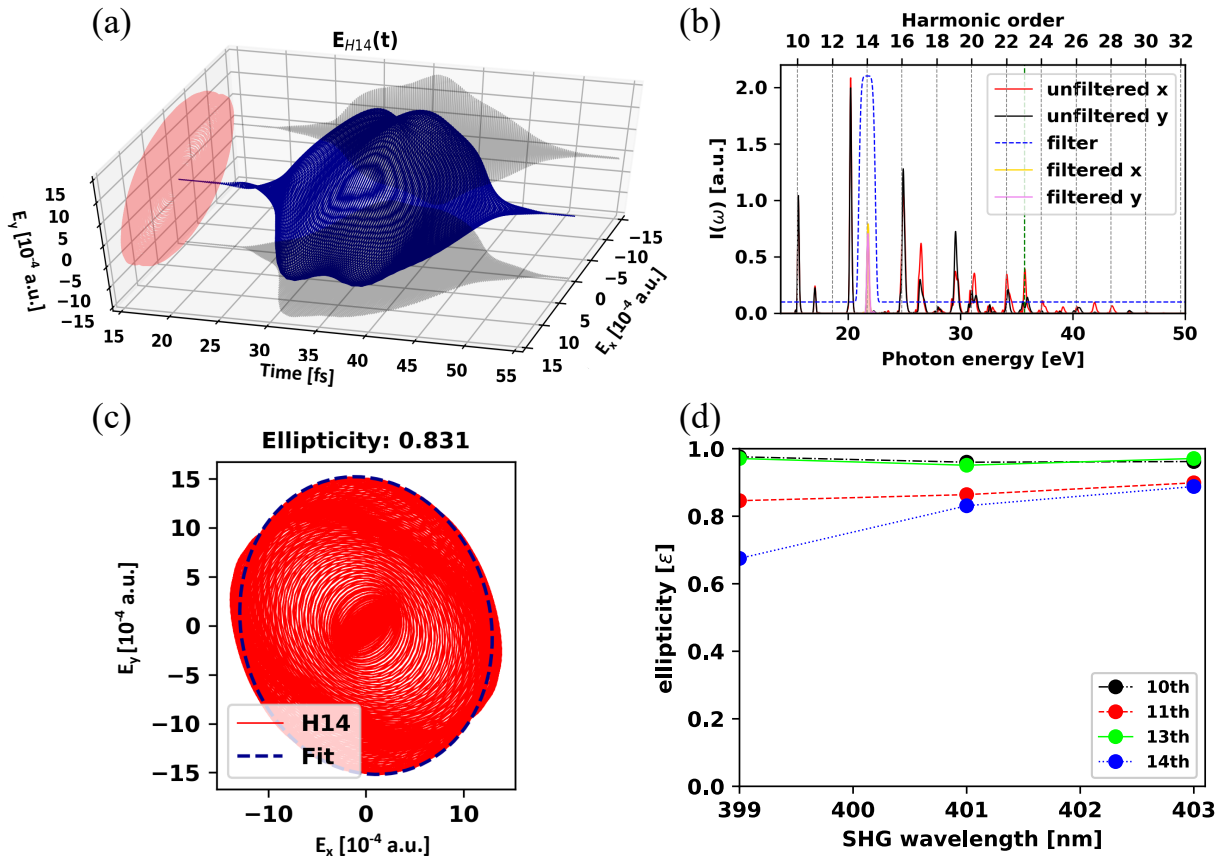


Figure 6.8: High harmonic generation from argon using a BCCR laser field with $\lambda_1 = 800\ nm$ and $\lambda_2 = 401\ nm$. (a) Temporal evolution of the ellipticity of the emitted Harmonics super-Gaussian filtered around $14^{th}$ harmonic. (b) Computed HHG spectrum from argon, Super-Gaussian filtered (blue curve) around $14^{th}$ harmonic. The green colored vertical dashed line is the harmonic cutoff. (c) The resulting harmonic field of the filtered harmonics (in red) is sliced at its maximum and fitted to an ellipse (in blue). (d) Effect of second harmonic frequency on the ellipticity of the harmonics

We examine how the ellipticity of the generated harmonics changes with wavelength of the second harmonic. For example, we show the ellipticity of the $14^{th}$ emitted harmonic for $\lambda_2 = 401\ nm$ in Figure 6.8(a). In Figure 6.8(b), we apply a super-Gaussian filter to the $14^{th}$ harmonic field (red curve) as shown in Figure 6.8(c). A specific cross-section is chosen at the peak of the harmonic field, and an ellipse is fitted onto it (indicated by the blue dashed curve). The ellipticity is calculated by determining the ratio between the semi-minor and semi-major axes of the ellipse. The dependence of the wavelength of the second harmonic field and the ellipticity of the emitted harmonics is presented in Figure 6.8(d).

We observe that when the peak intensity of the fundamental field is ($10^{14}\ Wcm^{-2}$), the ellipticity of the generated harmonics is significantly reduced for all the detectable harmonic orders in the TOF spectrometer. This observation indicates the presence of pronounced depolarization effects. Specifically, upon investigating harmonic orders from $10^{th}$ to the $14^{th}$ (as illustrated in Figure 6.8d), we find that the calculated ellipticity ranges from 0.65 to 0.98, same as the outcomes of our experimental study, without displaying any predictable particular trend. Notably, the $10^{th}$ and $13^{th}$ harmonics exhibit an almost circular elliptical nature. The estimated polarization degrees of individual harmonic orders exhibit similar overall characteristics and magnitudes as those derived from our experimental findings.

The disparity between the ellipticity values of the harmonics obtained from the experimental findings in Figure 6.5 and those deduced from the TDDFT calculations in Figure 6.8(d) can be attributed due to the use of idealized conditions within the theoretical framework, which do not align with the real-world experimental setup. Examples of deviations from these ideal conditions includes: i) slight variations in amplitudes and imperfect spatial alignment between the $\omega$ and $2\omega$ fields in the experimental setup, ii)

deviation from a precisely zero time delay between the $\omega$ and $2\omega$ pulses during the experiment, and iii) the influence of macroscopic effects [254] that are not included into the calculation. Importantly, our experimental methodology lacks the capability to distinguish between circularly polarized and non-polarized radiation. Consequently, minor contributions of non-polarized harmonics (potentially originating from depolarizing propagation effects [255]) cannot be excluded. Such factors are also absent in the TDDFT calculations, leading to the calculation of the maximum attainable ellipticity.

## 6.4 Conclusions and outlook

In summary, through a combination of state-of-the-art experiments, semi-classical analysis, and TDDFT simulations, we showcase an efficient generation and characterization of highly energetic and elliptic high harmonics originating from Ar atom. We also identify the underlying dynamics and the spectral-temporal characteristics of these elliptical high-order harmonics. Our study reveals that manipulating the BCCR field via precise focusing conditions can yield remarkably energetic (up to 400 $nJ$ at the source) elliptically polarized harmonic spectra, with a linear dependence of the central energy on the central wavelength of the SHG. While specific harmonic regions display significant ellipticity, with some nearing circularity (for instance, $10^{th}$ or $13^{th}$ harmonics), other detectable high harmonics exhibit comparatively lower ellipticity. Our TDDFT simulations support these experimental findings.

With appropriate tuning and enhancing the focusing conditions, we achieved notably high energy content per pulse for the highly elliptical XUV emission (400 $nJ$ at the source), a significant enhancement compared to prior results. This innovative approach, hinging on a short-pulse laser, coupled with variable SHG central wavelengths, holds promise for generating spatially diverse elliptically polarized high harmonics. Results from our TDDFT simulations supporting the experimental findings is a step forward for the application of TDDFT approach in the study of ultrafast laser driven dynamics in gases and solids.

HHG in solids presents a more intricate picture, where the phenomenon emerges from the interplay of electronic bands and the laser field. Here, the harmonics stem from the intraband and interband transitions of electrons within the solid material. While HHG in gases provides a clearer platform to study the fundamental physics of light-matter interaction, HHG in solids delves into the complex interactions between electrons and the crystalline lattice. Bridging the understanding between these two realms not only enriches our knowledge of ultrafast processes but also holds promise for novel applications in fields ranging from condensed matter physics to advanced materials and beyond. In the next chapter, I report the findings of our work on the study of HHG from a promising 2D material using TDDFT method, and propose an efficient way to enhance the harmonic yield by suitably modifying the electronic band structure by strain engineering.

# Chapter 7

# Tuning high harmonic generation from strain engineered 2D semiconductor

In chapter 6, tunable energetic highly-elliptical HHG in the XUV regime is theoretically studied and compared with the experimental findings for an atomic case (Argon). In this chapter, using a full *ab initio* approach based on DFT [93] and real-time TDDFT [256], we study the strong-field nonlinear optical properties of freestanding pristine phosphorene and strain induced band gap modified phosphorene systems. We demonstrate the pronounced sensitivity of the HHG process to the modulation of band structures in monolayer black phosphorene, achieved through the applied biaxial tensile and compressive strain.

2D materials, which are quantum confined systems [7, 257], exhibit remarkable sensitivity to external perturbations due to their atomic-scale thickness [258]. Among the plethora of 2D materials synthesized in recent years [259], monolayer black phosphorene stands out for its unique band gap, which falls between that of graphene (0 $eV$) [15], and transition-metal dichalcogenides (TMDs) (1 $eV - 2$ $eV$) [22]. Consequently, monolayer phosphorene displays efficient photo-response in the infrared (IR) range. Given its highly anisotropic properties [16], remarkable carrier mobility, substantial band gap, and exceptional mechanical resilience that can withstand considerable deformation before failure, monolayer black phosphorene is increasingly gaining prominence as a competitive candidate in the field of 2D materials, particularly for optoelectronics. Despite its inherent instability at ambient temperatures, various emerging ambient stabilization techniques for phosphorene have been introduced [166], opening new avenues to explore its potential in IR optoelectronics and high harmonic spectroscopy.

One intriguing aspect of this 2D material is the capacity to adjust the band gap through structural engineering [12, 41, 141, 260]. Extensive investigations into the impact of different types of strains (uni-axial or biaxial) applied along the two anisotropic lattice vectors on the ground state properties of phosphorene, employing density functional theory, have been conducted in previous studies [261–263]. In the following section 7.1, the experimental methods to induce biaxial tensile and compressive strains are highlighted.

## 7.1 Biaxial Strain engineering techniques

### 7.1.1 Thermal expansion

Biaxial strain can be applied through differential thermal expansion, as explained in the work of Ahn et al. [264]. This method relies on a large difference in thermal expansion coefficients between the 2D material and the substrate. When the thermal expansion coefficient of the 2D material is greater than that of the substrate and when the 2D material is strongly attached to the substrate and the system is heated or cooled, the difference in expansion generates a homogeneous tensile biaxial strain. On the other hand, when the thermal expansion coefficient of the 2D material is lower than the that of the substrate, the difference in expansion generates a compressive biaxial strain. The thermal strain will be balanced equally in two orthogonal directions if the substrate is amorphous, cubic, or has a (0001)

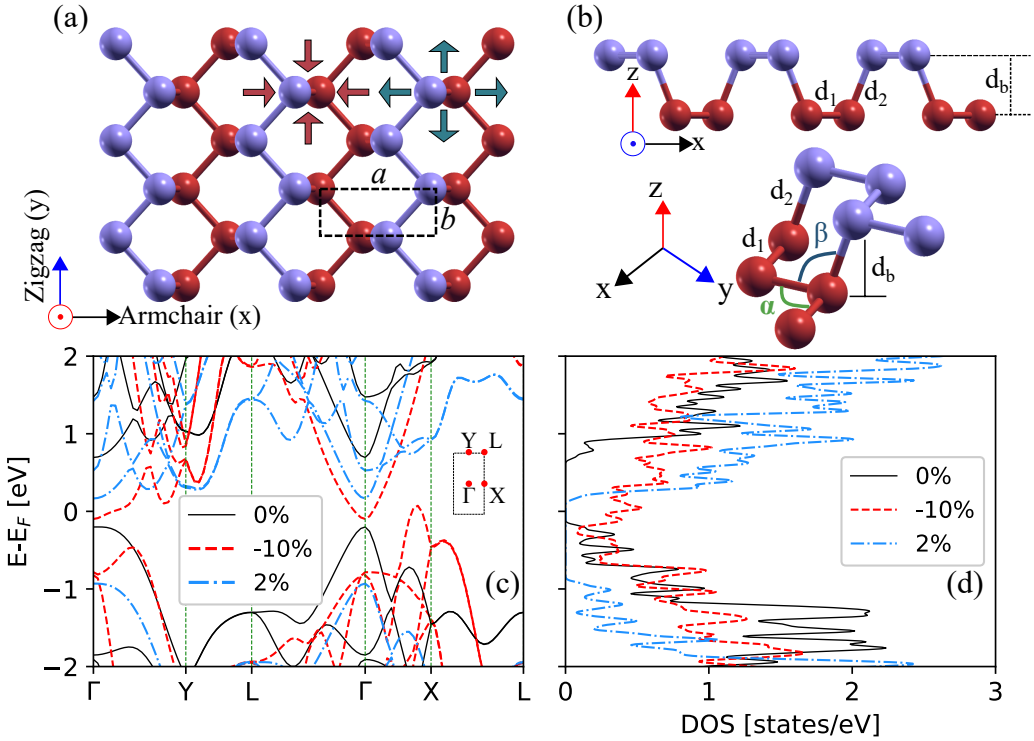


Figure 7.1: Atomic structure of monolayer black phosphorene and it's corresponding band structure and density of states (DOS): (a) top view along with it's crystallographic directions x (armchair), y (zigzag). Black colored dashed rectangular box represents the unit cell structure. Schematic of the application of biaxial compressive or '-ve' strain (red arrows) and tensile or '+ve' strain (dark green arrows) are also shown. (b) Side view with the geometrical parameters: $d_1$ and $d_2$ are the bond lengths, $d_b$ is the buckling length. $\alpha$ and $\beta$ are the bond angles. Purple and red colored spheres represent phosphorous atoms in two different planes. (c) Electronic band structure and (d) corresponding DOS of relaxed pristine (black solid curve), $-10\%$ compressive (red dashed curve), $2\%$ tensile (blue curve) strained phosphorene along high symmetry points, represented with green vertical dashed lines. Inset in (c) shows irreducible Brillouin zone (BZ) with high symmetry points of phosphorene.

surface in a hexagonal crystal or a (001) surface in a tetragonal crystal.

### 7.1.2 Piezoelectric straining

Piezoelectric materials can be used to strain 2D materials by applying an external electric field. This approach allows for both tensile and compressive strains to be applied to the 2D material [265–267]. The hybrid substrate incorporates a $[Pb(Mg_{1/3}Nb_{2/3})O_3]_{0.72} - [PbTiO_3]_{0.28}$ (PMN-PT) layer, which changes in thickness upon the application of an external electric field. When an appropriate electrical bias is applied to a 2D material deposited on PMN-PT, the substrate compresses in the horizontal direction and elongates in the vertical direction, leading to a homogeneous in-plane biaxial compressive strain on the 2D material [265]. By reversing the bias direction, a tensile strain can also be applied [266].

## 7.2 Numerical results and discussion

### 7.2.1 Geometry optimization

In this work, structural optimization and electronic structure calculations of pristine and strained phosphorene systems were carried out using DFT [93] using a plane-wave basis set and ultrasoft pseudo-potential within GGA proposed by Perdew, Burke, and Ernzerhof (PBE) for the exchange

and correlation energy [96], as implemented in quantum espresso (QE) [268] package. In order to simulate a monolayer of black phosphorous, we created a unit cell with periodic boundary conditions. To prevent interactions between system and the periodic images of slabs along the $z$-axis, we introduced a substantial vacuum of 16 Å. The wave functions were expanded in plane waves up to an energy cutoff of 60 $eV$. For Brillouin zone integration, we used the **k**-point sets generated by the $12 \times 12 \times 1$ Monkhorst-Pack [269] mesh. During the simulation, we performed atomic relaxation until the final force on each atom was less than 0.001 $eV$/Å, and electronic energy convergence of $10^{-6}$ $eV$ was achieved.

Black phosphorous, which is the most stable allotrope of phosphorous was first synthesized in 1914 by Bridgman [270]. It is a layered material in which each of the layers are stacked together by the vdW interactions. Unlike graphene, which consists of a planar layer of carbon atoms, black phosphorene is a non-planar layer of phosphorus atoms. The unit cell contains four phosphorus atoms, two lying in one plane and the remaining two in another parallel plane. This arrangement gives rise to a puckered honeycomb structure, with each phosphorus atom forming covalent bonds with three adjacent atoms, resulting in an anisotropic crystal structure, as shown in Figure 7.1(a,b). In our calculations, the optimized lattice constants of pristine phosphorene, which are $a = 4.62$ Å, and $b = 3.29$ Å align well with existing literature [163, 164] and experimental data [165]. The optimized geometrical parameters of pristine phosphorene (shown in Figure 7.1b), such as the in-plane and out-of-plane bond lengths $d_1$ and $d_2$, respectively, buckling length ($d_b$), angle among in-plane and out-of-plane atoms $\alpha$ and $\beta$, respectively are summarized in the Table 7.1.

| Strain | $a$ (Å) | $b$ (Å) | $d_1$ (Å) | $d_2$ (Å) | $d_b$ (Å) | $\alpha$ (deg) | $\beta$ (deg) | $E_g$ ($eV$) |
|---|---|---|---|---|---|---|---|---|
| 0% | 4.62 | 3.29 | 2.22 | 2.26 | 2.11 | 104.08 | 95.6 | 0.9 |
| -10% | 4.16 | 2.96 | 2.13 | 2.28 | 2.21 | 97.07 | 88.15 | - |
| 2% | 4.72 | 3.36 | 2.24 | 2.26 | 2.09 | 104.76 | 97 | 1.1 |

Table 7.1: Optimized geometrical parameters and band gap ($E_g$) values of pristine and strained phosphorene systems. Parameters such as lattice constants $a$, $b$, bond lengths $d_1$, $d_2$, buckling length $d_b$, bond angles $\alpha$, $\beta$ are depicted in Figure 7.1(b).

After geometry optimization of pristine and strained phosphorene within DFT framework, we then use octopus package [219, 220] for further time-dependent calculations, after ensuring energy and force convergence criterion are met. To investigate the laser driven temporal evolution of electron dynamics in pristine and strained phosphorene systems, we utilized semi-periodic boundary conditions. The simulation box size was set to 30 Bohr along the non-periodic direction (i.e. along $z$-axis), with absorbing regions of 3 Bohr on both sides of the system. These precautionary absorbing regions were implemented to prevent any undesirable reflection of field-accelerated electrons at the borders of the simulation box. For the absorbing regions, we employed the complex absorbing potential (CAP) method [228], setting the CAP height to $-1$ atomic units (a. u.). For the real-space sampling, a grid spacing of 0.46 Bohr was used along all three directions, and the 2D Brillouin zone is sampled using a $38 \times 46$ Monkhorst-Pack [269] **k**-points grid. To study the nonlinear response, we calculated the time evolution of the wave functions and estimated the time-dependent electronic current by propagating the Kohn-Sham equations in real time and real space within TDDFT implemented within octopus package[219, 220], within the GGA with exchange and correlations of PBE [96].

### 7.2.2 Numerical simulations within TDDFT framework

Here, we applied biaxial tensile (+ ve) and compressive (- ve) strain along armchair (AC) or $x$ and zigzag (ZZ) or $y$ directions by tuning the lattice constants $a$ and $b$ of pristine phosphorene (Figure 7.1(a)). Strain ($\varepsilon$) is defined as, $\varepsilon = (a_\varepsilon - a_0)/a_0$, where $a_0$ and $a_\varepsilon$ are the pristine and strained lattice constants, respectively. As Table 7.1 clearly illustrates, the application of strains has an impact on various geometrical parameters. Specifically, when subjected to a tensile strain of $\varepsilon = 2\%$, certain parameters such as $d_1$, $d_2$, $d_b$, $\alpha$, and $\beta$ exhibit slight changes. This strain causes an increase in the

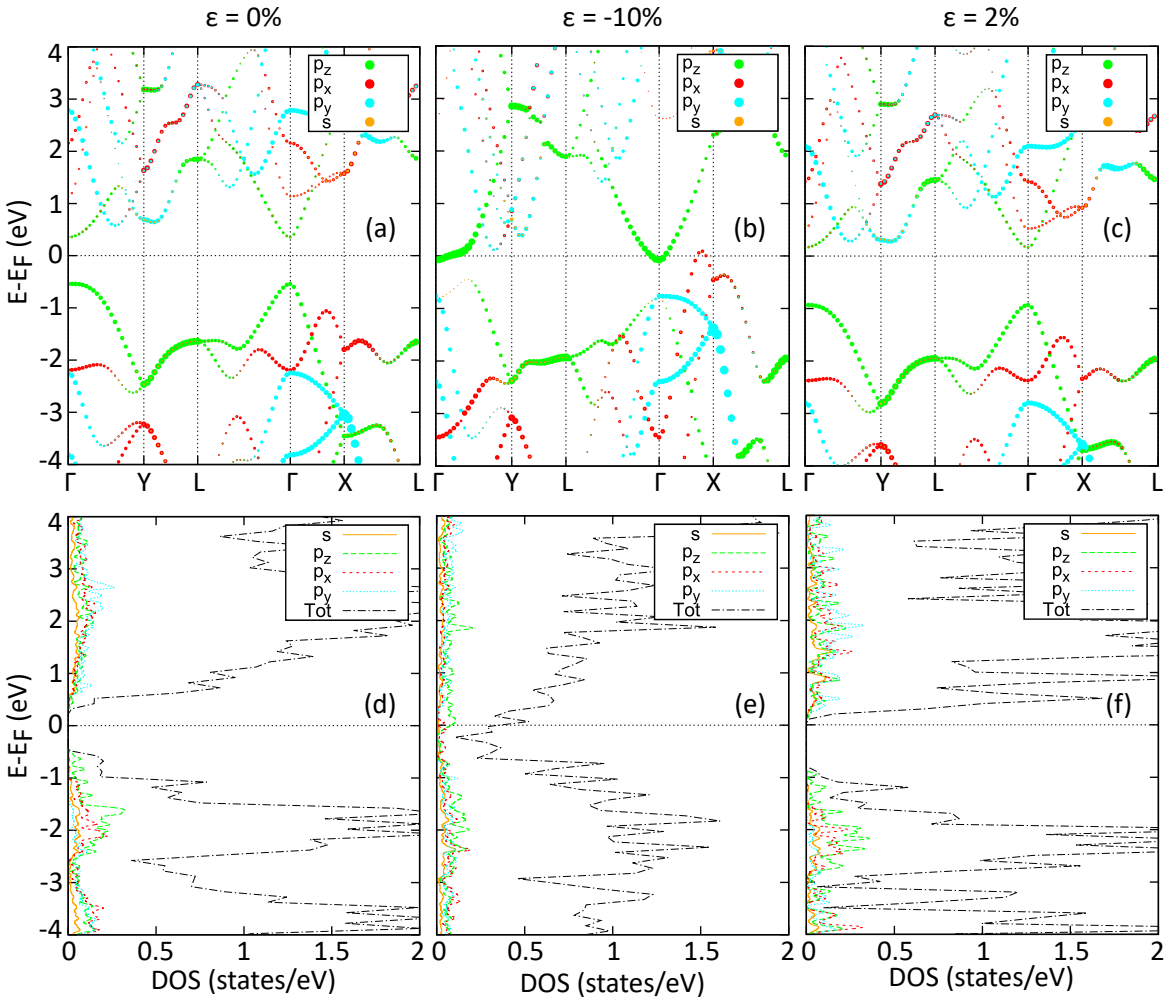


Figure 7.2: (a-c) Projected band structure and (d-f) partial density of states of 0%, -10%, and 2% strained phosphorene systems.

lattice constants $a$ and $b$ due to elongation. Conversely, a strain of $\varepsilon = -10\%$ results in a decrease in the lattice constants $a$ and $b$, leading to a significant change in the geometrical parameters. It is noteworthy that these strains are well below the damage threshold, as reported in existing literature [271]. As outlined in Table 7.1, when a $-10\%$ strain is applied in comparison to the pristine case, we observe the following changes in certain parameters: $d_2$ and $d_b$ increase by 0.8% and 4.7%, respectively, while $d_1$, $\alpha$, and $\beta$ decrease by 4%, 6.7%, and 7.7%, respectively. Clearly, compressive strain exerts a substantial influence on the phosphorene system. Consequently, the atomic structure is subsequently re-optimized, and the electronic properties of the elongated or compressed phosphorene lattice are compared to those of the pristine case.

We will now investigate the differences in the electronic band structure and emphasize the significant changes in electronic properties when subjected to biaxial strain. In the case of the pristine phosphorene, we observe a direct band gap of 0.9 $eV$ at the $\Gamma-$point, while experimental reports indicate a band gap ranging from $2.05 - 2.2$ $eV$ [272]. As illustrated in Figure 7.1(c) (depicted in black) for pristine phosphorene, the primary contributions to the valence band maximum (VBM) and conduction band minimum (CBM) near the $\Gamma-$point arise from the $p_z$ orbital, as demonstrated through the analysis of projected bands and partial densities of states (PDOS) [Figure 7.2(a,d)]. With a $\varepsilon$ of 2%, the band gap expands to 1.1 $eV$, with a slight downshift in both valence and conduction bands. The VBM and CBM still predominantly originate from the $p_z$ orbital at the $\Gamma-$point [see Figure 7.2(c,f)].

However, with a $\varepsilon$ of -10%, the compressive strain significantly reduces the in-plane interatomic P-P bond length ($d_1$) and enhances the in-plane $p_{x,y}$ orbital contributions. Consequently, the superposition

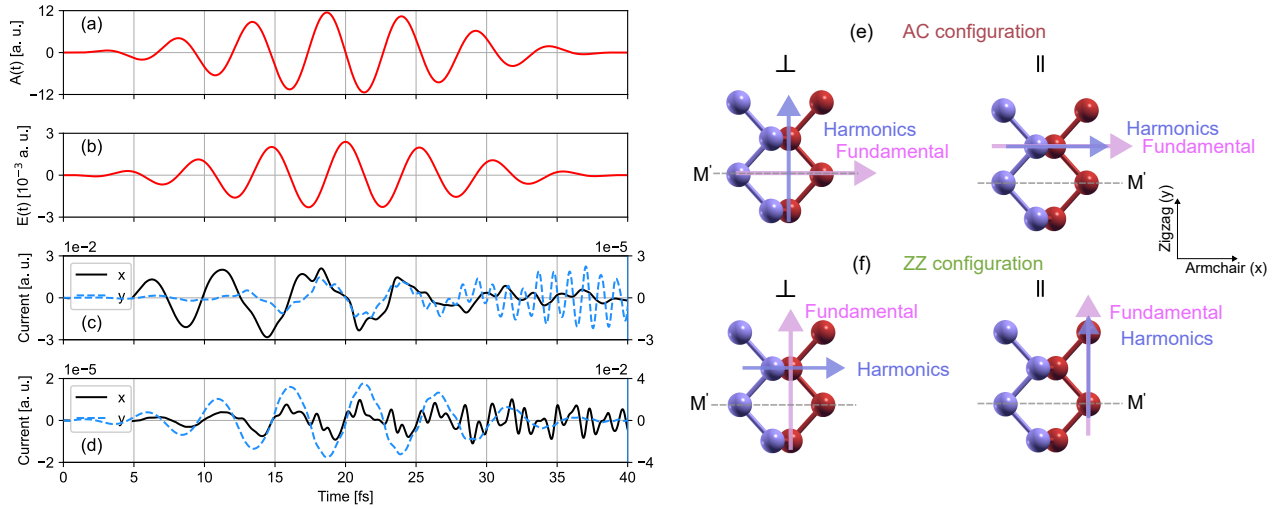


Figure 7.3: (a) The applied vector potential $\boldsymbol{A}(t)$, (b) corresponding electric field $\boldsymbol{E}(t)$ and the induced electronic currents that are parallel and perpendicular to the incident laser polarization along (c) AC and (d) ZZ for pristine phosphorene.

of atomic orbitals leads to shift in the energy of the states, leading to an indirect band gap closure as the VBM and CBM intersect along the $\Gamma \longrightarrow X$ path, as indicated by the red dashed lines in Figure 7.1(c). Projected bands and PDOS analysis reveal that, while the CBM still primarily originates from the $p_z$ orbitals [see Figure 7.2(b,e)] at the $\Gamma-$point, the in-plane orbital contributions of $p_x$ and $p_y$ become predominant in the VBM along the $\Gamma \longrightarrow X$ path and cross the Fermi level [Figure 7.2(b,e)]. As a result, a greater electronic density of states (DOS) near the VBM and CBM is observed compared to the other two cases, as depicted in Figure 7.1(d) in red. These effects lead to a transition from a semiconducting to metallic state in phosphorene induced by compressive strain. The computed band gap values for both pristine and strained phosphorene systems, as listed in Table 7.1, align well with existing literature [273].

Such strain induced local structural changes [6] and their consequent effects on electronic properties have a direct influence on the time-dependent nonlinear responses in phosphorene. To investigate this, we considered a driving laser field, which is described in the velocity gauge, i.e. in terms of a vector potential to treat purely in-plane perturbations, given as

$$\boldsymbol{A}(t) = -\frac{cE_0}{\omega_0} f(t) \cos\left(\omega_0 t + \phi\right) , \tag{7.1}$$

where the speed of light is denoted as $c$ and $\omega_0$ is the carrier frequency of the driving laser pulse. The envelope of the vector potential, denoted as $f(t)$, is defined as a sine squared function, given by $f(t) = sin^2(\pi t/2\tau)$ for $0 < t < 2\tau$, and otherwise, $f(t) = 0$. Here, $\tau$ represents the pulse duration at full width half maximum (FWHM), which is 20 $fs$ in our case. The field amplitude $E_0$ can be expressed in terms of the peak intensity of the laser ($I_0$) in atomic units as $E_0 = \sqrt{I_0/3.51 \times 10^{16}}\ Wcm^{-2}$, where $I_0 = 2 \times 10^{11}\ Wcm^{-2}$. In this study, we have used a central wavelength of $\lambda = 1600\ nm$ (corresponding to a photon energy of 0.77 $eV$), and a zero carrier envelope phase ($\phi = 0$). The corresponding electric field is defined as $\boldsymbol{E}(t) = -\partial \boldsymbol{A}(t)/(c\ \partial t)$. The applied laser waveform, i.e. the vector potential and the corresponding electric field is shown in Figure 7.3(a) and (b), respectively. The selection of pulse parameters is tailored to represent the Mid-IR laser regime available at the ELI ALPS facility [215, 224], and is well-suited for investigating HHG in solid-state materials. Here, we assumed dipole approximation and the contributions from magnetic component of the electromagnetic field are neglected. Any other relativistic terms, such as spin orbit coupling are not considered in this study. The pristine and strained phosphorene samples are excited by the laser polarized either along AC or ZZ direction, where $\overline{\Gamma X}$ and $\overline{\Gamma Y}$ depicted in the BZ in Figure 7.1(c) correspond to the AC and ZZ directions, respectively. From now on, $\overline{\Gamma X}$ and $\overline{\Gamma Y}$ will be used as a substitute for AC and ZZ,

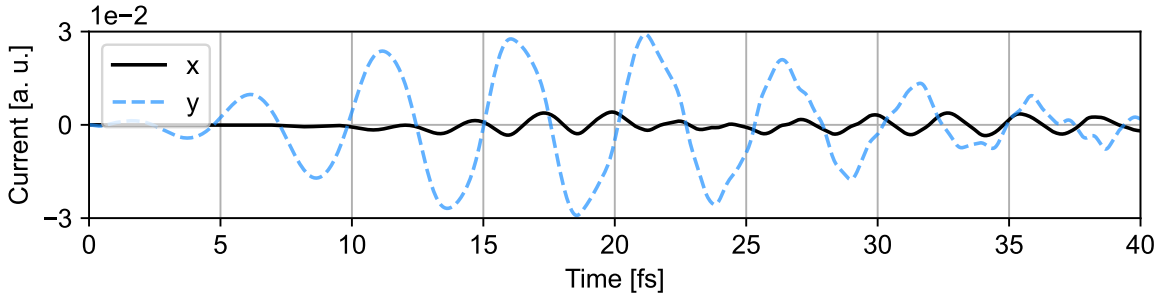


Figure 7.4: The perpendicular ($x$) and parallel ($y$) induced electronic currents w.r.t. the incident laser polarization along ZZ direction in $-10\%$ strained phosphorene.

respectively.

To calculate the HHG spectrum, we obtain total electronic current in the system, $\boldsymbol{J}(t) = \partial/\partial t \int_\Omega d^3\boldsymbol{r}\boldsymbol{j}(\boldsymbol{r},t)$, which is obtained by integrating the microscopic electronic current density, $\boldsymbol{j}(\boldsymbol{r},t)$, over the unit cell, where $\Omega$ is the unit cell volume [274]. The microscopic electron current can be written as

$$\partial/\partial t \int_\Omega d^3\boldsymbol{r}\boldsymbol{j}(\boldsymbol{r},t) = -\int_\Omega d^3\boldsymbol{r} n(\boldsymbol{r},t)\nabla v(\boldsymbol{r},t) \ , \tag{7.2}$$

where $n(\mathbf{r},t)$ is the time-dependent electron density of the material driven by laser field. External potential $v(\boldsymbol{r},t)$ corresponds to both the electron-nuclei potential $v_0(\boldsymbol{r})$ and the applied laser field. The HHG spectrum $[I(\omega)]$ is obtained by applying a discrete Fourier-transform ($\mathcal{FT}$) to $\boldsymbol{J}(t)$, which is given as

$$I(\omega) = \left|\mathcal{FT}\big(\boldsymbol{J}(t)\big)\right|^2 \ . \tag{7.3}$$

Time-dependent dipole currents can reveal the nonlinear anisotropic response of a system. In the context of crystal symmetry, we examine the polarization components of the harmonic radiation that is parallel and perpendicular to the linearly polarized fundamental field. For a specific laser polarization direction (either along $\overline{\Gamma X}$ or $\overline{\Gamma Y}$), significant electronic currents and corresponding harmonic radiation are generated in both directions, i.e. parallel and perpendicular to the laser polarization, owing to the inherent anisotropy of phosphorene crystal, as explained in the subsequent section. The resulting electronic currents for pristine phosphorene can be seen in Figure 7.3(c) and Figure 7.3(d). In Figure 7.3(c), the electronic current parallel to the electric field (in the $x$ direction) exhibits a significantly higher magnitude than the contribution in the perpendicular direction (along $y$). Similarly, in Figure 7.3(d), when the laser polarization is along the ZZ direction, the parallel current component (in the $y$ direction) surpasses the perpendicular current component (in the $x$ direction) by a substantial margin. Examining Figure 7.3(c,d), it becomes evident that the parallel electronic current component is nearly three orders of magnitude greater than the perpendicular component. Schematics in Figure 7.3(e,f) illustrate the laser polarization's orientation with respect to the crystal structure.

In the AC configuration, the laser is polarized along the AC direction, and similarly, for the ZZ configuration it is along ZZ direction. Each of these scenarios contains two outcomes: the harmonic radiation's parallel ($\parallel$) and perpendicular ($\perp$) polarization components, depending on the laser's polarization direction. When the laser is polarized along the ZZ direction and $\varepsilon = -10\%$, there is a noticeable change in the crystal structure, as indicated in Table 7.1, which consequently affects the electronic properties. In this case, the two current components are observed to have comparable amplitudes (refer to Figure 7.4).

The total electronic current signal in phosphorene exhibits distinct characteristics in both the directions parallel and perpendicular to the laser polarization. This behavior is a consequence of the material's inherent anisotropy, i.e. the inversion and mirror reflection symmetries are only along ZZ direction which is particularly evident in Figure 7.3(e,f). As a consequence of this inversion symmetry,

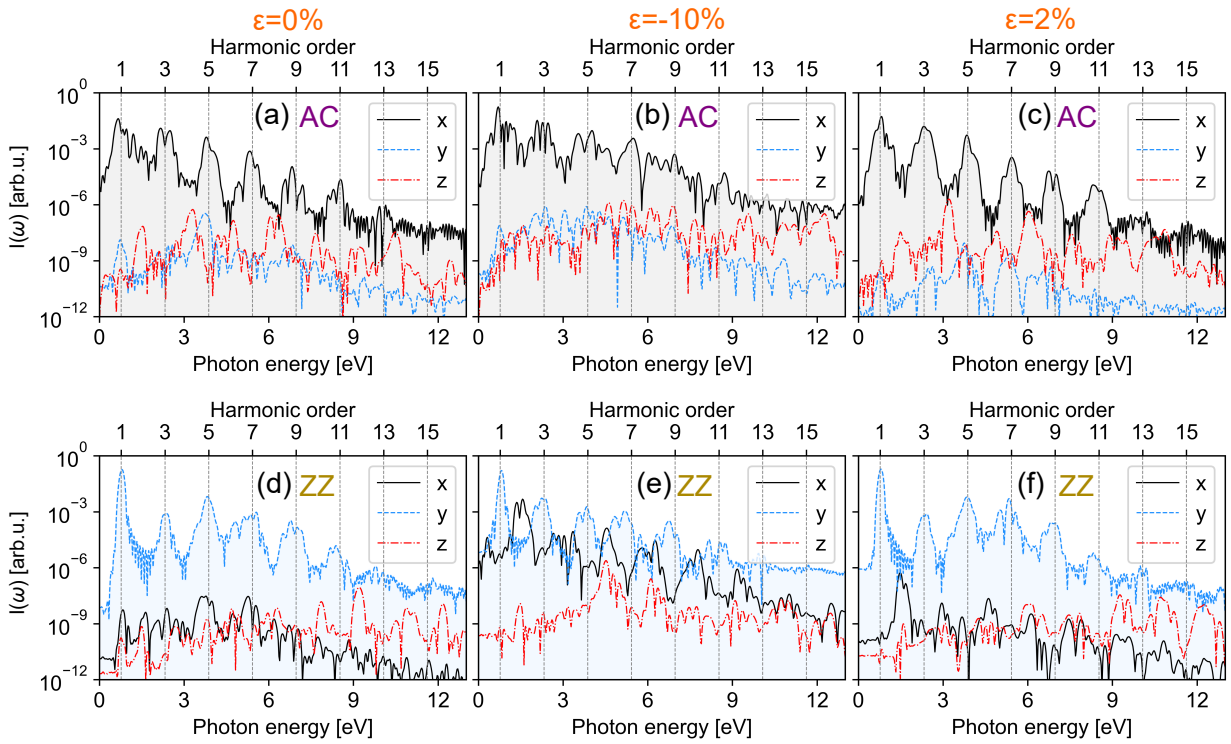


Figure 7.5: High harmonic spectrum of pristine, −10%, 2% strained phosphorene driven by the laser polarized along AC (a,b,c) and the same when the laser is polarized along ZZ (d,e,f).

only odd harmonics are generated when the laser polarization aligns with it [231, 275]. These symmetry conditions and the symmetry-imposed selection rules leads to the generation of electronic currents along both the $x$ and $y$ directions when the incident laser polarization is parallel to the AC direction. However, it is important to note that the perpendicular component of the current is significantly weaker, approximately three orders of magnitude smaller, compared to the parallel current component along the $x$ direction (see Figure 7.3c).

We examine the HHG spectra of pristine phosphorene (Figure 7.5(a,d)), phosphorene with a -10% strain (Figure 7.5(b,e)), and phosphorene with a 2% strain (Figure 7.5(c,f)). These systems are driven by a laser polarized along the AC direction (Figure 7.5(a-c)) and the ZZ direction (Figure 7.5(d-f)). Our investigation involves resolving the harmonics in both parallel and perpendicular configurations, which correspond to the harmonics depicted in Figure 7.6(a,b). Distinctive harmonic radiation patterns are observed for the AC and ZZ cases in all panels, indicating a clear anisotropic HHG response. In all cases, except for the −10% strained ZZ configuration (Figure 7.4), the parallel component of the harmonics significantly surpasses the perpendicular component.

The HHG spectrum for pristine and strained systems displays distinct characteristics when the laser is polarized along AC and ZZ directions, as shown in Figure 7.6(a,b). These differences stem from the inherent anisotropy of the phosphorene crystal. In the case of parallel harmonic components, i.e., along the $x$ direction for the AC configuration (represented by the black lines in Figure 7.5(a-c)), and along the $y$ direction for the ZZ configuration (indicated by the blue lines in Figure 7.5(d-f)), we observe that, for both pristine and strained structures, the fundamental peak emerges at a frequency of $\omega$ (0.77 $eV$). Subsequently, we notice the appearance of odd integer multiples of the driving laser frequency, as evident in Figure 7.6(a,b). This pattern suggests that the inversion symmetry of the system remains preserved, even when subjected to biaxial compressive and tensile strains. In each case, the intensity of the HHG peaks gradually decreases, but remains distinctly visible up to the 13th harmonic. In both the AC and ZZ scenarios, the application of a compressive strain ($\varepsilon = -10\%$) results in a notable enhancement of the harmonic intensity compared to the pristine condition.

Furthermore, in the AC case with $\varepsilon = -10\%$, the HHG peaks exhibit increased strength and

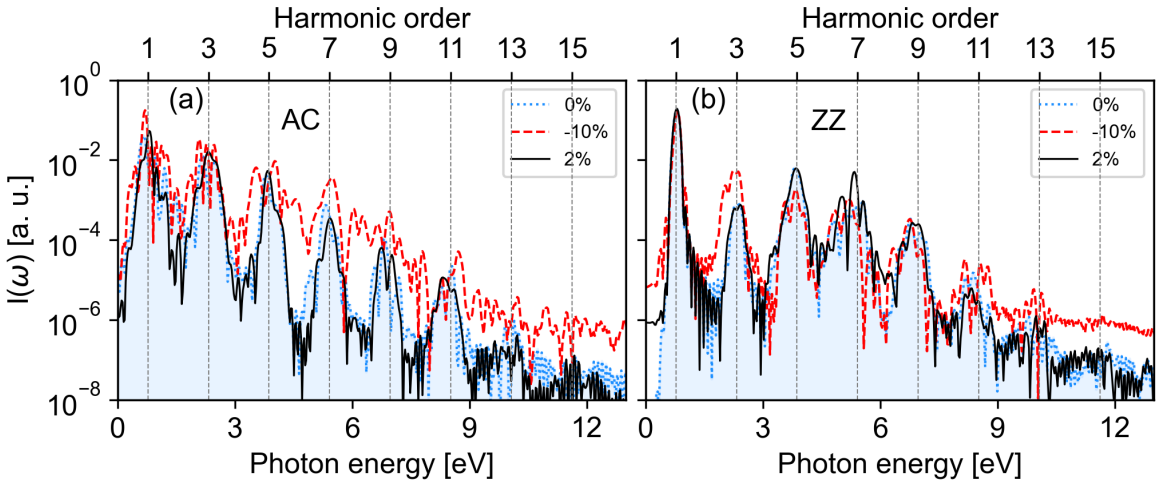


Figure 7.6: HHG spectra of strained phosphorene systems driven by a laser polarized along AC (a) and ZZ (b).

broader spectral width, as evident in Figure 7.6(a). Conversely, in the ZZ case, there is no consistent enhancement observed. Remarkably, in the $-10\%$ strain scenario, due to the finite electronic population at the Fermi level (as demonstrated along the $\overline{\Gamma X}$ and $\overline{\Gamma Y}$ directions in Figure 7.1(c,d)), some states remain available for field-induced excitations. This explains why even when the field is oriented along the ZZ direction, a significant current and HHG signal can be obtained in the perpendicular direction. As illustrated in Figure 7.2(b), along the $\overline{\Gamma X}$ direction (i.e., the AC orientation), electronic states in proximity to the Fermi level ($E_f$) significantly contribute to field-induced transitions, resulting in a noticeable enhancement of strain-induced high harmonic generation (HHG). For instance, in the AC configuration with a -10% strain, the high harmonic spectrum, starting from H5 as depicted in Figure 7.6(a), clearly exhibits a nearly tenfold increase in harmonic intensity. Particularly in the -10% strain case, substantial alterations in the crystal structure (refer to Table 7.1) lead to a noteworthy modification of the effective electron-nuclei potential, as described in Equation 7.2. This results in distinct new features in the electronic band dispersion, ultimately impacting the microscopic electronic current and, consequently, the HHG signal.

The proximity of states in the conduction band plays a pivotal role, as it makes it easier for free carriers to be excited by the laser field from the valence band to these lower states. This, in turn, contributes to enhanced HHG[276]. Additionally, due to the applied strain, both the conduction and valence bands shift downward. This downward shift is more pronounced in the case of $\varepsilon = -10\%$ when compared to $\varepsilon = 2\%$. However, in the $\varepsilon = -10\%$ scenario, the availability of electronic states in the downward-shifted valence band along $\overline{\Gamma Y}$ is relatively limited in comparison to the $\varepsilon = 2\%$ case. Consequently, the harmonic yield for the ZZ configuration is expected to be higher in the case of $\varepsilon = 2\%$ compared to the other cases. To provide a clearer understanding of these results, we present the computed number of electrons excited from the valence band to the conduction band during the laser pulse in Figure 7.7, corresponding to Figure 7.6.

It is a well-established fact that in a semiconductor, when an electron recombines with an existing hole in the valence band, it results in the emission of a photon with energy that is equal to or beyond the band gap energy. Consequently, it becomes apparent that harmonics below the band gap are not generated through interband contributions but rather exclusively originate from intraband current. On the other hand, above the band gap, harmonics can arise from both interband and intraband currents. In the case of pristine phosphorene, with a band gap of 0.9 $eV$ and an induced photon energy of 0.77 $eV$, recombination of electrons and holes in different bands becomes possible. In this scenario, both interband and intraband processes jointly contribute to the generation of harmonics above the band gap. To assess the extent of interband transitions in our studied systems, we computed the temporal evolution of the total number of excited electrons from valence band to the conduction

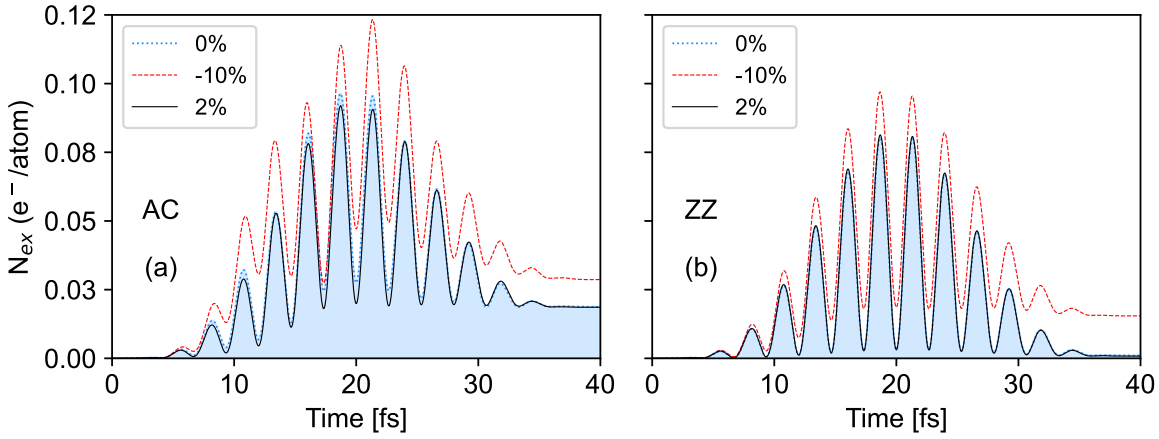


Figure 7.7: Total number of excited electrons per atom to the conduction bands during the laser pulse which is polarized along AC (a) and along ZZ (b).

band is by projecting the time-evolved wave functions ($|\psi_{i,\mathbf{k}}(t)\rangle$) on to the basis of ground state wave functions ($|\psi^{GS}_{j,\mathbf{k}}\rangle$), and given as [277]

$$N_{ex}(t) = N_e - \frac{1}{N_{\mathbf{k}}} \sum_{i,j}^{occ} \sum_{\mathbf{k}}^{BZ} |\langle \psi_{i,\mathbf{k}}(t) | \psi^{GS}_{j,\mathbf{k}} \rangle|^2 \ , \tag{7.4}$$

where $N_e$, $N_{\mathbf{k}}$, $\psi_{i,\mathbf{k}}$, and $\psi_{j,\mathbf{k}}$ are the total number of electrons in the system, the total number of $\mathbf{k}$-points used to sample the Brillouin zone (BZ), kohn-sham state at the $i$-th band at the $\mathbf{k}$-point $\mathbf{k}$, and the ground state kohn-sham state at the $j$-th band at the $\mathbf{k}$-point $\mathbf{k}$, respectively. The sum over the band indices $i$, and $j$ run over all occupied states. Hence, $N_{ex}(t)$ illustrates the interband current. The temporal evolution of $N_{ex}$ exhibits a sub-cycle periodicity matching the induced laser field, as observed in Figure 7.7(a) for the AC case and Figure 7.7(b) for the ZZ configuration. Figure 7.7 clearly illustrates that the number of excited electrons is higher when the laser is polarized along the AC direction. Consequently, this can lead to a greater higher harmonic yield along the AC direction, consistent with the observations in Figure 7.6a,b. It is noteworthy that the anisotropic electronic band dispersion results in flatter bands along $\overline{\Gamma Y}$ (ZZ) in comparison to $\overline{\Gamma X}$ (AC direction). This suggests a lower effective mass and higher carrier mobility along AC direction compared to the ZZ direction. As a result, the interband current is significantly more pronounced in the AC direction, as demonstrated by the respective $N_{ex}$ values (compare both panels in Figure 7.7). This means that a notable difference in charge excitation along different directions is expected.

For the $-10\%$ strain in the AC case, the laser-induced excited electrons reach a peak value of 0.12 $e^-$/atom at approximately 21 fs and then oscillate around 0.035 $e^-$/atom [Figure 7.7(a)]. Values of $e^-$/atom obtained for both 0% and 2% strain cases are similar, with the 0% case slightly higher than the 2% case. In the ZZ configuration, the maximum number of excited electrons reaches 0.10 $e^-$/atom for the -10% strain case and then decreases to 0.02 by the end of the laser pulse. However, for the 0% and 2% strain cases, the excited electrons (slightly higher in the 2% case compared to the 0% case) return to almost zero after each half cycle in the ZZ configuration, while in the AC configuration for all cases, a fraction of excited electrons remains effectively in the conduction bands at the end of the laser pulse ($\sim 40\ fs$).

Additionally, to validate our analysis and to calculate laser-driven subcycle electron dynamics, the momentum-resolved excited electrons distribution $N_{ex}(\mathbf{k};t)$ is calculated in the following way [277]

$$N_{ex}(\mathbf{k};t) = \frac{1}{N_{\mathbf{k}}} \left( N_e - \sum_{i,j}^{occ} |\langle \psi_{i,\mathbf{k}}(t) | \psi^{GS}_{j,\mathbf{k}} \rangle|^2 \right) . \tag{7.5}$$

We examine the momentum-resolved sub-cycle dynamics of excited electrons at three specific time

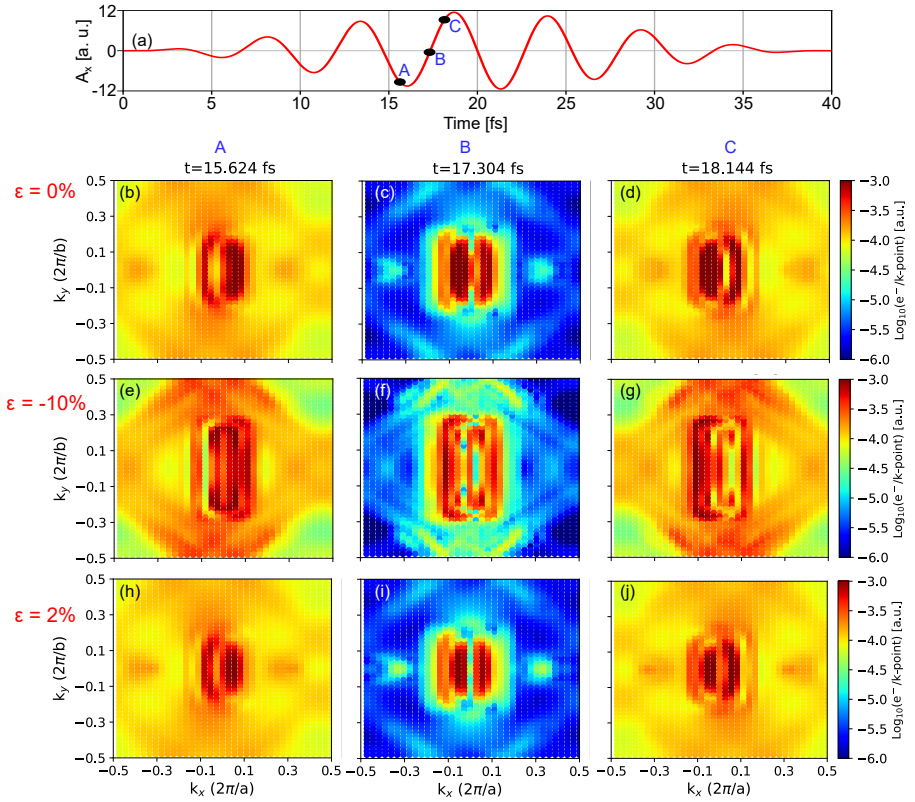


Figure 7.8: Time-dependent electron dynamics in strain-free and strained phosphorene. (a) Vector potential of the driving laser pulse polarized along AC (x-direction). Snap shots of the sub-cycle dynamics of momentum-resolved excited electrons near the peak and minimum of the vector potential (marked as A, B, C in (a)) for pristine phosphorene (b,c,d), -10% (e,f,g), and 2% (h,i,j) strained phosphorene. The oscillation features of the excited electrons in the BZ in panels (a-c) for pristine, (d-f) for -10, and (g-i) for +2 show evidence of intraband process significantly contributes to HHG.

points, labeled as A, B, and C, in Figure 7.8(a), for three different scenarios: pristine or 0% strain (top), -10% strain (middle), and 2% strain (bottom) phosphorene systems [Figure 7.8(b-j)]. Notably, it's intriguing to observe that the concentration of excited electron density is centered around the Γ-point for all cases. In the cases of 0% and 2% strained phosphorene, both the VBM and CBM are located at the Γ−point. Consequently, the probability of electron transition is maximized at Γ. However, in the -10% strained system, the VBM and CBM overlap in the vicinity of the Γ−point, as seen in the $\overline{\Gamma X}$ band dispersion in Figure 7.1(c). This results in a higher concentration of excited electron density in and around the Γ−point for this specific case. At the time instance denoted by B in Figure 7.8(a), which corresponds to the period of lowest excitation, electrons disperse across broader regions in the Brillouin Zone (BZ) under compressive strain, as shown in Figure 7.8(f). Consequently, the number of excited electrons at each momentum point $(\mathbf{k}_x, \mathbf{k}_y)$ increases. This observation confirms that intraband and interband processes collectively enhance the harmonic yield for the -10% strain case. At the time instances marked as A and C in Figure 7.8(a), a substantial portion of the BZ exhibits a higher density of excited electrons. It is evident that the excited electrons arrange themselves from the left to right boundaries in the BZ and vice versa. These sub-cycle oscillations of excited electrons, driven by the laser field, coupled with the movement of excited electrons into larger regions of the BZ, highlight the collective contribution of intraband and interband processes to HHG and the resulting enhanced harmonic yield, in comparison to pristine and strained phosphorene cases, as will be discussed further.

In order to investigate the characteristics of the HHG spectrum, we computed the peak harmonic intensity ($I_n^{max}$) for specific harmonics ($n$) as a function of the peak laser intensity ($I_L$). Figure 7.9 represents the scaling behavior of harmonic peaks for $n$ values of 5, 7, 9, and 11 as a function of $I_L$, which ranges between $0.1 - 0.4\ TWcm^{-2}$. In all the configurations depicted in Figure 7.9, when

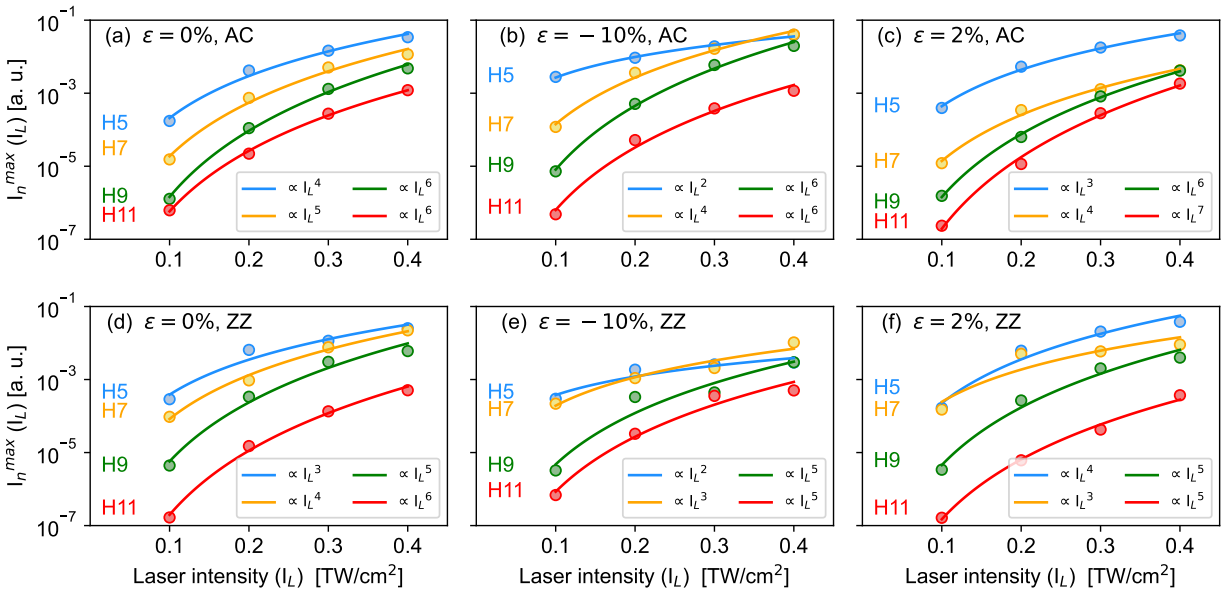


Figure 7.9: Calculated peak harmonic intensity as a function of peak laser intensity $I_L$ for 0% strain (a,d), -10% (b,e), and 2% strain (c,f) for representative harmonics n = 5 (blue circles), 7 (orange circles), 9 (green circles), and 11 (red circles) obtained for laser polarized along AC (a-c) and along ZZ (d-f). Solid lines are obtained by fitting data to power law, yielding exponents showing the non-perturbative scaling of the harmonic process. The resulting exponents are mentioned in the legends of individual panel.

considering harmonics with $n = 5$ and $n = 7$, the fitting of the data to a power-law model $I^p$ yielded values for $p$ that fell within the range of 2 to 5. Additionally, for higher-order harmonics, such as H9 and H11, the values of $p$ ranged between 5 and 7. This power-law fitting of the data indicates the non-perturbative nature of the high-order harmonics, as reflected in the scaling of individual harmonic peaks with $I_L$. It's important to note that in the perturbative regime, the radiation is confined to frequencies that are only a few times higher than the frequency of the driving field. Moreover, in the perturbative regime, the $n^{th}$ harmonic would scale linearly with $I_L^n$, where $I_L$ represents the peak intensity of the laser, and the harmonic yield would decrease exponentially [231, 278].

For each harmonic peak, we compare the relative change in harmonic intensity and total harmonic yield for the AC and ZZ cases, as depicted in Figure 7.10. The relative change in harmonic intensity is defined as $I_n^\varepsilon / I_n^{\varepsilon=0}$, where $I_n^\varepsilon$ and $I_n^{\varepsilon=0}$ represent the $n^{th}$ order harmonic peak intensity with and without strain, respectively. In line with the HHG signals (as seen in Figure 7.6), when the laser is polarized along the AC direction (Figure 7.10(a)), a compressive strain of -10% enhances HHG intensities by 100% to 400% for all harmonic orders. Notably, H7 is the most significantly affected, followed by H9, H13, and H11 [as depicted in Figure 7.10(a)]. Conversely, under tensile strain, the relative harmonic intensity decreased for all harmonics except the 5th order, as shown in Figure 7.10(a). When the laser polarization is along ZZ direction, each harmonic responds differently to the applied strain (Figure 7.9(b)), reflecting the absence of a systematic variation in HHG intensity. The variations in HHG peak intensities and harmonic yield between the AC and ZZ cases are consistent with the anisotropic band dispersion of phosphorene and its distinct characteristics.

The harmonic yield, integrated from the 2nd to the 15th order, as a function of applied strain (Figure 7.10(c)), shows an almost threefold enhancement in the total yield when a -10% strain is applied in the AC case. This highlights the potential to tailor the HHG yield using a combination of appropriate strain and the direction of the laser's electric field.

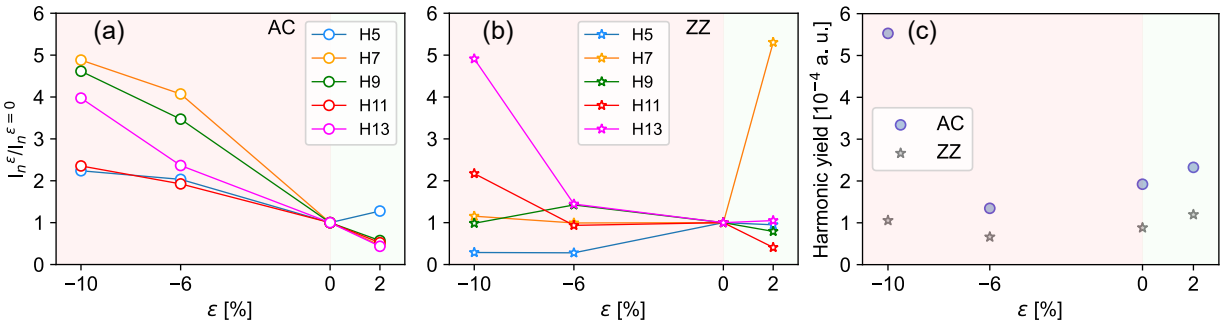


Figure 7.10: The relative change in harmonic intensity as a function of applied strain for representative harmonics for AC case (a) and ZZ case (b). (c) Harmonic yield (integrated from 2nd order to 15th order) as a function of applied strain for both AC and ZZ cases.

## 7.3 Conclusions and outlook

To conclude, using advanced TDDFT simulations, we have explored the impact of ultrashort laser-induced non-linear response and the yield of non-perturbative HHG up to the 13th order from a monolayer phosphorene. We specifically investigated the influence of biaxial compressive and tensile strain on HHG from 2D phosphorene. Our findings reveal that altering the crystal structure of phosphorene through biaxial strain offers an effective means to customize its electronic structure and HHG in terms of harmonic intensity and spectral width.

Due to the inherent in-plane anisotropy of phosphorene, the HHG yield is higher in the AC configuration compared to the ZZ configuration. It's worth noting that the laser pulse parameters used in our study fall within the Mid-IR regime, making them suitable for probing HHG in solid-state band-gap materials. Such parameters are available in advanced laser facilities like the ELI ALPS facility. Our analysis demonstrates that applying a -10% compressive strain can enhance the harmonic yield by a factor of three. This unique response can be attributed to the engineering of the electronic band structure through external compressive strain, resulting in a significant increase in the number of excited electrons, ultimately leading to enhanced HHG. Our results and insights pave the way for tuning the HHG process through band engineering via the application of strain, offering opportunities for the experimental exploration of strain-induced strong-field nonlinear responses in this promising 2D nanostructure.

Given the growing interest in developing compact, table-top sources of coherent extreme ultraviolet radiation, which have broad applications across various scientific and technological domains, and considering the expanding spectrum of potential uses for 2D materials, our study highlights the potential of phosphorene and similar 2D nanostructures. With their easily adjustable band structures through strain engineering, these 2D materials hold significant promise for the design and optimization of innovative devices in attoscience and the creation of stable, table-top HHG sources.

# Chapter 8

# Summary and Outlook

Temperature dependent response of a material is crucial in assessing its stability, functionality and potential applications. With increase in the operating temperature in laboratory environment, the electronic properties and lattice vibrations in any material will modify. For instance, at 300 $K$ or beyond, material surface separates the heated electrons within the material from otherwise non-conducting space. Such gradient promotes emission of electrons across the surface boundary and results in thermionic emission, and strongly depends on the work function, potential barrier, surface structure, electronic properties of the material. When transitioning from a bulk phase to a gas-like state, surface structure changes and the confinement effects [12, 279] can have significant implications on the behavior and properties of the material. Confinement effects arise when a material's dimensionality is reduced from bulk to two-dimensional or one-dimensional or zero-dimensional, altering its physical, chemical, and thermodynamic characteristics. These effects are particularly pronounced when a material is confined to dimensions on the order of nanometers or smaller, leading to phenomena that differ from those observed in bulk systems. In nanoscale confinement, the quantization of energy levels becomes significant. This can lead to discrete energy states that affect electronic properties, influencing phenomena such as optical absorption and emission. Dimensionality of the material impacts the electronic structure of the ground state and consequently their time-dependent evolution under any external field.

As is well known, motion of electrons and ions are an ultrafast phenomenon ($\sim 10^{-15}$ $s$ for electrons and $\sim 10^{-12}$ $s$ for ions). Understanding and tuning ultrafast electronic processes in materials offer opportunities to unlock new scientific insights and technological breakthroughs with far-reaching impacts. These ultrafast processes can be captured with laser assisted advanced metrology techniques and show strong dependence on the intensity of the external perturbation. By probing different electron dynamics with respect to the different dimensionality will provide contrasting perspective. Any real-time experiment will have its own complexities. Numerical simulations and suitable theoretical models helps in understanding the intricate details and provides support to the experiments. In this dissertation, using simulations, I have investigated the electron dynamics in atoms, metals and two-dimensional nanostructures under the influence of an external perturbation, such as DC and AC field. The doctoral thesis begins with a brief introduction to the significance of the ultrafast electron dynamics in materials along with the factors that influence the dynamics and the characteristics of various electron emission processes. It is followed by methodology chapter, in which each of the theoretical approaches that were used in this dissertation are explained in detail. Then the key findings of my research are explained in detail in the rest of the chapters. In the following, I summarize the important findings in my doctoral thesis:

1. Electron emitters play a significant role in laser experiments, particularly in the field of ultrafast and high-intensity laser physics. In such experiments, intense electric fields results in laser-induced electron emission phenomena. These emitted electrons can be utilized in various applications, such as material characterization, particle acceleration, radiation sources, to name a few. Coatings play a crucial role in improving the efficiency of the electron emitters. To enhance the electron emission efficiency from metallic surfaces, I have investigated the role of different physical factors,

such as different metallic coatings, thickness and work function of the coating material, and the operating temperature on electron emission. To estimate and analyze the electron emission from a coated metal target, we established a formalism based on Fowler's treatment of electron emission, along with Fermi-Dirac statistics of the electron energy distribution, a three-dimensional parabolic energy dispersion for the target metal and thickness dependent energy dispersion for the coating metal. The surface coating induces a high potential field resulting in enhanced electron emission flux. This formulation holds good for any metal/semiconductor combination. We particularly examined the role of thickness of the coating material which is found to play an important role on the emission properties. From our numerical simulations, I have determined that at higher temperatures (exceeding 1500 $K$), the electron emission flux becomes noticeably prominent for the thinner coating, whereas a thicker coating demonstrates enhanced emission efficiency at lower temperatures. Our results suggest that by tuning the thickness of the coating layer, it is possible to tune the electron emission operating at a desired operating temperature. The understanding of electron emission phenomena, and suitable estimation of current from the coated surfaces, as presented in this analysis, hold potential practical significance for the creation of effective and adaptable field emitters and thin film devices. These results were published in [T1] and discussed in Chapter 3. However, confinement effects arises due to change in the dimensionality of the material. This demands a quantum description of low-dimensional material's characteristics, such as two-dimensional semiconductors, whose electron emission properties are probed in the next chapter.

2. As mentioned earlier, two-dimensional materials offer several advantages compared to their bulk counterparts, such as tunable band gap, high carrier mobility, enhanced optical properties and mechanical strength, to name a few. To investigate the thermionic flux from a promising two-dimensional nanostructure, we choose a semiconductor that was recently synthesized [280], for which we have combined an *ab-initio* quantum simulation tool and semiclassical description of emission. Based on density functional theory calculations, we determine the electronic bands and the band edges in phosphorene, followed by establishing a suitable dispersion relation using the tight-binding model. By using Fowler's approach for electron emission and incorporating the Fermi-Dirac statistics for electrons, the expression to calculate thermionic emission and photo-thermionic flux are derived. With the numerical simulations, I have demonstrated that black phosphorene, a two-dimensional allotrope of phosphorous, has potential to be an efficient photo-thermionic electron emitter. In addition, I have prescribed how the electron emission flux can be further enhanced by photon irradiation and validated with the experimental findings. Our simulation results suggest that due to the intrinsic anisotropic energy dispersion of phosphorene, it's emission flux is higher when compared to well established graphene. This makes two-dimensional phosphorene a viable contender for photo-thermionic emission and energy conversion technologies relying on thermionic emission. The present methodology offers a fundamental understanding of the photo-thermionic features of two-dimensional phosphorene, exhibiting features that matches well with the experimental findings. These results are reported in our published article [T2] and discussed in Chapter 4 of this thesis. As mentioned earlier, the electron dynamics show strong dependence on the external perturbation. Often in experiments, a pulsed laser field is used to study the ultrafast electron dynamics in metals or semiconductors. The semi-analytical approach to describe material properties and external perturbation, i.e. monochromatic field (discussed in Chapter 3 and 4) must be appropriately modified to investigate the ultrafast laser driven electron dynamics in metals and semiconductors, which is further investigated in next chapters.

3. Efficient three-dimensional description of ultrafast laser pulse and its interaction with the material can lead to exact estimation of ultrafast thermal evolution processes. Femtosecond laser driven ultrafast thermionic emission results in electron bunches that have a wide range of applications, such as high-gain harmonic generation free electron laser, laser accelerators, among many others. I have investigated the thermal evolution in gold coated glass substrate irradiated by an ultrashort

laser pulse. Gold being a noble [200] transition metal has wide range of applications ranging from biomedicine [202], twistronics [203], flexible integrated electronics [201]. Additionally, gold coated mirrors are present everywhere in the ultrafast laser optics. Ultrafast electron emission in metal nanofilms are important in studies that apply to all these applications. To determine the spatio-temporal evolution of electron and lattice temperatures, I have implemented a three-dimensional two-temperature model, which takes in to account the three-dimensional laser pulse profile focused obliquely on to the sample. The associated thermionic emission properties are determined using modified Richardson-Dushman equation with space-charge effects and are solved self-consistently in our approach. Furthermore, I have determined the role of laser polarization and its angle of incidence on the spatio-temporal evolution of electron and lattice temperatures, and subsequently on the thermionic electron emission processes. I showed the role of temperature dependent reflectivity on the laser energy absorption. The maximum surface electron temperature monotonically rises with laser incidence angle for P polarized laser, while an opposite trend is noticed in S polarized case. A strong dependence of thermionic emission duration on the laser incidence angle and contrasting polarization dependent behaviour is observed. Additionally, I showed the strong dependence of thermionic current duration on the intrinsic electron-lattice thermalization duration of the sample. The conclusions drawn from our analysis and insights help in understanding and tuning ultrafast thermionic emission and associated atomic-level mechanisms in metals and also in semiconductors that behave like metals upon interaction with ultrafast lasers. This understanding could lead to enhancement of both thermionic emission current and its duration, thereby contributing to the development of designing efficient ultrafast thermionic emitters. These results are reported in our published article [T3] and discussed in Chapter 5.

4. Laser-matter interactions not only affect the electron emission but also for each laser cycle, sub-cycle electron dynamics changes during the laser-matter interaction period. These sub-cycle dynamics needs to be captured for better understanding of material's response, which could lead to high harmonic generation, which involves the non-linear interaction of the laser field with an atom, or a molecule, or a solid-state medium, that results in the harmonics emission that are integer multiples of the driving laser frequency. High harmonic generation has emerged as a promising technique because of its ability to generate high-frequency light in the extreme ultraviolet and soft X-ray regions of the electromagnetic spectrum. While the initial high harmonic generation models were often based on the single-active electron approximation or time-dependent Schrödinger equation approach, the inclusion of multielectron effects in the study of high harmonics generation in atoms is of paramount importance as it enables a more accurate and comprehensive understanding of the complex physical processes underlying this phenomenon. Hence, in Chapter 6 we use time-dependent density functional theory approach, which takes into account the multielectrons effects to investigate the ultrafast electron dynamics in Ar atom irradiated by a linear polarized laser and then a bi-circular counter rotating laser fields. I have validated our numerical approach with experimental findings [233], by obtaining a significant feature of the high harmonic generation spectrum of Ar atom, such as the presence of Cooper minimum at $\sim 48\ eV$.

   Bi-chromatic circular counter rotating laser fields create an environment of extremely strong and complex electromagnetic interactions with matter. This makes them invaluable for exploring fundamental strong-field physics phenomena, such as high harmonic generation, non-linear optics, etc. The counter-rotating nature of these laser fields allows enhanced control over the electron trajectories and dynamics. By adjusting the relative phases and intensities of the two beams, we can steer and manipulate electronic processes with high precision. Through a combination of state-of-the-art experiments, semi-classical analysis, and time-dependent density functional theory simulations we have showcased an efficient way to generate and characterize highly energetic and elliptically polarized higher-order harmonics from argon [T4]. Using time-dependent density functional theory approach, I have shown that by appropriately tuning the central wavelength

of the second harmonic, the central frequency of the high harmonic radiation is continuously tuned. Our numerical simulations support the experimental findings, which reveal that the highly elliptical HHG radiation from argon can be tuned for an energy range of $\Delta E \approx 150\ meV$ in the spectral range of $\approx 20\ eV$. We anticipate that the ability to adjust energetic and highly elliptical high harmonic generation spectra could eliminate the limitations imposed by the need for few-cycle driving pulses in the generation of isolated circular attosecond pulses. These results are reported in the article that was just accepted in the *Physical Review A* journal [T4] and discussed in Chapter 6.

5. Advancements in both fabrication techniques and the underlying fundamental knowledge of two-dimensional materials have paved the way for their effective utilization in a wide array of device applications ranging from nonlinear optics, optoelectronics, photodetection, and many more. As mentioned before, phosphorene is a relatively new, promising member in the family of two-dimensional materials has attracted immense attention in the research community due to its distinctive features such as an adjustable bandgap, high carrier mobility, and noteworthy intrinsic in-plane anisotropy, which we studied in Chapter 4. Now, using these inherent structural and electronic traits, we investigated the ultrafast electron dynamics and high harmonic generation from laser driven phosphorene surface. We explored the impact of external strain on the electronic band structure and associated nonlinear effects in phosphorene. Our analysis reveals that strong field-driven processes within such systems can be optimized and controlled through biaxial tensile (+ ve) and compressive strain (- ve) engineering, effectively modifying the electronic structure. The application of strain, ranging from $-10\%$ to $2\%$, yields intriguing outcomes. Specifically, a $-10\%$ strain induces bandgap closure, whereas a $2\%$ strain increases the gap by $22\%$, relative to the pristine phosphorene value of $0.9\ eV$. These changes are found to significantly influence the high harmonic generation output.

   The closing of the bandgap due to strain, especially within the range of $2\%$ to $-10\%$, contributes to an increased electronic density of states near the $\Gamma-$point, which results in enhanced electronic excitation, as evident in the results shown in Chapter 7. The intrinsic in-plane anisotropy of phosphorene has proved to be a significant factor, with harmonic yield displaying higher intensity when the laser polarization aligns along the armchair direction compared to the zigzag direction across all strain conditions. Electronic band structure engineering through external application of compressive strain had resulted in an increased number of excited electrons, which eventually leads to an enhanced high harmonic generation. Particularly striking is the nearly three times more enhancement in harmonic yield achieved under $-10\%$ strain along the armchair direction. These results are uploaded in *arXiv* [T5] and will be soon submitted for publication in peer reviewed journal. This comprehensive study widens the horizons of phosphorene research, uncovering uncharted territory and highlighting its potential for applications in extreme-ultraviolet and attosecond nanophotonics, as well as an efficient table-top high harmonic generation sources.

In light of the key findings and the thesis points discussed above, the main significance of this doctoral thesis is to investigate and understand the effects, both in presence and absence of pulsed laser fields, on the electronic structure properties, electron emission, and the subsequent ultrafast electron dynamics in materials of different dimensions. Our results based on state-of-the-art simulation approaches and theoretical modeling are compared/understood with respect to recent experiments, particularly focusing on their utility in applied science and engineering. The thorough simulations-based investigation carried out in this thesis proposes ways to enhance the photo and laser-induced thermionic emission properties in metal and semiconductor nanostructures, which has wide range of applications, such as thermionic emission based high temperature solar converters, thermionic energy converters, high-brightness ultrafast electron imaging tools, to name a few. Using appropriate optimized computational tools and numerical methods presented in this dissertation, we investigated the photo-induced thermionic emission from metals and two-dimensional semiconductor nanomaterials and explored the potential of phosphorene and alike materials for applications as an stable table-top high harmonic generation sources. Often the results presented in my dissertation, for example the

emission current estimation from our analytical model in the case of phosphorene is successfully tested against experiments, as explained in Chapter 4. Additionally, high harmonic generation from argon under the influence of linear and bi-chromatic counter rotating laser fields, as explained in Chapter 6 were benchmarked with experimental findings, complimenting and explaining the experimental traits. With numerical simulations presented in this dissertation, we aim to mimic the real-time laser-matter experiments, bypassing experimental challenges that will provide a complementary tool to experiments to understand ultrafast electron dynamics in metals, atoms and two-dimensional materials for future applications. It is worth stressing that the theoretical approaches that were used in my dissertation are not limited to the materials reported here, but can also be extended to other similar metals/semiconductors. Therefore, we strongly believe that our results will encourage new experimental ventures to investigate ultrafast electron dynamics and enhance the subsequent electron emission properties in two-dimensional materials.

# Chapter 9

# Magyar nyelvű összefoglaló

Egy anyag stabilitásának, funkcionalitásának és lehetséges alkalmazásainak felméréséhez elengedhetetlen az anyag fizikai hatásokra való hőmérsékletfüggő válaszának ismerete. Laboratóriumi körülmények között az anyag elektronikus tulajdonságai és rácsrezgései a hőmérséklet növelésével megváltoznak. Az anyag hőmérsékletének 300 $K$ felé emelésével például az anyag felületén elkülönülnek az elektronok az anyagon belül az egyébként nem vezető térben. Az így kialakuló gradiens elősegíti a felülethatáron lezajló elektronemissziót, így termionikus emisszióhoz vezetve. Ez erős függést mutat az anyag munkafüggvényétől, felületi potenciáljától, felületi szerkezetétől, és az anyag elektromos tulajdonságaitól. A szilárd fázisból gázszerű állapotba való átmenet során a felületi szerkezet változásai, valamint a kvantumbezárásos jelenségek jelentős kihatással bírhatnak az anyag viselkedésére és tulajdonságaira. Kvantumbezárásos jelenségek akkor lépnek fel, amikor az anyag dimenzionalitása háromdimenziósról kettő, egy, vagy nulla dimenziósra csökken, melynek hatására a fizikai, kémiai és termodinamikai tulajdonságai is megváltoznak. Ezek a hatások kimondottan erősen jelentkeznek akkor, ha az anyag kiterjedése nanométeres vagy az alatti méreteket ölt, olyan jelenségekhez vezetve, melyek különböznek a háromdimenziós anyagokban tapasztalhatóktól. Ez a kvantumbezárás diszkrét energiaállapotokhoz vezethet, befolyásolva az olyan jelenségeket, mint az optikai abszorpció és emisszió. Az anyag dimenzionalitása hatással van az alapállapot elektromos szerkezetére, és így annak egy külső tér hatása alatt lezajló időbeli fejlődésére is.

Mint az közismert, az elektronok és ionok mozgása ultragyors időskálán zajlik (kb. $\sim 10^{-15}$ $s$ és $sim10^{-12}$ $s$ karakterisztikus idővel). Ezeknek az anyagokban lezajló ultragyors elektromos folyamatoknak a megértésével lehetőséget kapunk új tudományos ismeretek megszerzéséhez, és sokrétű hatású technológiai áttöréseket érhetünk el. Az ilyen ultragyors folyamatok, melyek megfigyelése lézerrel támogatott korszerű mérési technikák segítségével kivitelezhető, erős függést mutatnak a külső hatás intenzitásától. A különböző elektrondinamikai folyamatok vizsgálata különböző anyagi dimenzionalitások esetében kontrasztos perspektívát nyújt. Minden különböző valós idejű kísérletnek sajátságos komplexitása van; azonban numerikus szimulációk és megfelelő elméleti modellek segítséget nyújtanak az összetett részletek megértésében, és segítséget nyújtanak a kísérletekhez. Ebben a doktori disszertációban szimulációk segítségével az elektronok dinamikáját vizsgáltam atomokban, fémekben és kétdimenziós nanoszerkezetekben külső perturbáció, például állandó és időfüggő elektromos tér hatására. A disszertáció egy rövid bevezetéssel kezdődik, mely az anyagokban lezajló ultragyors elektrondinamikai jelenségek jelentőségét, valamint az elektronemisszió dinamikáját és karakterisztikáját befolyásoló tényezőket mutatja be. Ezt a módszertani fejezet követi, melyben részletesen ismertetjük a disszertációban alkalmazott elméleti módszerek mindegyikét. Ezután kutatásom legfontosabb eredményeit fejtem ki a soron következő fejezetekben. Az alábbiakban doktori értekezésem főbb eredményeit foglalom össze:

1. A lézerekkel folytatott kísérletekben, különösen az ultragyors és a nagyintenzitású lézerfizika területén, jelentős szerepet játszanak az elektronemissziós források. Az ilyen kísérletekben az intenzív elektromos terek lézerindukált elektronemissziós jelenségekhez vezetnek. A kibocsátott elektronok ezután többféle módon alkalmazhatók, például anyagelemzésre, részecskegyorsításra,

vagy sugárforrásként. A bevonatok döntő szerepet játszanak az elektronemisszió hatékonyságának javításában. A fémfelületek elektronemissziós hatékonyságának növelése érdekében megvizsgáltam az elektronemisszió függését olyan különböző fizikai tényezőktől, mint a fémbevonatok anyagi minősége, a bevonóanyag vastagsága és munkafüggvénye, valamint a működési hőmérséklet. A bevonatos fém céltárgyakból származó elektronemisszió becslésére és elemzésére kidolgoztunk egy, az elektronemisszió Fowler-féle leírásán alapuló formalizmust, az elektronok energiaeloszlásának Fermi-Dirac-statisztikájának, a fém céltárgy háromdimenziós parabolikus energiadiszperziójának, és a bevonófém vastagságfüggő energiadiszperziójának figyelembe vételével. A felületi bevonat erős potenciálteret alakít ki, ami fokozott elektronemissziós fluxust eredményez. A kidolgozott formalizmus bármely fém/félvezető kombinációra érvényes. Munkánkban kiemelten vizsgáltuk a bevonóanyag vastagságának szerepét, amelyről bebizonyosodott, hogy fontos szerepet játszik az emissziós tulajdonságokban. Numerikus szimulációinkból megállapítotuk, hogy magasabb hőmérsékleten (1500 $K$ felett) a vékonyabb bevonat esetében az elektronemissziós fluxus jelentősen megnő, míg a vastagabb bevonat alacsonyabb hőmérsékleten mutat fokozott emissziós hatékonyságot. Eredményeink arra utalnak, hogy a bevonatréteg vastagságának hangolásával a kívánt üzemi hőmérsékleten működő elektronemisszió hangolható. Az elektronemissziós jelenségek megértése, valamint a bevonatolt felületekről származó elektronáram megfelelő becslése, ahogyan azt ebben az elemzésben bemutatjuk, potenciális gyakorlati jelentőséggel bír nagy hatékonyságú, adaptálható téremissziós források és vékonyréteg-eszközök létrehozásában. Ezeket az eredményeket, melyek publikálásra kerültek [T1], az 3. fejezetben tárgyaljuk. A kvantumbezárásos jelenségek azonban az anyag dimenzionalitásának megváltozásából származnak. Ezek megkövetelik az olyan alacsony dimenziójú anyagok tulajdonságainak kvantumos leírását, mint a kétdimenziós félvezetők. Az ilyen anyagok elektronemissziós tulajdonságait a következő fejezetben tárgyaljuk.

2. Ahogy korábban említettük, a kétdimenziós anyagok számos előnnyel rendelkeznek háromdimenziós társaikhoz képest. Ilyen előny többek között a tiltott sáv szélességének hangolhatósága, a magas töltéshordozó-mobilitás, a kedvezőbb optikai tulajdonságok, és a magasabb mechanikai szilárdság. Hogy egy ígéretes kétdimenziós nanoszerkezetből származó termionikus áramlást vizsgáljunk, egy, a közelmúltban szintetizált félvezetőt választottunk [280], amelynek leírásához kombináltunk egy *ab-initio* kvantumszimulációs módszert az emisszió félklasszikus leírásával. Sűrűségfunkcionál-elméleti számítások segítségével meghatároztuk az elektronsávokat és a sávszéleket a foszforénben, majd egy megfelelő diszperziós összefüggést állítottunk fel a szoros kötésű modell segítségével. Fowler módszerét alkalmazva az elektronemisszióra, valamint az elektronokra vonatkozó Fermi-Dirac statisztika figyelembe vételével levezettünk egy képletet a termionikus emisszió és a foto-termionikus fluxus meghatározására. Numerikus szimulációk segítségével megmutattam, hogy a fekete foszforén, a foszfor kétdimenziós allotrópja, potencionálisan hatékony foto-termionikus elektronemissziós forrás lehet. Emellett megmutattam, hogy az elektronemissziós fluxus tovább növelhető fotonbesugárzással, mely eredményt kísérleti eredmények igazolnak. Szimulációs eredményeink azt mutatják, hogy a foszforén eredendő anizotropikus energiájának köszönhetően emissziós fluxusa magasabb a már jól ismert grafénénál. Ez az eredmény a kétdimenziós foszforént esélyes versenyzővé teszi a foto-termionikus emisszió területén, és az ezt alkalmazó energiakonverziós technológiákban. Jelen módszertan alapvető megértéssel ruház fel bennünket a kétdimenziós foszforén foto-termionikus tulajdonságait illetően, kísérleti eredményeknek megfelelő jellemzőket mutatva. Ezen eredményeink, melyek publikálásra kerültek [T2], a 4. fejezetben kerülnek bemutatásra. Azonban, amint korábban említettem, az elektrondinamikát jelentősen befolyásolják a külső perturbációk. A kísérletek során gyakran lézerimpulzusokat alkalmaznak a fémes vagy félvezető anyagokban lezajló ultragyors elektrondinamika tanulmányozására. A 3. és 4. fejezetben bemutatott, az anyagi tulajdonságok és a külső perturbáció (monokromatikus tér) hatását leíró félanalitikus modellünket módosítanunk kell úgy, hogy az megfelelően leírja az ultragyors lézer által vezérelt elektrondinamikát fémekben és félvezetőkben. Ezt a soron következő fejezetekben tárgyaljuk.

3. Az ultragyors háromdimenziós lézerimpulzusok, valamint anyaggal való kölcsönhatásuk hatékony háromdimenziós leírása lehetővé teszi az ultragyors hőmérsékletváltozás pontos becslését. A femtoszekundumos ultragyors termionikus emisszió által olyan elektroncsomagok keletkeznek, melyek a magas hatásfokú szabadelektron-lézerektől a lézergyorsítókig számos területen alkalmazhatók. Munkámban vizsgáltam a hőhatás időbeli fejlődését ultrarövid lézerimpulzussal megvilágított aranybevonattal ellátott üveg szubsztráton. Az arany, mint nemes [200] átmenetifém, számos alkalmazással rendelkezik a biomedicinától [202], a twistronikán [203] át a hajlékony integrált elektronikáig [201], és az aranybevonattal ellátott tükrök az ultragyors lézeroptika mindennapos elemét képezik. A fém nanofilmekben lezajló ultrarövid elektronemisszió vizsgálatával olyan eredményekre juthatunk, melyek mindezen alkalmazási területek számára fontosak. Az elektron- és a rácshőmérséklet tér- és időbeli fejlődésének meghatározásához megalkottam egy háromdimenziós modellt, amely figyelembe veszi a mintára ferdén fókuszált háromdimenziós lézerimpulzus intenzitásprofilját. A kapcsolódó termionikus emissziós tulajdonságokat a Richardson-Dushman-egyenlet módosított változatának segítségével határozzuk meg a tér-töltés hatások figyelembe vételével, annak önkonzisztens módon való megoldásával. Meghatároztam továbbá a lézer polarizációjának és beesési szögének szerepét az elektron- és rácshőmérséklet tér-időbeli alakulásában, valamint a termionikus emissziós folyamatokban. Kimutattam a hőmérsékletfüggő reflexió szerepét a lézerenergia elnyelődésében. P-polarizált lézer esetén a maximális felületi elektronhőmérséklet monoton módon emelkedik a lézer beesési szögével, míg S-polarizált esetben ellentétes tendencia figyelhető meg. A termionikus emisszió időtartamát illetően erős függést figyelhetünk meg a a lézer beesési szögétől, valamint ellentétes módon a polarizációtól. Emellett kimutattam a termionikus áram időtartamának erős függését a minta eredendő elektron-rács termalizációs időtartamától is. Az elemzésünkből levont következtetések és meglátások segítenek a fémekben való ultragyors termionemisszió és a kapcsolódó atomi szintű mechanizmusok megértésében és finomhangolásában, valamint a fémekhez hasonlóan viselkedő félvezetőkben is az ultragyors lézerrel való kölcsönhatás során. Ez a tudás termionemissziós áram erősségének és időtartamának növeléséhez vezethet, elősegítve ezzel a hatékony ultragyors termionemissziós emitterek tervezését. Ezekről az eredményekről a [T3] publikált cikkünkben számoltunk be, és az 5 fejezetben tárgyaljuk.

4. A lézer-anyag kölcsönhatások nemcsak az elektronemissziót befolyásolják. Minden egyes lézerciklus esetében az elektronok ciklus alatti dinamikája is megváltozik a lézer-anyag kölcsönhatás időtartama alatt. Az anyagi válasz pontosabb megértése érdekében meg kell ismernünk ezt a ciklus alatti dinamikát is, ami a magasharmonikus-keltéshez vezethet. Ez a folyamat a lézertér atommal, molekulával vagy periodikus közeggel való nemlineáris kölcsönhatásából ered, és a lézer frekvenciájának egész számú többszörösével rezgő hullámok, felharmonikusok kibocsátását eredményezi. A magasharmonikus-generálás ígéretes technika, mivel képes nagyfrekvenciájú fény keltésére az elektromágneses spektrum extrém ultraibolya és lágy röntgen tartományaiban. Míg az első magasharmonikus-generálást leíró modellek legtöbbször az egy aktív elektron közelítésen vagy az időfüggő Schrödinger-egyenlet megoldásán alapultak, az atomokban történő magasharmonikus-generálás során fellépő többelektronos hatások leírása kiemelkedő jelentőségű, mivel lehetővé teszi a jelenség hátterében álló összetett fizikai folyamatok pontosabb és átfogóbb megértését. Ezért a 6. fejezetben a többelektronos hatásokat figyelembe vevő időfüggő sűrűségfunkcionál-elméleti megközelítést alkalmazzunk, hogy megvizsgáljuk az ultragyors elektrondinamikát lineárisan polarizált lézerrel, majd kétkörös ellenforgó lézermezőkkel besugárzott Ar atomban. Numerikus megközelítésünket kísérleti eredményekkel validáltam [233], az Ar atom magasharmonikus spektrumának egy fontos jellemzőjének, a Cooper-minimumnak reprodukálásával $\sim 48\ eV$-nál.

   A kétszínű ellenforgó cirkulárisan polarizált lézertek olyan környezetet hoznak létre, melyben rendkívül erős és összetett kölcsönhatások játszódnak le az anyaggal. Ez felbecsülhetetlenné teszi őket az alapvető erős térbeli jelenségek, például a magasharmonikus-generáció, a nemlineáris optika, és hasonlóak vizsgálatához. E lézermezők ellenforgó jellege lehetővé teszi az elektronok pályájának és dinamikájának fokozott irányítását. A két mező relatív fázisának és intenzitásának beállításával nagy pontossággal irányíthatjuk és manipulálhatjuk az elektron-kölcsönhatásokat. A legko-

rszerűbb kísérletek, a félklasszikus analízis és az időfüggő sűrűségfunkcionál-elméleti szimulációk kombinációjával bemutattunk egy hatékony módját a nagyenergiájú és elliptikusan polarizált magasharmonikus sugárzás előállításának és jellemzésének argonból [T4]. Időfüggő sűrűségfunkcionál-elmélet segítségével megmutattam, hogy a másodharmonikus központi hullámhosszának megfelelő hangolásával a magas harmonikus sugárzás központi frekvenciája folytonosan hangolható. Numerikus szimulációink alátámasztják a kísérleti eredményeket, amelyek szerint az argonból származó erősen elliptikus HHG sugárzás $\Delta E \approx 150\ meV$ energiatartományban hangolható $\approx 20\ eV$ spektrális tartományban. Arra számítunk, hogy az intenzív és erősen elliptikus magasharmonikus spektrum hangolásának képessége kiküszöbölheti azokat a korlátokat, amelyeket az izolált cirkulárisan polarizált attoszekundumos impulzusok előállítása során a néhány ciklusos meghajtó impulzusok szükségessége jelent. Ezekről az eredményekről egy, a *Physical Review A* folyóiratban nemrég publikálásra elfogadott cikkünkben számolunk be [T4], és a 6. fejezetben tárgyaljuk.

5. A kétdimenziós anyagokkal kapcsolatos alapvető ismeretek, és a kapcsolódó előállítási eljárások terén elért előrelépések megnyitották az utat a kétdimenziós anyagok hatékony felhasználása előtt az alkalmazások széles skáláján, a nemlineáris optikától kezdve az optoelektronikán át a fotodetektálásig. Mint már említettük, a foszforén a kétdimenziós anyagok családjának egy viszonylag új, ígéretes tagja, amely jelentős figyelmet kapott a kutatóközösségben olyan különleges tulajdonságai miatt, mint az állítható sávhézag, a magas töltéshordozó mozgékonyság, és a figyelemre méltó síkbeli anizotrópia, amelyet a 4. fejezetben tanulmányoztunk. Most ezeket az eredendő szerkezeti és elektronikai tulajdonságokat felhasználva vizsgáljuk az ultragyors elektron dinamikát és a magasharmonikus-keltést a lézerrel megvilágított foszforénfelületén. Megvizsgáltuk a külső mechanikai feszültség hatását az elektron-sávszerkezetre és a kapcsolódó nemlineáris hatásokra a foszforénben. Elemzésünk azt mutatja, hogy az ilyen anyagokon belüli erős tér által indukált folyamatok optimalizálhatók és szabályozhatók biaxiális húzó- (+ve) és nyomófeszültség (-ve) alkalmazásával, mely által az elektronszerkezet megfelelően módosítható. A $-10\%$-tól 2%-ig terjedő mechanikai feszültség alkalmazása érdekes eredményeket hoz. A $-10\%$-os feszültség a sávhézag bezáródását idézi elő, míg a 2%-os feszültség a sávhézagot 22%-kal növeli az érintetlen foszforén $0,9\ eV$-os értékéhez képest. Ezek a változások jelentősen befolyásolják a magasharmonikus-keltés hatékonyságát.

   A sávhézag feszültség hatására bekövetkező záródása, különösen a 2% és $-10\%$ közötti tartományban, hozzájárul a Γ-pont közelében lévő elektronállapot-sűrűség növekedéséhez, ami fokozott elektronikus gerjesztést eredményez, mint az a 7. fejezetben bemutatott eredményekből is kitűnik. A foszforén saját síkbeli anizotrópiája jelentős tényezőnek bizonyult, ugyanis a harmonikus hozam nagyobb intenzitást mutat, amikor a lézer polarizációja a karosszék-geometria irányában áll, mint amikor a cikk-cakk geometria irányában, minden vizsgált mechanikai feszültség alkalmazása mellett. Az elekton-sávszerkezet külső mechanikai feszültség alkalmazásával való módosítása a gerjesztett elektronok számának növekedését eredményezte, ami végül fokozott magasharmonikus-keltési hatékonysághoz vezet. Különösen szembetűnő a keltési hatásfok közel háromszoros növekedése a a karosszék-geometria irányában kifejtett $-10\%$-os mechanikai feszültség esetében. Ezen eredmények feltöltésre kerültek az arXiv repozitórumba [T5], és hamarosan publikációra kerülnek referált folyóiratban. Ez az átfogó tanulmány szélesíti a foszforén kutatásának horizontját, felfedezve eddig feltérképezetlen területeket, és rávilágít annak potenciális alkalmazásaira az extrém-ultraibolya és attoszekundumos nanofotonikában, valamint hatékony asztali nagyharmonikus-keltő forrásként.

A fentiekben tárgyalt legfontosabb eredmények és tézisek fényében a doktori értekezésem fő jelentősége az elektronszerkezeti tulajdonságokra, az elektronemisszióra és az azt követő ultragyors elektrondinamikára gyakorolt hatások vizsgálata és megértése különböző méretű anyagokban, mind lézerimpulzusok terének hatása alatt, mind anélkül. A legkorszerűbb szimulációs megközelítéseken és elméleti modellezésen alapuló eredményeinket összehasonlítjuk és értelmezzük a legfrissebb kísérleti eredményekkel, különös tekintettel azok felhasználhatóságára az alkalmazott tudományban és az

anyagmérnöki területeken. Az értekezésben bemutatott átfogó, szimuláción alapuló kutatás javaslatokat tesz a fém- és félvezető nanoszerkezetek foto- és lézerindukált termionikus emissziós tulajdonságainak javítására, amelyeknek olyan széleskörű alkalmazási lehetőségei vannak, mint - csupán néhányat említve - a termionikus emisszión alapuló magas hőmérsékletű napelemek, termionikus energiaátalakítók, vagy nagy fényerejű ultragyors elektron képalkotó eszközök. A disszertációban bemutatott megfelelő optimalizált számítási eszközök és numerikus módszerek segítségével megvizsgáltuk a fémek és kétdimenziós félvezető nanoanyagok fotoindukált termionikus emisszióját, és feltártuk a foszforén és hasonló anyagok alkalmazási lehetőségeit stabil asztali magasharmonikus forrásként. A disszertációmban bemutatott eredményeket számos esetben alátámasztottuk kísérleti eredményekkel, például az analitikus modellünkből származó emissziós áram becslését foszforén esetében, ahogyan azt a 4. fejezetben kifejtettük. Ezen túlmenően, ahogyan azt a 6. fejezetben kifejtettem, az argonból lineárisan polarizált, valamint kétszínű ellenforgó cirkulárisan polarizált lézertek hatására történő magasharmonikus-keltést is összehasonlítotuk kísérleti eredményekkel, kiegészítve és megmagyarázva a kísérletileg megfigyelt jelenségeket. A disszertációban bemutatott numerikus szimulációkkal célunk a valós idejű lézer-anyag kísérleteket utánozni, így megkerülve a kísérleti kihívásokat. A szimulációk így a kísérleteket kiegészítő eszközt alkothatnak a fémek, atomok és kétdimenziós anyagok ultragyors elektrondinamikájának megértéséhez a jövőbeli alkalmazásokhoz. Hangsúlyozzuk, hogy a disszertációmban alkalmazott elméleti megközelítések nem korlátozódnak az itt bemutatott anyagokra, hanem más hasonló fémekre/félvezetőkre is kiterjeszthetők. Ebből kifolyólag meggyőződésünk, hogy eredményeink új kísérleti törekvéseket ösztönöznek az ultrarövid elektrondinamika vizsgálatára és a kétdimenziós anyagok későbbi elektronemissziós tulajdonságainak javítására.

# Acknowledgements

Quite often, scientific work is rarely accomplished by an individual. The research presented in my dissertation was no exception. I firmly believe that the completion of my thesis on time would not have been possible without the invaluable support and encouragement of several talented individuals. I extend my heartfelt gratitude to all of them, which I would like to express as follows.

First and foremost, I express my sincere gratitude to my supervisor, Dr. Mousumi Upadhyay Kahaly, for not only giving me the opportunity to undertake this research but also for her guidance throughout the thesis. Her constant support and valuable insights have been instrumental to overcome various obstacles encountered during the course of my research. Her optimistic approach towards addressing challenges and her confidence in my abilities have greatly motivated me to excel in all the collaborative projects we embarked upon. Furthermore, I extend my gratitude to Dr. Subhendu Kahaly, my co-supervisor, for his invaluable insights and constructive feedback, instrumental in guiding me towards optimal pathways to achieve the ultimate objective. His determination to perfection has been a strong source of motivation and helped me to learn numerous valuable insights in my research career.

I would also like to extend my gratitude to Dr. Sanjay Kumar Mishra, Prof. Sándor Varró, Dr. Péter Dombi, and Dr. Péter Földi for their support during my thesis. I thank Judit Zelina for promptly proofreading my thesis and providing valuable suggestions. Additionally, I wish to acknowledge my former team member, Dr. Kalyani Chordiya and my colleagues, Dr. Lénárd Gulyas Oldal and Dr. Chinmoy Biswas for their support during the thesis. Special thanks to my current team member, Nagy Gergely Norbert, for supporting me with his useful insights and especially for translating thesis summary from English to Hungarian.

I would like to acknowledge the collaborative efforts of Dr. Emmanouil Skantzakis and his team from the Foundation for Research and Technology - Hellas, at the Institute of Electronic Structure & Laser (FORTH-IESL), Greece for their contributions that led to an excellent article.

I feel deep sense of gratitude for having forged lifelong friendship while working at ELI-ALPS. I am deeply grateful to Arjun Nayak Puttur, Mathieu Dumergue, Antonia Morabito, Naveed Ahmed, Abhishek Gupta, Monika Agarwal, Swathi Shenoy and Harshitha Nandiga Gopalakrishna for always being there for me and for the joyous time spent together, without which my work would have been more stressful. Special thanks to both Arjun Nayak Puttur and Mathieu Dumergue for their guidance at times, which helped me overcome hurdles in my thesis.

Without the unconditional love and support of my wonderful parents, Madas Srinivas and Madas Meenakshi, I would not be in the position I am today. I am forever indebted to the sacrifices they have made for my well-being and growth. Furthermore, I am grateful to have my sister Roopa, my niece, Maanvi, and my nephew, Daksh in my life. Their unconditional love towards me had helped me overcome many hurdles throughout the thesis. I consider myself fortunate to have my wife, Divya, in my life. Her presence has brought me inner peace. I sincerely thank her for understanding me, supporting me, and always being there for me through thick and thin, without which I could not have finished the thesis on time.

The work presented here could not have been concluded without the financial support of the ELI-ALPS project (GINOP-2.3.6-15-2015-00001), which is financed by the European Union and co-financed by the European Regional Development Fund. I also acknowledge project No. 2019-2.1.13-TÉT-IN-2020-00059, which has been implemented with support provided by the National Research,

Development and Innovation Fund of Hungary, and financed under the 2019-2.1.13-TÉT-IN funding scheme. In addition, I would like to thank KIFÜ, ELI-ALPS IT department and HPC administrators for providing computation resources throughout my thesis work. I acknowledge the support provided by the ÚNKP-23-4 - New National Excellence Program of the Ministry for Culture and Innovation from the Source of the National Research, Development and Innovation Fund.

# Bibliography


[1] Gang Hee Han, Dinh Loc Duong, Dong Hoon Keum, Seok Joon Yun, and Young Hee Lee. "van der Waals Metallic Transition Metal Dichalcogenides". *Chemical Reviews*, 118(13), 2018, pp. 6297–6336. DOI: 10.1021/acs.chemrev.7b00618.

[2] Subhamoy Ghatak, Atindra Nath Pal, and Arindam Ghosh. "Nature of Electronic States in Atomically Thin $MoS_2$ Field-Effect Transistors". *ACS Nano*, 5(10), 2011, pp. 7707–7712. DOI: 10.1021/nn202852j.

[3] Steve M. Young and Charles L. Kane. "Dirac Semimetals in Two Dimensions". *Physical Review Letters*, 115(12), 2015. DOI: 10.1103/physrevlett.115.126803.

[4] K. Ozdogan, M. Upadhyay Kahaly, H. N. Alshareef, and U. Schwingenschlögl. "Anomalous enhancement of the thermoelectric figure of merit by V co-doping of Nb-SrTiO3". *Applied Physics Letters*, 100(19), 2012. DOI: 10.1063/1.4714541.

[5] Eleftherios Goulielmakis, Zhi-Heng Loh, Adrian Wirth, Robin Santra, Nina Rohringer, Vladislav S. Yakovlev, Sergey Zherebtsov, Thomas Pfeifer, Abdallah M. Azzeer, Matthias F. Kling, Stephen R. Leone, and Ferenc Krausz. "Real-time observation of valence electron motion". *Nature*, 466(7307), 2010, pp. 739–743. DOI: 10.1038/nature09212.

[6] M. Upadhyay Kahaly, S. Nazir, and U. Schwingenschlögl. "Band structure engineering and vacancy induced metallicity at the GaAs-AlAs interface". *Applied Physics Letters*, 99(12), 2011. DOI: 10.1063/1.3643049.

[7] M. Upadhyay Kahaly, Shikha Misra, and S. K. Mishra. "Photo-assisted electron emission from illuminated monolayer graphene". *Journal of Applied Physics*, 121(20), 2017, p. 205110. DOI: 10.1063/1.4984318.

[8] Shijing Tan, Adam Argondizzo, Cong Wang, Xuefeng Cui, and Hrvoje Petek. "Ultrafast Multiphoton Thermionic Photoemission from Graphite". *Physical Review X*, 7(1), 2017. DOI: 10.1103/physrevx.7.011004.

[9] Sha Li and R. R. Jones. "High-energy electron emission from metallic nano-tips driven by intense single-cycle terahertz pulses". *Nature Communications*, 7(1), 2016. DOI: 10.1038/ncomms13405.

[10] Young Duck Kim, Yuanda Gao, Ren-Jye Shiue, Lei Wang, Ozgur Burak Aslan, Myung-Ho Bae, Hyungsik Kim, Dongjea Seo, Heon-Jin Choi, Suk Hyun Kim, Andrei Nemilentsau, Tony Low, Cheng Tan, Dmitri K. Efetov, Takashi Taniguchi, Kenji Watanabe, Kenneth L. Shepard, Tony F. Heinz, Dirk Englund, and James Hone. "Ultrafast Graphene Light Emitters". *Nano Letters*, 18(2), 2018, pp. 934–940. DOI: 10.1021/acs.nanolett.7b04324.

[11] Gongtao Wu, Xianlong Wei, Song Gao, Qing Chen, and Lianmao Peng. "Tunable graphene micro-emitters with fast temporal response and controllable electron emission". *Nature Communications*, 7(1), 2016. DOI: 10.1038/ncomms11513.

[12] Mousumi Upadhyay Kahaly and Umesh V. Waghmare. "Contrast in the Electronic and Magnetic Properties of Doped Carbon and Boron Nitride Nanotubes: A First-Principles Study". *The Journal of Physical Chemistry C*, 112(10), 2008, pp. 3464–3472. DOI: 10.1021/jp072340d.

[13] Matthew P. McDonald, Rusha Chatterjee, Jixin Si, Boldizsár Jankó, and Masaru Kuno. "Dimensional crossover in semiconductor nanostructures". *Nature Communications*, 7(1), 2016. DOI: 10.1038/ncomms12726.

[14] Melanie Müller, Alexander Paarmann, and Ralph Ernstorfer. "Femtosecond electrons probing currents and atomic structure in nanomaterials". *Nature Communications*, 5(1), 2014. DOI: 10.1038/ncomms6292.

[15] K. S. Novoselov, A. K. Geim, S. V. Morozov, D. Jiang, Y. Zhang, S. V. Dubonos, I. V. Grigorieva, and A. A. Firsov. "Electric Field Effect in Atomically Thin Carbon Films". *Science*, 306(5696), 2004, pp. 666–669. DOI: 10.1126/science.1102896.

[16] S. Madas, S. K. Mishra, S. Kahaly, and M. Upadhyay Kahaly. "Superior Photo-thermionic electron Emission from Illuminated Phosphorene Surface". *Scientific Reports*, 9(1), 2019. DOI: 10.1038/s41598-019-44823-x.

[17] D. Pacilé, J. C. Meyer, Ç. Ö. Girit, and A. Zettl. "The two-dimensional phase of boron nitride: Few-atomic-layer sheets and suspended membranes". *Applied Physics Letters*, 92(13), 2008. DOI: 10.1063/1.2903702.

[18] Pranab Kumar Das, D. Di Sante, I. Vobornik, J. Fujii, T. Okuda, E. Bruyer, A. Gyenis, B. E. Feldman, J. Tao, R. Ciancio, G. Rossi, M. N. Ali, S. Picozzi, A. Yadzani, G. Panaccione, and R. J. Cava. "Layer-dependent quantum cooperation of electron and hole states in the anomalous semimetal $WTe_2$". *Nature Communications*, 7(1), 2016. DOI: 10.1038/ncomms10847.

[19] Yu Saito, Tsutomu Nojima, and Yoshihiro Iwasa. "Highly crystalline 2D superconductors". *Nature Reviews Materials*, 2(1), 2016. DOI: 10.1038/natrevmats.2016.94.

[20] Guorui Chen, Lili Jiang, Shuang Wu, Bosai Lyu, Hongyuan Li, Bheema Lingam Chittari, Kenji Watanabe, Takashi Taniguchi, Zhiwen Shi, Jeil Jung, Yuanbo Zhang, and Feng Wang. "Evidence of a gate-tunable Mott insulator in a trilayer graphene moiré superlattice". *Nature Physics*, 15(3), 2019, pp. 237–241. DOI: 10.1038/s41567-018-0387-2.

[21] Xiaomeng Liu, Kenji Watanabe, Takashi Taniguchi, Bertrand I. Halperin, and Philip Kim. "Quantum Hall drag of exciton condensate in graphene". *Nature Physics*, 13(8), 2017, pp. 746–750. DOI: 10.1038/nphys4116.

[22] Qing Hua Wang, Kourosh Kalantar-Zadeh, Andras Kis, Jonathan N. Coleman, and Michael S. Strano. "Electronics and optoelectronics of two-dimensional transition metal dichalcogenides". *Nature Nanotechnology*, 7(11), 2012, pp. 699–712. DOI: 10.1038/nnano.2012.193.

[23] A. N. Grigorenko, M. Polini, and K. S. Novoselov. "Graphene plasmonics". *Nature Photonics*, 6(11), 2012, pp. 749–758. DOI: 10.1038/nphoton.2012.262.

[24] Saptarshi Das, Hong-Yan Chen, Ashish Verma Penumatcha, and Joerg Appenzeller. "High Performance Multilayer $MoS_2$ Transistors with Scandium Contacts". *Nano Letters*, 13(1), 2012, pp. 100–105. DOI: 10.1021/nl303583v.

[25] Kelvin J. A. Ooi and Dawn T. H. Tan. "Nonlinear graphene plasmonics". *Proceedings of the Royal Society A: Mathematical, Physical and Engineering Sciences*, 473(2206), 2017, p. 20170433. DOI: 10.1098/rspa.2017.0433.

[26] Hassan A. Hafez, Sergey Kovalev, Klaas-Jan Tielrooij, Mischa Bonn, Michael Gensch, and Dmitry Turchinovich. "Terahertz Nonlinear Optics of Graphene: From Saturable Absorption to High-Harmonics Generation". *Advanced Optical Materials*, 8(3), 2019, p. 1900771. DOI: 10.1002/adom.201900771.

[27] Fengnian Xia, Han Wang, Di Xiao, Madan Dubey, and Ashwin Ramasubramaniam. "Two-dimensional material nanophotonics". *Nature Photonics*, 8(12), 2014, pp. 899–907. DOI: 10.1038/nphoton.2014.271.

[28] Zhipei Sun, Amos Martinez, and Feng Wang. "Optical modulators with 2D layered materials". *Nature Photonics*, 10(4), 2016, pp. 227–238. DOI: 10.1038/nphoton.2016.15.

[29] Francesco Bonaccorso, Luigi Colombo, Guihua Yu, Meryl Stoller, Valentina Tozzini, Andrea C. Ferrari, Rodney S. Ruoff, and Vittorio Pellegrini. "Graphene, related two-dimensional crystals, and hybrid systems for energy conversion and storage". *Science*, 347(6217), 2015. DOI: 10.1126/science.1246501.

[30] Babak Anasori, Maria R. Lukatskaya, and Yury Gogotsi. "2D metal carbides and nitrides (MXenes) for energy storage". *Nature Reviews Materials*, 2(2), 2017. DOI: 10.1038/natrevmats.2016.98.

[31] Karim Khan, Ayesha Khan Tareen, Muhammad Aslam, Yupeng Zhang, Renheng Wang, Zhengbiao Ouyang, Zhongyi Gou, and Han Zhang. "Recent advances in two-dimensional materials and their nanocomposites in sustainable energy conversion applications". *Nanoscale*, 11(45), 2019, pp. 21622–21678. DOI: 10.1039/c9nr05919a.

[32] John R. Schaibley, Hongyi Yu, Genevieve Clark, Pasqual Rivera, Jason S. Ross, Kyle L. Seyler, Wang Yao, and Xiaodong Xu. "Valleytronics in 2D materials". *Nature Reviews Materials*, 1(11), 2016. DOI: 10.1038/natrevmats.2016.55.

[33] Stephan Roche, Johan Åkerman, Bernd Beschoten, Jean-Christophe Charlier, Mairbek Chshiev, Saroj Prasad Dash, Bruno Dlubak, Jaroslav Fabian, Albert Fert, Marcos Guimarães, Francisco Guinea, Irina Grigorieva, Christian Schönenberger, Pierre Seneor, Christoph Stampfer, Sergio O Valenzuela, Xavier Waintal, and Bart van Wees. "Graphene spintronics: the European Flagship perspective". *2D Materials*, 2(3), 2015, p. 030202. DOI: 10.1088/2053-1583/2/3/030202.

[34] Yuan Cao, Valla Fatemi, Shiang Fang, Kenji Watanabe, Takashi Taniguchi, Efthimios Kaxiras, and Pablo Jarillo-Herrero. "Unconventional superconductivity in magic-angle graphene superlattices". *Nature*, 556(7699), 2018, pp. 43–50. DOI: 10.1038/nature26160.

[35] Vinod K. Sangwan and Mark C. Hersam. "Neuromorphic nanoelectronic materials". *Nature Nanotechnology*, 15(7), 2020, pp. 517–528. DOI: 10.1038/s41565-020-0647-z.

[36] Toan Trong Tran, Kerem Bray, Michael J. Ford, Milos Toth, and Igor Aharonovich. "Quantum emission from hexagonal boron nitride monolayers". *Nature Nanotechnology*, 11(1), 2015, pp. 37–41. DOI: 10.1038/nnano.2015.242.

[37] Kenneth Lopata and Niranjan Govind. "Modeling Fast Electron Dynamics with Real-Time Time-Dependent Density Functional Theory: Application to Small Molecules and Chromophores". *Journal of Chemical Theory and Computation*, 7(5), 2011, pp. 1344–1355. DOI: 10.1021/ct200137z.

[38] Mousumi Upadhyay Kahaly, Saibabu Madas, Boris Mesits, and Subhendu Kahaly. "Tunable ultrafast thermionic emission from femtosecond-laser hot spot on a metal surface by control of laser polarization and angle of incidence: A numerical investigation". *Applied Surface Science*, 643, 2024, p. 158668. DOI: 10.1016/j.apsusc.2023.158668.

[39] Shambhu Ghimire and David A. Reis. "High-harmonic generation from solids". *Nature Physics*, 15(1), 2018, pp. 10–16. DOI: 10.1038/s41567-018-0315-5.

[40] T. P. Kaloni, M. Upadhyay Kahaly, Y. C. Cheng, and U. Schwingenschlögl. "Ge-intercalated graphene: The origin of the p-type to n-type transition". *EPL (Europhysics Letters)*, 99(5), 2012, p. 57002. DOI: 10.1209/0295-5075/99/57002.

[41] Mousumi Upadhyay Kahaly. "Defect states in carbon nanotubes and related band structure engineering: A first-principles study". *Journal of Applied Physics*, 105(2), 2009. DOI: 10.1063/1.3072695.

[42] A. Sommerfeld. "Zur Elektronentheorie der Metalle auf Grund der Fermischen Statistik". *Zeitschrift fur Physik*, 47(1-2), 1928, pp. 1–32. DOI: 10.1007/bf01391052.

[43] M Ali Omar. *Elementary solid state physics: principles and applications*. Pearson Education India, 1975.

[44] A. Modinos. *Field, Thermionic, and Secondary Electron Emission Spectroscopy*. Boston, MA: Springer US, 1984. ISBN: 978-1-4757-1450-0. DOI: 10.1007/978-1-4757-1448-7.

[45] John C. Inkson. "The electron-electron interaction near an interface". *Surface Science*, 28(1), 1971, pp. 69–76. DOI: 10.1016/0039-6028(71)90085-9.

[46] J. A. Appelbaum and D. R. Hamann. "Variational Calculation of the Image Potential near a Metal Surface". *Physical Review B*, 6(4), 1972, pp. 1122–1130. DOI: 10.1103/physrevb.6.1122.

[47] Norton D. Lang. "The Density-Functional Formalism and the Electronic Structure of Metal Surfaces". In: *Solid State Physics*. Elsevier, 1974, pp. 225–300. DOI: 10.1016/s0081-1947(08)60204-0.

[48] J Harris and R O Jones. "Dynamical corrections to the image potential". *Journal of Physics C: Solid State Physics*, 6(24), 1973, pp. 3585–3604. DOI: 10.1088/0022-3719/6/24/018.

[49] J Harris and R O Jones. "Image force for a moving charge". *Journal of Physics C: Solid State Physics*, 7(20), 1974, pp. 3751–3754. DOI: 10.1088/0022-3719/7/20/012.

[50] S. C. Miller and R. H. Good. "A WKB-Type Approximation to the Schrödinger Equation". *Physical Review*, 91(1), 1953, pp. 174–179. DOI: 10.1103/physrev.91.174.

[51] Lin Wu. "Modeling of electron emission : its physics and novel applications". PhD thesis. DOI: 10.32657/10356/15554.

[52] E. L. Murphy and R. H. Good. "Thermionic Emission, Field Emission, and the Transition Region". *Physical Review*, 102(6), 1956, pp. 1464–1473. DOI: 10.1103/physrev.102.1464.

[53] Owen Willans Richardson and A. F. A. Young. "The thermionic work-functions and photo-electric thresholds of the alkali metals". *Proceedings of the Royal Society of London. Series A, Containing Papers of a Mathematical and Physical Character*, 107(743), 1925, pp. 377–410. DOI: 10.1098/rspa.1925.0032.

[54] Shigehiko Yamamoto. "Electron emission and work function—Past, present and future". *Applied Surface Science*, 251(1-4), 2005, pp. 4–13. DOI: 10.1016/j.apsusc.2005.03.115.

[55] Saibabu Madas, S. K. Mishra, and Mousumi Upadhyay Kahaly. "Enhanced electron emission from coated metal targets: Effect of surface thickness on performance". *AIP Advances*, 8(3), 2018, p. 035019. DOI: 10.1063/1.5012861.

[56] Ralph Howard Fowler and Lothar Nordheim. "Electron emission in intense electric fields". *Proceedings of the Royal Society of London. Series A, Containing Papers of a Mathematical and Physical Character*, 119(781), 1928, pp. 173–181. DOI: 10.1098/rspa.1928.0091.

[57] R. E. Burgess, H. Kroemer, and J. M. Houston. "Corrected values of Fowler-Nordheim field emission functions v (y) and s (y)". *Physical Review*, 90(4), 1953, pp. 515–515. DOI: 10.1103/physrev.90.515.

[58] Ch. Kleint. "A. Modinos. Field, thermionic, and secondary electron emission spectroscopy. Plenum Press, New York and London 1984, 375 S." *Crystal Research and Technology*, 23(7), 1988, pp. 900–900. DOI: 10.1002/crat.2170230711.

[59] S. G. Christov. "General Theory of Electron Emission from Metals". *physica status solidi (b)*, 17(1), 1966, pp. 11–26. DOI: 10.1002/pssb.19660170103.

[60] Kevin L. Jensen, Patrick G. O'Shea, and Donald W. Feldman. "Generalized electron emission model for field, thermal, and photoemission". *Applied Physics Letters*, 81(20), 2002, pp. 3867–3869. DOI: 10.1063/1.1521491.

[61] H. Vincenti, S. Monchocé, S. Kahaly, G. Bonnaud, Ph. Martin, and F. Quéré. "Optical properties of relativistic plasma mirrors". *Nature Communications*, 5(1), 2014, p. 3403. ISSN: 2041-1723. DOI: 10.1038/ncomms4403.

[62] Ludovic Chopineau, Adrien Denoeud, Adrien Leblanc, Elkana Porat, Philippe Martin, Henri Vincenti, and Fabien Quéré. "Spatio-temporal characterization of attosecond pulses from plasma mirrors". *Nature Physics*, 17(8), 2021, pp. 968–973. DOI: 10.1038/s41567-021-01253-9.

[63] M. Thévenet, A. Leblanc, S. Kahaly, H. Vincenti, A. Vernier, F. Quéré, and J. Faure. "Vacuum laser acceleration of relativistic electrons using plasma mirror injectors". *Nature Physics*, 12(4), 2015, pp. 355–360. DOI: 10.1038/nphys3597.

[64] B. Rethfeld, K. Sokolowski-Tinten, D. von der Linde, and S.I. Anisimov. "Timescales in the response of materials to femtosecond laser excitation". *Applied Physics A*, 79(4-6), 2004, pp. 767–769. DOI: 10.1007/s00339-004-2805-9.

[65] SI Anisimov, BL Kapeliovich, TL Perelman, et al. "Electron emission from metal surfaces exposed to ultrashort laser pulses". *Zh. Eksp. Teor. Fiz*, 66(2), 1974, pp. 375–377.

[66] W. Nessler, S. Ogawa, H. Nagano, H. Petek, J. Shimoyama, Y. Nakayama, and K. Kishio. "Femtosecond Time-Resolved Study of the Energy and Temperature Dependence of Hot-Electron Lifetimes in $Bi_2Sr_2CaCu_2O_{8+\delta}$". *Physical Review Letters*, 81(20), 1998, pp. 4480–4483. DOI: 10.1103/physrevlett.81.4480.

[67] J. Chen, W.-K. Chen, J. Tang, and P. M. Rentzepis. "Time-resolved structural dynamics of thin metal films heated with femtosecond optical pulses". *Proceedings of the National Academy of Sciences*, 108(47), 2011, pp. 18887–18892. DOI: 10.1073/pnas.1115237108.

[68] John A. Tomko, Evan L. Runnerstrom, Yi-Siang Wang, Weibin Chu, Joshua R. Nolen, David H. Olson, Kyle P. Kelley, Angela Cleri, Josh Nordlander, Joshua D. Caldwell, Oleg V. Prezhdo, Jon-Paul Maria, and Patrick E. Hopkins. "Long-lived modulation of plasmonic absorption by ballistic thermal injection". *Nature Nanotechnology*, 16(1), 2020, pp. 47–51. DOI: 10.1038/s41565-020-00794-z.

[69] Kilian R. Keller, Ricardo Rojas-Aedo, Huiqin Zhang, Pirmin Schweizer, Jonas Allerbeck, Daniele Brida, Deep Jariwala, and Nicolò Maccaferri. "Ultrafast Thermionic Electron Injection Effects on Exciton Formation Dynamics at a van der Waals Semiconductor/Metal Interface". *ACS Photonics*, 9(8), 2022, pp. 2683–2690. DOI: 10.1021/acsphotonics.2c00394.

[70] G. D. Mahan. "Thermionic refrigeration". *Journal of Applied Physics*, 76(7), 1994, pp. 4362–4366. DOI: 10.1063/1.357324.

[71] Can Kerse, Hamit Kalaycıoğlu, Parviz Elahi, Barbaros Çetin, Denizhan K. Kesim, Önder Akçaalan, Seydi Yavaş, Mehmet D. Aşık, Bülent Öktem, Heinar Hoogland, Ronald Holzwarth, and Fatih Ömer Ilday. "Ablation-cooled material removal with ultrafast bursts of pulses". *Nature*, 537(7618), 2016, pp. 84–88. DOI: 10.1038/nature18619.

[72] John A. Tomko, Michael J. Johnson, David R. Boris, Tzvetelina B. Petrova, Scott G. Walton, and Patrick E. Hopkins. "Plasma-induced surface cooling". *Nature Communications*, 13(1), 2022. DOI: 10.1038/s41467-022-30170-5.

[73] T.Q. Qiu and C.L. Tien. "Femtosecond laser heating of multi-layer metals—I. Analysis". *International Journal of Heat and Mass Transfer*, 37(17), 1994, pp. 2789–2797. DOI: 10.1016/0017-9310(94)90396-4.

[74] J. E. Beraun J. K. Chen. "NUMERICAL STUDY OF ULTRASHORT LASER PULSE INTERACTIONS WITH METAL FILMS". *Numerical Heat Transfer, Part A: Applications*, 40(1), 2001, pp. 1–20. DOI: 10.1080/104077801300348842.

[75] B.H. Christensen, K. Vestentoft, and P. Balling. "Short-pulse ablation rates and the two-temperature model". *Applied Surface Science*, 253(15), 2007, pp. 6347–6352. DOI: 10.1016/j.apsusc.2007.01.045.

[76] Evgeny L. Gurevich, Yoann Levy, Svetlana V. Gurevich, and Nadezhda M. Bulgakova. "Role of the temperature dynamics in formation of nanopatterns upon single femtosecond laser pulses on gold". *Physical Review B*, 95(5), 2017. DOI: 10.1103/physrevb.95.054305.

[77] Aeaby C. D. and Aditi Ray. "Two-temperature model for ultrafast melting of Au-based bimetallic films interacting with single-pulse femtosecond laser: Theoretical study of damage threshold". *Physical Review B*, 107(19), 2023. DOI: 10.1103/physrevb.107.195402.

[78] Yiming Zhang, Beat Neuenschwander, and Valerio Romano. "Numerical study of the influence of picosecond laser spot size on laser ablation of metal for high laser fluence cases". In: *Laser Applications in Microelectronic and Optoelectronic Manufacturing (LAMOM) XXII*. Vol. 10091. SPIE. 2017, pp. 154–164.

[79] Jie Li, Jian Lu, Andrew Chew, Seunghwoi Han, Jialin Li, Yi Wu, He Wang, Shambhu Ghimire, and Zenghu Chang. "Attosecond science based on high harmonic generation from gases and solids". *Nature Communications*, 11(1), 2020. DOI: 10.1038/s41467-020-16480-6.

[80] P. M. Kraus, B. Mignolet, D. Baykusheva, A. Rupenyan, L. Horný, E. F. Penka, G. Grassi, O. I. Tolstikhin, J. Schneider, F. Jensen, L. B. Madsen, A. D. Bandrauk, F. Remacle, and H. J. Wörner. "Measurement and laser control of attosecond charge migration in ionized iodoacetylene". *Science*, 350(6262), 2015, pp. 790–795. DOI: 10.1126/science.aab2160.

[81] Marc Levenson. *Introduction to Nonlinear Laser Spectroscopy 2e*. Elsevier, 2012.

[82] Paul J. Campagnola, Andrew C. Millard, Mark Terasaki, Pamela E. Hoppe, Christian J. Malone, and William A. Mohler. "Three-Dimensional High-Resolution Second-Harmonic Generation Imaging of Endogenous Structural Proteins in Biological Tissues". *Biophysical Journal*, 82(1), 2002, pp. 493–508. DOI: 10.1016/s0006-3495(02)75414-3.

[83] Bahaa E. A. Saleh and Malvin Carl Teich. *Fundamentals of Photonics*. John Wiley & Sons, Inc., 1991. DOI: 10.1002/0471213748.

[84] Shambhu Ghimire, Anthony D. DiChiara, Emily Sistrunk, Pierre Agostini, Louis F. DiMauro, and David A. Reis. "Observation of high-order harmonic generation in a bulk crystal". *Nature Physics*, 7(2), 2010, pp. 138–141. DOI: 10.1038/nphys1847.

[85] Peter G. Hawkins, Misha Yu. Ivanov, and Vladislav S. Yakovlev. "Effect of multiple conduction bands on high-harmonic emission from dielectrics". *Physical Review A*, 91(1), 2015. DOI: 10.1103/physreva.91.013405.

[86] Georges Ndabashimiye, Shambhu Ghimire, Mengxi Wu, Dana A. Browne, Kenneth J. Schafer, Mette B. Gaarde, and David A. Reis. "Solid-state harmonics beyond the atomic limit". *Nature*, 534(7608), 2016, pp. 520–523. DOI: 10.1038/nature17660.

[87] G. Vampa, T. J. Hammond, N. Thiré, B. E. Schmidt, F. Légaré, C. R. McDonald, T. Brabec, D. D. Klug, and P. B. Corkum. "All-Optical Reconstruction of Crystal Band Structure". *Physical Review Letters*, 115(19), 2015. DOI: 10.1103/physrevlett.115.193603.

[88] Dieter Bauer and Kenneth K. Hansen. "High-Harmonic Generation in Solids with and without Topological Edge States". *Physical Review Letters*, 120(17), 2018. DOI: 10.1103/physrevlett.120.177401.

[89] M. Garg, M. Zhan, T. T. Luu, H. Lakhotia, T. Klostermann, A. Guggenmos, and E. Goulielmakis. "Multi-petahertz electronic metrology". *Nature*, 538(7625), 2016, pp. 359–363. DOI: 10.1038/nature19821.

[90] O. Schubert, M. Hohenleutner, F. Langer, B. Urbanek, C. Lange, U. Huttner, D. Golde, T. Meier, M. Kira, S. W. Koch, and R. Huber. "Sub-cycle control of terahertz high-harmonic generation by dynamical Bloch oscillations". *Nature Photonics*, 8(2), 2014, pp. 119–123. DOI: 10.1038/nphoton.2013.349.

[91] Max Born and Robert Oppenheimer. "Zur quantentheorie der molekeln". *Annalen der physik*, 389(20), 1927, pp. 457–484.

[92] P. Hohenberg and W. Kohn. "Inhomogeneous Electron Gas". *Physical Review*, 136(3B), 1964, B864–B871. DOI: 10.1103/physrev.136.b864.

[93] W. Kohn and L. J. Sham. "Self-Consistent Equations Including Exchange and Correlation Effects". *Physical Review*, 140(4A), 1965, A1133–A1138. DOI: 10.1103/physrev.140.a1133.

[94] A. D. Becke. "Density-functional exchange-energy approximation with correct asymptotic behavior". *Physical Review A*, 38(6), 1988, pp. 3098–3100. DOI: 10.1103/physreva.38.3098.

[95] John P. Perdew and Yue Wang. "Accurate and simple analytic representation of the electron-gas correlation energy". *Physical Review B*, 45(23), 1992, pp. 13244–13249. DOI: 10.1103/physrevb.45.13244.

[96] John P. Perdew, Kieron Burke, and Matthias Ernzerhof. "Generalized Gradient Approximation Made Simple". *Physical Review Letters*, 77(18), 1996, pp. 3865–3868. DOI: 10.1103/physrevlett.77.3865.

[97] Erich Runge and E. K. U. Gross. "Density-Functional Theory for Time-Dependent Systems". *Physical Review Letters*, 52(12), 1984, pp. 997–1000. DOI: 10.1103/physrevlett.52.997.

[98] Dario Rocca. "Time-dependent density functional perturbation theory: new algorithms with applications to molecular spectra". PhD thesis. 2007.

[99] Giovanni Onida, Lucia Reining, and Angel Rubio. "Electronic excitations: density-functional versus many-body Green's-function approaches". *Reviews of Modern Physics*, 74(2), 2002, pp. 601–659. DOI: 10.1103/revmodphys.74.601.

[100] K. Yabana and G. F. Bertsch. "Time-dependent local-density approximation in real time". *Physical Review B*, 54(7), 1996, pp. 4484–4487. DOI: 10.1103/physrevb.54.4484.

[101] A. Block, M. Liebel, R. Yu, M. Spector, Y. Sivan, F. J. Garcıéa de Abajo, and N. F. van Hulst. "Tracking ultrafast hot-electron diffusion in space and time by ultrafast thermomodulation microscopy". *Science Advances*, 5(5), 2019, eaav8965. DOI: 10.1126/sciadv.aav8965.

[102] V. Unikandanunni, F. Rigoni, M. C. Hoffmann, P. Vavassori, S. Urazhdin, and S. Bonetti. "Ultrafast electron dynamics in platinum and gold thin films driven by optical and terahertz fields". *Applied Physics Letters*, 120(2), 2022, p. 021601. DOI: 10.1063/5.0068086.

[103] Alexander Block, Renwen Yu, Ieng-Wai Un, Sebin Varghese, Matz Liebel, Niek F. van Hulst, Shanhui Fan, Klaas-Jan Tielrooij, and Yonatan Sivan. "Observation of Negative Effective Thermal Diffusion in Gold Films". *ACS Photonics*, 2023. DOI: 10.1021/acsphotonics.2c01916.

[104] P. Bresson, J-F. Bryche, M. Besbes, J. Moreau, P-L. Karsenti, P. G. Charette, D. Morris, and M. Canva. "Improved two-temperature modeling of ultrafast thermal and optical phenomena in continuous and nanostructured metal films". *Physical Review B*, 102(15), 2020. DOI: 10.1103/physrevb.102.155127.

[105] C.W. Cheng, S.Y. Wang, K.P. Chang, and J.K. Chen. "Femtosecond laser ablation of copper at high laser fluence: Modeling and experimental comparison". *Applied Surface Science*, 361, 2016, pp. 41–48. DOI: 10.1016/j.apsusc.2015.11.055.

[106] Sergey A. Lizunov, Alexander V. Bulgakov, Eleanor E. B. Campbell, and Nadezhda M. Bulgakova. "Melting of gold by ultrashort laser pulses: advanced two-temperature modeling and comparison with surface damage experiments". *Applied Physics A*, 128(7), 2022. DOI: 10.1007/s00339-022-05733-4.

[107] Zhaoling Qiu, Lan Jiang, Jie Hu, Hailin Liu, Wei Liu, Zihao Li, Shaoqian Wang, Zhicheng Chen, and Xushi Niu. "High-quality micropore drilling by using orthogonally polarized femtosecond double-pulse bursts". *Applied Surface Science*, 613, 2023, p. 156033. DOI: 10.1016/j.apsusc.2022.156033.

[108] Haruyuki Sakurai, Kuniaki Konishi, Hiroharu Tamaru, Junji Yumoto, and Makoto Kuwata-Gonokami. "Direct correlation of local fluence to single-pulse ultrashort laser ablated morphology". *Communications Materials*, 2(1), 2021. DOI: 10.1038/s43246-021-00138-x.

[109] D. M. Riffe, R. M. More, X. Y. Wang, M. C. Downer, D. L. Fisher, T. Tajima, and J. L. Erskine. "Femtosecond thermionic emission from metals in the space-charge-limited regime". *Journal of the Optical Society of America B*, 10(8), 1993, p. 1424. DOI: 10.1364/josab.10.001424.

[110] Bochao Li, Chang Yang, Hao Li, Boyu Ji, Jingquan Lin, and Toshihisa Tomie. "Thermionic emission in gold nanoparticles under femtosecond laser irradiation observed with photoemission electron microscopy". *AIP Advances*, 9(2), 2019, p. 025112. DOI: 10.1063/1.5082772.

[111] Judit Budai, Zsuzsanna Pápa, Péter Petrik, and Péter Dombi. "Ultrasensitive probing of plasmonic hot electron occupancies". *Nature Communications*, 13(1), 2022. DOI: 10.1038/s41467-022-34554-5.

[112] D. M. Riffe and Richard B. Wilson. "Excitation and relaxation of nonthermal electron energy distributions in metals with application to gold". *Physical Review B*, 107(21), 2023. DOI: 10.1103/physrevb.107.214309.

[113] Jörn Bonse and Stephan Gräf. "Maxwell Meets Marangoni—A Review of Theories on Laser-Induced Periodic Surface Structures". *Laser & Photonics Reviews*, 14(10), 2020, p. 2000215. DOI: 10.1002/lpor.202000215.

[114] Zhongyang Wang, Zhengquan Zhang, Zhizhan Xu, and Qiang Lin. "Space-time profiles of an ultrashort pulsed Gaussian beam". *IEEE Journal of Quantum Electronics*, 33(4), 1997, pp. 566–573. DOI: 10.1109/3.563385.

[115] S.Y. Wang, Y. Ren, C.W. Cheng, J.K. Chen, and D.Y. Tzou. "Micromachining of copper by femtosecond laser pulses". *Applied Surface Science*, 265, 2013, pp. 302–308. DOI: 10.1016/j.apsusc.2012.10.200.

[116] S.-S. Wellershoff, J. Hohlfeld, J. Güdde, and E. Matthias. "The role of electron-phonon coupling in femtosecond laser damage of metals". *Applied Physics A Materials Science & Processing*, 69(S1), 1999, S99–S107. DOI: 10.1007/s003399900305.

[117] J. K. Chen, W. P. Latham, and J. E. Beraun. "The role of electron–phonon coupling in ultrafast laser heating". *Journal of Laser Applications*, 17(1), 2005, pp. 63–68. DOI: 10.2351/1.1848522.

[118] Paul McEuen and C Kittel. *Introduction to solid state physics*. Wiley, 2005.

[119] Ana Sousa-Castillo, Óscar Ameneiro-Prieto, Miguel Comesaña-Hermo, Renwen Yu, José M. Vila-Fungueiriño, Moisés Pérez-Lorenzo, Francisco Rivadulla, F. Javier Garcıéa de Abajo, and Miguel A. Correa-Duarte. "Hybrid plasmonic nanoresonators as efficient solar heat shields". *Nano Energy*, 37, 2017, pp. 118–125. DOI: 10.1016/j.nanoen.2017.05.014.

[120] C Kittel. *Introduction to Solid State Physics*. John and Wiley, 1996.

[121] Yuwen Zhang and J. K. Chen. "Ultrafast melting and resolidification of gold particle irradiated by pico- to femtosecond lasers". *Journal of Applied Physics*, 104(5), 2008, p. 054910. DOI: 10.1063/1.2975972.

[122] PG Klemens and RK Williams. "Thermal conductivity of metals and alloys". *International metals reviews*, 31(1), 1986, pp. 197–215.

[123] Touloukian Y. S., Powell R. W., Ho C. Y., and Klemens P. G. "Thermal conductivity, nonmetallic solids". *Thermophysical Properties of Matter*, 1, 1970, pp. 132–137.

[124] J Lombard, F Detcheverry, and S Merabia. "Influence of the electron–phonon interfacial conductance on the thermal transport at metal/dielectric interfaces". *Journal of Physics: Condensed Matter*, 27(1), 2014, p. 015007. DOI: 10.1088/0953-8984/27/1/015007.

[125] Max Born and Emil Wolf. "Basic properties of the electromagnetic field". *Principles of optics*, 44, 1980, pp. 1–70.

[126] A. Vial and T. Laroche. "Comparison of gold and silver dispersion laws suitable for FDTD simulations". *Applied Physics B*, 93(1), 2008, pp. 139–143. DOI: 10.1007/s00340-008-3202-4.

[127] P. G. Etchegoin, E. C. Le Ru, and M. Meyer. "An analytic model for the optical properties of gold". *The Journal of Chemical Physics*, 125(16), 2006, p. 164705. DOI: 10.1063/1.2360270.

[128] P. G. Etchegoin, E. C. Le Ru, and M. Meyer. "Erratum: "An analytic model for the optical properties of gold" [J. Chem. Phys. 125, 164705 (2006)]". *The Journal of Chemical Physics*, 127(18), 2007, p. 189901. DOI: 10.1063/1.2802403.

[129] M Born and E Wolf. *Principles of Optics*. Pergamon Press Ltd., Oxford., 1964.

[130] J. Leng, J. Opsal, H. Chu, M. Senko, and D.E. Aspnes. "Analytic representations of the dielectric functions of materials for device and structural modeling". *Thin Solid Films*, 313-314, 1998, pp. 132–136. DOI: 10.1016/s0040-6090(97)00799-2.

[131] P. B. Johnson and R. W. Christy. "Optical Constants of the Noble Metals". *Physical Review B*, 6(12), 1972, pp. 4370–4379. DOI: 10.1103/physrevb.6.4370.

[132] Neil W Ashcroft and N David Mermin. "Introduction to Solid State Physics". *NY: Brooks Cole*, 1976.

[133] Andrew N. Smith and Pamela M. Norris. "Influence of intraband transitions on the electron thermoreflectance response of metals". *Applied Physics Letters*, 78(9), 2001, pp. 1240–1242. DOI: 10.1063/1.1351523.

[134] D. Fisher, M. Fraenkel, Z. Henis, E. Moshe, and S. Eliezer. "Interband and intraband (Drude) contributions to femtosecond laser absorption in aluminum". *Physical Review E*, 65(1), 2001. DOI: 10.1103/physreve.65.016409.

[135] Han Zhang, Jie Tang, Jinshi Yuan, Yasushi Yamauchi, Taku T. Suzuki, Norio Shinya, Kiyomi Nakajima, and Lu-Chang Qin. "An ultrabright and monochromatic electron point source made of a LaB6 nanowire". *Nature Nanotechnology*, 11(3), 2015, pp. 273–279. DOI: 10.1038/nnano.2015.276.

[136] Guohai Chen and Yenan Song. "Field Emission from Lateral Multiwalled Carbon Nanotube Yarn Emitters". *Frontiers in Materials*, 3, 2016. DOI: 10.3389/fmats.2016.00048.

[137] Zurita Zulkifli, Subramanian Munisamy, Mohd Zamri Mohd Yusop, and Masaki Tanemura. "Effect of surface morphology on the field emission property of ZnO films". *physica status solidi (c)*, 11(7-8), 2014, pp. 1349–1352. DOI: 10.1002/pssc.201300613.

[138] S. Sridhar, L. Ge, C. S. Tiwary, A. C. Hart, S. Ozden, K. Kalaga, S. Lei, S. V. Sridhar, R. K. Sinha, H. Harsh, K. Kordas, P. M. Ajayan, and R. Vajtai. "Enhanced Field Emission Properties from CNT Arrays Synthesized on Inconel Superalloy". *ACS Applied Materials & Interfaces*, 6(3), 2014, pp. 1986–1991. DOI: 10.1021/am405026y.

[139] Jun Jiang, Jihua Zhang, Tao Feng, Bingyao Jiang, Yongjin Wang, Fumin Zhang, Lijuan Dai, Xi Wang, Xianghuai Liu, and Shichang Zou. "Improved emission stability of HfC-coated carbon nanotubes field emitters". *Solid State Communications*, 135(6), 2005, pp. 390–393. DOI: 10.1016/j.ssc.2005.05.018.

[140] P. Ruffieux, O. Gröning, M. Bielmann, and P. Gröning. "Hydrogen chemisorption on sp 2 -bonded carbon: Influence of the local curvature and local electronic effects". *Applied Physics A*, 78(7), 2004, pp. 975–980. DOI: 10.1007/s00339-003-2417-9.

[141] Mousumi Upadhyay Kahaly and Umesh V. Waghmare. "Contrast in the Electronic and Magnetic Properties of Doped Carbon and Boron Nitride Nanotubes: A First-Principles Study". *The Journal of Physical Chemistry C*, 112(10), 2008, pp. 3464–3472. DOI: 10.1021/jp072340d.

[142] Mousumi Upadhyay Kahaly. "Defect states in carbon nanotubes and related band structure engineering: A first-principles study". *Journal of Applied Physics*, 105(2), 2009, p. 024312. DOI: 10.1063/1.3072695.

[143] Hongyuan Yuan, Shuai Chang, Igor Bargatin, Ning C. Wang, Daniel C. Riley, Haotian Wang, Jared W. Schwede, J. Provine, Eric Pop, Zhi-Xun Shen, Piero A. Pianetta, Nicholas A. Melosh, and Roger T. Howe. "Engineering Ultra-Low Work Function of Graphene". *Nano Letters*, 15(10), 2015, pp. 6475–6480. DOI: 10.1021/acs.nanolett.5b01916.

[144] Clare M. Collins, Richard J. Parmee, William I. Milne, and Matthew T. Cole. "High Performance Field Emitters". *Advanced Science*, 3(5), 2016, p. 1500318. DOI: 10.1002/advs.201500318.

[145] Kamarul Aizat Abdul Khalid, Thye Jien Leong, and Khairudin Mohamed. "Review on Thermionic Energy Converters". *IEEE Transactions on Electron Devices*, 63(6), 2016, pp. 2231–2241. DOI: 10.1109/ted.2016.2556751.

[146] Jicai Deng, Lan Zhang, Binglin Zhang, Ning Yao, and Lili Fang. "Field emission from metal-coated nanocrystalline graphitic films". *Journal of Vacuum Science & Technology B: Microelectronics and Nanometer Structures*, 25(2), 2007, p. 536. DOI: 10.1116/1.2539763.

[147] Frederick Seitz. *The modern theory of solids*. McGraw-Hill Book Company, Incorporated, 1940.

[148] Sujeet Agarwal, Shikha Misra, S.K. Mishra, and M.S. Sodha. "Three region model and quantum enhancement of thermionic and photoelectric electron emission from negatively charged metallic surfaces". *Canadian Journal of Physics*, 90(3), 2012, pp. 265–275. DOI: 10.1139/p2012-014.

[149] S. K. Mishra, M. S. Sodha, and Shikha Misra. "Quantum effects in electron emission from and accretion on negatively charged spherical particles in a complex plasma". *Physics of Plasmas*, 19(7), 2012, p. 073705. DOI: 10.1063/1.4737163.

[150] Ajoy K Ghatak and S Lokanathan. *Quantum mechanics: theory and applications*. Macmillan, 2004.

[151] Y. S. Ang and L. K. Ang. "Current-Temperature Scaling for a Schottky Interface with Non-parabolic Energy Dispersion". *Physical Review Applied*, 6(3), 2016. DOI: 10.1103/physrevapplied.6.034013.

[152] Shikha Misra, S. K. Mishra, and M. S. Sodha. "Photoelectric sheath formation around small spherical objects in space". *Physics of Plasmas*, 22(4), 2015, p. 043705. DOI: 10.1063/1.4918946.

[153] Shikha Misra, M. Upadhyay Kahaly, and S. K. Mishra. "Thermionic emission from monolayer graphene, sheath formation and its feasibility towards thermionic converters". *Journal of Applied Physics*, 121(6), 2017, p. 065102. DOI: 10.1063/1.4975788.

[154] Mahendra Singh Sodha. "Introduction". In: *Springer Series on Atomic, Optical, and Plasma Physics*. Springer India, 2014, pp. 3–7. DOI: 10.1007/978-81-322-1820-3_1.

[155] Shikha Misra, M. Upadhyay Kahaly, and S. K. Mishra. "Thermionic emission from monolayer graphene, sheath formation and its feasibility towards thermionic converters". *Journal of Applied Physics*, 121(6), 2017. DOI: 10.1063/1.4975788.

[156] S.K. Mishra, M. Upadhyay Kahaly, and Shikha Misra. "Efficient utilization of multilayer graphene towards thermionic convertors". *International Journal of Thermal Sciences*, 121, 2017, pp. 358–368. DOI: 10.1016/j.ijthermalsci.2017.07.018.

[157] Karthik Thimmavajjula Narasimha, Chenhao Ge, Jason D. Fabbri, William Clay, Boryslav A. Tkachenko, Andrey A. Fokin, Peter R. Schreiner, Jeremy E. Dahl, Robert M. K. Carlson, Z. X. Shen, and Nicholas A. Melosh. "Ultralow effective work function surfaces using diamondoid monolayers". *Nature Nanotechnology*, 11(3), 2015, pp. 267–272. DOI: 10.1038/nnano.2015.277.

[158] J. D. Illige, C. M. Yu, and S. A. Letts. "Metal coatings for laser fusion targets by electroplating". *Journal of Vacuum Science and Technology*, 18(3), 1981, pp. 1209–1213. DOI: 10.1116/1.570895.

[159] Chao Xu, Xiaoqiang Peng, Junfeng Liu, Hao Hu, Tao Lai, Qilin Yang, and Yupeng Xiong. "A High Efficiency and Precision Smoothing Polishing Method for NiP Coating of Metal Mirror". *Micromachines*, 13(8), 2022, p. 1171. DOI: 10.3390/mi13081171.

[160] M. S. Mrudul and Gopal Dixit. "High-harmonic generation from monolayer and bilayer graphene". *Physical Review B*, 103(9), 2021. DOI: 10.1103/physrevb.103.094308.

[161] Zhiyuan Lou, Yinghui Zheng, Candong Liu, Luyao Zhang, Xiaochun Ge, Yanyan Li, Jun Wang, Zhinan Zeng, Ruxin Li, and Zhizhan Xu. "Ellipticity dependence of nonperturbative harmonic generation in few-layer MoS2". *Optics Communications*, 469, 2020, p. 125769. DOI: 10.1016/j.optcom.2020.125769.

[162] Zhen Zhu, Baojuan Dong, Teng Yang, and Zhi-Dong Zhang. *Fundamental Band Gap and Alignment of Two-Dimensional Semiconductors Explored by Machine Learning*. 2017. arXiv: 1708.04766 [cond-mat.mes-hall].

[163] Jingsi Qiao, Xianghua Kong, Zhi-Xin Hu, Feng Yang, and Wei Ji. "High-mobility transport anisotropy and linear dichroism in few-layer black phosphorus". *Nature Communications*, 5(1), 2014. DOI: 10.1038/ncomms5475.

[164] Poya Yasaei, Bijandra Kumar, Tara Foroozan, Canhui Wang, Mohammad Asadi, David Tuschel, J. Ernesto Indacochea, Robert F. Klie, and Amin Salehi-Khojin. "High-Quality Black Phosphorus Atomic Layers by Liquid-Phase Exfoliation". *Advanced Materials*, 27(11), 2015, pp. 1887–1892. DOI: 10.1002/adma.201405150.

[165] L. Cartz, S. R. Srinivasa, R. J. Riedner, J. D. Jorgensen, and T. G. Worlton. "Effect of pressure on bonding in black phosphorus". *The Journal of Chemical Physics*, 71(4), 1979, pp. 1718–1721. DOI: 10.1063/1.438523.

[166] Yonghong Zeng and Zhinan Guo. "Synthesis and stabilization of black phosphorus and phosphorene: Recent progress and perspectives". *iScience*, 24(10), 2021, p. 103116. DOI: 10.1016/j.isci.2021.103116.

[167] Saptarshi Das, Wei Zhang, Marcel Demarteau, Axel Hoffmann, Madan Dubey, and Andreas Roelofs. "Tunable Transport Gap in Phosphorene". *Nano Letters*, 14(10), 2014, pp. 5733–5739. ISSN: 1530-6984. DOI: 10.1021/nl5025535.

[168] Ahmed H. Zewail. "4D ULTRAFAST ELECTRON DIFFRACTION, CRYSTALLOGRAPHY, AND MICROSCOPY". *Annual Review of Physical Chemistry*, 57(1), 2006, pp. 65–103. DOI: 10.1146/annurev.physchem.57.032905.104748.

[169] Hyotcherl Ihee, Vladimir A. Lobastov, Udo M. Gomez, Boyd M. Goodson, Ramesh Srinivasan, Chong-Yu Ruan, and Ahmed H. Zewail. "Direct Imaging of Transient Molecular Structures with Ultrafast Diffraction". *Science*, 291(5503), 2001, pp. 458–462. DOI: 10.1126/science.291.5503.458.

[170] M. Merano, S. Sonderegger, A. Crottini, S. Collin, P. Renucci, E. Pelucchi, A. Malko, M. H. Baier, E. Kapon, B. Deveaud, and J.-D. Ganière. "Probing carrier dynamics in nanostructures by picosecond cathodoluminescence". *Nature*, 438(7067), 2005, pp. 479–482. DOI: 10.1038/nature04298.

[171] Hiromichi Niikura, F. Légaré, R. Hasbani, A. D. Bandrauk, Misha Yu. Ivanov, D. M. Villeneuve, and P. B. Corkum. "Sub-laser-cycle electron pulses for probing molecular dynamics". *Nature*, 417(6892), 2002, pp. 917–922. DOI: 10.1038/nature00787.

[172] Bradley J. Siwick, Jason R. Dwyer, Robert E. Jordan, and R. J. Dwayne Miller. "An Atomic-Level View of Melting Using Femtosecond Electron Diffraction". *Science*, 302(5649), 2003, pp. 1382–1385. DOI: 10.1126/science.1090052.

[173] C. Ropers, D. R. Solli, C. P. Schulz, C. Lienau, and T. Elsaesser. "Localized Multiphoton Emission of Femtosecond Electron Pulses from Metal Nanotips". *Physical Review Letters*, 98(4), 2007. DOI: 10.1103/physrevlett.98.043907.

[174] Peter Hommelhoff, Catherine Kealhofer, and Mark A. Kasevich. "Ultrafast Electron Pulses from a Tungsten Tip Triggered by Low-Power Femtosecond Laser Pulses". *Physical Review Letters*, 97(24), 2006. DOI: 10.1103/physrevlett.97.247402.

[175] B Barwick, C Corder, J Strohaber, N Chandler-Smith, C Uiterwaal, and H Batelaan. "Laser-induced ultrafast electron emission from a field emission tip". *New Journal of Physics*, 9(5), 2007, pp. 142–142. DOI: 10.1088/1367-2630/9/5/142.

[176] J. Dunn, A. L. Osterheld, R. Shepherd, W. E. White, V. N. Shlyaptsev, and R. E. Stewart. "Demonstration of X-Ray Amplification in Transient Gain Nickel-like Palladium Scheme". *Physical Review Letters*, 80(13), 1998, pp. 2825–2828. DOI: 10.1103/physrevlett.80.2825.

[177] S. W. Downey, L. A. Builta, D. C. Moir, T. J. Ringler, and J. D. Saunders. "Simple laser-driven, metal-photocathode electron source". *Applied Physics Letters*, 49(15), 1986, pp. 911–913. DOI: 10.1063/1.97532.

[178] E. Räsänen, A. Castro, J. Werschnik, A. Rubio, and E.K.U. Gross. "Coherent quantum switch driven by optimized laser pulses". *Physica E: Low-dimensional Systems and Nanostructures*, 40(5), 2008, pp. 1593–1595. DOI: 10.1016/j.physe.2007.09.181.

[179] Yong Ma, Jiarui Zhao, Yifei Li, Dazhang Li, Liming Chen, Jianxun Liu, Stephen J. D. Dann, Yanyun Ma, Xiaohu Yang, Zheyi Ge, Zhengming Sheng, and Jie Zhang. "Ultrahigh-charge electron beams from laser-irradiated solid surface". *Proceedings of the National Academy of Sciences*, 115(27), 2018, pp. 6980–6985. DOI: 10.1073/pnas.1800668115.

[180] Guangqing Du, Qing Yang, Feng Chen, Jinhai Si, and Xun Hou. "Insight into the thermionic emission regimes under gold film thermal relaxation excited by a femtosecond pulse". *Applied Surface Science*, 257(21), 2011, pp. 9177–9182. DOI: 10.1016/j.apsusc.2011.05.128.

[181] T. Balasubramni, S.H. Kim, and S.H. Jeong. "Enhanced two temperature modeling of ultrashort laser ablation for the investigation of thermionic emission characteristics". *Applied Surface Science*, 255(24), 2009, pp. 9601–9604. DOI: 10.1016/j.apsusc.2009.04.080.

[182] Guangqing Du, Qing Yang, Feng Chen, Xiangwei Meng, Hao Bian, Jinhai Si, and Xun Hou. "Ultrafast dynamics of thermionic emission on Au film under femtosecond laser excitation". *Applied Physics A*, 112(2), 2012, pp. 479–483. DOI: 10.1007/s00339-012-7436-y.

[183] Dwight E. Gray, ed. *American Institute of Physics Handbook, Third Edition*. McGraw-Hill, New York, 1972.

[184] Hye Kyung Kim, Alexander S. Hyla, Paul Winget, Hong Li, Chelsea M. Wyss, Abraham J. Jordan, Felipe A. Larrain, Joseph P. Sadighi, Canek Fuentes-Hernandez, Bernard Kippelen, Jean-Luc Brédas, Stephen Barlow, and Seth R. Marder. "Reduction of the Work Function of Gold by N-Heterocyclic Carbenes". *Chemistry of Materials*, 29(8), 2017, pp. 3403–3411. DOI: 10.1021/acs.chemmater.6b04213.

[185] Sha Tao and Benxin Wu. "Early-stage effects of residual charges in a metal target on emitted electrons induced by femtosecond laser–metal interactions". *Physics Letters A*, 381(4), 2017, pp. 404–407. DOI: 10.1016/j.physleta.2016.10.060.

[186] G. M. Caruso, F. Houdellier, S. Weber, M. Kociak, and A. Arbouet. "High brightness ultrafast transmission electron microscope based on a laser-driven cold-field emission source: principle and applications". *Advances in Physics: X*, 4(1), 2019, p. 1660214. DOI: 10.1080/23746149.2019.1660214.

[187] R.J. Dwayne Miller. "Mapping Atomic Motions with Ultrabright Electrons: The Chemists' Gedanken Experiment Enters the Lab Frame". *Annual Review of Physical Chemistry*, 65(1), 2014, pp. 583–604. DOI: 10.1146/annurev-physchem-040412-110117.

[188] Michael Förster, Timo Paschen, Michael Krüger, Christoph Lemell, Georg Wachter, Florian Libisch, Thomas Madlener, Joachim Burgdörfer, and Peter Hommelhoff. "Two-Color Coherent Control of Femtosecond Above-Threshold Photoemission from a Tungsten Nanotip". *Physical Review Letters*, 117(21), 2016. DOI: 10.1103/physrevlett.117.217601.

[189] Joel A. Berger, B. L. Rickman, T. Li, A. W. Nicholls, and W. Andreas Schroeder. "Excited-state thermionic emission in III-antimonides: Low emittance ultrafast photocathodes". *Applied Physics Letters*, 101(19), 2012, p. 194103. DOI: 10.1063/1.4766350.

[190] Krystyna Kolwas and Anastasiya Derkachova. "Impact of the Interband Transitions in Gold and Silver on the Dynamics of Propagating and Localized Surface Plasmons". *Nanomaterials*, 10(7), 2020, p. 1411. DOI: 10.3390/nano10071411.

[191] Joao Cunha, Tian-Long Guo, Giuseppe Della Valle, Alemayehu Nana Koya, Remo Proietti Zaccaria, and Alessandro Alabastri. "Controlling Light, Heat, and Vibrations in Plasmonics and Phononics". *Advanced Optical Materials*, 8(24), 2020, p. 2001225. DOI: 10.1002/adom.202001225.

[192] Nathawat Poopakdee, Zeina Abdallah, James W. Pomeroy, and Martin Kuball. "In situ Thermoreflectance Characterization of Thermal Resistance in Multilayer Electronics Packaging". *ACS Applied Electronic Materials*, 4(4), 2022, pp. 1558–1566. DOI: 10.1021/acsaelm.1c01239.

[193] X.J. Zhou, B. Wannberg, W.L. Yang, V. Brouet, Z. Sun, J.F. Douglas, D. Dessau, Z. Hussain, and Z.-X. Shen. "Space charge effect and mirror charge effect in photoemission spectroscopy". *Journal of Electron Spectroscopy and Related Phenomena*, 142(1), 2005, pp. 27–38. DOI: 10.1016/j.elspec.2004.08.004.

[194] Adam M. Darr, Caleb R. Darr, and Allen L. Garner. "Theoretical assessment of transitions across thermionic, field, and space-charge-limited emission". *Physical Review Research*, 2(3), 2020. DOI: 10.1103/physrevresearch.2.033137.

[195] Josh Barnes and Piet Hut. "A hierarchical O(N log N) force-calculation algorithm". *Nature*, 324(6096), 1986, pp. 446–449. DOI: 10.1038/324446a0.

[196] S. Hellmann, K. Rossnagel, M. Marczynski-Bühlow, and L. Kipp. "Vacuum space-charge effects in solid-state photoemission". *Physical Review B*, 79(3), 2009. DOI: 10.1103/physrevb.79.035402.

[197] S. Hellmann, T. Ott, L. Kipp, and K. Rossnagel. "Vacuum space-charge effects in nano-ARPES". *Physical Review B*, 85(7), 2012. DOI: 10.1103/physrevb.85.075109.

[198] L-P Oloff, M Oura, K Rossnagel, A Chainani, M Matsunami, R Eguchi, T Kiss, Y Nakatani, T Yamaguchi, J Miyawaki, M Taguchi, K Yamagami, T Togashi, T Katayama, K Ogawa, M Yabashi, and T Ishikawa. "Time-resolved HAXPES at SACLA: probe and pump pulse-induced space-charge effects". *New Journal of Physics*, 16(12), 2014, p. 123045. DOI: 10.1088/1367-2630/16/12/123045.

[199] Christophe Bauer, Jean-Pierre Abid, and Hubert H. Girault. "Size dependence investigations of hot electron cooling dynamics in metal/adsorbates nanoparticles". *Chemical Physics*, 319(1-3), 2005, pp. 409–421. DOI: 10.1016/j.chemphys.2005.06.040.

[200] Maria Balcerzak. *Noble Metals, Analytical Chemistry of*. 2021. DOI: 10.1002/9780470027318.a2411.pub3.

[201] Masahito Takakuwa, Kenjiro Fukuda, Tomoyuki Yokota, Daishi Inoue, Daisuke Hashizume, Shinjiro Umezu, and Takao Someya. "Direct gold bonding for flexible integrated electronics". *Science Advances*, 7(52), 2021. DOI: 10.1126/sciadv.abl6228.

[202] Min Xu, Yiling Song, Jinping Wang, and Nan Li. "Anisotropic transition metal–based nanomaterials for biomedical applications". *VIEW*, 2(4), 2021, p. 20200154. DOI: 10.1002/viw.20200154.

[203] Max Heyl and Emil J. W. List-Kratochvil. "Only gold can pull this off: mechanical exfoliations of transition metal dichalcogenides beyond scotch tape". *Applied Physics A*, 129(1), 2022. DOI: 10.1007/s00339-022-06297-z.

[204] Alina LaPotin, Kevin L. Schulte, Myles A. Steiner, Kyle Buznitsky, Colin C. Kelsall, Daniel J. Friedman, Eric J. Tervo, Ryan M. France, Michelle R. Young, Andrew Rohskopf, Shomik Verma, Evelyn N. Wang, and Asegun Henry. "Thermophotovoltaic efficiency of 40%". *Nature*, 604(7905), 2022, pp. 287–291. DOI: 10.1038/s41586-022-04473-y.

[205] Rohith Mittapally, Byungjun Lee, Linxiao Zhu, Amin Reihani, Ju Won Lim, Dejiu Fan, Stephen R. Forrest, Pramod Reddy, and Edgar Meyhofer. "Near-field thermophotovoltaics for efficient heat to electricity conversion at high power density". *Nature Communications*, 12(1), 2021. DOI: 10.1038/s41467-021-24587-7.

[206] Dejiu Fan, Tobias Burger, Sean McSherry, Byungjun Lee, Andrej Lenert, and Stephen R. Forrest. "Near-perfect photon utilization in an air-bridge thermophotovoltaic cell". *Nature*, 586(7828), 2020, pp. 237–241. DOI: 10.1038/s41586-020-2717-7.

[207] Jared W. Schwede, Igor Bargatin, Daniel C. Riley, Brian E. Hardin, Samuel J. Rosenthal, Yun Sun, Felix Schmitt, Piero Pianetta, Roger T. Howe, Zhi-Xun Shen, and Nicholas A. Melosh. "Photon-enhanced thermionic emission for solar concentrator systems". *Nature Materials*, 9(9), 2010, pp. 762–767. DOI: 10.1038/nmat2814.

[208] Gang Xiao, Guanghua Zheng, Min Qiu, Qiang Li, Dongsheng Li, and Mingjiang Ni. "Thermionic energy conversion for concentrating solar power". *Applied Energy*, 208, 2017, pp. 1318–1342. DOI: 10.1016/j.apenergy.2017.09.021.

[209] Matthew F. Campbell, Thomas J. Celenza, Felix Schmitt, Jared W. Schwede, and Igor Bargatin. "Progress Toward High Power Output in Thermionic Energy Converters". *Advanced Science*, 8(9), 2021, p. 2003812. DOI: 10.1002/advs.202003812.

[210] Lan Jiang and Hai-Lung Tsai. "Improved Two-Temperature Model and Its Application in Ultrashort Laser Heating of Metal Films". *Journal of Heat Transfer*, 127(10), 2005, pp. 1167–1173. DOI: 10.1115/1.2035113.

[211] Taeho Shin, Samuel W. Teitelbaum, Johanna Wolfson, Maria Kandyla, and Keith A. Nelson. "Extended two-temperature model for ultrafast thermal response of band gap materials upon impulsive optical excitation". *The Journal of Chemical Physics*, 143(19), 2015, p. 194705. DOI: 10.1063/1.4935366.

[212] Dmitriy S. Ivanov and Leonid V. Zhigilei. "Combined atomistic-continuum modeling of short-pulse laser melting and disintegration of metal films". *Physical Review B*, 68(6), 2003. DOI: 10.1103/physrevb.68.064114.

[213] Chengping Wu and Leonid V. Zhigilei. "Microscopic mechanisms of laser spallation and ablation of metal targets from large-scale molecular dynamics simulations". *Applied Physics A*, 114(1), 2013, pp. 11–32. DOI: 10.1007/s00339-013-8086-4.

[214] Mikhail I. Arefev, Maxim V. Shugaev, and Leonid V. Zhigilei. "Kinetics of laser-induced melting of thin gold film: How slow can it get?" *Science Advances*, 8(38), 2022. DOI: 10.1126/sciadv.abo2621.

[215] Sergei Kühn et al. "The ELI-ALPS facility: the next generation of attosecond sources". *Journal of Physics B: Atomic, Molecular and Optical Physics*, 50(13), 2017, p. 132002. DOI: 10.1088/1361-6455/aa6ee8.

[216] NAVINDER SINGH. "TWO-TEMPERATURE MODEL OF NONEQUILIBRIUM ELECTRON RELAXATION: A REVIEW". *International Journal of Modern Physics B*, 24(09), 2010, pp. 1141–1158. DOI: 10.1142/s0217979210055366.

[217] Rambabu Rajpoot, Amol R Holkundkar, and Jayendra N Bandyopadhyay. "Polarization control of attosecond pulses using bi-chromatic elliptically polarized laser". *Journal of Physics B: Atomic, Molecular and Optical Physics*, 54(22), 2021, p. 225401. DOI: 10.1088/1361-6455/ac3f97.

[218] Tingting Fan et al. "Bright circularly polarized soft X-ray high harmonics for X-ray magnetic circular dichroism". *Proceedings of the National Academy of Sciences*, 112(46), 2015, pp. 14206–14211. DOI: 10.1073/pnas.1519666112.

[219] Xavier Andrade, Joseba Alberdi-Rodriguez, David A Strubbe, Micael J T Oliveira, Fernando Nogueira, Alberto Castro, Javier Muguerza, Agustin Arruabarrena, Steven G Louie, Alán Aspuru-Guzik, Angel Rubio, and Miguel A L Marques. "Time-dependent density-functional theory in massively parallel computer architectures: the octopus project". *Journal of Physics: Condensed Matter*, 24(23), 2012, p. 233202. DOI: 10.1088/0953-8984/24/23/233202.

[220] Xavier Andrade, David Strubbe, Umberto De Giovannini, Ask Hjorth Larsen, Micael J. T. Oliveira, Joseba Alberdi-Rodriguez, Alejandro Varas, Iris Theophilou, Nicole Helbig, Matthieu J. Verstraete, Lorenzo Stella, Fernando Nogueira, Alán Aspuru-Guzik, Alberto Castro, Miguel A. L. Marques, and Angel Rubio. "Real-space grids and the Octopus code as tools for the development of new simulation approaches for electronic systems". *Physical Chemistry Chemical Physics*, 17(47), 2015, pp. 31371–31396. DOI: 10.1039/c5cp00351b.

[221] Lixin He, Qingbin Zhang, Pengfei Lan, Wei Cao, Xiaosong Zhu, Chunyang Zhai, Feng Wang, Wenjing Shi, Muzi Li, Xue-Bin Bian, Peixiang Lu, and André D. Bandrauk. "Monitoring ultrafast vibrational dynamics of isotopic molecules with frequency modulation of high-order harmonics". *Nature Communications*, 9(1), 2018. DOI: 10.1038/s41467-018-03568-3.

[222] A. Ferré et al. "Multi-channel electronic and vibrational dynamics in polyatomic resonant high-order harmonic generation". *Nature Communications*, 6(1), 2015. DOI: 10.1038/ncomms6952.

[223] André D. Bandrauk, Szczepan Chelkowski, Shinnosuke Kawai, and Huizhong Lu. "Effect of Nuclear Motion on Molecular High-Order Harmonics and on Generation of Attosecond Pulses in Intense Laser Pulses". *Physical Review Letters*, 101(15), 2008. DOI: 10.1103/physrevlett.101.153901.

[224] Dimitris Charalambidis et al. "The Extreme Light Infrastructure—Attosecond Light Pulse Source (ELI-ALPS) Project". In: *Springer Series in Chemical Physics*. Springer International Publishing, 2017, pp. 181–218. DOI: 10.1007/978-3-319-64840-8_10.

[225] Alberto Castro, Miguel A. L. Marques, and Angel Rubio. "Propagators for the time-dependent Kohn–Sham equations". *The Journal of Chemical Physics*, 121(8), 2004, pp. 3425–3433. DOI: 10.1063/1.1774980.

[226] Miguel A.L. Marques, Micael J.T. Oliveira, and Tobias Burnus. "Libxc: A library of exchange and correlation functionals for density functional theory". *Computer Physics Communications*, 183(10), 2012, pp. 2272–2281. DOI: 10.1016/j.cpc.2012.05.007.

[227] C. Hartwigsen, S. Goedecker, and J. Hutter. "Relativistic separable dual-space Gaussian pseudopotentials from H to Rn". *Physical Review B*, 58(7), 1998, pp. 3641–3662. DOI: 10.1103/physrevb.58.3641.

[228] Umberto De Giovannini, Ask Hjorth Larsen, and Angel Rubio. "Modeling electron dynamics coupled to continuum states in finite volumes with absorbing boundaries". *The European Physical Journal B*, 88(3), 2015. DOI: 10.1140/epjb/e2015-50808-0.

[229] Xi Chu and Shih-I Chu. "Time-dependent density-functional theory for molecular processes in strong fields: Study of multiphoton processes and dynamical response of individual valence electrons of $N_2$ in intense laser fields". *Physical Review A*, 64(6), 2001. DOI: 10.1103/physreva.64.063404.

[230] K. Burnett, V. C. Reed, J. Cooper, and P. L. Knight. "Calculation of the background emitted during high-harmonic generation". *Physical Review A*, 45(5), 1992, pp. 3347–3349. DOI: 10.1103/physreva.45.3347.

[231] Xi Liu, Xiaosong Zhu, Liang Li, Yang Li, Qingbin Zhang, Pengfei Lan, and Peixiang Lu. "Selection rules of high-order-harmonic generation: Symmetries of molecules and laser fields". *Physical Review A*, 94(3), 2016. DOI: 10.1103/physreva.94.033410.

[232] Arjun Nayak et al. "Saddle point approaches in strong field physics and generation of attosecond pulses". *Physics Reports*, 833, 2019, pp. 1–52. DOI: 10.1016/j.physrep.2019.10.002.

[233] C.-G. Wahlström, J. Larsson, A. Persson, T. Starczewski, S. Svanberg, P. Salières, Ph. Balcou, and Anne L'Huillier. "High-order harmonic generation in rare gases with an intense short-pulse laser". *Physical Review A*, 48(6), 1993, pp. 4709–4720. DOI: 10.1103/physreva.48.4709.

[234] John W. Cooper. "Photoionization from Outer Atomic Subshells. A Model Study". *Physical Review*, 128(2), 1962, pp. 681–693. DOI: 10.1103/physrev.128.681.

[235] D. Gabor. "Theory of communication. Part 1: The analysis of information". *Journal of the Institution of Electrical Engineers - Part III: Radio and Communication Engineering*, 93(26), 1946, pp. 429–441. DOI: 10.1049/ji-3-2.1946.0074.

[236] L. Cohen. "Time-frequency distributions-a review". *Proceedings of the IEEE*, 77(7), 1989, pp. 941–981. DOI: 10.1109/5.30749.

[237] O. Melchert, B. Roth, U. Morgner, and A. Demircan. "OptFROG — Analytic signal spectrograms with optimized time–frequency resolution". *SoftwareX*, 10, 2019, p. 100275. DOI: 10.1016/j.softx.2019.100275.

[238] K. Varjú ‖, Y. Mairesse, B. Carré, M. B. Gaarde, P. Johnsson, S. Kazamias, R. López-Martens, J. Mauritsson, K. J. Schafer, PH. Balcou, A. L'huillier, and P. Salières. "Frequency chirp of harmonic and attosecond pulses". *Journal of Modern Optics*, 52(2-3), 2005, pp. 379–394. DOI: 10.1080/09500340412331301542.

[239] Anne Weber, Birger Böning, Björn Minneker, and Stephan Fritzsche. "Generation of elliptically polarized high-order harmonic radiation with bi-elliptical two-color laser beams". *Physical Review A*, 104(6), 2021. DOI: 10.1103/physreva.104.063118.

[240] D. B. Milošević and W. Becker. "X-ray harmonic generation by orthogonally polarized two-color fields: Spectral shape and polarization". *Physical Review A*, 100(3), 2019. DOI: 10.1103/physreva.100.031401.

[241] Ofer Kfir, Patrik Grychtol, Emrah Turgut, Ronny Knut, Dmitriy Zusin, Dimitar Popmintchev, Tenio Popmintchev, Hans Nembach, Justin M. Shaw, Avner Fleischer, Henry Kapteyn, Margaret Murnane, and Oren Cohen. "Generation of bright phase-matched circularly-polarized extreme ultraviolet high harmonics". *Nature Photonics*, 9(2), 2014, pp. 99–105. DOI: 10.1038/nphoton.2014.293.

[242] A M Koushki, R Sadighi-Bonabi, M Mohsen-Nia, and E Irani. "High-order harmonic generation of CO and $N_2$ molecules under linearly- and bi circularly-polarized laser pulses by TD-DFT". *Laser Physics*, 28(7), 2018, p. 075404. DOI: 10.1088/1555-6611/aabed5.

[243] C. J. Joachain, N. J. Kylstra, and R. M. Potvliege. *Atoms in Intense Laser Fields*. Cambridge University Press, 2011. DOI: 10.1017/cbo9780511993459.

[244] Ofer Kfir, Eliyahu Bordo, Gil Ilan Haham, Oren Lahav, Avner Fleischer, and Oren Cohen. "In-line production of a bi-circular field for generation of helically polarized high-order harmonics". *Applied Physics Letters*, 108(21), 2016. DOI: 10.1063/1.4952436.

[245] Ofer Kfir, Patrik Grychtol, Emrah Turgut, Ronny Knut, Dmitriy Zusin, Avner Fleischer, Eliyahu Bordo, Tingting Fan, Dimitar Popmintchev, Tenio Popmintchev, Henry Kapteyn, Margaret Murnane, and Oren Cohen. "Helicity-selective phase-matching and quasi-phase matching of circularly polarized high-order harmonics: towards chiral attosecond pulses". *Journal of Physics B: Atomic, Molecular and Optical Physics*, 49(12), 2016, p. 123501. DOI: 10.1088/0953-4075/49/12/123501.

[246] Edward D. Palik. "Preface". In: *Handbook of Optical Constants of Solids*. Ed. by Edward D. Palik. Burlington: Academic Press, 1997, pp. xvii–xviii. ISBN: 978-0-12-544415-6. DOI: https://doi.org/10.1016/B978-012544415-6.50003-0.

[247] Ofer Kfir, Sergey Zayko, Christina Nolte, Murat Sivis, Marcel Möller, Birgit Hebler, Sri Sai Phani Kanth Arekapudi, Daniel Steil, Sascha Schäfer, Manfred Albrecht, Oren Cohen, Stefan Mathias, and Claus Ropers. "Nanoscale magnetic imaging using circularly polarized high-harmonic radiation". *Science Advances*, 3(12), 2017. DOI: 10.1126/sciadv.aao4641.

[248] J. Jilili, I. Tolbatov, F. Cossu, A. Rahaman, B. Fiser, and M. Upadhyay. Kahaly. "Atomic scale interfacial magnetism and origin of metal-insulator transition in $(LaNiO_3)_n/(CaMnO_3)_m$ superlattices: a first principles study". *Scientific Reports*, 13(1), 2023. DOI: 10.1038/s41598-023-30686-w.

[249] Florian Siegrist, Julia A. Gessner, Marcus Ossiander, Christian Denker, Yi-Ping Chang, Malte C. Schröder, Alexander Guggenmos, Yang Cui, Jakob Walowski, Ulrike Martens, J. K. Dewhurst, Ulf Kleineberg, Markus Münzenberg, Sangeeta Sharma, and Martin Schultze. "Light-wave dynamic control of magnetism". *Nature*, 571(7764), 2019, pp. 240–244. DOI: 10.1038/s41586-019-1333-x.

[250] A. Ferré, C. Handschin, M. Dumergue, F. Burgy, A. Comby, D. Descamps, B. Fabre, G. A. Garcia, R. Géneaux, L. Merceron, E. Mével, L. Nahon, S. Petit, B. Pons, D. Staedter, S. Weber, T. Ruchon, V. Blanchet, and Y. Mairesse. "A table-top ultrashort light source in the extreme ultraviolet for circular dichroism experiments". *Nature Photonics*, 9(2), 2014, pp. 93–98. DOI: 10.1038/nphoton.2014.314.

[251] J. Hofbrucker, A. V. Volotka, and S. Fritzsche. "Maximum Elliptical Dichroism in Atomic Two-Photon Ionization". *Phys. Rev. Lett.*, 121, 5 2018, p. 053401. DOI: 10.1103/PhysRevLett.121.053401.

[252] P. Lambropoulos. "Multiphoton Ionization of One-Electron Atoms with Circularly Polarized Light". *Phys. Rev. Lett.*, 29, 8 1972, pp. 453–455. DOI: 10.1103/PhysRevLett.29.453.

[253] Nicola Mayer, Serguei Patchkovskii, Felipe Morales, Misha Ivanov, and Olga Smirnova. "Imprinting Chirality on Atoms Using Synthetic Chiral Light Fields". *Phys. Rev. Lett.*, 129, 24 2022, p. 243201. DOI: 10.1103/PhysRevLett.129.243201.

[254] Philippe Antoine, Anne L'Huillier, Maciej Lewenstein, Pascal Salières, and Bertrand Carré. "Theory of high-order harmonic generation by an elliptically polarized laser field". *Physical Review A*, 53(3), 1996, pp. 1725–1745. DOI: 10.1103/physreva.53.1725.

[255] Lou Barreau, Kévin Veyrinas, Vincent Gruson, Sébastien J. Weber, Thierry Auguste, Jean-François Hergott, Fabien Lepetit, Bertrand Carré, Jean-Christophe Houver, Danielle Dowek, and Pascal Salières. "Evidence of depolarization and ellipticity of high harmonics driven by ultrashort bichromatic circularly polarized fields". *Nature Communications*, 9(1), 2018. DOI: 10.1038/s41467-018-07151-8.

[256] M.A.L. Marques and E.K.U. Gross. "TIME-DEPENDENT DENSITY FUNCTIONAL THEORY". *Annual Review of Physical Chemistry*, 55(1), 2004, pp. 427–455. DOI: 10.1146/annurev.physchem.55.091602.094449.

[257] Mousumi Upadhyay Kahaly and Umesh V. Waghmare. "Effect of curvature on structures and vibrations of zigzag carbon nanotubes: A first-principles study". *Bulletin of Materials Science*, 31(3), 2008, pp. 335–341. DOI: 10.1007/s12034-008-0053-x.

[258] Nicolas Tancogne-Dejean and Angel Rubio. "Atomic-like high-harmonic generation from two-dimensional materials". *Science Advances*, 4(2), 2018. DOI: 10.1126/sciadv.aao5207.

[259] Beatriz Mendoza-Sánchez and Yury Gogotsi. "Synthesis of Two-Dimensional Materials for Capacitive Energy Storage". *Advanced Materials*, 28(29), 2016, pp. 6104–6135. DOI: 10.1002/adma.201506133.

[260] T. P. Kaloni, M. Upadhyay Kahaly, Y. C. Cheng, and U. Schwingenschlögl. "Mechanism of Si intercalation in defective graphene on SiC". *Journal of Materials Chemistry*, 22(44), 2012, p. 23340. DOI: 10.1039/c2jm35127g.

[261] Baisheng Sa, Yan-Ling Li, Jingshan Qi, Rajeev Ahuja, and Zhimei Sun. "Strain Engineering for Phosphorene: The Potential Application as a Photocatalyst". *The Journal of Physical Chemistry C*, 118(46), 2014, pp. 26560–26568. DOI: 10.1021/jp508618t.

[262] Junbeom Seo, Sungwoo Jung, and Mincheol Shin. "The Performance of Uniaxially Strained Phosphorene Tunneling Field- Effect Transistors". *IEEE Electron Device Letters*, 38(8), 2017, pp. 1150–1152. DOI: 10.1109/led.2017.2712259.

[263] Mohsen Yarmohammadi, Mohammad Mortezaei, and Kavoos Mirabbaszadeh. "Anisotropic basic electronic properties of strained black phosphorene". *Physica E: Low-dimensional Systems and Nanostructures*, 124, 2020, p. 114323. DOI: 10.1016/j.physe.2020.114323.

[264] Geun Ho Ahn, Matin Amani, Haider Rasool, Der-Hsien Lien, James P. Mastandrea, Joel W. Ager III, Madan Dubey, Daryl C. Chrzan, Andrew M. Minor, and Ali Javey. "Strain-engineered growth of two-dimensional materials". *Nature Communications*, 8(1), 2017. DOI: 10.1038/s41467-017-00516-5.

[265] Yeung Yu Hui, Xiaofei Liu, Wenjing Jie, Ngai Yui Chan, Jianhua Hao, Yu-Te Hsu, Lain-Jong Li, Wanlin Guo, and Shu Ping Lau. "Exceptional Tunability of Band Energy in a Compressively Strained Trilayer $MoS_2$ Sheet". *ACS Nano*, 7(8), 2013, pp. 7126–7131. DOI: 10.1021/nn4024834.

[266] Fei Ding, Hengxing Ji, Yonghai Chen, Andreas Herklotz, Kathrin Dörr, Yongfeng Mei, Armando Rastelli, and Oliver G. Schmidt. "Stretchable Graphene: A Close Look at Fundamental Parameters through Biaxial Straining". *Nano Letters*, 10(9), 2010, pp. 3453–3458. DOI: 10.1021/nl101533x.

[267] Wenjing Jie, Yeung Yu Hui, Yang Zhang, Shu Ping Lau, and Jianhua Hao. "Effects of controllable biaxial strain on the Raman spectra of monolayer graphene prepared by chemical vapor deposition". *Applied Physics Letters*, 102(22), 2013, p. 223112. DOI: 10.1063/1.4809922.

[268] Paolo Giannozzi et al. "QUANTUM ESPRESSO: a modular and open-source software project for quantum simulations of materials". *Journal of Physics: Condensed Matter*, 21(39), 2009, p. 395502. DOI: 10.1088/0953-8984/21/39/395502.

[269] Hendrik J. Monkhorst and James D. Pack. "Special points for Brillouin-zone integrations". *Physical Review B*, 13(12), 1976, pp. 5188–5192. DOI: 10.1103/physrevb.13.5188.

[270] P. W. Bridgman. "TWO NEW MODIFICATIONS OF PHOSPHORUS." *Journal of the American Chemical Society*, 36(7), 1914, pp. 1344–1363. DOI: 10.1021/ja02184a002.

[271] Qun Wei and Xihong Peng. "Superior mechanical flexibility of phosphorene and few-layer black phosphorus". *Applied Physics Letters*, 104(25), 2014, p. 251915. DOI: 10.1063/1.4885215.

[272] Liangbo Liang, Jun Wang, Wenzhi Lin, Bobby G. Sumpter, Vincent Meunier, and Minghu Pan. "Electronic Bandgap and Edge Reconstruction in Phosphorene Materials". *Nano Letters*, 14(11), 2014, pp. 6400–6406. DOI: 10.1021/nl502892t.

[273] Can Wang, Qinglin Xia, Yaozhuang Nie, and Guanghua Guo. "Strain-induced gap transition and anisotropic Dirac-like cones in monolayer and bilayer phosphorene". *Journal of Applied Physics*, 117(12), 2015. DOI: 10.1063/1.4916254.

[274] Nicolas Tancogne-Dejean, Oliver D. Mücke, Franz X. Kärtner, and Angel Rubio. "Impact of the Electronic Band Structure in High-Harmonic Generation Spectra of Solids". *Physical Review Letters*, 118(8), 2017. DOI: 10.1103/physrevlett.118.087403.

[275] Lei Jia, Zhiya Zhang, D. Z. Yang, Yanqing Liu, M. S. Si, G. P. Zhang, and Y. S. Liu. "Optical high-order harmonic generation as a structural characterization tool". *Physical Review B*, 101(14), 2020. DOI: 10.1103/physrevb.101.144304.

[276] Rui Qin and Zi-Yu Chen. "Strain-controlled high harmonic generation with Dirac fermions in silicene". *Nanoscale*, 10(47), 2018, pp. 22593–22600. DOI: 10.1039/c8nr07572g.

[277] Nicolas Tancogne-Dejean, Oliver D. Mücke, Franz X. Kärtner, and Angel Rubio. "Ellipticity dependence of high-harmonic generation in solids originating from coupled intraband and interband dynamics". *Nature Communications*, 8(1), 2017. DOI: 10.1038/s41467-017-00764-5.

[278] Eleftherios Goulielmakis and Thomas Brabec. "High harmonic generation in condensed matter". *Nature Photonics*, 16(6), 2022, pp. 411–421. DOI: 10.1038/s41566-022-00988-y.

[279] M. Upadhyay Kahaly and U. Schwingenschlögl. "Enhanced solar light absorption of graphene by interaction with anisole". *Carbon*, 77, 2014, pp. 76–79. DOI: 10.1016/j.carbon.2014.05.005.

[280] Han Liu, Adam T. Neal, Zhen Zhu, Zhe Luo, Xianfan Xu, David Tománek, and Peide D. Ye. "Phosphorene: An Unexplored 2D Semiconductor with a High Hole Mobility". *ACS Nano*, 8(4), 2014, pp. 4033–4041. DOI: 10.1021/nn501226z.

# Own publications

[T1] **Saibabu Madas**, S. K. Mishra, and Mousumi Upadhyay Kahaly. "Enhanced electron emission from coated metal targets: Effect of surface thickness on performance". *AIP Advances*, 8(3), 2018, p. 035019. DOI: 10.1063/1.5012861. **IF: 1.6**

[T2] **Saibabu Madas**, S. K. Mishra, S. Kahaly, and M. Upadhyay Kahaly. "Superior Photothermionic electron Emission from Illuminated Phosphorene Surface". *Scientific Reports*, 9(1), 2019. DOI: 10.1038/s41598-019-44823-x. **IF: 4.9**

[T3] Mousumi Upadhyay Kahaly, **Saibabu Madas**, Boris Mesits, and Subhendu Kahaly. "Tunable ultrafast thermionic emission from femtosecond-laser hot spot on a metal surface by control of laser polarization and angle of incidence: A numerical investigation". *Applied Surface Science*, 643, 2024, p. 158668. DOI: 10.1016/j.apsusc.2023.158668. **IF: 6.7**

[T4] E. Vassakis, **Saibabu Madas**, L. Spachis, T. Lamprou, I. Orfanos, S. Kahaly, M. Upadhyay Kahaly, D. Charalambidis, and E. Skantzakis. "Energetic, tunable, highly elliptically polarized higher harmonics generated by intense two-color counter-rotating laser fields". *Physical Review A*, 2023. **IF: 2.9. Just accepted**

[T5] **Saibabu Madas**, Subhendu Kahaly, and Mousumi Upadhyay Kahaly. *Controlling high-harmonic generation from strain engineered monolayer phosphorene. arXiv.* 2023.

## Other scientific publications

[C1] Manju, Megha Jain, **Saibabu Madas**, Pargam Vashishtha, Parasmani Rajput, Govind Gupta, Mousumi Upadhyay Kahaly, Kemal Özdoğan, Ankush Vij, and Anup Thakur. "Oxygen vacancies induced photoluminescence in $SrZnO_2$ nanophosphors probed by theoretical and experimental analysis". *Scientific Reports*, 10(1), 2020. DOI: 10.1038/s41598-020-74436-8. **IF: 4.9**

**IF**: Impact factor
Cumulative impact factor: 21
**MTMT number**: 10082058